Ultrasound mediated luminescence tomography using contrast agents

Qimei Zhang

Thesis submitted to the University of Nottingham
for the degree of Doctor of Philosophy

March 2016



Abstract

The achievable spatial resolution of fluorescence and bioluminescence imaging in deep tissue is severely limited by strong tissue scattering and absorption. The hybrid technique ultrasound (US) mediated fluorescence tomography (USMFT) has been investigated in the past decade, with the aim to obtain fluorescence images with optical contrast and US resolution. However, the very low modulation depth due to the intrinsic incoherent properties of fluorescence leads to low signal-to-noise ratio. In this thesis, the techniques of US mediated luminescence tomography (USMLT, including US mediated bioluminescence tomgoraphy (USMBLT) and USMFT) are investigated with the aim to improve the effect of US on light intensity via application of contrast agents.

The mechanisms of USMBLT are firstly studied through incorporating the effect of US into NIRFAST, an open source software package for simulation of light propagation. The influence of US on optical properties (reduced scattering coefficient, absorption coefficient, and refractive index) and concentration of source particles are studied. Effects of US pressure, US position, and source particle concentration on the modulation depth are investigated and the signal-to-noise ratio for *in vivo* detection is calculated. It is demonstrated that the dominant effect in the generation of USMBL signal is US induced variation in the concentration of the source particles, and this effect is at least two orders of magnitude greater than that caused by changes in the optical properties. It is also found that modulation depth increases linearly with increase of US pressure. The maximum modulation depth can be obtained when the US focal zone overlaps the bioluminescence source region. The modulated fluence rate increases linearly with increase of the concentration but the modulation depth is independent of the concentration. Results for signal-to-noise ratio calculation confirm the feasibility of applying

USMBLT in preclinical imaging of mice to improve the spatial resolution of bioluminescence imaging.

Secondly, fluorophore labelled microbubbles are studied as a contrast agent to increase the modulation depth of USMFT. Upon application of US the size of the microbubbles oscillate changing the intermolecular distances of the fluorophores labelled on the monolayer of the microbubbles resulting in modulated fluorescence emission intensity. Increased modulation depth is observed both from simulation and experiment. The influence of factors including microbubble radius, US pressure, labelling concentration on the US modulated fluorescence emission are simulated. It was shown that the effects of the three factors are closely related to each other, and it is difficult to decouple their effects. Generally the maximum modulated signal can be obtained within the region $C \in (2\,\text{mol\%}\ 5\,\text{mol\%})$ and $R_0 \in (1.5\,\mu\text{m}\ 5\,\mu\text{m})$. However microbubbles with a higher fluorophore labelling concentration or a bigger radius require higher US pressure to obtain its maximum volumeric oscillation and the highest modulated signal. The results suggest that it is desirable to produce microbubble suspensions with narrow size distribution, so that most of the microbubbles can be labelled by an optimized concentration and exposed to an appropriate US pressure.

Thirdly, liposome based contrast agents are studied for use in USMFT for the first time. Compared with microbubbles, liposomes have the advantages that they have better stability, less US scattering, and can be manufactured with a defined size in nanometer scale. Liposomes are labelled with pyrene which has well-known concentration dependent excimer formation characteristic. The acousto-fluorescence dynamics of liposomes containing lipids with pyrene labelled on the fatty acid tail group (PyPC) and the head group (PyPE) were compared. An increase in excimer emission intensity following exposure to US was observed for both cases studied. The increased intensity and rise time constants were found to be different for the PyPC and PyPE labelled liposomes, and dependent on the applied US pressure and exposure time. The greatest US On-to-Off ratio of excimer emission intensity (130%) and smallest rise time constant (0.33 s) are achieved through the use of the PyPC labelled liposomes. Possible mechanisms underlying the observed increase of the excimer emission intensity in PyPC

system is considered to arise from the "wagging" of acyl chains which involves fast response and requires lower US energy. This is accompanied with the increased lipid lateral diffusivity, mechanisms also active in the PyPE system.

Finally, DiD-DiR labelled liposomes based on fluorescence resonance energy transfer (FRET) are studied. The excitation and emission spectra are located close or within near-infrared window, where the penetration depth is up to several centimetres. Measurements of emisison spectra show that strong FRET and self-quenching exist in the DiD-DiR labelled liposomes. The fluorescence emission intensity changes upon application of US, with the change trend dependent on fluorophore types, detection wavelength, and fluorophore concentration. Line scanning of a tube buried at a depth of 1 cm in a heavily scattering phantom shows a contrast of 8.5% can be obtained using 0.5 mol% DiD-DiR labelled liposomes through detection at DiR emission wavelength (around 740 nm - 790 nm). The resolution can be improved by a factor of 6.3 compared with its no US counterpart. These results suggest that DiD-DiR labelled liposome has potential to be used as contrast agent of USMFT for deep tissue imaging. Further application for *in vivo* imaging is discussed.

Publications arising from this thesis

The following publications have been produced as a result of this work:

Papers:

Zhang, Q.; Moles, M. D.; O'Shea, P.; Morgan, S. P.; Mather, M. L., Nanoscale excimer-emitting liposome contrast agents for ultrasound mediated fluorescence imaging, submitted to PloS ONE. 2016.

Zhang, Q.; Mather, M. L.; Morgan, S. P., Numerical Investigation of the Mechanisms of Ultrasound-modulated Bioluminescence Tomography, IEEE Transactions on Biomedical Engineering, 62(9), 2015, pp. 2135-43.

Conferences:

Conference publications:

Zhang, Q.; Moles, M. D.; Mather, M. L.; Morgan, S. P., Ultrasound modulated fluorescence emission from Pyrene-labelled liposome contrast agents, Twelfth International Conference on Photonics and Imaging in Biology and Medicine (PIBM 2014), 92300Z, Wuhan, China; Jun. 2014.

Conference presentations:

Zhang, Q.; Morgan, S. P.; Mather, M. L., Nanoscale donor-acceptor labelled liposome contrast agent for ultrasound mediated fluorescence tomography, SPIE Medical Imaging, San Diego, USA; Feb. 2016.

Zhang, Q.; Moles, M. D.; Mather, M. L.; Morgan, S. P., Ultrasound modulated optical tomography using liposomes as contrast agents, Optics within Life Sciences 2014 (OWLS 2014), Ningbo, China; Jun. 2014.

Acknowledgements

I would firstly like to express my sincere appreciation to my supervisors Prof. Steve Morgan and Prof. Melissa Mather for their invaluable guidance, support, and patience throughout this project. This thesis would not have been possible without the input from them.

I would also like to thank Dr. Matthew Moles to train me to work in a chemical/biology laboratory. I am very grateful to Prof. Paul O'Shea for giving me the access to his laboratory. Thanks also go to Dr. Haowen Ruan for his guidance to USMOT in the beginning of this project, to Dr. Bowen Tian for his help in making microbubbles, to Dr. Diwei He and Dr. Baptiste Jayet for valuable discussions, and to the technicians in the University of Nottingham for their help. I am also very grateful for access to the University of Nottingham High Performance Computing Facility at late stage of my PhD. I would also like to thank all my colleagues and friends who have made the office a rather interesting and pleasant place to work.

I would like to acknowledge the University of Nottingham and China Scholarship Council (CSC) for the financial support.

Finally, I would like to thank my parents for their endless moral support and Uncle Dr. Erfu Yang for his guidance and suggestions.

List of abbreviations

AOM - Acousto-Optical Modulator

ATP - Adenosine-5′-triphosphate

BLI - Bioluminescence Imaging

BRET - Bioluminescence Resonance Energy Transfer

BLT - Bioluminescence Tomography

CCD - Charge Coupled Device

CPS - Counts Per Second

CW - Continuous Wave

DOPC - Digital Optical Phase Conjugation

ELuc - Enhanced Green-emitting Luciferase

FD - Frequency Domain

FDOT - Fluorescence Diffuse Optical Tomography

FEM - Finite Element Method

FFT - Fast Fourier Transform

Fluc - Firefly Luciferase

FLIM - Fluorescence Lifetime Imaging

FLI - Fluorescence Imaging

FRET - Fluorescence Resonance Energy Transfer

FWHM - Full Width Half Maximum

Gluc - Gaussia Luciferase

HIFU - High Intensity Focused US

HDL - High Density Lipoproteins

IC - Inertial Cavitation

ICCD - Intensified Charge Coupled Device

ICG - Indocyanine Green

LIA - Lock-in Amplifier

Lux - Bacterial Luciferase

Mluc - Metridia Luciferase

MI - Mechanical Index

NA - Numerical Aperture

NIR - Near Infrared

NIRFAST - Near Infrared Fluorescence and Spectral Tomography

PAI - Photoacoustic Imaging

PBS - Phosphate Buffered Saline

PM - Polymeric Micelle

PMT - Photomultiplier Tube

POCL - Peroxyoxalate Chemiluminescence

PRPA - Peak Rarefaction Pressure Amplitude

QD - Quantum Dot

Rluc - Renilla Luciferase

SNR - Signal-to-noise ratio

TD - Time Domain

3D - Three-dimensional

2D - Two-dimensional

TMFT - Temperature Modulated Fluorescence Tomography

TRUE - Time-reversed Ultrasonically Encoded

US - Ultrasound

USMBLT - US Mediated Bioluminescence Tomography

USMCLT - US Mediated Chemiluminescence Tomography

USMFT - US Mediated Fluorescence Tomography

USMLT - US Mediated Luminescence Tomography

USMOT - US Modulated Optical Tomography

USF - US Switchable Fluorescence

Vluc - Vargula Luciferase

Contents

1 Introduction **1**

1.1 A review of fluorescence and bioluminescence imaging techniques and their applications 2

1.1.1 Challenges of fluorescence and bioluminescence imaging 2

1.1.2 Fluorescence microscopy 4

1.1.3 Fluorescence diffuse optical tomography 5

1.1.4 Fluorescence lifetime imaging 7

1.1.5 Bioluminescence imaging 8

1.2 A review of hybrid fluorescence and US imaging techniques 10

1.2.1 US modulated luminescence tomography 11

1.2.2 US switchable fluorescence imaging 16

1.2.3 Time-reversed ultrasonically encoded optical focusing (TRUE) based methods 17

1.3 A review of contrast agents 18

1.3.1 Types of carriers for contrast agents 18

1.3.2 Behaviour of microbubbles and detection techniques 21

1.3.3 Contrast agents in hybrid fluorescence and US imaging 24

1.4 Conclusion 25

1.5 Outline of the thesis 26

2 Numerical investigation of the mechanisms of USMBLT **29**

2.1 Introduction 29

2.2 Simulation methods 31

2.2.1 Forward light modelling 31

2.2.2 Ultrasound modulation of sample optical properties and luciferase concentration 31

2.2.3 Methods of numerical simulation 34

2.2.4 SNR analysis of *in vivo* application of USMBLT 36

2.3 Simulation results 38

2.3.1 Effect of US on optical properties and bioluminescence intensity 39

2.3.2 Calculation of the US modulated bioluminescence fluence rate . 40

2.3.3 Effect of $\Delta\mu_s'/\mu_{s0}'$, $\Delta\mu_a/\mu_{a0}$, $\Delta n/n_0$, and $\Delta q/q_0$ on modulation depth 44

2.3.4 Effect of luciferase concentration on modulation depth 46

2.3.5 Effect of US position on modulation depth 47

2.3.6 SNR analysis of *in vivo* detection 51

2.4 Discussion and conclusions 52

3 Theoretical and experimental evaluation of fluorophore labelled microbubble system **55**

3.1 Introduction 55

3.2 Theoretical models 57

3.2.1 Fluorescence quenching in fluorophore labelled microbubbles . . 57

3.2.2 Volumetric oscillation of microbubble 59

3.2.3 Light propagation in scattering medium 61

3.3 Simulation results 67

3.3.1 Fluorescence quenching in fluorophore labelled microbubbles . . 67

3.3.2 Oscillation of microbubble radius and fluorescence emission intensity when applying US 69
3.3.3 Influence of R_0, C, and P_A 75
3.3.4 Modulation depth and SNR in a scattering phantom 83
3.4 Experiment 88
3.4.1 Preparation of fluorophore labelled microbubbles 89
3.4.2 Experimental setup 90
3.4.3 Scattered and fluorescence signal from fluorophore-labelled microbubble 92
3.5 Discussion and conclusions 96

4 Characterization of pyrene-labelled liposomes contrast agent 99

4.1 Introduction 99
4.2 Preparation of pyrene labelled liposomes 102
4.3 Fluorescence spectrum measurements 104
4.4 Acousto-fluorescence system 107
4.4.1 Experimental setup 107
4.4.2 Calculation of the maximum counting rate 110
4.4.3 Calculation of the concentration distribution 112
4.5 Acousto-fluorescence measurements 115
4.5.1 Movement of lipids in labelled liposomes 116
4.5.2 Comparison of tail labelled liposome with head labelled liposome 117
4.5.3 Possible mechanisms for the US mediated fluorescence variation 120
4.5.4 Short exposure measurements 122
4.6 Cavitation effects at high pressure 125
4.7 Influence of temperature on excimer formation 127

4.8 Discussion and conclusions 130

5 US mediated near infrared fluorescence imaging in scattering phantom using FRET based nanoscale liposomes 132

5.1 Introduction 132

5.2 Preparation of DiD, DiD-DiR or DiR labelled liposomes 137

5.3 Measurements of emission spectra 138

5.4 Quantitative study of FRET and self-quenching 142

5.4.1 Calculation of FRET and self-quenching efficiency 142

5.4.2 Calculation of $FRET1$ and N_{FRET} 148

5.5 Characterization of fluorophores labelled liposomes 151

5.5.1 Measurements of US mediated fluorescence variation 151

5.5.2 Proposed mechanisms of the US mediated fluorescence variation 155

5.5.3 Influence of US pressure and exposure time 161

5.6 Line scanning imaging in heavily scattering phantom 163

5.6.1 Line scanning imaging 163

5.7 Discussion and conclusions 179

6 Conclusions and future work 181

6.1 Conclusions 181

6.2 Future work 184

6.2.1 Experimental demonstration of USMBLT 185

6.2.2 Further optimization of fluorophore labelled liposomes 185

6.2.3 Further investigation of mechanisms 187

6.2.4 Future applications of USMFT using fluorophore labelled liposomes 189

6.2.5 Concerns for *in vivo* imaging using the fluorophore labelled liposomes 190

References **192**

Appendix A **218**

Appendix B **222**

Appendix C **225**

Appendix D **227**

Appendix E **230**

CHAPTER 1

Introduction

Luminescence refers to the creation of light by processes that do not involve heat. Fluorescence and bioluminescence are the two most commonly used luminescence in biomedical studies. Compared with the currently available imaging technologies such as magnetic resonance imaging (MRI), computed tomography (CT), positron emission tomography (PET), and single photon emission computed tomographic (SPECT), optical imaging is a modality that is cost-effective, rapid, and relatively easy to use [1]. Biomedical optical imaging can provide quantitative information on structural, functional, and physiological changes from microscopic to macroscopic levels for objective diagnosis and follow-up [2, 3]. The main limitation of optical imaging is that high imaging resolution cannot be achieved in deep imaging depth, due to the strong scattering of optical radiation in tissues. This thesis investigated a hybrid luminescence and ultrasound (US) imaging technique named US mediated luminescence tomography (USMLT). In this chapter, USMLT is introduced and compared with other techniques. Pure fluorescence imaging (FLI) and bioluminescence imaging (BLI) techniques are firstly reviewed with a focus on deep tissue imaging in Section 1.1. Several hybrid techniques that combine luminescence with US are then reviewed and compared in Section 1.2. Section 1.3 introduces the contrast agents used in biomedical optical imaging, especially in the field of hybrid fluorescence and US imaging. The work and the contributions of this thesis are then outlined in Section 1.5.

1.1 A review of fluorescence and bioluminescence imaging techniques and their applications

During the past several decades, the use of both FLI and BLI has increased tremendously and had a dramatic effect on biomedical research. In fluorescence based techniques, an external light source is used to excite fluorescent agents (genetic reporters or exogenous fluorophores), which undergo a transition from an excited electronic stage to a lower electronic state and emit light. The emitted fluorescence is measured by highly sensitive optical detectors such as photomultiplier tube (PMT) or charge coupled device (CCD) camera using appropriate filters to eliminate the bleed-through of the excitation light. The detected signals are then analyzed or post-processed to form an image. Fluorescence has been used for many years for *in vitro* studies such as cell culture assays, cell imaging, and tissue staining. In recent years it has been extended to *in vivo* imaging, offering non-invasive visualization of specific biological processes in their intact and native physiological state [4–6].

BLI is another optical imaging technique used for *in vivo* small animal studies. It is based on the generation of visible light by a living organism (bioluminescence) resulting from enzyme-catalysed oxidation reactions [7]. Bioluminescence is a biological process that requires an enzyme known as luciferase, a substrate known as luciferin, and oxygen. Some luciferases require other cofactors such as adenosine-5'-triphosphate (ATP) and magnesium ions for full activity [8]. Bioluminescence can be regarded as a particular case of chemiluminescence, which designates emission of light through a process that a chemical reaction produces the electronically excited substance. Bioluminescence therefore does not require external light source and there is an extremely low background [1].

1.1.1 Challenges of fluorescence and bioluminescence imaging

An important part of the research conducted in FLI and BLI is concerned with the development of novel approaches to improve sensitivity, spatial resolution, optical contrast, imaging depth and quantification. These parameters are limited by factors in-

cluding tissue scattering, absorption, and autofluorescence.

Scattering

It has been widely known that the use of FLI and BLI in biological studies is limited by the interaction of light with various tissue components (e.g. membranes, different organelles). In the fluorescence process, both the excitation light and the emitted fluorescence are scattered, which blurs fluorescence images limiting the spatial resolution. Therefore, for example, when the tumor foci are close to one another, the fluorescence signals can merge and appear to originate from a single focus. The scattering is stronger for fluorophore targets that located further away from the illumination and detection area [6]. Another important consequence of scattering is that it amplifies the effect of the wavelength-varying absorption spectrum of tissue chromophores, causing the shape and peak position of detected fluorescence spectra to vary depending on the path lengths traversed by light in tissue [6]. In the bioluminescence process there is no excitation source, therefore scattering only along light propagation path from bioluminescence emitters to the detector needs to be considered. As a result BLI has a higher sensitivity than FLI for *in vivo* detection of tumors and is able to indicate microscopic nodules [9].

Absorption and near-infrared (NIR) spectral window

Absorption by tissue components, in particular hemoglobin, in the wavelength (λ) range of visible light limits effective light penetration to hundreds of micrometers up to a few millimeters. Other biological components such as water and lipids are optically transparent from the visible to the NIR spectral range but strongly absorb light in the infrared. The combined absorption of these components translates into an optical imaging window from approximately $\lambda = 650\,\text{nm}$ to $1000\,\text{nm}$ where the absorption coefficient of tissue is at a minimum [10]. Tissue scattering also decreases with increase of wavelength [11]. For example, the reduced scattering coefficient of skin decreased from around $7\,\text{mm}^{-1}$ at $\lambda = 500\,\text{nm}$ to around $1\,\text{mm}^{-1}$ at $\lambda = 900\,\text{nm}$ [12]. Therefore for whole-body or deep tissue imaging fluorescence and bioluminescence emitters that operate in the NIR spectral window are desired. Extensive efforts have been devoted to study such imaging agents [13, 14]. Fluorophores are relatively more available than

bioluminescence emitters and there have been a wide variety of NIR fluorophores developed (e.g. indocyanine green [15], porphyrin [16–18], BODIPY analogs [19]). There have been also some red-shifted luciferin analogues investigated, but most of them peaked at wavelengths less than 645 nm [20]. Recently a novel firefly luciferin analogue has been synthesized which produces different far-red to NIR bioluminescence emission, with a maximum wavelength up to 706 nm [20]. Apart from the novel synthesized luciferin, bioluminescence resonance energy transfer (BRET) has also been investigated as a method to obtain NIR emission [21]. It was demonstrated recently that when directly attached to a NIR quantum dot (QD), firefly *P. pyralis* luciferase variants (PPyGRTS) can effectively transfer bioluminescence energy with high efficiency to the QDs (emitting wavelength maximum: $\lambda = 800\,\text{nm}$) [22].

Autofluorescence

Another challenge of FLI is autofluorescence, namely, the natural emission of light by biological structures when they have absorbed light. There are a wide variety of molecules present in living tissue (e.g. tryptophan, NADH, pyridoxine, collagen) that can act as biochemical sources of autofluorescence [6]. Desired fluorescence signals from the molecular probe of interest can be masked or overestimated by non-specific signals coming from autofluorescence of tissue. Because the main excitation peaks for the natural fluorophores are usually in the visible part of the spectrum, their impact on NIR FLI is often negligible [6]. This is another advantage of NIR fluorophores. In the case of BLI, there is no autofluorescence since no external light source is used, and there is virtually no endogenous bioluminescence from mammalian cells. This intrinsic characteristic of BLI makes it a more sensitive technique than FLI with the ability to detect tumors significantly earlier [1]. However signal levels of bioluminescence are typically two to three orders of magnitude smaller than that of FLI [6]. This makes US modulation of bioluminescence extremely difficult to achieve.

1.1.2 Fluorescence microscopy

Fluorescence microscopy can provide cellular and subcellular images with extraordinary contrast, single-molecule sensitivity, and molecular specificity with high spatial

resolution (approximately 200 nm laterally, 500 nm axially [23]). With the increasing availability of genetically encoded fluorescent proteins, dyes, and probes, it has become possible to image protein expression, localization, and a large number of activities in living cells in real time. Confocal fluorescence microscopy has the ability to produce thin (0.5 to 1.5 µm) optical sections through fluorescent specimens and allows researchers to render three-dimensional (3D) images. To improve the resolution further, some super-resolution fluorescence microscopy techniques such as saturated structured-illumination microscopy, stimulated emission depletion microscopy, photoactivated localization microscopy, fluorescence photoactivation localization microscopy, and stochastic optical reconstruction microscopy have been developed [24].

There are also some microscopic methodologies for *in vivo* imaging developed, namely, intravital microscopy. Their imaging depth is however limited to less than several hundred microns due to tissue absorption and scattering. Multiphoton microscopy is one of the advanced high-resolution intravital microscopy techniques. It is based on the simultaneous absorption of two or more low-energy infrared photons whose combined energies induce fluorescence in the visible range in a thin optical section. As infrared photons can penetrate much deeper into tissue, imaging depth of multiphoton microscopy can get up to 1 mm [25]. To obtain high resolution fluorescence images in tissue deeper than 1 mm, hybrid techniques need to be used.

1.1.3 Fluorescence diffuse optical tomography

In vivo FLI has become one of the most commonly used pre-clinical imaging modality during the last decade. It can be classified into two general categories: planar and tomographic imaging [26]. The planar imaging technique can produce two-dimensional (2D) images of a plane parallel to the sources and detectors but can not resolve depth. Fluorescence diffuse optical tomography (FDOT, the other name is fluorescence molecular tomography) employs a setup comprising of a set of external light sources and detectors. By applying a tomographic scheme FDOT can provide cross-sectional or full 3D images. The reconstruction of the distribution of fluorophore concentration and lifetime requires the use and the inversion of an appropriate model accounting for both

photon propagation (e.g., diffusion approximation of the radiative transport equation) and fluorescence phenomena. The reconstruction is always ill-posed and underdetermined, and requires complex and computer-intensive reconstruction techniques. Since FDOT is fast for data acquisition, noninvasive, highly sensitive, and relatively inexpensive as compared with MRI and CT, it is very attractive for longitudinal studies of small animals to track disease progression or drug effects in real time [27].

FDOT approaches can be broadly classified into three groups according to how the tissue is illuminated and the light is detected [28]:

- Continuous-wave (CW) FDOT is based on the measurement of the attenuation of a steady state excitation light.

- Frequency-domain (FD) FDOT is based on the measurement of the phase and demodulation of an amplitude-modulated excitation typically at frequencies of 100 MHz - 1 GHz.

- Time-resolved FDOT exploits the measurement of the temporal distortion of an excitation photon pulses in the 100 fs - 100 ps range.

CW approaches are generally operationally simpler and significantly more economic and robust. Therefore they are the most frequently used one to recover the concentration. FD and time-resolved FDOT are more costly, but can derive fluorescence lifetime. Generally, they provide data set with a higher information content which can lead to better reconstruction of deeply-embedded markers [28].

There have been several approaches developed to improve the resolution and contrast of the reconstructed FDOT images. Recently Pontus Svenmarker et. al. [27] used upconverting nanoparticles doped with rare-earth elements as a contrast agent. It was demonstrated that the spatial resolution of FDOT can be improved by exploiting the nonlinear optical emission properties of the upconverting core-shell nanoparticles as compared with the traditionally used fluorophores. Besides, the upconverting core-shell nanoparticles are able to emit anti-stokes-shift light at two emission bands. Using

this as *a priori* estimation of the fluorescence source depth, an improved image detectability for FDOT was reported [29]. However, the resolution of FDOT is still limited to several millimeters.

1.1.4 Fluorescence lifetime imaging

The fluorescence lifetime refers to the average time a fluorophore with a single exponential decay function stays in its excited state before emitting a photon [30]. It is usually in the range of a few nanoseconds. Importantly, fluorescence lifetime is an intrinsic property of the probe molecule and is independent of the excitation light or the fluorophore concentration. However, fluorescence lifetime is sensitive to many environmentally factors, such as local pH, blood supply, viscosity, temperature, refractive index, ion concentrations, and the presence of fluorescence quenchers [31]. Therefore the technique of FLIM can be used to measure the molecular environment parameters, protein-interaction, and the metabolic state of cells and tissues. Advantageously compared with intensity based techniques, fluorescence lifetime based techniques are less dependent on the local concentration of the probe. It is inherently robust in the presence of absorption and scattering, and does not have to cope with problems like donor bleed-through, directly excited acceptor fluorescence, or photobleaching.

The nanosecond time resolution required to measure fluorescence lifetimes can be obtained either in time domain (TD) or in FD. TD-FLIM uses a short pulsed light source (femtoseconds to picoseconds) to excite the sample and the subsequent fluorescence emission decay is recorded directly by high-speed detectors (most frequently PMT). FD-FLIM uses a modulated light source of a certain frequency to excite the sample. The phase shift and amplitude demodulation ratio of the emission relative to the excitation are measured by gain-modulated detector. Fluorophores with longer lifetimes have larger phase shift and smaller amplitude demodulation ratio [32].

Extracting lifetime requires time-resolved measurements at the nanosecond timescales, increasing the complexity of the source/detector systems. Therefore applications of FLIM have been restricted mainly to microscopy techniques. In very recent years whole-body lifetime-based molecular imaging also emerged. Rice et. al. [33, 34] ap-

plied TD fluorescence lifetime multiplexing for the detection of fluorescent proteins in whole animals. Lifetime multiplexing was demonstrated to be able to separate extrinsic fluorescence from autofluorescence. Different fluorescent proteins placed under the skin of a nude mouse, or in deeper organs such as lungs and brain were simultaneously discriminated. This is enabled through separation of the decay portion of a measured TD signal into individual components based on their distinct fluorescence lifetimes. A greater than 20-fold improvement in sensitivity compared with conventional CW imaging was obtained. However, because identical fluorophores have the same lifetimes, it is difficult to distinguish these fluorophores which will limit the achievable resolution of FLIM. Another disadvantage of the lifetime based imaging is that it cannot be used for BLI.

1.1.5 Bioluminescence imaging

Compared with fluorescence, there is no autofluorescence background for bioluminescence, therefore high detectability down to a few emitted photons is possible [35]. BLI provides valuable insight into biological processes in intact cells and small animal models. It has been widely applied in cancer research including tumor detection, tumor metastasis, tumor angiogenesis, and induced apoptosis [36]. For drug research, BLI has been used to image protein-protein interaction, protease activity, and protein degradation in entire mouse physiological systems for large-scale screening of compounds which may be potential future drugs [36]. BLI has also been used to monitor gene expression and cellular events in living tissues [37].

As mentioned in Section 1.1.3, traditional planar imaging techniques cannot obtain 3D localization information such as the depth of the internal light source. Therefore, bioluminescence tomography (BLT) is being investigated based on conventional planar BLI and appropriate models of light transfer in biological tissues. The goal of BLT is to locate and quantitatively reconstruct the 3D distribution of the intensity and position of the internal light source using the scattered bioluminescent signal on the surface of the small animal [36]. Due to the insufficient measurements and highly diffusive nature of the photon propagation within biological tissues, BLT reconstruction is still a

very challenging ill-posed inverse problem. There have been several reconstruction algorithms developed to address the ill-posed problem. Multispectral information was shown to provide a means of estimating the depth of a bioluminescence object, due to the wavelength-dependent attenuation of tissue [38, 39]. A Conjugate Gradient-based reconstruction algorithm using Compressive Sensing was designed to take advantage of the sparsity of the bioluminescent source [40]. It was shown that Compressive Sensing based method improves reconstruction quality, and allows robust reconstruction from minimal data sets. However, the current reconstruction methods for BLT are usually time-consuming and require large amounts of storage memory. Besides, it usually requires knowledge of the optical properties of the heterogeneous tissue to perform BLT. Therefore combination of BLT with another modalities such as diffuse optical tomography is required. However this makes the imaging procedure more complex. In addition, the resolution of BLT is still limited to millimeter scales.

Bioluminescence brightness

The signal-to-noise ratio (SNR) of BLI is dependent on the amount of light detected by the photon counting system. Therefore it is critical to use a luciferase that can generate the brightest bioluminescence inside the tissue.

Widely distributed in nature, luciferase from the North American firefly (Fluc), Renilla (Rluc), and bacterial (Lux) are the three most commonly studied luciferases. Fluc and Rluc cells can generate brighter bioluminescence than that of Lux cells. Besides, variations, stabilized and red-shifted Fluc and Rluc are available. A detailed comparison of advantages and disadvantages of the three different luciferases can be found in [41]. Other popular luciferases include Gaussia luciferase (Gluc), Metridia luciferase (Mluc), and Vargula luciferase (Vluc).

To date, elaborate efforts have been directed to establish novel luciferases from new organisms that can exert a bright, stable, red-shifted bioluminescence [42]. It was experimentally observed that the surface radiance coming out of a mouse can reach 1×10^8 photons/s/cm^2/sr using human brain metastatic NSCLC cell line PC9-BrM3 marked with the Fluc reporter gene [43]. It can even reach 2×10^{11} photons/s/cm^2/sr with self-inactivating lentiviral construct encoding Fluc, green fluorescent protein (GFP),

EF-1α promoter and a 2A ribosomal skip sequence, given an intraperitoneal injection of 150 mg/Kg of D-luciferin into preclinical mice [44]. It was shown that in combination with different mutations of Fluc, it is possible to obtain luciferases that generate more than 10-fold higher luminescence intensity than the wild-type enzyme [45, 46]. An enhanced luciferase (ELuc) emitting green light from cloned Brazilian click beetle *Pyrearinus termitilluminans* can also exhibit a light signal in mammalian cells that is over 10-fold stronger than Fluc, by optimizing its cDNA sequence for mammalian expression [47]. An engineered luciferase derived from a deep sea shrimp *Oplophorus gracilirostris*, named NanoLuc, was established by Hall et al [48]. This luciferase molecule can emit approximately 150-fold brighter and more stable bioluminescence than that of RLuc or FLuc in the presence of a novel coelenterazine analogue. In addition, BRET has been applied to help solving the low brightness of bioluminescence. In BRET process, the excited energy of a luminescent substrate is transferred to an acceptor by a Förster resonance energy transfer (FRET) mechanism. The brightest luminescent protein reported to date is Nano-lantern [49]. It is a chimera of enhanced Rluc and Venus, a fluorescent protein with high BRET efficiency.

Other factors that can influence the light level indirectly include cellular luciferase concentration (affected by reporter gene transfer, promotor activity, enzyme degradation, and enzyme velocity), bioavailability of luciferin (affected by injection route, cardiovascular condition and blood composition, intracellular luciferin concentration), local oxygen/ATP concentrations, and wavelength of bioluminescence [50]. It was shown that a quantitative correlation between signal strength and cell numbers exists for all luciferases [41]. It was claimed that the most effective means of obtaining a brighter signal is to increase the concentration of active luciferase, while decreasing the deactivated one as much as possible [51].

1.2 A review of hybrid fluorescence and US imaging techniques

Deep-tissue (> 1 mm) optical imaging is desirable for both tissue biology studies and preclinical/clinical applications. However, the resolution obtained by pure FLI and

BLI techniques, described in the previous section, is very limited due to scattering and absorption of the tissue. Since US in the few MHz range has a scattering coefficient two to three orders of magnitude less than light [52] in tissue, it can achieve relatively higher spatial resolution (below a few hundred micrometers). Thus, hybrid fluorescence and US imaging techniques combining the advantages of fluorescence and ultrasonic imaging have been investigated during the past years. The relevant techniques include US modulated fluorescence [53, 54], US modulated luminescence [55], Ultrasound switching fluorescence (USF) imaging [56–60], and Time-reversed ultrasonically encoded (TRUE) optical focusing based methods [61–63]. It is worth mentioning here that this thesis will only discuss techniques related with FLI or BLI. Therefore US modulated optical tomography (USMOT) using coherent light source based on intensity modulation through fluctuation of speckles formed by multiply scattered coherent light is not reviewed. Photoacoustic imaging (PAI) is also a hybrid technique combining optics and US. However, PAI is based on detection of acoustical (rather than fluorescence) emission converted from optical absorption by chromophores (intrinsic tissue chromophores or exogenous probes). It is not a FLI technique thus is not reviewed in this section.

1.2.1 US modulated luminescence tomography

Since it was first proposed in 2006 [53], US modulated fluorescence tomography (USMFT) has been explored as an approach to increase spatial resolution of FLI while maintaining a large imaging depth. Briefly, a focused US beam is used to modulate the diffused fluorescence photons in the focal zone in an illuminated scattering medium. The photons are modulated at the US frequency. By detecting and analyzing the modulated fluorescence photons, fluorescence images can be obtained with ultrasonic spatial resolution.

A current difficulty of USMFT is the weak modulation of light it produces, quantified by measurement of the modulation depth which is defined as the ratio between modulated light intensity (AC signal) and unmodulated light intensity (DC signal). The modulation depth for USMFT is of the order of 10^{-6} to 10^{-4} [64] as compared to 10^{-3}

that is achieved using a coherent laser source. In relation to imaging, the low modulation depth leads to low SNR and thus high sensitivity is required for the signal detection device.

To improve the detection sensitivity of USMFT, a quadrature detection approach which cross-correlates (phase shift by π) the US and a gain-modulated, image-intensified CCD camera was proposed [65]. The optical detector was gain-modulated at the US frequency and the photon intensity was measured as the phase shift, $\Delta\Phi$, between the US and detector-gain driving signals varied. The maximum and minimum photon intensity were measured at $\Delta\Phi = 0^\circ$ and 180° respectively. Thus, the photon modulation was $M = I_{\Delta\Phi=0^\circ} - I_{\Delta\Phi=180^\circ}$. The results showed a 0.2 % modulation depth and therefore further proved the feasibility of using USMFT to obtain high spatial resolution fluorescence images. An increase of the modulation depth was also demonstrated by using microbubbles. This will be discussed in detail later in Section 1.3.3.

US modulated bioluminescence tomography (USMBLT) is still under investigation but the first US modulated chemiluminescence tomography (USMCLT) experiment has been demonstrated [55]. Similar with fluorescence, chemiluminescence is also incoherent light. The difference is that no external light source is used. In the published USMCLT experiment [55] 'Glow sticks' were embedded in tissue phantoms and the chemiluminescence was modulated by US and detected using a lock-in amplifier. The SNR was found to be 80 and the image lateral resolution was 3 mm at a depth of 7 mm within a tissue phantom with a scattering coefficient of 30 cm^{-1}. This represents a 3.5 times improvement in spatial resolution compared to the conventional unmodulated optical tomography. US enhanced chemiluminescence was demonstrated recently [66]. A peroxyoxalate chemiluminescence (POCL) system that includes ICG fluorophores to chemically excite the pigment was stimulated by US irradiation and the ultrasonically enhanced chemiluminescence intensity was detected. The ultrasonic enhancement mechanism of POCL was assumed to involve sonochemistry, which prompts the POCL reaction that originates in acoustic cavitation derived from the locally emerging high-temperature and high-pressure region. The full-width-at-half-maximum (FWHM) of the scanning image of a buried target is 6 mm and is comparable with the applied US

focal zone. A drawback of this technique is that it involves application of hydrogen peroxide (H_2O_2, the free radicals produced by socochemical reaction may also produce long-lived hydrogen peroxide [67]). This molecular is long-lived once produced and has been shown to induce single strand breaks in DNA *in vitro* [67]. Therefore damage of cell and tissue may be caused by this technique and it is unlikely to be directly applicable to biological systems.

In addition to the imaging systems, method for reconstruction of the density of a luminescent source in a highly scattering medium was also presented [68]. The reconstruction algorithm is based on the solution to a hybrid inverse source problem for the diffusion equation. The modulation of absorption coefficient, diffusion coefficient and refractive index by a standing plane wave were included in the diffusion approximation. It was shown that it is possible to uniquely reconstruct the source. Multiple US frequencies were used to increase the number of measurements and aid reconstruction. The spatial resolution was improved by a factor of 10 compared with conventional BLI.

These studies provide support to the hypothesis that US modulation techniques could be applied to improve the spatial resolution of BLT. The inverse problems of USM-CLT/USMBLT and BLT are very similar as they aim to determine the source density distribution in the volume from boundary measurements of multiple scattered light based on radiative transport. Therefore it can be expected that existing BLT reconstruction algorithms can be modified to be applied in the reconstruction of USM-CLT/USMBLT. The US will introduce small changes in optical properties in local regions of the tissue sample and so the measured data will be weighted by these changes. By scanning US and detecting US modulated luminescence signal, it is possible to increase the number of measurements that is expected to aid in overcoming the ill-posed inverse problem. As mentioned earlier bioluminescence has a low light level, therefore US modulation of bioluminescence is very difficult to achieve.

Mechanisms of US modulation

There are three mechanisms for US modulation of incoherent light proposed at the time of writing.

- The first mechanism is similar to the mechanism of USMOT. An US field will induce periodic displacement of tissue components such as scatters, absorbers, and surrounding medium. This can lead to variations of the scattering coefficient, absorption coefficient and refractive index and a further modulation of the exit location and amplitude of the exit photons [69, 70]. Specifically, the modulated reduced scattering coefficient and absorption coefficient can lead to a change of the total mean free path and thus lead to a change of the exit location of survival photons [69]. The modulated refractive index can distort the light path that would be straight in the absence of US modulation and thus also affect the exit location [69]. The modulated signal due to modulation of the exit position is contributed by individual survival photons that periodically switch the status from being detected to not being detected, while the modulated signal due to modulation of amplitude is by the weight change due to ultrasonic modulation [69]. The modulated exit position and amplitude can thereby lead to a modulation of both the excitation and the emission light. For a coherent light source the modulated scattering coefficient and refractive index can also lead to a change of the optical path length and thus induce a phase variation. A modulated excitation light and the corresponding modulated fluorescent signals can thereby be induced for the coherent light. Results obtained from a Monte Carlo based method [69] show that the modulation depth contributed by the variations of exit location are three orders of magnitude higher than that contributed by amplitude variations, but two to three orders lower than that due to phase variation for coherent light.

- Secondly, when the fluorophore concentration is low, the oscillation of ultrasonic pressure can cause an oscillation of the fluorophore concentration, thus inducing a modulated emission light [71].

- Thirdly, when the fluorophore concentration is high or quenchers are adopted, the quenching efficiency will be modulated as a result of the volumetric oscillation of the contrast agent used, or the position vibration of polystyrene microspheres [71]. The quenching from volume oscillation is by the non-radiative en-

ergy transfer between fluorophores, and thus is termed as FRET quenching. The quenching from polystyrene microspheres is due to physical interactions (collisions) between the emission light with microspheres, and thus termed as collisional quenching [72].

The effect of variation of the refractive index, scattering coefficient, and the fluorescence concentration on the modulated fluorescence signals was investigated by solving a modified diffusion equation describing the photon transport in the US field with a finite element method (FEM) [70]. The simulation results show that the power of the modulated fluorescence signal is proportional to the square of the acoustical pressure, and the pressure is proportional to the variation of the refractive index or fluorescence concentration. The linear relationship between the modulated fluorescence signal and the average fluorophore concentration in the US focal zone were also demonstrated in previous experiments by Kobayashi et al. [73] and theoretically derived by Yuan et al. by solving a rate equation with a two-energy-level model [71].

For the third mechanism, the quenching can be self-quenching (SQ) or quenching caused by other quenchers. It was demonstrated that when the distance between two fluorophores is short enough (around nm order) and the Stokes shift is not large enough - i.e. there is an overlap of the excitation spectrum and the emission spectrum - the excitation-induced emission will be absorbed by an adjacent fluorophore, and thus results in SQ [74]. If fluorophores are labelled on the outside surface of a contrast agent such as microbubbles, the ultrasonic field can lead to a volume vibration of the microbubbles and thus cause a change of the fluorophore concentration, therefore modulating the SQ efficiency. If quenchers exist, the fluorescence lifetime will decrease drastically with change of concentration, due to energy transfer to quenchers [75]. Therefore the fluorescence modulation efficiency could be significantly improved when using microbubbles labelled with fluorophores and quenchers.

1.2.2 US switchable fluorescence imaging

US switchable fluorescence (USF) imaging [56, 59, 60] (or Temperature modulated fluorescence tomography (TMFT) [57, 58]) is another hybrid approach which combines the high intensity focused US (HIFU) as heater of the medium with the recently emerged temperature-sensitive fluorescence contrast agents. If the temperature of the medium in the US focus is increased above a temperature threshold, the fluorescence emission intensity and lifetime can change significantly, while the fluorophores outside of the focal volume remain the same. By scanning the HIFU across the interest region, the distribution of the contrast agents can be imaged in a highly scattering medium. The resolution depends on the physical size of the volume in which fluorophores are switched on, and it is generally smaller than the physical size of the US focus. Using contrast agent with excellent switching properties, a spatial resolution beyond the acoustic diffraction limit was obtained [59]. It was estimated that the thermal bio-effect can be ignored however non-thermal bio-effect is higher than requirement of United States Food and Drug Administration (FDA) for human diagnostic US scanners.

A light-pulse-delay-technique was used in TMFT to reduce the unwanted background fluorescence generated by non-100%-off fluorophores [56]. The light-pulse-delay-technique took advantage of the increased lifetime of the switched-on fluorophores. Briefly, the sample was illuminated by pico-second (ps) light pulses, and only late arriving photons were acquired. Compared with FDOT, the depth-to-resolution of TMFT was improved from ~ 10 to ~ 100.

Despite the above mentioned advantages of TMFT, it has one main issue that it has very strict requirement for the sensitivity of the applied contrast agent to temperature. For example, the contrast agents need to have a large ON-to-OFF ratio in fluorescence intensity, a sharp temperature transition between OFF and ON states and an adjustable switching threshold [59]. In addition, thermal and non-thermal bio-effects of HIFU can be a concern for further preclinical and clinical *in vivo* applications and need to be fully investigated.

1.2.3 Time-reversed ultrasonically encoded optical focusing (TRUE) based methods

Time reversed ultrasonically encoded (TRUE) optical focusing is a novel concept proposed in 2011 [76] that aims at delivering light into any dynamically defined location inside a scattering medium by combining ultrasonic encoding with optical phase conjugation [77–80]. In this method, a laser light is first modulated by an acousto-optic modulator (AOM). The light illuminating the scattering medium thus has a frequency of $f_s = f_o - f_a$ (f_o and f_a are the laser frequency and the frequency shift due to AOM respectively). A focused ultrasonic wave of the same frequency f_a traverses the medium and modulates part of the diffused light to frequencies of $f_+ = f_o$ and $f_- = f_o - 2f_a$. The light coming out from the medium gets to a selective phase conjugation mirror and only the light with the frequency of f_+ is holographically recorded and reversed (phase conjugated). Due to the reversibility principle of beam path, the time reversed light traces back the original trajectories and therefore is focused to the US focal zone. The US focal zone therefore becomes a virtual source inside a scattering medium.

The application of TRUE method in FLI was later demonstrated by several groups [61–63]. A focused fluorescence excitation by phase conjugating the US modulated photons travels 'time reversely' to the US focus. All of the fluorescence emission from the focused excitation was collected and measured outside the tissue. Fluorescent objects located at 2.5 mm depth inside biological tissue were imaged with a lateral resolution of 36 µm $\times$ 52 µm and an axial resolution of 657 µm was achieved [61]. There are two phase conjugation schemes. One is the digital optical phase conjugation scheme (DOPC) which consists of a CMOS camera and a spatial light modulator [61, 62]. The other is the analogue scheme which uses phase conjugation mirror made from photorefractive polymer or $Bi_{12}SiO_{20}$ crystal [63]. Both of the two schemes have been used in FLI with TRUE method. DOPC has the advantage that it has high optical gain therefore can provide high excitation light to excite detectable fluorescence at the US focus, which is compensation for the low US modulation efficiency. However, the response time of analogue phase conjugation mirror is faster than DOPC [63].

One limitation of TRUE method is that it can only be used with coherent light source. Therefore it can not be used for BLI or FLI involving incoherent excitation light. Besides, the holographic methods require more complex setup than USMFT and TMFT. In addition, the dynamic *in vivo* environment might make time reversal of light vulnerable. This is because the movements due to breathing, heart beats, or blood flow can change the speckle and make the hologram blurred. However, this might be overcome by using a Nd:YVO4 laser crystal which has a response time around 50 µs, faster than the speckle decorrelation time of around 1 ms caused by movements [81, 82].

A comparison of Fluorescence microscopy, FDOT, FLIM, BLT, USMLT(USMFT, USMCLT, USMBLT), USF, and TRUE are shown in Table 1.1.

1.3 A review of contrast agents

Contrast agents are materials that interact with the incident radiation to produce visible changes on the resulting imaging [83]. For high resolution imaging in deep tissues contrast agents are the other major component apart from the optical imaging system. Ideal contrast agents should significantly increase contrast, effectively improve imaging depth or accuracy, and provide molecular specific information [84]. In this thesis various contrast agents are used to increase modulation depth or On-to-Off ratio of USMLT. In this section contrast agents in the field of biomedical optical imaging are reviewed, with a focus on hybrid fluorescence and US imaging.

1.3.1 Types of carriers for contrast agents

It is essential to use microparticulate carriers to reach the required local concentration of fluorophores that respond to US. Using carriers can also improve the effective delivery of contrast agents. Carriers that offer potential for USMLT include microbubbles, liposomes, and polymeric micelles (PMs), all of which comprising a core-shell structure.

Microbubbles are gas-liquid emulsions consisting of a gaseous core surrounded by a

Table 1.1: Comparison of FLI and BLI techniques.

Techniques	Resolution	Imaging depth	Advantages	Disadvantages
Fluorescence microscopy	∼200 nm laterally, 500 nm axially [23]	∼1 mm at best	• Extraordinary contrast • Single-molecule sensitivity • Molecular specificity • Real time observation	• Limited to superficial surface
FDOT	∼1 mm at a depth of 1 cm	Up to several centimetres	• Deep tissue *in vivo* imaging	• Poor spatial resolution • Require complex and computer intensive reconstruction algorithms
BLT	Several millimetres	Up to several centimetres	• Deep tissue in vivo imaging • No autofluorescence background, higher sensitivity/detectability/SNR compared with FLI	• Require complex and computer intensive reconstruction algorithms • Signal level generally not as bright as fluorescence • Limited NIR bioluminescence emitters
USMLT	US resolution, less than 1 mm	Up to several centimetres	• High resolution for deep tissue imaging	• Require contrast agents to improve modulation depth
USF	∼ 260 µm at a depth of 2 cm [56]	Up to several centimetres	• High resolution for deep tissue imaging	• Possible bioeffect due to temperature increase • Strict requirement for contrast agents
TRUE	36 µm × 52 µm laterally, 657 µm axially at 2.5 mm [61]	2.5 mm [61]	• High resolution for deep tissue imaging	• Not applicable for BLI • Vulnerable to dynamic *in vivo* environment

shell and are usually 1 to 10 micrometer in size. They are widely used for US imaging as the gaseous core causes a very high echogenic response that results in a high contrast on US images [85]. However, microbubbles stay within the vascular compartment and do not leak into the extra-vascular space due to their micro size. This limits their use for imaging of disease that are reflected on vascular endothelial cells only [86].

Liposomes are artificial vesicles of spherical shape. Their size can be controlled to vary from 30 nm to several micrometres [87]. They can pass through vascular walls due to their nanoscale size, making microvascular targeting possible, even potentially overcome the formidable blood brain barrier. Liposomes are formed traditionally from amphiphilic lipids. One part of the lipid molecule is hydrophilic and the other part is hydrophobic [88]. Therefore lipids have the unique feature to be able to compartmentalise and solubilise both hydrophilic and hydrophobic materials by nature. Liposomes have a liquid core surrounded by either a single lipid layer, bilayer, or multiple layers. The liquid inside the liposomes can be the same or different from the outside buffer. Due to their small size, amphipathic characteristic, good biocompatibility and biodegradablity, liposomes have been widely used in biomedical, biophysics, and biochemistry research. For example, liposomes were used to construct animal cell models filled with biochemicals and macromolecules [89]. They were used widely as drug delivery carriers in medicine and pharmacology [88, 90, 91]. Incorporated with other functionalised lipids or proteins, liposomes are being developed for the creation of biosensing platforms [92, 93].

PMs are colloidal dispersions built from amphiphilic block copolymers (i.e., polymers consisting of a hydrophilic segment and a hydrophobic segment) [94]. The copolymers self assemble in aqueous environments into spherical structures (micelles) at concentrations equal to or above critical micelle concentration. Contrast/imaging agent can be partitioned into the hydrophobic core and utilize it as a depot, while the hydrophilic shell is a physical barrier that prevents micelle aggregation. PMs have been extensively developed to deliver various drugs. By modifying the block copolymers to contain chemicals that can sense a specific biological environment, PMs may be designed for target site triggered drug release [95]. Similar to liposomes, the size of PMs can be con-

trolled to be in the range of several tens to hundreds of nanometers. This significantly affects their longevity in the blood stream and their efficiency of tumor tissue accumulation and penetration. The disadvantages of PMs include difficult polymer synthesis and possible chronic liver toxicity due to slow metabolic process [96].

1.3.2 Behaviour of microbubbles and detection techniques

Microbubbles behaviour

Microbubbles will be forced into a volume pulsation when insonified by an US wave [97]. In the simplest situation, the size of the microbubble decreases in the positive half cycle of the US wave, and increases in the negative half cycle. For small amplitude of US, the size oscillation varies linearly with the US pressure. However, for high amplitude of US, non-linearity can occur with size compression either weaker [98] or stronger [99] relative to expansion. The scattered US can have harmonic, sub-harmonic, and ultra-harmonic components, with the frequency being integer multiples of the fundamental frequency (harmonic frequency), half the driving frequency (sub-frequency), and odd multiples of half the driving frequency (ultra-frequency) respectively [100]. If the amplitude increases further, the insonified microbubbles will expand from the negative pressure of the US field and collapse in a violent and rapid implosion, which is termed as inertial cavitation(IC) [101]. All of the three states (linear, non-linear, and collapse) of microbubble oscillation can be used for imaging. On the other hand, bubble collapse can radiate damaging shock waves and cause the gas within the bubble to attain a very high temperature (thousands of Kelvin), thereby producing large numbers of potentially highly destructive free radicals [102]. Therefore it is very important to understand the transmission threshold between these states.

The mechanical index (MI) [102] was defined to determine IC, which is the estimated peak refaction pressure amplitude (PRPA, in MPa) divided by the square root of the US frequency (in MHz). An MI of 0.4 is the lowest IC value for which inertial cavitation is expected from diagonostic US when optimally sized gas bodies are present and an MI of 1.9 is the highest diagnostic US maximum exposure limit allowed by the FDA [103]. The MI uses only two factors: PRPA and US frequency. Church [102] investigated the

effect of another factor, pulse length, on MI and gave a modified MI equation which divides the above mentioned MI by the IC threshold for multiple cycles of US. The IC threshold was based on the maximum radius criterion ($R_{max} = 2R_0$) and the maximum temperature criterion ($T_{max} = 5000\,\mathrm{K}$), which are the lowest and highest thresholds for air bubbles [102]. Bader et al. [103] developed the cavitation index (I_{CAV}) to predict the thresholds for microbubble rupture and stable cavitation (sustained small amplitude oscillations of the bubble about its equilibrium). The cavitation index is defined as PRPA (in MPa) divided by the US frequency (in MHz). Briefly, if the US frequency is between 800 kHz and 14 MHz, microbubble rupture is predicted for $I_{CAV} > 0.02$, and stable cavitation is predicted for $0.09 \leq I_{CAV} \leq 0.45$. The former is most appropriate for contrast imaging applications, and the latter is associated with potential beneficial bioeffects. An 'IC dose' was also defined to quantitatively measure the amount of the IC activity [101, 104]. The IC dose was calculated as the cumulated root mean squared broadband noise amplitude in the frequency domain. It was investigated that IC dose will increase with increase of PRPA, pulse length, exposure time and the microbubbles concentration [104].

Detection techniques

The most direct detection technique of oscillation of microbubbles is using ultra-fast framing camera or a streak camera combined with an optical microscope. Optical observations of microbubbles during acoustic insonation have been performed by several groups to study microbubble dynamics [105–109]. Capturing the compression, expansion and breakup of the microbubbles requires a frame rate in the MHz range and shutter duration of the order of tens to hundreds of nanoseconds. Precise timing of the frames with respect to a streak image, which shows the diameter of a single microbubble as a function of time, allows visualization of the changes of the microbubble. The effect of microbubble resting diameter, pressure, frequency, and pulse length of US on microbubble oscillation and rupture can thus be analyzed. The parameters available for optical analysis include resting diameter, peak expansion diameter, and final state of microbubble.

However, these cameras are very expensive, with approximately $200,000 - $400,000

for an ultra-fast framing camera and $150,000 - $200,000 for a fast streak camera, depending on the performance of the system [110]. This prohibits their widespread use for high throughput microbubble characterization.

Light scattering techniques have been developed as a practical and simple approach for measurements of dynamics of an individual microbubble [111–113]. The intensity of the light scattered by an individual microbubble depends on factors such as particle size, optical index of refraction of the core and shell, and shell thickness. A pressure induced size change of the microbubble will induce a change in the scattered light intensity which can be predicated using a combination of Mie theory with microbubble models. A microfluidic system combined with the light scattering technique was developed which enables the measurement of single echogenic microbubble response to US excitation isolated from physical boundaries and other microparticles [114]. This system facilitates high throughput for collection of large data sets suitable for statistical analysis.

It was also demonstrated that the acoustic response at a certain distance away from the microbubble is a function of its radial dynamics [106, 115]. The emitted pressure wave from the microbubble can be determined from the second time derivative of its volume [115]. By recording the acoustic response using a calibrated transducer, the radius response can thereby be reconstructed. However, this requires a known initial microbubble radius and thus needs to be combined with an optical system. Compared with the ultra-high speed optical detection, the acoustical method is better for detecting higher harmonic oscillations which can be invisible in the optical method. However low frequency features might not be captured due to a limited frequency band of the transducer.

Another technique, demonstrated recently, is an optical confocal microscope system combined with an ultra-bright xenon strobe light with a $\sim 10\,\mu m$ pulse width, and a ps-gated and intensified charge-coupled device (ICCD) camera [110]. The strobe light illuminated the microbubbles and the transmitted light through the microbubble was detected by the ICCD camera triggered and gated on/off by a high rate imager. The camera capture window was determined by the gate-on width, which was set to be

20 ns. The gating pulse was subsequently delayed by 100 ns relative to each ultrasonic pulse and a total of 44 images were acquired to reconstruct a bubble oscillation. Using this system the high-speed microbubble oscillation along both the horizontal (via the ICCD camera) and vertical (via the confocal system) directions can be investigated on the same microbubble.

1.3.3 Contrast agents in hybrid fluorescence and US imaging

It has been demonstrated that USMF signal can be significantly enhanced when mixing the fluorescent solution with microbubbles [116]. This is because the volumetric oscillation of microbubbles can significantly enhance the modulation of the fluorophore concentration. The possibility of enhancing the USMF signals in a scattering medium further by labeling microbubbles with fluorophores and quenchers was analyzed theoretically [54] and demonstrated experimentally [117, 118]. The fluorophore-labelled microbubbles were produced by conjugating NHS-ester-attached fluorophores on the surface of amine-functionalized microbubbles [117], or by using ATTO 532-NHS and ATTO 647N-NHS dyes as donor and acceptor respectively [118]. A similar maximum modulation depth of around 35% was observed at 405 kPa US pressure for the two protocols. Compared with the considerably low USMF signal when no microbubbles are adopted, the modulation depth is much increased. This is because the oscillation of microbubbles leads to a change of the proximity of fluorophores on the surface of the microbubble, which further modulates the fluorescence emission.

There have been several contrast agents investigated for TMFT, such as the temperature-sensitive ICG loaded pluronic nanocapsules [58]. As the temperature changes, the interiors of nanocapsules made from PM (Pluronic-F127) change their hydrophobicity/hydrophilicity, which in turn changes the quantum efficiency and lifetime of the loaded ICG. Another contrast agent used in TMFT is the DBD-AA (fluorophore) labelled PNIPAM (thermosensitive polymer) [56]. The fluorescence lifetime of the DBD-AA remains almost constant at $\sim$4 ns when the environment temperature is below 31 °C, and jumps quickly to another constant of $\sim$14 ns for temperatures above 32 °C. Similar results are found for the fluorescence intensity, which is $\sim$4-5 times stronger

when temperature is above 32 °C than for temperature below 31 °C. More recently a family of contrast agents for TMFT based on ICG-encapsulated PNIPAM NPs was synthesized [59]. These contrast agents have good switching properties and enable FLI in deep tissue beyond the acoustic diffraction limit. However, several problems need to be overcome before these TMFT contrast agents can be used for further *in vivo* applications. For example, the transition temperature of these contrast agents need to be adjusted to be slightly higher than the body temperature (37 °C).

Endogenous optical absorption (e.g. hemoglobin) may be used to form various types of images in PAI. To further enhance the absorption or obtain complementary information, contrast agents have been investigated substantially. Fluorescent molecules such as ICG, Alexa Fluor 750, and Evans blue were used directly or were conjugated to other contrast agents. Noble metal nanoparticles (e.g. gold nanoparticles) have been widely used due to their intrinsic optical absorption, spectral selectivity based on their surface plasmon resonance, effective surface modification, and high technical maturity of preparation [84]. The optical properties and optical-to-acoustic conversion efficiency of nanoparticles are sensitive to their size and shape, therefore a variety of them have been investigated including nanosphere, nanoshell, nanorod, nanocage, nanocluster, nanostar, and nanobeacon [84]. More recently, photosensitizer based contrast agents were also evaluated for PAI and showed a strong photoacoustic signal [119]. These photosensitizers preferentially accumulate in tumors due to the enhanced permeation and retention effect and therefore offer tumor-targeted imaging.

1.4 Conclusion

FLI and BLI are non-ionizing, rapid, inexpensive imaging techniques that can provide unique structural, functional, and physiological information. However, high imaging resolution can hardly be achieved in deep tissue using the current state-of-art techniques due to tissue scattering and absorption. The hybrid imaging technique, USMLT, that uses US to modulate diffusely propagating light has the potential to improve the spatial resolution of fluorescence or bioluminescence images. The bottleneck for

USMLT is the very low modulation depth due to the intrinsic incoherent characteristics of the light used. To increase modulation depth contrast agents that have good acousto-optical property (can change light intensity significantly once exposed to US) need to be developed. The work of this thesis focuses on studying the underlying modulation mechanisms of USMLT and increasing the effect of US on the variation of light intensity of USMLT. This is achieved firstly through developing a model that can simulate the luminescence intensity with or without application of US. This model is used to calculate modulation depth and analysis the mechanisms of USMBLT. A contrast agent that has already been developed, fluorophore-labelled microbubbles, is studied theoretically and its influence on modulation depth is experimentally demonstrated. Pyrene labelled liposomes is then first proposed as a contrast agent in this work and its acousto-optical property is characterized. This is further improved by developing donor-acceptor labelled liposomes that has a NIR fluorescence emission which is essential for deep tissue imaging.

1.5 Outline of the thesis

In this thesis, the hybrid imaging technique USMLT is investigated. Several contrast agents to improve the effect of US on the fluorescence variation of USMLT are developed and the underlying mechanisms are discussed.

In this chapter, FLI and BLI techniques are reviewed. Several hybrid fluorescence and US imaging techniques are reviewed and compared. The contrast agents that have already been developed for hybrid fluorescence and US imaging techniques are also reviewed.

In the second chapter the mechanisms of USMBLT are studied numerically by modification of an open source tool for simulation of diffusely propagating light, Near Infrared Fluorescence and Spectral Tomography (NIRFAST). Influences of US on optical properties (reduced scattering coefficient, absorption coefficient, and refractive index) and concentration of source particles are analysed. The US modulated bioluminescence fluence rates are simulated. Effects of the optical properties, source particle concentra-

tion, US pressure, and US position on the modulation depth are investigated. The SNR for *in vivo* detection is also calculated to explore the feasibility of applying USMBLT for imaging pre-clinical models.

In the third chapter the application of fluorophore labelled microbubbles in USMFT is theoretically investigated. Initial experiments were also performed to demonstrate the increased modulation depth. The fluorophores were labelled on the shell of the microbubbles, which were tuned to be self-quenched. Upon application of US the microbubbles oscillate changing the intermolecular distances of the fluorophores resulting in a modulated fluorescence signal. The volumetric oscillation of fluorophore labelled microbubble and its fluorescence emission intensity with or without application of US are simulated. The influences of factors including microbubble radius, fluorophore concentration, and US pressure on the US modulated fluorescence signal are studied. The theoretical modulation depth and SNR with fluorophore labelled microbubbles located inside a scattering medium are simulated.

In the fourth and fifth chapters a new approach to enhancement of fluorescent signals by US based on the use of nanoscale fluorophore labelled liposomes is proposed and demonstrated experimentally. Liposomes containing lipids with pyrene labelled on the fatty acid tail group and the head group are optically excited and the excimer fluorescence emissions are compared in the absence and presence of an US field. An increase in excimer emission intensity following exposure to US is observed.

In the fifth chapter another contrast agent which is donor-acceptor labelled nanoscale liposomes is investigated. The FRET without applying US is estimated from the spectra of donor only liposomes, acceptor only liposomes, and donor-acceptor labelled liposomes at a range of fluorophore concentrations. The acousto-fluorescence characteristics are studied by measuring and analyzing the instantaneous fluorescence variation when applying US. The influence of US on the fluorescence variation is studied by varying US pressure and exposure time. Line scanning images of a tube buried deep inside a scattering phantom are obtained with the donor-acceptor labelled nanoscale liposomes located inside the tube. Possible mechanisms are also discussed.

In the final chapter, the research findings developed in this thesis are summarized. Pos-

sible future work such as application of the developed fluorophore labelled liposomes for *in vivo* imaging are discussed.

CHAPTER 2

Numerical investigation of the mechanisms of USMBLT

2.1 Introduction

Unlike fluorescence, bio- (or chemi-) luminescence does not require the use of excitation light to produce emission. In relation to imaging this eliminates the possibility of cross-talk detection of the bleed-through of the excitation light and any light generated by autofluorescence. In addition, there is no intrinsic bioluminescence generated by mammalian cells. Therefore BLT has a high sensitivity and can achieve very high SNR [120]. This enables accurate detection of as few as a thousand tumor cells *in vivo* [50] or subtle changes non-invasively. However, due to light scattering and absorption in biological tissue, BLT has a limited resolution (several millimeters).

As introduced in Section 1.2.1 USMLT has been investigated to improve the resolution of luminescence imaging in deep tissue. US was used to modulate the luminescence light generated within an optically scattering medium and the modulated light was detected using a PMT and a lock-in amplifier. Line-scans of one sample containing two luminescent targets show a 3.5 times improvement in spatial resolution compared with conventional BLI [55]. A reconstruction algorithm for the source distribution for USMBLT was also investigated [68]. US with various wave vectors is used to modulate

the density of the medium. Unique recovery of the source distribution was achieved and the resolution was improved by a factor of 10 compared with conventional BLI. These studies provide support to the hypothesis that US modulation techniques could be applied to improve the spatial resolution of BLT.

The propagation of light has been modeled mainly through two ways. One is Monte Carlo simulations in which light moves as ballistic photons going through a random walk [121]. It will encounter absorption and scattering events with the probability of an event depending on the optical properties. The other is diffusion theory in which light is treated as a concentration of optical energy and diffuses down a concentration gradient [122]. Monte Carlo model is believed to be the best estimation of light distribution in tissue however the computation takes a long time, while models based on diffusion theory require a shorter time and are still accurate for most cases for tissues when using visible to NIR wavelength of light [123]. Comparison of Monte Carlo simulation and diffusion theory shows that in a region near the source, diffusion theory fails to accurately describe the light distribution. However, the two approach agreement at distances exceeding one transport mean free path ($1/[\mu_a + \mu_s(1-g)]$) [123]. The majority of models based on diffusion theory falls into two categories of being either analytical or numerical. Analytical models are limited to simple geometries with nearly homogeneous distribution, while numerical models have the advantage of being able to model complex geometries with heterogeneous distribution.

In this chapter, a numerical method is used to study the mechanisms of USMBLT. NIRFAST [124], which simulates light propagation in biological tissue based on the finite element method (FEM), is modified to incorporate the effects of US modulation. The dominance of four factors (reduced optical scattering coefficient, optical absorption coefficient, refractive index, and concentration of the bioluminescent target (luciferase)) on the strength of light modulation is studied. The influences of US pressure, frequency, and position on the modulation depth of the detected light are analysed. The feasibility of applying USMBLT for imaging pre-clinical models is also investigated by calculating the SNR of USMBLT using the optical properties of mouse tissue reported in literature.

2.2 Simulation methods

2.2.1 Forward light modelling

The fluence rate of the US modulated bioluminescence (USMBL) signal from a source located inside a tissue sample is calculated through modification of the numerical model of light transport NIRFAST. The fluence rate (W/mm^2) of bioluminescent photons detected at the surface of a tissue sample is calculated using the forward model in NIRFAST, which solves the following diffusion approximation of the radiative transport equation in the frequency domain [124]:

$$-\nabla\cdot k(r)\nabla\Phi(r,w) + (\mu_a(r) + iw/c_m(r))\Phi(r,w) = q_0(r,w) \tag{2.2.1}$$

where $k(r) = 1/3(\mu_a(r) + \mu_s'(r))$ is the diffusion coefficient, $\mu_a(r)$ is the absorption coefficient, $\mu_s'(r)$ is the reduced scattering coefficient, $\Phi(r,w)$ is the photon fluence rate at the position r, w (radians/s) is the angular frequency of modulation, $c_m(r) = c_0/n(r)$ is the speed of light in the medium, c_0 is the speed of light in vacuum, $n(r)$ is the refractive index, and $q_0(r,w)$ is an isotropic source term. Each term on the left of Eq. 2.2.1 is a loss of photons, and the term on the right describes the source of the light.

To solve the diffusion approximation by FEM, a tetrahedral mesh comprised of a number of elements joined at vertex nodes is generated representing the tissue sample. The mesh is assigned the optical properties of the sample and contains an internal bioluminescence source. The simulations in this chapter are based on Eq. 2.2.1.

2.2.2 Ultrasound modulation of sample optical properties and luciferase concentration

In order to investigate the underlying mechanisms of USMBLT the NIRFAST model is modified to account for the US induced temporal oscillation of the sample optical properties (reduced scattering coefficient, absorption coefficient, and refractive index). Changes in the bioluminescence intensity due to the oscillation of luciferase concentration are also taken into account.

In this chapter the US field is considered to be generated by a focused US transducer with the focal zone being approximated as a thin cylinder (2-mm diameter, 18-mm long). Only the US focal zone is considered and it is assumed to propagate without attenuation in a linear manner as a plane wave with stratified pressure amplitude variation along the long axis of the cylinder. The acoustic pressure of an US field at spatial position $\boldsymbol{r}$ and time t can thus be expressed as:

$$P_{US}(r,t) = P_A \sin(\boldsymbol{kr} - w_{us}t + \varphi) \tag{2.2.2}$$

where $\boldsymbol{k}$ is the US wave vector with the corresponding scalar being $k = 2\pi/\lambda_{us}$, λ_{us} is the US wavelength, w_{us} is the US angular frequency, φ is the phase of the US. P_A is the US pressure amplitude. In this simulation only linear US propagation is considered so P_A represents the pressure amplitude at the fundamental frequency at the US focal zone.

Ultrasonic modulation physically causes the compression and rarefaction of the tissue which modifies its optical properties. The particle displacement *A(**r**,t)* caused by the acoustic wave propagation can be expressed as:

$$A(\boldsymbol{r},t) = A_0 \sin(\boldsymbol{kr} - w_{us}t + \varphi) \tag{2.2.3}$$

A_0 is the particle displacement amplitude, which is related to P_A, w_{us}, the mass density of the sample ρ_0, and the acoustic velocity in the sample v_a such that $A_0 = P_A/(w_{us}\rho_0 v_a)$ [125].

The particle displacement consequently leads to variations in the optical parameters including the absorption coefficient, scattering coefficient, and refractive index. Expressions for these US induced variations can be expressed as [69]:

$$\Delta n = n_0 \eta k A(\boldsymbol{r},t) \tag{2.2.4}$$

$$\Delta \mu_s' = \mu_{s0}'[1 + 0.37\eta]kA(\boldsymbol{r},t) \tag{2.2.5}$$

$$\Delta \mu_a = \mu_{a0} k A(\boldsymbol{r},t) \tag{2.2.6}$$

where Δn, $\Delta\mu_s'$ and $\Delta\mu_a$ are the changes in the refractive index, reduced scattering coefficient and absorption coefficient respectively, and n_0, μ_{s0}', and μ_{a0} are the corresponding equilibrium values in the absence of US modulation. η is the elasto-optic coefficient which is related to the adiabatic piezo-optical coefficient of the sample $\partial n/\partial p$, ρ_0, and v_a such that $\eta = \partial n/\partial p \rho_0 v_a^2$ [126]. Here it was assumed that (1) the size of the scatterer in tissue is not changed with US; (2) $5 < 2\pi r/(\lambda/n_{med}) < 50$ and $1 < n_p/n_{med} < 1.1$, where r and n_p are the radius and the refractive index of the scatterer respectively, n_{med} is the refractive index of the medium; (3) the refractive index change of the scatterer is equal to that of the medium [69]. These assumptions could approximately represent the case of real tissue. It also needs to be noted that these equations are only valid for plane US wave without considering attenuation and nonlinear frequency components. The particle displacement amplitude in Eq. 2.2.3 needs to be changed if nonlinear US components are induced.

US also has an effect on the bioluminescence intensity from the bioluminescence source. In the unmodulated case the bioluminescence intensity generated from an ATP/luciferin-luciferase bioluminescence reaction solution can be expressed as [51]:

$$I_{lm0} = QYk_{cat}C_0 \tag{2.2.7}$$

where I_{lm0} (photons/s/L) is the bioluminescence intensity from unit volume of the solution, QY (photons/molecule) is the quantum yield of bioluminescence reactions, defined as the efficiency of the production of a photon from a single reactant molecule. k_{cat} (s^{-1}) is the catalytic constant, which represents the turnover molecule number of the reaction for the substrate by a single enzyme molecule per second [51]. C_0 (molecule/L) is the concentration of the active enzyme (luciferase that reacts with luciferin) at the site of interest in the tissue. QY and k_{cat} (s^{-1}) are constants, therefore the bioluminescence intensity is only influenced by the concentration of the active enzyme.

The active enzyme concentration under the interaction of an US field can be written as [71]

$$C_1 = C_0(1 + \beta_a' P_{US}(r,t)) \tag{2.2.8}$$

where $\beta'_a = \frac{k}{\rho_0 v_a w} \frac{|1+\hat{\varepsilon}-i(\hat{\varepsilon}+\frac{2}{3}\hat{\varepsilon}^2)|}{|1+\hat{\varepsilon}-i[\hat{\varepsilon}+\frac{4}{9}(\rho+\frac{1}{2})\hat{\varepsilon}^2]|} + \beta_a$ is the effective compressibility. The first part of β'_a describes the influence of particle oscillation. $\hat{\varepsilon} = (w_{us}a^2/2\gamma)^{1/2}$, a is the radius of the enzyme molecule, γ is fluid kinematic viscosity, $\rho = \rho_l/\rho_0$, ρ_l is the enzyme density which can be estimated from the molecule radius and the molar mass. The second part of β'_a describes the influence of volume changes of tissue, where $\beta_a = 1/K$ is the compressibility of tissue and $K = v_a^2\rho_0$ is the bulk modulus. Replacing C_0 in Eq. 2.2.7 with C_1 in Eq. 2.2.8, the bioluminescence intensity under the interaction of the US field is expressed as:

$$I_{lm} = QYk_{cat}C_0(1 + \beta'_a P_{US}(r,t)) \tag{2.2.9}$$

The relative variation of the bioluminescence intensity can then be expressed from Eq. 2.2.9 and Eq. 2.2.7 as:

$$\Delta q/q_0 = |I_{lm} - I_{lm0}|/I_{lm0} = \beta'_a P_{US}(r,t) \tag{2.2.10}$$

2.2.3 Methods of numerical simulation

The simulation in this chapter is based on an experimental system for USMLT using a chemiluminescent source [55]. The schematic of the simulated experiment is shown in Fig.2.1. The tissue phantom is modeled as a rectangular slab (55 mm $\times$ 55 mm $\times$ 15 mm) containing a cylindrical bioluminescent source (1-mm diameter, 5-mm height) in the centre of the slab. The detector is modeled as a circular disk of 8 mm diameter located on the surface of the tissue phantom. Mesh creation tool in NIRFAST is used to create the meshes of the tissue phantom slab, cylindrical bioluminescent source, and the circular detector. Generally the tissue slab and cylindrical source are discretised into tetrahedral elements with average edge lengths of 0.3 mm and 0.1 mm respectively using the Delaunay Triangulation method. The circular detector is discretised into triangles of average edge length of 0.2 mm. These element sizes are chosen as they are sufficiently small to confer numerical stability and accuracy to the diffusion computations without being computationally expensive. The vertices of the Delaunay Triangulation are used as point sources and point detectors forming the source and detector

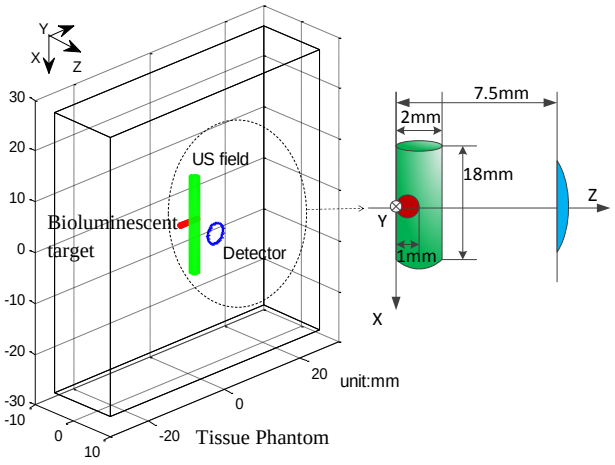


Figure 2.1: Simulated experimental setup based on the USMLT system in [55]. The tissue phantom is modeled as a rectangular slab (55 mm $\times$ 55 mm $\times$ 15 mm) containing a cylindrical bioluminescent source (1-mm diameter, 5-mm height, red) at a depth of $z = 0.5$ mm. The US focal zone (green) is simplified as a 2-mm diameter, 18-mm long cylinder and the detector (blue) as a disk located at $z = 7.5$ mm.

respectively.

The temporal and spatial variation of the tissue optical properties are calculated through Eq. 2.2.4, Eq. 2.2.5, and Eq. 2.2.6. The US modulated optical properties are then assigned to nodes in the 3D mesh representing the tissue phantom. This assignment is achieved through identification of nodes that lay inside the US field by comparing the spatial coordinates of the individual nodes to that of the cylindrical US focal zone. Nodes outside the US field are assigned equilibrium properties of the tissue being modeled. The region of the bioluminescence source is divided into several layers along the direction of US propagation, each with an allocated pressure and thus a modulated bioluminescence intensity determined using Eq. 2.2.9. The bioluminescence fluence rate at a particular time is then calculated at the detector at the boundary in the presence and absence of US (Φ_{US} and Φ_{DC}) respectively using Eq. 2.2.1. The US modulated fluence rate Φ_{AC} is then calculated as:

$$\Phi_{AC} = \Phi_{US} - \Phi_{DC} \tag{2.2.11}$$

Note that optical parameters in Eq. 2.2.1 and bioluminescence concentration are time-independent, however, under the influence of US pressure they will change with time.

In this chapter the temporal change is simulated by calculating Φ_{AC} at different phases of US within a period. Each of the calculated values represents the US modulated bioluminescence fluence rate at one time point within the US period. The temporal changes are then obtained by connecting the US modulated fluence rates at all these phases in sequence. The modulation depth is obtained through dividing the amplitude of the US modulated fluence rates by the bioluminescence fluence rate in the absence of US, namely:

$$m = max\{\Phi_{AC}\}/\Phi_{DC} \tag{2.2.12}$$

2.2.4 SNR analysis of *in vivo* application of USMBLT

In this section the method used to calculate the SNR that could be achieved in the *in vivo* application of USMBLT is described. The detection system is considered to consist of a PMT, a transimpedance amplifier and a lock-in amplifier (LIA). The SNR for such a system can be expressed as:

$$SNR = P_m/P_n \tag{2.2.13}$$

where P_m is the power of the detected modulated signal, $P_n = P_{ns} + P_{dc} + P_a$ is the total noise power, with P_{ns}, P_{dc} and P_a relating to the power of the noise arising from the bioluminescence light (modulated signal and unmodulated signal), dark current and ambient light respectively.

The output voltage of the transimpedance amplifier relating to the bioluminescence modulated by US with a frequency of f_{US} is:

$$v_{AC} = V_{AC}sin(2f_{US}t) \tag{2.2.14}$$

where

$$V_{AC} = 2\pi SL_{AC}hfE_{Ano}RM \tag{2.2.15}$$

S is the effective area of the PMT, L_{AC} (photons/s/cm^2/sr) is the modulated surface radiance, h is Planck's constant, $f = c/\lambda$ is the light frequency with λ being the light wavelength. E_{Ano} is the anode radiance sensitivity of the PMT at the bioluminescence

wavelength, R and M are the input impedance and gain of the transimpedance amplifier respectively. The power of the optical modulated signal can therefore be expressed as:

$$P_m = V_{AC}^2/2 \tag{2.2.16}$$

For a PMT, the current measured at the anode is the result of the multiplication of electrons emitted at the cathode. The number of electrons generated at the cathode follows a Poisson random process. Within a time period of Δt the number of electrons at the cathode can be expressed as:

$$N = I_{Cath}\Delta t/e \tag{2.2.17}$$

where

$$I_{Cath} = 2\pi S(L_{AC} + L_{DC})hfE_{Cath} \tag{2.2.18}$$

is the cathode current, e is the electron charge, L_{DC} is the unmodulated surface radiance, $L_{AC} = mL_{DC}$, m is the modulation depth, and E_{Cath} is the cathode radiance sensitivity. The shot noise X can then be expressed as:

$$X = N - \overline{N} \tag{2.2.19}$$

where $\overline{N}$ is the mean number of electrons generated.

The noise current at the anode and the noise related to the voltage output from the transimpedance amplifier can then be expressed as:

$$I_{Ano} = XeG/\Delta t \tag{2.2.20}$$

and

$$V = I_{Ano}RM \tag{2.2.21}$$

respectively, where G is the PMT gain.

Therefore the variance of the noise voltage is:

$$\delta_V^2 = (eGRM/\Delta t)^2 \delta_X^2 \tag{2.2.22}$$

According to the property of Poisson process $\delta_X^2 = \delta_N^2 = \overline{N}$. Following Parseval's theory the total noise power equals twice the variance of the noise voltage, thus the output noise power due to signal is:

$$P_{ns} = 2\delta_V^2 \tag{2.2.23}$$

The calculations in this chapter are based on the assumption that a lock-in amplifier is used in detection, therefore the bandwidth of the system is determined by the lock-in amplifier. The bandwidth of the lock-in amplifier is given by $B = 1/(2\Delta t)$, and the output noise power due to signal can then be expressed as:

$$P_{ns} = (2\sqrt{eI_{Cath}B}GRM)^2 \tag{2.2.24}$$

2.3 Simulation results

In this section the US modulated bioluminescence signal and modulation depth are calculated. The effects of factors including US pressure, US frequency, US position, and luciferase concentration on modulation depth of USMBLT are investigated. The SNR of USMBLT is calculated to analyze its feasibility for *in vivo* application.

The parameters used in the simulations are listed in Table 2.1. The optical properties are based on typical literature values observed in biological tissue [127]. Calculation of the SNR in the simulated experiment is based on the calculated modulation depth and the parameters of instrumentation used in previous experimental studies [55]. Table 2.2 shows parameters from the datasheets of a Hamamatsu H5783-20 PMT and Stanford Instruments SR445A transimpedance amplifier. The radiance emitted at the surface of the mouse is based on literature values from BLT which are found to lie in the range of 10^6 photons s^{-1} cm^{-2} sr^{-1} to 10^{11} photons s^{-1} cm^{-2} sr^{-1}[44, 128].

Table 2.1: Parameters used to simulate the tissue phantom and bioluminescence source. Values taken from the literatures.

Symbol	Meaning	Value
$\partial n/\partial p$	adiabatic piezo-optical coefficient	$1.466 \times 10^{-10}\mathrm{m^2\,N^{-1}}$ [126]
v_a	acoustic velocity in water	$1500\,\mathrm{m\,s^{-1}}$
ρ_0	medium density	$1000\,\mathrm{kg\,m^{-3}}$
n_0	equilibrium refractive index	1.4
μ'_{s0}	equilibrium reduced scattering coefficient	$1\,\mathrm{mm^{-1}}$ [127]
μ_{a0}	equilibrium absorption coefficient	$0.02\,\mathrm{mm^{-1}}$ [127]
γ	kinematic viscosity of water	$10^{-6}\mathrm{m^2\,s^{-1}}$ [129]
QY	quantum yield	0.48 photons/molecule [51]
k_{cat}	catalytic constant	$3 \times 10^{-2}\mathrm{s^{-1}}$ [51]
$C_m[C_0 = (C_m N_A)/kDa]$	luciferase concentration	$20\,\mathrm{mg\,ml^{-1}}$ [130]
β_a	compressibility of medium	$4.6 \times 10^{-10}\mathrm{Pa^{-1}}$ [131]
m	molar mass of luciferase	$62\,\mathrm{kg\,mol^{-1}}$ [132]
r_0	radius of luciferase	3 nm [133]
T	temperature	293 K

Table 2.2: Parameters used in SNR calculations based on instrument datasheet.

Symbol	Meaning	Value
E_{Ano}	PMT anode radiance sensitivity	$3.9 \times 10^4\,\mathrm{A\,W^{-1}}$
E_{cath}	PMT cathode radiance sensitivity	$78\,\mathrm{mA\,W^{-1}}$
G	PMT gain	4×10^5
R	input impedance of transimpedance amplifier	$500\,\Omega$
M	gain of transimpedance amplifier	5
λ	light wavelength	650 nm
B	lock-in bandwidth	0.1 Hz

2.3.1 Effect of US on optical properties and bioluminescence intensity

The US induced changes in the reduced optical scattering coefficient, optical absorption coefficient, refractive index, and luciferase concentration dependent bioluminescence emission intensity relative to their equilibrium values ($\Delta\mu'_s/\mu'_{s0}$, $\Delta\mu_a/\mu_{a0}$, $\Delta n/n_0$, and $\Delta q/q_0$) are calculated using Eq. 2.2.4, Eq. 2.2.5, Eq. 2.2.6, and Eq. 2.2.10 respectively. The applied US field is calculated using Eq. 2.2.3. $\Delta\mu'_s/\mu'_{s0}$, $\Delta\mu_a/\mu_{a0}$, $\Delta n/n_0$, and $\Delta q/q_0$ against the maximum US pressure over a medically relevant pressure range up to 10 MPa with an arbitrary US frequency of 1 MHz are shown in Fig. 2.2. It should be noted that these relative changes are independent of US frequencies.

Fig. 2.2 suggests US pressure has a linear influence on all the parameters studied over

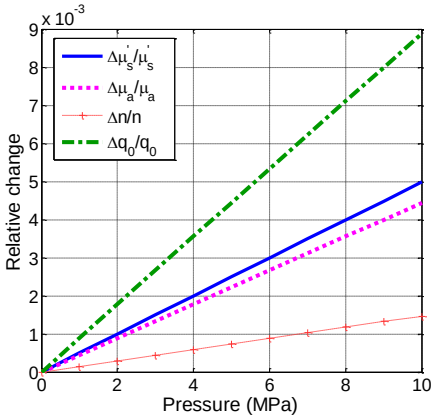


Figure 2.2: Effect of US pressure (peak amplitude, $f = 1\,\text{MHz}$) on the relative change in the reduced optical scattering coefficient, optical absorption coefficient, refractive index, and concentration of the bioluminescent target, denoted as $\Delta\mu_s'/\mu_{s0}'$, $\Delta\mu_a/\mu_{a0}$, $\Delta n/n_0$, and $\Delta q/q_0$ respectively.

the pressure range considered. This relationship is clear from inspection of Eq. 2.2.4, Eq. 2.2.5, and Eq. 2.2.6 which describe the optical properties of the tissue phantom. The absolute value and rate of change for $\Delta n/n_0$ is the lowest of these parameters which corresponds to the smallest constant in Eq. 2.2.4. It can be predicted from Eq. 2.2.10 that $\Delta q/q_0$ is proportional to the applied US pressure as well. It is observed that $\Delta q/q_0$ undergoes the greatest change.

2.3.2 Calculation of the US modulated bioluminescence fluence rate

The US modulated bioluminescence fluence rate Φ_{AC} as US propagates through the focal zone is studied and the corresponding modulation depth is calculated in this section.

The spatial variation of US induced changes in $\Delta q/q_0$ over the bioluminescence source region along the US propagation direction (x direction) is calculated first. These variations are a result of the sinusoidal nature of the modeled US wave which produces a spatial and temporal variation in pressure in the focal zone. Fig. 2.3 shows the variation in $\Delta q/q_0$ caused by a 0.75 MHz, 1 MPa US wave along x direction over a time frame corresponding to one period of wave oscillation. The US phase ϕ is defined as zero when the sinusoidal US wave gets to the upper edge of the source area ($x = -0.5$).

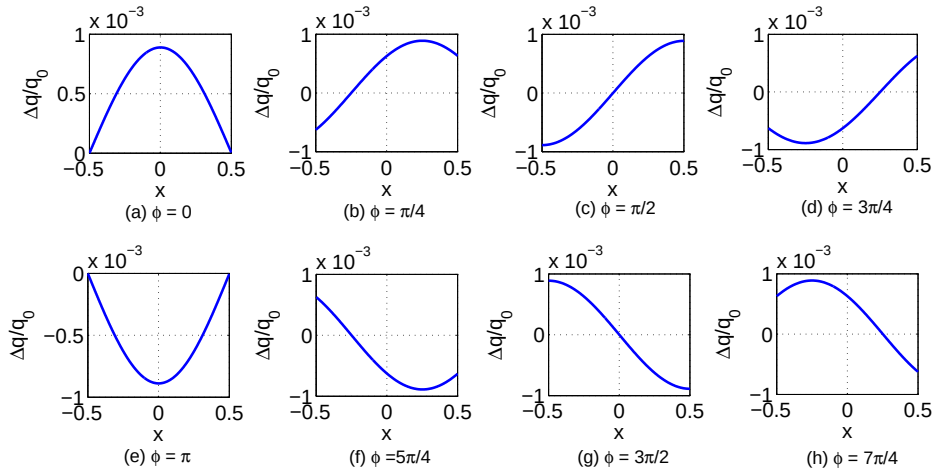


Figure 2.3: Distribution of $\Delta q/q_0$ along x direction at different US phases over one period. US frequency is 0.75 MHz.

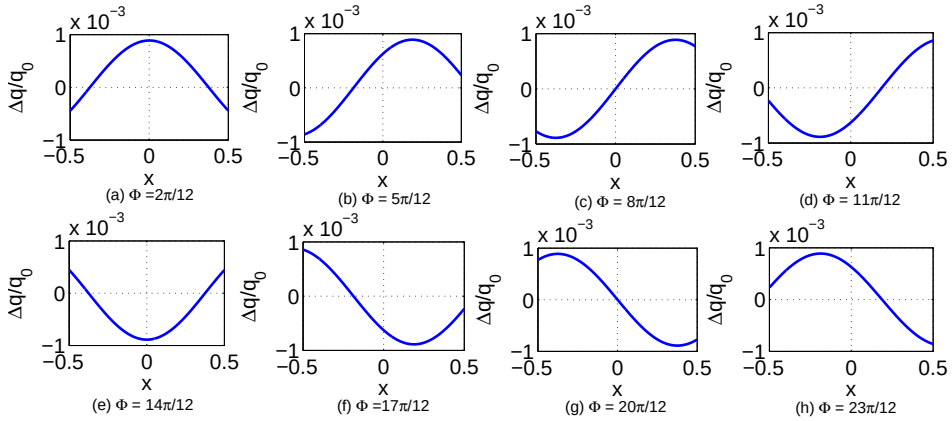


Figure 2.4: Distribution of $\Delta q/q_0$ along x direction at different US phases over one period. US frequency is 1 MHz.

Different US phases correspond to US distribution at different time points relative to the US propagation. Similarly Fig. 2.4 and Fig. 2.5 show the distribution of $\Delta q/q_0$ along x direction for US frequency of 1 MHz and 1.25 MHz respectively.

The observed spatial and temporal variation of $\Delta q/q_0$ in Fig. 2.3 results from the changing US pressure distribution as the sound propagates and it is dependent on the US frequency. The pressure distributions set up by each frequency will vary as a result of their differing wavelengths and their sizes relative to that of the bioluminescence source. Φ_{AC} normalized by Φ_{DC} (Φ_{AC}/Φ_{DC}) for US frequencies of 0.75 MHz, 1 MHz, and 1.25 MHz are calculated at 24 phases within one US period and shown in Fig. 2.6. US induced changes from both the concentration and the optical properties are included. For the three frequencies studied, the 1-mm diameter source simulated cor-

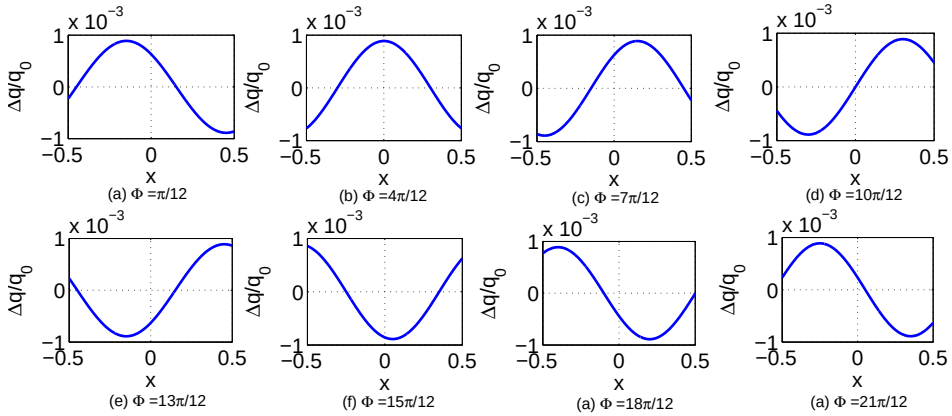
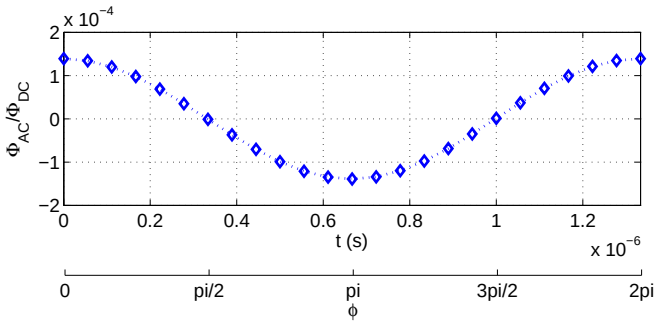


Figure 2.5: Distribution of $\Delta q/q_0$ along x direction at different US phases over one period. US frequency is 1.25 MHz.

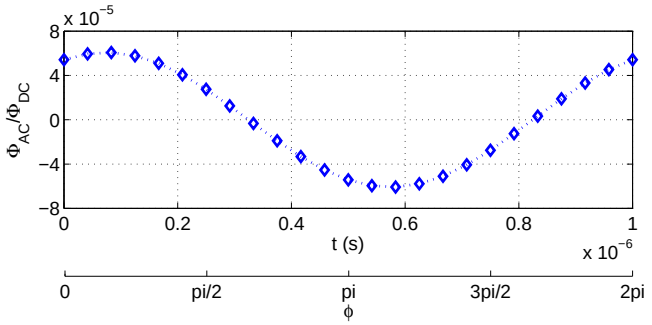
responds to distances equal to $\lambda/2$, $2\lambda/3$, and $5\lambda/6$ respectively. It needs to be mentioned that according to Nyquist theorem, for frequencies above 1.25 MHz it requires the node distance of the mesh to be smaller than 0.3 mm therefore the optical signals are not presented.

It is found from Fig. 2.6 that the normalized US modulated bioluminescence fluence rates for all the US frequencies studied oscillate at the US frequency. It is observed from Fig. 2.6a that at 0.75 MHz, $|\Phi_{AC}/\Phi_{DC}|$ is at a maximum when the distribution of $\Delta q/q_0$ along x direction is even symmetrical to $x = 0$ (shown in Fig. 2.3a, e). $|\Phi_{AC}/\Phi_{DC}|$ is zero when the distribution of $\Delta q/q_0$ along x direction is odd symmetrical to $x = 0$ (shown in Fig. 2.3c, g). A similar conclusion can be drawn from observation of the other two US frequencies.

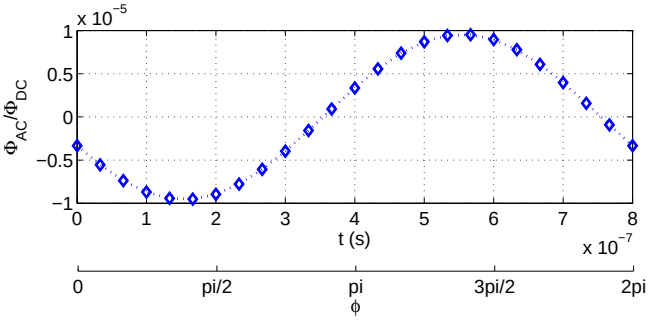
The oscillation of the normalized US modulated bioluminescence fluence rates is due to the summation of USMBL signals originating from each layer of the source region along the US transmission direction at the detector. When the US pressure distribution is even symmetrical to the centre axis of the cylindrical source, the USMBL signals from two symmetrical layers of the source are in phase and sum constructively at the detector so $|\Phi_{AC}/\Phi_{DC}|$ is the highest. When the US pressure distribution is odd symmetrical to the centre axis, the USMBL signals from the two symmetrical layers of the source are out of phase and sum destructively at the detector so $|\Phi_{AC}/\Phi_{DC}|$ is canceled and becomes zero. It should be noted that when the phase sum or absolute difference is π, $|\Phi_{AC}/\Phi_{DC}|$ have the same values. This is because the pressure distributions within the



(a)



(b)



(c)

Figure 2.6: Normalized US modulated bioluminescence fluence rate (Φ_{AC}/Φ_{DC}) over one US period for frequencies of (a) 0.75 MHz, (b) 1 MHz, and (c) 1.25 MHz.

source region at these conditions are either odd symmetrical or even symmetrical with each other (e.g. Fig. 2.3b, Fig. 2.3d, and Fig. 2.3f).

It is also found that the amplitude of the US modulated bioluminescence (modulation depth) varies with US frequency - the maximum modulation depth is found to decrease with an increase in frequency, as shown in Fig. 2.7. This is probably due to the increased region of $\Delta q/q_0$ that has opposite sign. For example, it can be seen that the region where $\Delta q/q_0$ has negative values in Fig. 2.5b is more than that of Fig. 2.3a and Fig. 2.4a. Furthermore, it needs to be mentioned that in this simulation the oscillating US modulated bioluminescence fluence rates are observed using a detector located at z axis with the x and y positions right in the center of the US field and the bioluminescence source. If detecting at other boundary positions or changing the size of the detector, the same conclusion in terms of $|\Phi_{AC}/\Phi_{DC}|$ can be drawn. This is because $|\Phi_{AC}/\Phi_{DC}|$ is an intrinsic characteristic depending only on the US, bioluminescence source, scattering medium, and is independent of the detector.

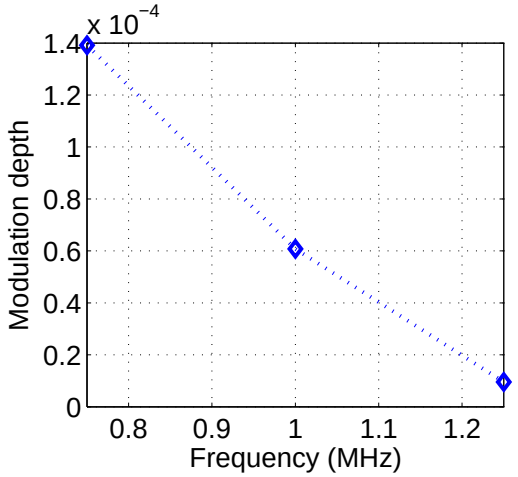


Figure 2.7: Modulation depth as a function of US frequency.

2.3.3 Effect of $\Delta\mu_s'/\mu_{s0}'$, $\Delta\mu_a/\mu_{a0}$, $\Delta n/n_0$, and $\Delta q/q_0$ on modulation depth

In this section the modulation depth arising individually from $\Delta\mu_s'/\mu_{s0}'$, $\Delta\mu_a/\mu_{a0}$, $\Delta n/n_0$, and $\Delta q/q_0$ is calculated (US frequency: 1 MHz) over a medically relevant pressure range up to 10 MPa (maximum value). It was observed from Fig. 2.6a that for $f = 1$ MHz, the maximum Φ_{AC} is obtained at $\varphi = \pi/6$. Dividing Φ_{AC} at $\varphi = \pi/6$ by

the unmodulated fluence rate Φ_{DC}, modulation depth can be obtained. The calculated modulation depths are shown in Fig. 2.8. A linear increase in the modulation depth with US pressure is observed for all the four factors studied. This linear relationship between modulation depth and US pressure is in agreement with the analytic solution obtained by Yuan et al. [71] and the experimental demonstration for both the case of the fluorescent source and an LED source from Jarrett [134]. Although all parameters studied show a linear trend with pressure, their absolute values and rates of change vary considerably. Fig. 2.8 shows the parameter with the greatest effect on modulation depth is the change in the bioluminescence emission intensity, which is due to the US induced change of luciferase concentration. In fact it can be seen that the modulation depth due to changes in the bioluminescence intensity is approximately two orders of magnitude greater than that caused by changes in the reduced scattering coefficient and absorption coefficient, and of the order of 10^5 times higher than that related to changes in the refractive index.

It is useful to briefly compare the simulated data with the experimental results obtained in phantom studies previously. In [55] a modulation depth of 3.6×10^{-4} (AC/DC = 3.6 µV/10 mV) was obtained for a phantom with $\mu_s = 0.21\,\mathrm{mm}^{-1}$ and $\mu_a = 5 \times 10^{-5}\mathrm{mm}^{-1}$ at an US frequency of 1 MHz and peak pressure at the focal zone of 0.42 MPa. Using the simulation described in this chapter the modulation depth at the same frequency, pressure and optical properties is calculated to be 2.4×10^{-5}. Differences can be attributed to values of parameters (e.g. parameters used to calculate the effective compressibility in Eq. 2.2.8), measurement errors in the experiments (e.g. peak US pressure), and assumptions made in the solutions (e.g. perfectly focused US). It is also worthy to mention that the modulation depth calculated for the case of change in bioluminescence intensity at 1 MPa maximum US pressure is 4.3×10^{-5}. This is comparable to the levels reported previously in fluorescence experimental results [135] and those predicted theoretically for fluorescence [71].

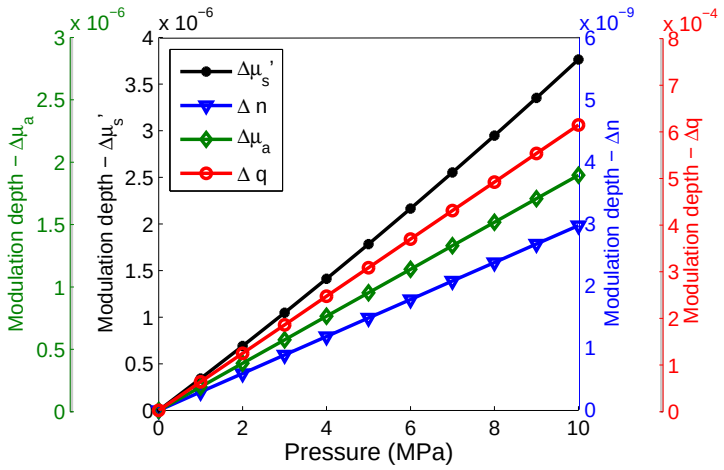
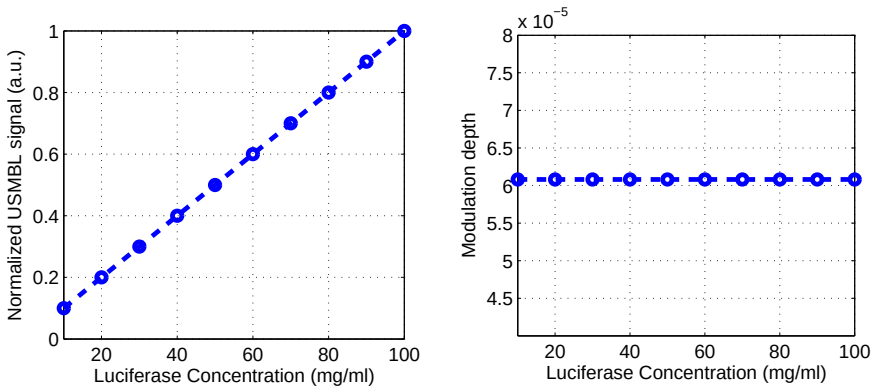


Figure 2.8: Modulation depth arising individually from $\Delta\mu_s'$, $\Delta\mu_a$, Δn, and Δq with respect to the maximum US pressure. $f = 1$ MHz.

2.3.4 Effect of luciferase concentration on modulation depth

In this section the dominance of the bioluminescence intensity on the modulation depth due to modulation of luciferase concentration is further investigated by studying the effect luciferase concentration has on the US modulated signal and modulation depth. Fig. 2.9 shows the results of these calculations over a biologically relevant concentration range of 10 mg/ml to 100 mg/ml. It is found that the USMBL signal varies with the concentration linearly. This linear relationship of modulated signal with source concentration is consistent with the expression (18) derived in [70]. It should be noted that in [136] the US modulated fluorescence signal was observed to only increase when the fluorophore concentration is low and it will decrease in the high concentration region. This is due to the 'inner filter effect', in which the excitation light is mostly absorbed by the fluorescent molecules near the light input region, and the fluorescence emission is reabsorbed by the fluorophores along the light transmission path in an optically dense solution [137]. However, the process of generating bioluminescence does not require excitation light for light emission thus no 'inner filter effect' exists for USMBLT. This is an advantage of USMBLT when the USMBL signal is used to quantify the luciferase concentration because the relationship is much simpler. The modulation depth is invariant with luciferase concentration as shown in Fig. 2.9b. This is because with increase of luciferase concentration the unmodulated bioluminescence also increases with the same rate.



(a) (b)

Figure 2.9: Influence of luciferase concentration on (a) normalised USMBL signal and (b) modulation depth.

2.3.5 Effect of US position on modulation depth

In this section the effect of US position on the fluence rates is studied by moving the US focal zone along z direction. The modulated bioluminescence signal (Φ_{AC}) and unmodulated bioluminescence signal (Φ_{DC}) corresponding to the US position (z) are calculated. The US position z is expressed as the coordinate of the central point of the US focal zone. The geometry of the US position is shown in Fig. 2.10. When $z = 1$, the left edge of the bioluminescent source is tangential to the US focal zone and the overlap between the two is the largest; when $1 < z < 2$, the bioluminescent source partially overlaps with the US focal zone; when $z = 2$, the bioluminescent source is tangential to the left edge of the US focal zone; when $z > 2$, the bioluminescent source is separate to the US focal zone. The signals are obtained using three groups of optical properties of 1) $\mu_s' = 0.12\,\mathrm{mm}^{-1}$, $\mu_a = 0.003\,\mathrm{mm}^{-1}$; 2) $\mu_s' = 1\,\mathrm{mm}^{-1}$, $\mu_a = 0.02\,\mathrm{mm}^{-1}$; and 3) $\mu_s' = 4\,\mathrm{mm}^{-1}$, $\mu_a = 0.16\,\mathrm{mm}^{-1}$. These optical properties are chosen based on the *in vivo* optical properties of human tissues which generally vary in the ranges of $\mu_s' = 0.12 - 4\ \mathrm{mm}^{-1}$, $\mu_a = 0.003 - 0.16\ \mathrm{mm}^{-1}$ [127]. The luciferase concentration used in this simulation is $20\,\mathrm{mg/ml}$.

The calculated results are shown in Fig. 2.11. It can be seen from Fig. 2.11a1 that Φ_{AC} keeps decreasing while moving the US focal zone away from the bioluminescent source until there is no overlap between the bioluminescent source and the US focal zone ($z = 2$). After this the US modulated bioluminescence signal Φ_{AC} is almost a constant.

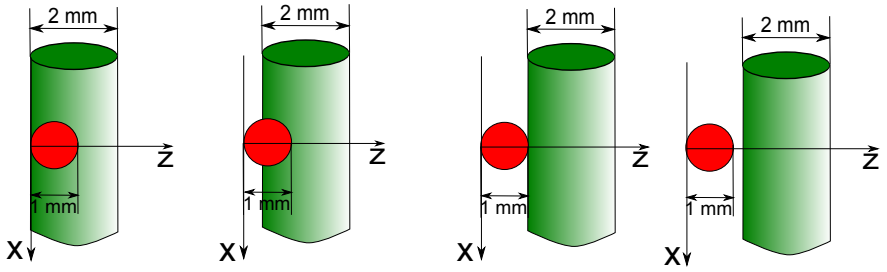


Figure 2.10: Geometry of US position. Red: bioluminescent target. Green: US field.

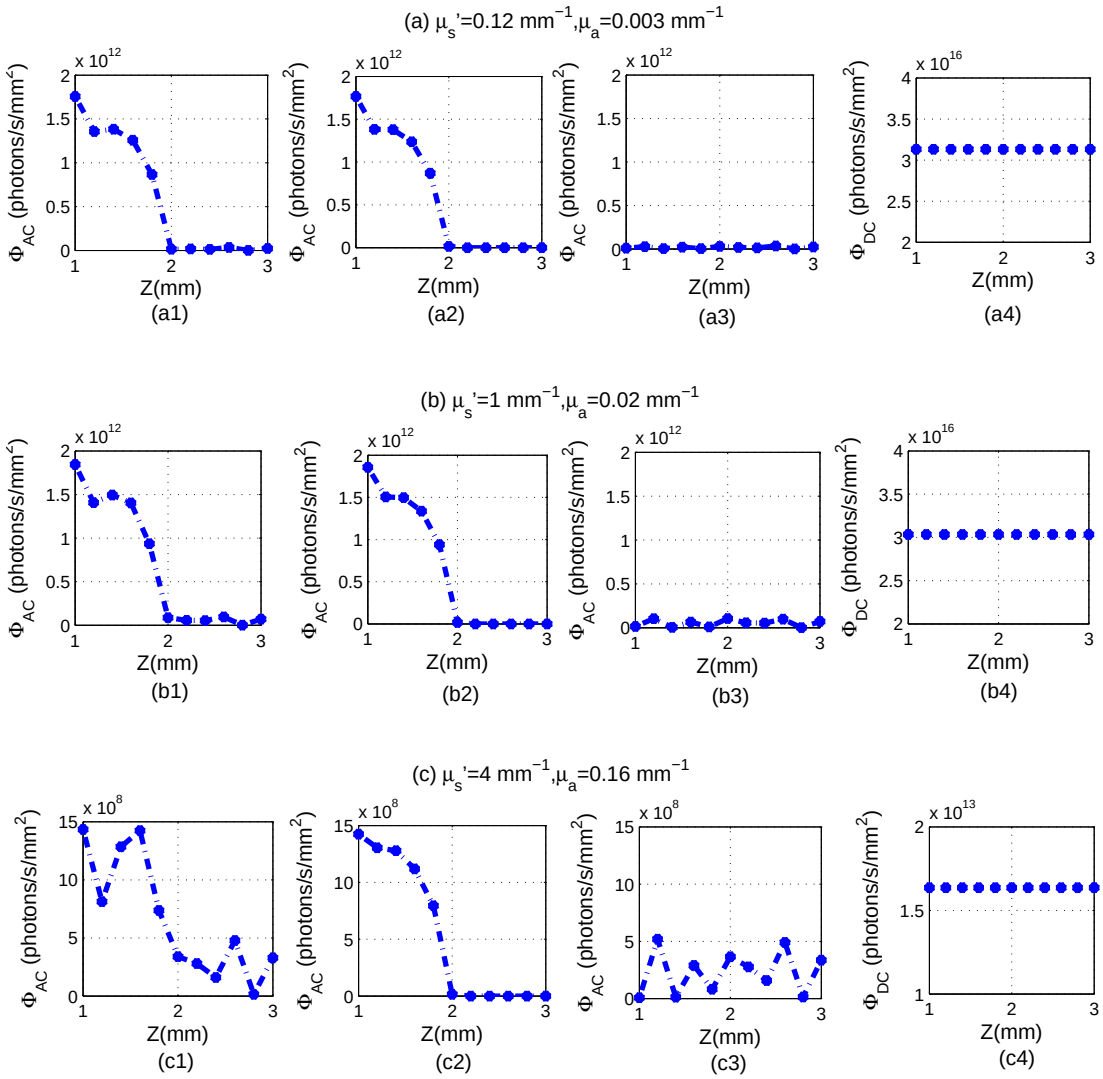


Figure 2.11: Influence of US position ($1 \leq z \leq 3$) on fluence rates for three groups of optical properties. (a1), (b1) and (c1) are US modulated signals considering both concentration and optical properties; (a2), (b2) and (c2) are US modulated signals considering only concentration; (a3), (b3) and (c3) are US modulated signals considering only optical properties; and (a4), (b4) and (c4) are unmodulated signals.

To investigate the reason for this US position dependent characteristic, the effects of the concentration of the source particles and optical properties are studied separately, as shown in Fig. 2.11a2 and a3. It can be seen that when taking into account only the contribution of the concentration, a similar trend is observed. However, when considering only the influence of the optical properties, Φ_{AC} is around two magnitudes lower than the situation only considering the influence of the concentrations. There is no obvious dependance of Φ_{AC} on US position. Therefore it is clear that the decrease of Φ_{AC} along z position of the US is mainly due to the reduced modulation of the concentration, resulting from the decreased overlap region of the US focal zone and the bioluminescent source. This observation is significant for application of USMBLT to improve the resolution of the bioluminescent images, because at the region where there is bioluminescent target the maximum modulated optical signal can be detected.

Similar trends can be obtained at the other two optical properties studied, as shown in group b and c of Fig. 2.11. In addition, by comparing the magnitudes of Φ_{AC} and Φ_{DC} for the three groups of optical properties, it can be seen that both Φ_{AC} and Φ_{DC} are lower for higher optical properties. This is because light scattering and absorption are higher in the simulated phantom with higher optical properties.

The modulation depths for the three groups of optical properties are also calculated. Fig. 2.12a, Fig. 2.12b and Fig. 2.12c show respectively the modulation depth when considering influence of both of luciferase concentration and the optical properties, influence of luciferase concentration only, and influence of optical properties only. It can be seen from Fig. 2.12a and Fig. 2.12b that modulation depths are roughly at the level of 10^{-5} for all the three groups of optical properties studied. Due to the dominance of the modulation of the concentration on the overall modulation depth, the optical properties of the medium have little influence on the modulation depths. The variations observed in Fig. 2.12c are owing to a quantization noise due to a relatively large mesh size. These variations can be reduced if using a smaller mesh size but with an increased simulation time.

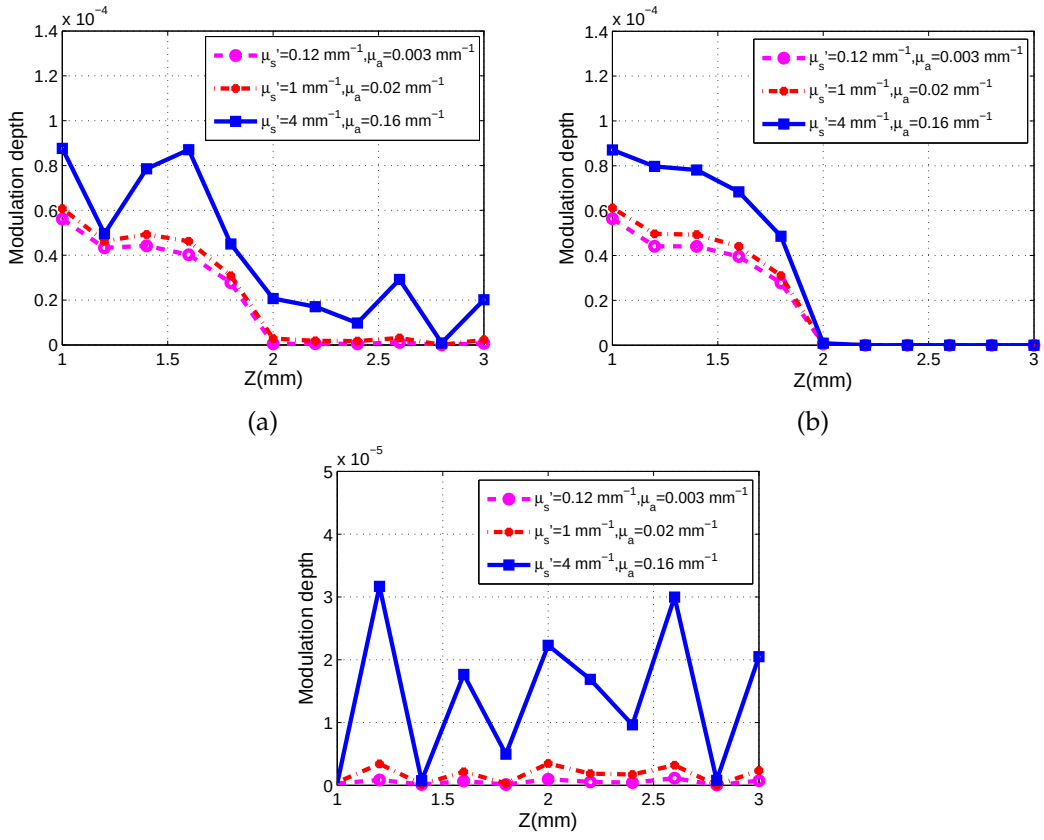
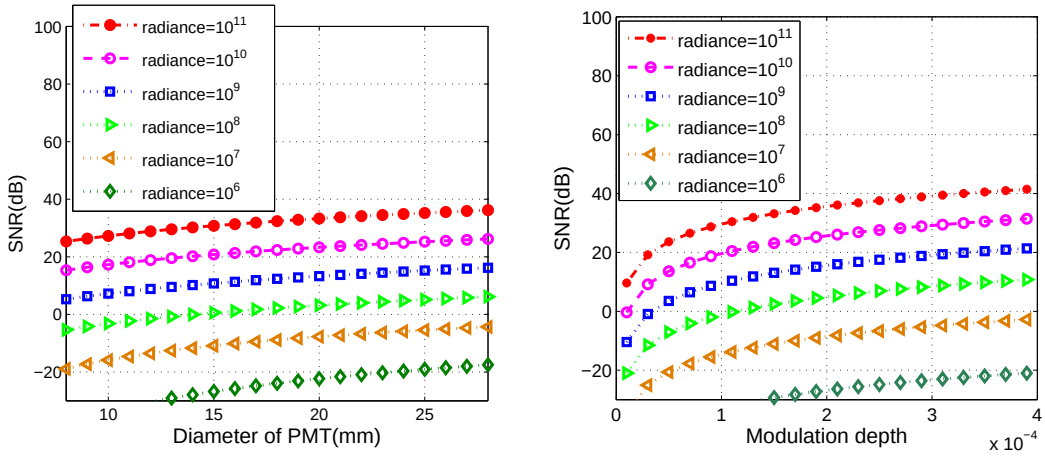


Figure 2.12: Influence of US position ($1 \leq z \leq 3$) on modulation depth at three groups of optical properties when considering (a) influence of both of the luciferase concentration and optical properties; (b) influence of the luciferase concentration only; (c) influence of the optical properties only. US frequency is 1 MHz.

2.3.6 SNR analysis of *in vivo* detection

In this section the effect of diameter of PMT window, surface radiance of bioluminescence and modulation depth on the SNR of USMBLT system are analysed based on the method described in Section 2.2. Fig. 2.13 shows the SNR calculated for six different surface radiances ($10^6, 10^7, 10^8, 10^9, 10^{10}$, and 10^{11} photons $s^{-1}\,cm^{-2}\,sr^{-1}$) as a function of diameter of the PMT window with a modulation depth of 6.1×10^{-5} (calculated from 1 MPa US at 1 MHz frequency) (Fig. 2.13a) and as a function of modulation depth for a fixed diameter of PMT window of 8 mm (Fig. 2.13b). The region of the surface radiance of $10^6 - 10^{11}$ photons $s^{-1}\,cm^{-2}\,sr^{-1}$ covers typical values found in the literature [43, 44, 138]. The contribution of the ambient light and the dark current to the noise power are estimated based on a noise voltage level of 0.4 μV_{rms}, as detected in a previous experiment [55].



(a) (b)

Figure 2.13: SNR simulation for USMBLT experiments for different surface radiance (unit: photons $s^{-1}\,cm^{-2}\,sr^{-1}$) (a) as a function of diameter of the PMT window with modulation depth of 6.1×10^{-5}; and (b) as a function of modulation depth with diameter of PMT window of 8 mm.

The feasibility of applying USMBLT to pre-clinical imaging is contingent on detection of modulated optical signals within the noise limits of current detector technologies. Results in Fig. 2.13 are based on calculations for a mouse model with detector capabilities matching that of a PMT used in previous experimental studies (Hamamatsu H5783-20). Fig.2.13a shows for a 8 mm diameter PMT window and modulation depth

of 6.1×10^{-5}, SNRs achieved with radiances ranging from 10^6 photons $s^{-1}\,cm^{-2}\,sr^{-1}$ to 10^8 photons $s^{-1}\,cm^{-2}\,sr^{-1}$ fall below the noise level of the simulated detector. However, for radiances above 10^9 photons $s^{-1}\,cm^{-2}\,sr^{-1}$ the SNRs are comfortably within the limits of the detector used in [55]. Apart from changing the radiance, the SNR can also be improved by increasing the diameter of PMT window as seen in Fig. 2.13a and the modulation depth as shown in Fig. 2.13b. It is noted that the nonlinear relationship of SNR with respect to radiance is caused by the $0.4\,\mu V_{rms}$ noise voltage level from dark current and ambient light.

Overall there are good prospects for the application of USMBLT in pre-clinical imaging. Besides, considerable effort has been directed to establish novel luciferases that can exert a brighter, stable, and red-shifted bioluminescence by mutation [46, 139], DNA optimization [47], or BRET with fluorescent proteins [49]. A novel luciferase Nanoluc has been established that can emit approximately 100-fold brighter and more stable bioluminescence than Fluc [42]. Such signal improvement will lead to greater SNRs and enhance the quality of USMBLT images. Other strategies to improve the modulated optical signal relate to the use of contrast agents such as microbubbles to increase the compressibility and as such have the capability to increase the US modulation of the bioluminescent source intensity, as indicated by Eq. 2.2.10.

2.4 Discussion and conclusions

In this chapter numerical simulations are carried out to investigate the mechanisms dominant in generation of USMBL signals in scattering tissue through modification of the NIRFAST software tool. The instantaneous change of the US modulated fluence rate with time is successfully modeled. Results demonstrate that the dominant effect in generation of USMBL is US induced variation in luciferase concentration. This effect is determined to be approximately two orders of magnitude greater than that caused by changes in the reduced scattering coefficient and absorption coefficient and of the order of 10^5 times higher than that related to changes in the refractive index.

The effects of US frequency, US pressure, US position and the concentration of the

source particles on the modulation depth are investigated. It is found that modulation depth increases linearly with increase of US pressure and decreases for higher US frequency. Maximum modulation depth can be obtained when the US focal zone is overlapped with the bioluminescence source region. The modulated fluence rate increases linearly with increase of the concentration but the modulation depth is independent of the concentration.

The SNR analysis is based on the detection capabilities of instrumentation used in previous experimental work. Results confirm the feasibility of applying USMBLT in preclinical imaging of mice to improve the spatial resolution of BLI. The measured USMBL signal has the potential to provide additional data for BLI reconstruction to make the inverse problem better conditioned. It is determined that for surface radiances above approximately 10^9 photons $s^{-1}\,cm^{-2}\,sr^{-1}$ the corresponding SNRs are detectable with devices currently used in USMLT experiments. This is a light level that can be achieved using the current available bioluminescent sources (e.g. firefly luciferase [44]). In addition, the development of novel luciferases that can exert bioluminescence above such radiance levels will further aid the practical application of the technique. Surface radiance lower than 10^9 photons $s^{-1}\,cm^{-2}\,sr^{-1}$ might also be detectable through increasing the modulation depth (e.g. by increasing the compressibility using microbubbles) or using a PMT with larger diameter optical window.

Finally it should be noted that these findings are based on simulations of a simplified experimental situation in which the tissue phantom is considered to be homogenous, unlike the case of real biological tissue. In addition, US propagation to the focal zone is not modeled and only the pressure at the fundamental frequency is considered with lock-in detection being applied to extract this component. It should be noted that, in the presence of non-linear propagation, generation of harmonic components will mean that higher US amplitudes will need to be generated at the transducer in order to generate sufficient pressure at the fundamental frequency. Within the US focal zone the effects of attenuation, absorption, scattering and beam divergence are also neglected. A more sophisticated model would make all the speed related parameters in Section 2.2 functions of position and time instead of constants. Further work will involve incorporation

of these effects into the NIRFAST software tool through the use of an acoustic toolbox such as k-Wave [140] to model propagation to, and pressure distribution within, the focal zone more accurately.

CHAPTER 3

Theoretical and experimental evaluation of fluorophore labelled microbubble system

3.1 Introduction

As introduced in Chapter 1 the technique of USMFT has potential to be a useful technique to obtain fluorescence images with optical contrast and US resolution in deep tissue. However, due to the intrinsic incoherent properties of fluorescence, this technique is limited by the very low modulation depth ($10^{-6} - 10^{-4}$ [64]) which results of low signal-to-noise ratios and poor image contrast.

Microbubbles, which have been used regularly as diagnostic US contrast agents, have been incorporated with fluorophores and used to enhance the modulation depth in USMFT [117, 141, 142]. The schematic of such fluorophore labelled microbubble with application of US is shown in Fig. 3.1. Microbubbles labelled by identical fluorophores were tuned to be self-quenched at an optimized concentration of fluorophore per microbubble. With application of US, the fluorophore-labelled microbubble oscillates and thus results in an alteration in the intermolecular spacing. At negative cycle of US the microbubble is compressed therefore the self-quenching of microbubble increases,

leading to a decreased fluorescence emission intensity. At positive cycle of US the microbubble is expanded, leading to an increased fluorescence emission intensity owing to the fluorescence recovery of the self-quenched fluorophores. Therefore the modulated fluorescence signal at US frequency is significantly increased. Another similar method involves unlike quenchers - using one type of fluorophores as donor and another type as acceptor [118]. Volumetric oscillation of microbubble changes the FRET efficiency between donor and acceptor and thus leads to an increased modulation depth.

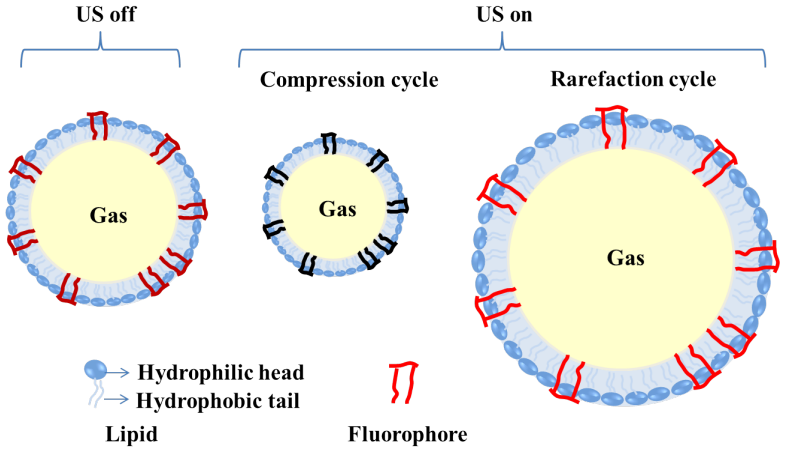


Figure 3.1: Schematic of the fluorophore labelled microbubble without and with application of US.

In this chapter the fluorophore labelled microbubble is theoretically and experimentally evaluated. Theoretical models of microbubble oscillation and fluorescence emission of fluorophore labelled microbubbles in a scattering medium are firstly described in Section 3.2. Section 3.3.1 shows calculation of the fluorescence quenching efficiency and fluorescence emission from a single fluorophore labelled microbubble in the absence of US. The volumetric oscillation and modulated fluorescence intensity in the presence of US are then presented in Section 3.3.2. Section 3.3.3 investigates the influence of parameters such as microbubble radius, fluorophore concentration, and US pressure on the modulated fluorescent signal. The modulation depth and SNR from a population of microbubbles located inside a scattering medium are also calculated, as shown in Section 3.3.4. Finally, fluorophore labelled microbubbles are produced and the modulated fluorescent signal is experimentally demonstrated in Section 3.4.

3.2 Theoretical models

When the scattered photons reach the region where fluorophore labelled microbubbles are located, the fluorophores in the shell of the microbubble are excited. In this Chapter the fluorescence emission intensity was calculated from a two-energy-level model [54]. Due to self-quenching, the fluorescence emission intensity is dependent on the radius of the microbubbles, which can be varied with application of US. There are several mathematical models proposed describing the dynamics of microbubbles in the presence of US field, such as Hoff model [143], Marmottant model [99, 103, 144], and modified Herring equation [98, 145]. These models differ both in complexity and in the range of radius increase (ratio of the maximum radius to the equilibrium radius) for which they can be used [145]. In this chapter, a model based on the modified Herring equation was used to describe the volumetric oscillation of microbubbles because it can provide satisfactory results for radius increase up to 4.5 [145]. Diffusion theory of light propagation was used to calculate the propagation of the excitation light and fluorescent emitted light in a scattering medium.

3.2.1 Fluorescence quenching in fluorophore labelled microbubbles

The emission intensity $S(r,t)$ (photons/s/mm^3) at position $r(x,y,z)$ and time t of fluorophore labelled microbubbles when excited can be expressed as [54]:

$$S(r,t) = \Phi \xi^{ex} N_0 A^{ex}(r)(1 - exp(-t/\tau)) \tag{3.2.1}$$

where ξ^{ex} is the extinction coefficient of the tissue at the excitation wavelength, $N_0 = N_B M$ is the fluorophore concentration in particles/ml, N_B is the microbubble concentration in particles/ml, $A^{ex}(r)$ is the photon fluence (photons/s/mm^2). Φ and τ are the quantum yield and lifetime of a fluorophore incorporated on the shell of the microbubble respectively [54]:

$$\Phi = \Phi_0 \frac{[\sqrt{\frac{4\pi}{M}}\frac{R}{\tilde{r}_0}]^6}{1 + [\sqrt{\frac{4\pi}{M}}\frac{R}{\tilde{r}_0}]^6} \tag{3.2.2}$$

$$\tau = \tau_0 \frac{[\sqrt{\frac{4\pi}{M}}\frac{R}{\tilde{r}_0}]^6}{1+[\sqrt{\frac{4\pi}{M}}\frac{R}{\tilde{r}_0}]^6} \tag{3.2.3}$$

where Φ_0 and τ_0 are the natural quantum yield and natural lifetime of the fluorophore respectively, $\tilde{r}_0$ is the Förster distance, R is the radius of microbubble. M is the total number of fluorescent molecules and quenchers per microbubble. Assuming the quenchers have the same number as fluorophores (e.g. fluorescence self-quenching) and they are evenly distributed on the shell of the microbubble,

$$M = \frac{4\pi R_0^2 C}{D^2} \tag{3.2.4}$$

where C is concentration (mol%) of the fluorophores expressed in the molar percentage of fluorophore and lipid, R_0 is the initial radius of microbubble, and D is lipid diameter.

The quenching efficiency can be calculated using FRET equation [141]:

$$E = \frac{1}{1+(\frac{r}{\tilde{r}_0})^6} \tag{3.2.5}$$

where r is the intermolecular distance of DiI molecules. In this study it is assumed that DiI is distributed on the shell of microbubble evenly, therefore theoretically there is equation

$$4\pi R_0^2 = Mr^2 \tag{3.2.6}$$

Replacing M in Eq. 3.2.6 with Eq. 3.2.4, the intermolecular distance of r can be expressed as:

$$r = \frac{D}{\sqrt{C}} \tag{3.2.7}$$

Combining Eq. 3.2.7 with Eq. 3.2.5 it can be seen that the quenching efficiency is dependent on the concentration of the fluorophores and is independent of the size of the microbubble.

3.2.2 Volumetric oscillation of microbubble

Microbubbles can oscillate linearly when insonified with relatively low US pressure at appropriate US frequency. With higher US pressure they can oscillate nonlinearly producing harmonics (integer multiples of the fundamental), subharmonics (half the driving frequency), and ultraharmonics (odd multiples of half the driving frequency). The harmonic component can help enable echoes from microbubbles to be distinguished from those due to tissue [146]. Subharmonics have been used to predict stable cavitation activity [103] and both the subharmonics and ultraharmonics have been investigated as effective modalities for noninvasive pressure measurement [147]. In this thesis the oscillation of the microbubble is modeled by solving the following modified Herring equation [98]:

$$\begin{aligned}\rho R\ddot{R} + \frac{3}{2}\rho\dot{R}^2 = (P_0 + \frac{2\sigma}{R_0} + \frac{2\chi}{R_0})(\frac{R_0}{R})^{3\gamma}(1 - \frac{3\gamma\dot{R}}{c}) - \frac{4\mu\dot{R}}{R} - \frac{2\sigma}{R}(1 - \frac{\dot{R}}{c}) \\ - \frac{2\chi}{R_0}(\frac{R_0}{R})^2(1 - \frac{3\dot{R}}{c}) - \frac{12\mu_{sh}\epsilon\dot{R}}{R(R-\epsilon)} - (P_0 + P_{US}(t))\end{aligned} \tag{3.2.8}$$

where R, $\dot{R}$, $\ddot{R}$ are the radius, instantaneous oscillation speed, and instantaneous oscillation acceleration speed respectively. $P_{US}(t) = P_A sin(2\pi f_{us} t)$ is the simplified driving pressure of US. The other parameters in Eq. 3.2.8 are listed in Table 3.1. The values in the table are used for calculation in this chapter unless otherwise stated. The values of ϵ, σ, P_0, ρ, γ, μ are obtained from [98]. The viscosity of lipid shell μ_{sh} is obtained from [54]. The shell elasticity modulus χ is from [148] where the experimental resonance curve measured with microbubble spectroscopy technology was fitted with the eigenfrequency derived from Marmottant model to obtain χ. The viscosity of the surrounding liquid is described in Eq. 3.2.8 as the factor $\frac{4\mu\dot{R}}{R}$. The sum of the gas-lipid and the lipid-water interfacial tensions are included as $\frac{2\sigma}{R}(1 - \frac{\dot{R}}{c})$. The influence of the lipid shell is included as $\frac{2\chi}{R_0}(\frac{R_0}{R})^2$ and $\frac{12\mu_{sh}\epsilon\dot{R}}{R(R-\epsilon)}$, which represent the elasticity and viscosity respectively. This model is validated in [98] by comparison of the predicated radial oscillations with those measured optically using microbubbles with phospholipid shell.

For calculation of the oscillation of the microbubble using the ordinary differential

Table 3.1: Parameters used in modified Herring equation.

Symbol	Meaning	Value
μ_{sh}	Viscosity of lipid shell	$\mu_{sh}\epsilon(\text{nm}\cdot\text{Pa}\cdot\text{s}) = 1.49R_0(\mu\text{m}) - 0.86$
ϵ	Thickness of lipid shell	1 nm
χ	Elasticity modulus of lipid shell	0.54 N/m
σ	Interfacial tension coefficient	0.051 N/m
γ	Polytropic gas exponent	1.07
P_0	Hydrostatic pressure	101 kPa
ρ	Tissue density	998 kg/m^3
c	Speed of sound in water	1500 m/s
μ	Viscosity in water	0.001 Pa · s
f_{us}	Frequency of US	2.25 MHz
P_A	US amplitude (Peak negative US pressure)	300 kPa
R_0	Initial microbubble radius	2.5 µm

equation solver in MATLAB Eq. 3.2.8 need to be normalized. Let $\tau = w_{us}t$, $R = rR_0$, and $P_a = pP_0$, then $\dot{R} = \dot{r}R_0w_{us}$, $\dot{R} = \ddot{r}R_0w_{us}^2$ can be obtained. The final non-dimensional form is

$$\begin{aligned}\frac{\rho R_0^2 w_{us}^2 r\ddot{r}}{P_0} + \frac{3\rho R_0^2 w_{us}^2 \dot{r}^2}{2P_0} = (1 + \frac{2\sigma}{R_0P_0} + \frac{2\chi}{R_0P_0})(\frac{1}{r})^{3\gamma}(1 - \frac{3\gamma R_0 w_{us}\dot{r}}{c}) - \frac{4\mu w_{us}\dot{r}}{P_0 r} \\ - \frac{2\sigma}{rP_0R_0}(1 - \frac{w_{us}R_0\dot{r}}{c}) - \frac{2\chi}{rR_0P_0}(\frac{1}{r})^2(1 - \frac{3w_{us}R_0\dot{r}}{c}) \\ - \frac{12\mu_{sh}\epsilon w_{us}\dot{r}}{P_0(rR_0 - \epsilon)r} - (1 + psin\tau)\end{aligned} \tag{3.2.9}$$

Insonifying microbubbles with US frequency at its resonance frequency is critical to obtain the maximum amplitude oscillation. The resonance frequency can be calculated as [99]:

$$f_0 = \frac{1}{2\pi}\sqrt{\frac{1}{\rho R_0^2}[3\gamma P_0 + \frac{2(3\gamma - 1)\sigma}{R_0} + \frac{4\chi}{R_0}}} \tag{3.2.10}$$

It can be seen from Eq. 3.2.10 that the resonance frequency is a function of microbubble radius with the other parameters being constants, as shown in Fig. 3.2. It can be seen from Fig. 3.2 that resonance frequency for 2.5 µm radius microbubble is around 2.25 MHz. In the Experimental Section 3.4 microbubbles with radius size centered at

2.5 µm was produced, therefore an US transducer with frequency 2.25 MHz was used in the experimental setup.

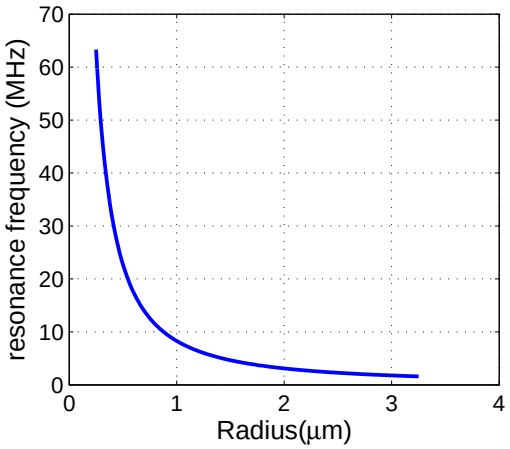


Figure 3.2: Resonance frequency of microbubble against its radius.

3.2.3 Light propagation in scattering medium

Simulation geometry and diffusion model

Suppose the simulation geometry is arranged such that the optical illumination is perpendicular to the air/tissue surface of a finite slab, as shown in Fig. 3.3. A fluorophore-labelled microbubble solution is injected into a tube which is located perpendicularly and overlaps the US focal zone. The $\lambda = 532$ nm laser source S excites the fluorophores labelled on microbubbles, and the fluorescence emission intensity is detected by a PMT D located outside of the scattering medium but very close to the surface. The effective diameter of the sensor of the PMT is D_{PMT}.

Diffusion theory is used to calculate the propagation of the excitation light and fluorescence emission in the scattering medium. The boundary condition is modeled using extrapolated zero boundary condition and the method of images to solve the relationship between fluence rate at the surface and flux coming into the tissue. The boundary conditions can be met by adding an infinite series of dipole photon sources [149]. In this thesis four dipoles ((M_1, N_1), (M_2, N_2), (M_3, N_3), and (M_4, N_4)) are retained, as shown in Fig. 3.3b. M_1 is an isotropic point source a distance z_0 into the medium, and N_1 is an isotropic negative or image source a distance $2z_b + z_0$ outside of the medium,

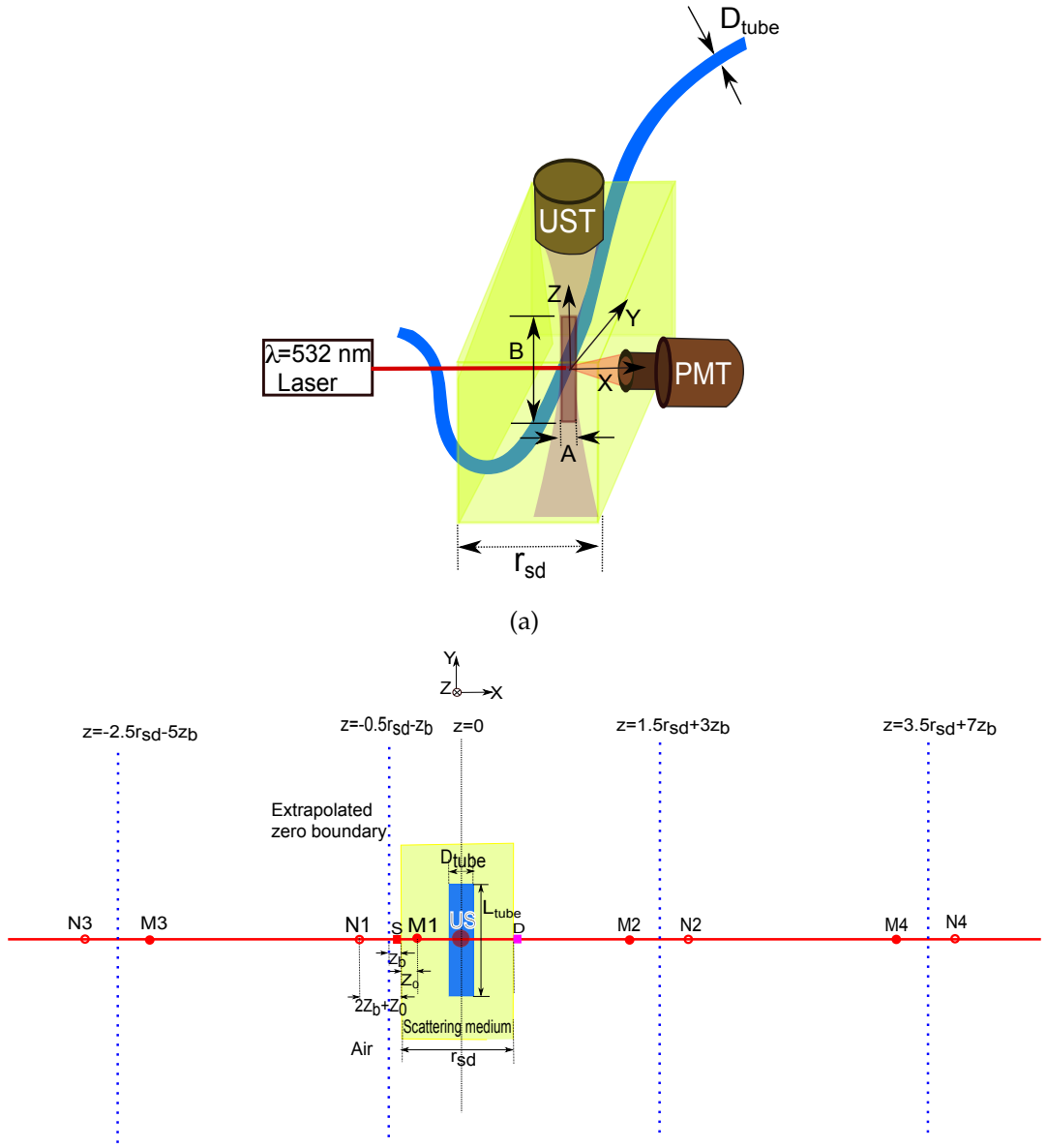


Figure 3.3: Geometry for calculation in a finite slab. The US pressure zone is simulated as a cylinder with bottom diameter $A = 2\,\text{mm}$ and height $B = 20\,\text{mm}$. The tube injecting the microbubble has a diameter $D_{tube} = 3\,\text{mm}$. Microbubbles located in $L_{tube} = 30\,\text{mm}$ of the overall tube are assumed to be excited. (a) 3D; (b) x-y plane. The boundary conditions can be met by adding an infinite series of dipole photon sources. Four dipoles ((M_1, N_1), (M_2, N_2), (M_3, N_3), and (M_4, N_4)) are retained in the calculation. S is the laser source; D is the photomultiplier tube (PMT) detector.

where $z_0 = 1/(\mu_s^{'ex})$ is the reduced transport distance, and z_b is the linear extrapolation distance [150]:

$$z_b = \frac{1 + R_{eff}}{1 - R_{eff}} \frac{2}{3\mu_s^{'ex}} \tag{3.2.11}$$

R_{eff} is the effective reflective coefficient and can be obtained from the relative index of refraction $n = n_{in}/n_{out}$ [150]:

$$R_{eff} = -1.440n^{-2} + 0.710n^{-1} + 0.668 + 0.0636n \tag{3.2.12}$$

$\mu_s^{'ex}$ is the reduced scattering coefficient at the excitation wavelength. The image sources and the sources are mutually symmetric with respect to the extrapolated zero boundary so that the diffuse fluence extrapolates to zero on the boundary. In this analysis, the center position of the coordinate system is located in the center of the scattering medium. The Cartesian coordinates of the sources are $M_1(-0.5r_{sd} + z_0, 0, 0)$, $N_1(-0.5r_{sd} - 2z_b - z_0, 0, 0)$, $M_2(-1.5r_{sd} + 2z_b - z_0, 0, 0)$, $N_2(-1.5r_{sd} + 4z_b + z_0, 0, 0)$, $M_3(-2.5r_{sd} - 4z_b + z_0, 0, 0)$, $N_3(-2.5r_{sd} - 6z_b - z_0, 0, 0)$, $M_4(3.5r_{sd} + 8z_b + z_0, 0, 0)$, $N_4(3.5r_{sd} + 6z_b - z_0, 0, 0)$ respectively. The US focus is located in the midnormal of the source and detector.

Calculation of photon fluence at US focal zone

The photon fluence (photons/s/mm^2) at position $r(x, y, z)$ can be calculated as:

$$\begin{aligned} A^{ex}(r) = P^{ex}[&\frac{exp(-k^{ex}r_{M1})}{4\pi D^{ex}r_{M1}} - \frac{exp(-k^{ex}r_{N1})}{4\pi D^{ex}r_{N1}} + \frac{exp(-k^{ex}r_{M2})}{4\pi D^{ex}r_{M2}} - \frac{exp(-k^{ex}r_{N2})}{4\pi D^{ex}r_{N2}} \\ &+ \frac{exp(-k^{ex}r_{M3})}{4\pi D^{ex}r_{M3}} - \frac{exp(-k^{ex}r_{N3})}{4\pi D^{ex}r_{N3}} + \frac{exp(-k^{ex}r_{M4})}{4\pi D^{ex}r_{M4}} - \frac{exp(-k^{ex}r_{N4})}{4\pi D^{ex}r_{N4}}] \end{aligned} \tag{3.2.13}$$

where P^{ex} (photons/s) is the source strength calculated from a laser source with 50 mW power and 532 nm wavelength, $k^{ex} = \sqrt{\mu_a^{ex}/D^{ex}}$, $D^{ex} = 1/3(\mu_a^{ex} + \mu_s^{'ex})$ and μ_a^{ex} are diffusion coefficient and absorption coefficient at the excitation wavelength respectively. r_{M1}, r_{N1}, r_{M2}, r_{N2}, r_{M3}, r_{N3}, r_{M4}, r_{N4} are the distances from the sources $M1$, $N1$, $M2$, $N2$, $M3$, $N3$, $M4$, $N4$ to the position r respectively. For the convenience of integration

over the region where fluorophore labelled microbubbles are located, the coordinates are changed to polar coordinates (ρ, θ, z), and thus

$$r_{M1} = \sqrt{(\rho cos\theta + 0.5r_{sd} - z_0))^2 + (\rho sin\vartheta)^2 + z^2} \tag{3.2.14}$$

$$r_{N1} = \sqrt{(\rho cos\vartheta + 0.5r_{sd} + 2z_b + z_0)^2 + (\rho sin\vartheta)^2 + z^2} \tag{3.2.15}$$

$$r_{M2} = \sqrt{(\rho cos\theta - 1.5r_{sd} - 2z_b + z_0))^2 + (\rho sin\vartheta)^2 + z^2} \tag{3.2.16}$$

$$r_{N2} = \sqrt{(\rho cos\vartheta - 1.5r_{sd} - 4z_b - z_0)^2 + (\rho sin\vartheta)^2 + z^2} \tag{3.2.17}$$

$$r_{M3} = \sqrt{(\rho cos\theta + 2.5r_{sd} + 4z_b - z_0))^2 + (\rho sin\vartheta)^2 + z^2} \tag{3.2.18}$$

$$r_{N3} = \sqrt{(\rho cos\vartheta + 2.5r_{sd} + 6z_b + z_0)^2 + (\rho sin\vartheta)^2 + z^2} \tag{3.2.19}$$

$$r_{M4} = \sqrt{(\rho cos\theta - 3.5r_{sd} - 8z_b - z_0))^2 + (\rho sin\vartheta)^2 + z^2} \tag{3.2.20}$$

$$r_{N4} = \sqrt{(\rho cos\vartheta - 3.5r_{sd} - 6z_b + z_0)^2 + (\rho sin\vartheta)^2 + z^2} \tag{3.2.21}$$

If $\rho \in [0, A/2]$, $\theta \in [0, 2\pi]$, and $z \in [-0.5D_{tube}, 0.5D_{tube}]$, the position r is inside the region Ω where fluorophore labelled microbubbles are exposed to US. This region is simplified as a cylinder with the diameter the same as the diameter (A) of the US focal zone and height the same as the diameter of the tube (D_{tube}).

Calculation of photon fluence at the detector

The fluorophores on the shell of the microbubble are excited when the scattered photons reach region Ω. The emission intensity $S(r,t)$ can be calculated using Eq. 3.2.1. The fluorescence fluence $U(r,t)$ (photons/s/mm^2) at the detector position $r_d(0.5r_{sd}, 0, 0)$ can be obtained by

$$U(r,t) = \int_\Omega S(r,t)G(r)d\Omega = \int_{-0.5D_{tube}}^{0.5D_{tube}} \int_0^{2\pi} \int_0^{A/2} S(r,t)G(r)rdzd\theta d\rho \tag{3.2.22}$$

where $G(r)(mm^{-2})$ is the Gaussian function,

$$G(r) = \frac{exp(-k^{ex}r_D)}{4\pi D_{ex} r_D} \tag{3.2.23}$$

r_D is the distance between the position r and the detector D,

$$r_D = \sqrt{(\rho cos\theta - 0.5 r_{sd})^2 + (\rho sin\theta)^2 + z^2} \tag{3.2.24}$$

In this simulation the emission intensity is integrated all over the region Ω where the tube and the US focal zone intersected, as calculated by Eq. 3.2.22. The concentration of the microbubbles is considered through its contribution to the emission intensity, as shown in Eq. 3.2.1. The refraction and attenuation of the microbubbles to the excitation and emission light are not considered in this model.

Calculation of background fluorescence

There will be some fluorescence emission from the microbubbles located outside the US focal zone. The fluorophores on these microbubbles are also excited and contribute to the overall detected fluorescence. This part of fluorescence emission is not modulated by the US and thus forms background. For convenience of integrating the background signal from the whole illumination area, the rectangular coordinate is rotated 90° around the x-axis so that $x_{bg} = x$, $y_{bg} = -z$, and $z_{bg} = y$. x_{bg}, y_{bg}, and z_{bg} are the new rectangular coordinate. Since M, N, E, and F are located in the x-axis, their coordinates are the same as in the previous coordinates. Therefore r_{M1}, r_{N1}, r_{M2}, r_{N2}, r_{M3}, r_{N3}, r_{M4}, r_{N4} and r_D are the same as shown previously. However the integration area becomes $\rho \in [0, D_{tube}/2]$, $\theta \in [0, 2\pi]$ and $z \in [-L_{tube}/2, L_{tube}/2]$. The parameters used in the calculation of fluorescence emission are summarised in Table 3.2. The values of the parameters μ_a^{ex}, $\mu_s^{'ex}$, μ_a^{em}, $\mu_s^{'em}$, ξ^{ex}, and $\tilde{r}_0$ are obtained from [54]. The values of the parameters Q_0, τ_0, and D are from literature [151], [152], and [153] respectively. C is based on [141], where 2 mol% was shown to be an effective fluorophore loading concentration to achieve fluorescence modulation.

Table 3.2: Parameters used in calculation of fluorescence emission intensity.

Symbol	Meaning	Value
w_{ex}	excitation wavelength	532 nm
w_{em}	emission wavelength	570 nm
μ_a^{ex}	absorption coefficient at excitation wavelength	$0.02\,\mathrm{mm}^{-1}$
$\mu_s^{'ex}$	reduced scattering coefficient at excitation wavelength	$2.3\,\mathrm{mm}^{-1}$
μ_a^{em}	absorption coefficient at emission wavelength	$0.018\,\mathrm{mm}^{-1}$
$\mu_s^{'em}$	reduced scattering coefficient at emission wavelength	$2\,\mathrm{mm}^{-1}$
ξ^{ex}	extinction coefficient at excitation wavelength	1.25×10^{-20} m^2
n	relative index of refraction	1.4
P^{ex}	source intensity	1.3381×10^{17} photons/s
Q_0	quantum yield (DiI)	0.38
τ_0	lifetime (DiI)	1.2 ns
$\tilde{r}_0$	Förster distance (DiI-DiI)	4.4 nm
D	lipid diameter	0.7 nm
N_B	microbubble concentration	2×10^7 particles/ml
C	fluorophore concentration (DiI)	2 mol %
A	diameter of US focal zone	2 mm
B	height of US focal zone	20 mm
D_{tube}	diameter of tube	3 mm
L_{tube}	length of tube	30 mm
r_{sd}	thickness of the tissue slab	2 cm
D_{PMT}	effective diameter of sensor of PMT	8 mm

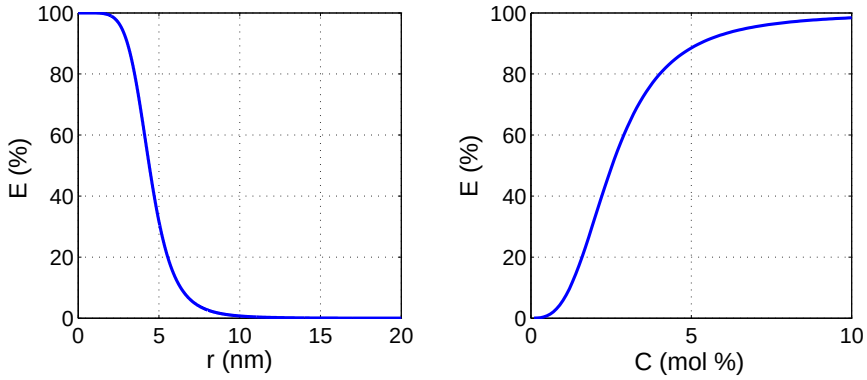
3.3 Simulation results

3.3.1 Fluorescence quenching in fluorophore labelled microbubbles

In this section the quenching efficiency is firstly calculated while varying the intermolecular distance and concentration of DiI fluorophores. The emission intensity from a single DiI fluorophore and a single microbubble at equilibrium state (in the absence of US) are then calculated and the influences of DiI concentration and microbubble radius are investigated. It has been shown that a maximum fluorescence signal can be observed at $C = 2\,\text{mol\%}$ [141]. Therefore C close to 2 mol% in the range of 0.1 mol% - 10 mol% was studied. Concentrations higher than 10 mol% might have severe disturbance to the lipid bilayer and further influence the stability of the microbubble, therefore are not considered. R_0 was varied in the range of 0.5 µm - 5 µm, which covers the range of microbubbles produced in the experimental section. Excitation and emission light propagation in the medium were not considered in this section.

The dependance of quenching efficiency on the intermolecular distance and the DiI concentration can be calculated from Eq. 3.2.5 and Eq. 3.2.7, as shown in Fig. 3.4. It can be seen from Fig. 3.4a that the quenching efficiency decreases with increase of intermolecular distance of DiI. At the Förster distance $\tilde{r}_0 = 4.4\,\text{nm}$, quenching efficiency equals 50%. Fig. 3.4b shows that the quenching efficiency increases with increase of the DiI concentration. It needs to be mentioned that the quenching efficiency is independent of microbubble size, as suggested by Eq. 3.2.7. Therefore in the case without applying US, the quenching efficiency of DiI is the same for microbubbles with different sizes.

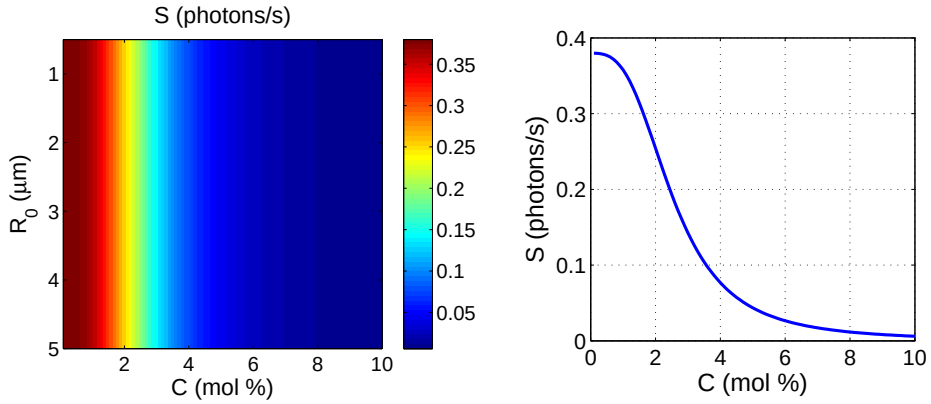
The steady-state ($t = \infty$) fluorescence emission intensity from a single fluorophore on the shell of the microbubble can be calculated through substituting Eq.3.2.2 and Eq.3.2.3 into Eq.3.2.1. Since only a single fluorophore is involved without considering light propagation, ξ^{ex}, N_0 and $A^{ex}(r)$ were all assigned a value of 1. The calculated intensity is shown in Fig.3.5. It can be seen that the emission intensity decreases with increase of DiI concentration. Similar to the quenching efficiency, the emission intensity of a single fluorophore is observed to be independent of the size of the microbubble. This



(a) (b)

Figure 3.4: Quenching efficiency (E) against (a) intermolecular distance (r) and (b) DiI concentration (C).

is because R_0 can be omitted through substituting Eq. 3.2.1 with Eq. 3.2.2 and Eq. 3.2.4.

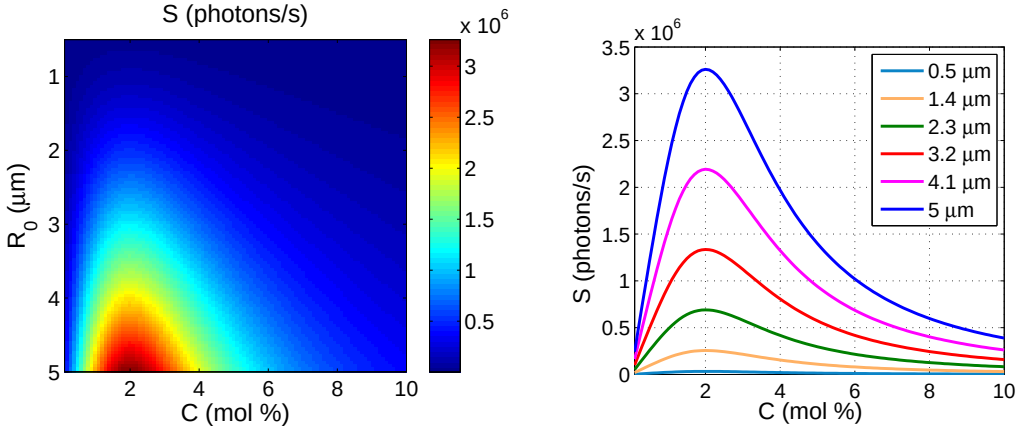


(a) (b)

Figure 3.5: Emission intensity (S) from a single fluorophore on the microbubble. R_0: microbubble radius; C: DiI concentration.

The fluorescence emission intensity from a single microbubble is also calculated through multiplying the emission intensity of a single fluorophore by the total number of fluorophores. Fig. 3.6 shows with increase of DiI concentration, the emission intensity firstly increases and then decreases. The peak is at 2 mol % concentration regardless of the microbubble radius. This is because the size of the microbubble has no influence on the quenching efficiency of the fluorophores, as mentioned previously. The peak concentration of 2 mol % is the same as the experimental results shown in Fig. 3 of [141]. If there were no self-quenching of DiI, the emission intensity from one microbubble would keep increasing with DiI concentration since there would be more

DiI molecules in one microbubble. However, due to the self-quenching effect the emission intensity from a single fluorophore decreases, as suggested by Fig. 3.5. At lower concentration, the self-quenching efficiency is low, therefore the overall emission intensity increases with increase of DiI concentration. However, at higher concentration the intermolecular distance becomes shorter and the self-quenching efficiency becomes higher, as suggested by Fig. 3.4. This leads to the decrease of emission intensity with further increase of DiI concentration. Fig. 3.6 also shows that at fixed DiI concentration, the emission intensity increases with increase of microbubble radius. This is because the size of the microbubble is a scaling factor that determine the number of the fluorophores located on the shell of the microbubble (Eq. 3.2.4).



(a) (b)

Figure 3.6: Emission intensity (S) from a single microbubble against microbubble radius (R_0) and DiI concentration (C). (a) 2D map; (b) cross-sections of the 2D map.

3.3.2 Oscillation of microbubble radius and fluorescence emission intensity when applying US

In this section the oscillation of microbubble radius and the fluorescence emission intensity when applying US was investigated. The oscillation of microbubble radius was obtained by solving Eq. 3.2.9 using the ordinary differential equation function ODE45 of Matlab. The radius was then used in Eq. 3.2.2 and Eq. 3.2.3 to calculate the time varying quantum yield and lifetime, which were further used in Eq.3.2.1 to calculate the fluorescence emission intensity. As in Section 3.3.1 a single microbubble was studied without considering light propagation, therefore ξ^{ex}, N_B and $A^{ex}(r)$ were assigned

to be 1.

Oscillation of microbubble ($R_0 = 2.5\,\mu m$) ***at US pressure*** $100\,kPa$

Fig. 3.7 shows the oscillation of size and the fluorescence emission intensity of one microbubble with $R_0 = 2.5\,\mu m$ when applying an US field with $P_A = 100\,kPa$, $f_{US} = 2.25\,MHz$, and number of cycles $N_C = 10$. The signals in time domain and frequency domain expressed in a single-sided amplitude spectrum with DC component removed were shown. It can be seen that at the first positive cycle of US, both of the radius of the microbubble and the fluorescence emission intensity reduce, with the lowest values obtained when the US pressure is zero. At the first negative cycle of US, both of the radius of the microbubble and the fluorescence emission intensity increase from the lowest values until the US pressure reaches the peak compression pressure. The radius and the fluorescence emission intensity then oscillates with an approximate similar phases with US.

It was also observed from Fig. 3.7a and Fig. 3.7b that R and S at the first four cycles were more irregular compared with the latter six cycles. This is because of an overlapping of an inertia oscillation following the first US cycle with the variations induced by the second US cycle. Between the fifth cycle and the penultimate cycle of US both of R and S have constant amplitudes. After the last US cycle, inertia damped oscillation can be seen which ends after around four further cycles of oscillation. The oscillation induced by the last US cycle is similar to the oscillation when only 1 pulse of US is applied. The oscillation of radius and fluorescence emission intensity with 1 and 50 pulses of US can be found in Fig. A.1 and Fig. A.2 in Appendix A.

The amplitude spectra of the radius and the fluorescence emission intensity (Fig. 3.7c and Fig. 3.7d) show clear peaks at the US frequency (2.25 MHz) (0.28 µm and 1.7×10^5 photons/s). There are also second harmonics at 4.5 MHz and subharmonics at 1.125 MHz observed for both of the oscillations of size and fluorescence emission intensity. The oscillation amplitudes of the radius at 4.5 MHz and 1.125 MHz are around 0.01 µm and 0.19 µm respectively. The oscillation amplitudes of the fluorescence emission intensity at 4.5 MHz and 1.125 MHz are around 2.5×10^4 photons/s and 1.1×10^5 photons/srespectively.

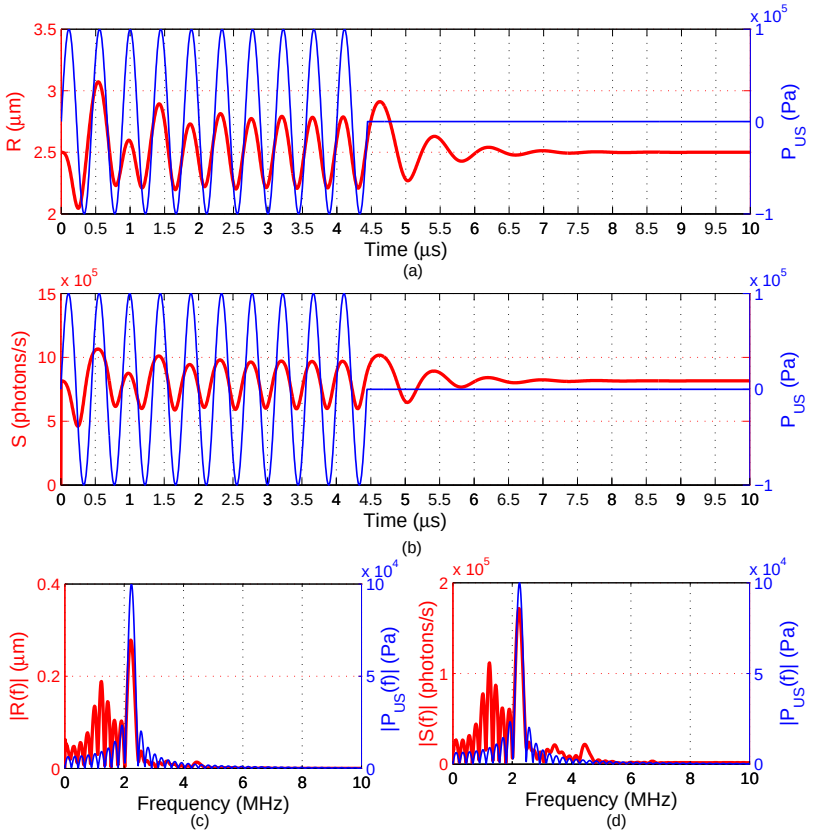


Figure 3.7: Oscillation of microbubble radius (R) and the fluorescence emission intensity (S) for $P_A = 100\,\text{kPa}$ and $R_0 = 2.5\,\mu\text{m}$. (a) Radius of microbubble (left y axis) and US pressure (right y axis) in time domain; (b) fluorescence emission intensity (left y axis) and US pressure (right y axis) in time domain; (c) radius of microbubble (left y axis) and US pressure (right y axis) in frequency domain; (d) fluorescence emission intensity (left y axis) and US pressure (right y axis) in frequency domain.

Oscillation of microbubble with $R_0 = 2.5\,\mu m$ ***and*** $P_A = 500\,kPa$

The dynamics of a fluorophore labelled microbubble at higher US pressure was investigated, as shown in Fig. 3.8 for 10 cycles of US at $P_A = 500\,kPa$. Compared with Fig. 3.7a size changes both at the positive cycle and at the negative cycle of US are bigger. It can be seen there are only five distinguishable cycles of oscillation in the time domain. In the frequency domain there are harmonic, sub-harmonic, and ultra-harmonic frequency components. The sub-harmonic component is even stronger than oscillation at the fundamental frequency. The size expansion amplitude ($\sim$3 µm) is bigger than size compression amplitude ($\sim$2 µm). However, decrease amplitude of the fluorescence emission intensity ($\sim 8 \times 10^5$ photons/s) is bigger than the increase amplitude of the fluorescence emission intensity ($\sim 4 \times 10^5$ photons/s). It can also been seen that the increased fluorescence emission intensity has a flat region while at the corresponding time durations the radius increases from $\sim 4\,\mu m$ to its peak and then decreases back to $\sim 4\,\mu m$. This is because at around $R_0 = 4\,\mu m$ the quenching efficiency is extremely low and the microbubble has its maximum possible fluorescence emission. Further increase of the microbubble radius makes no contribution to the emission intensity. This suggests that C=2 mol% is relatively low for $P_A = 500\,kPa$ so increase of quenching at the compression cycle of pressure has more effect on intensity than decrease of quenching at the rarefactional cycle of US. The oscillation of radius and fluorescence emission intensity with 1 and 50 pulses of US can be found in Fig. A.3 and Fig. A.4 in Appendix A respectively.

Oscillation of microbubble with $R_0 = 0.75\,\mu m$ ***and*** $P_A = 100\,kPa$

Oscillation of microbubbles with a smaller size was also investigated, as shown in Fig. 3.9 for $R_0 = 0.75\,\mu m$, $N_C = 10$ and $P_A = 100\,kPa$. It can be seen the size expansion is stronger than size compression, and the decrease of the fluorescence emission intensity is stronger than the increase of the fluorescence emission intensity. The biggest radius (highest fluorescence emission intensity) is obtained at the lowest US pressure with a small time lag due to inertance. The smallest radius (lowest fluorescence emission intensity) is obtained at the highest US pressure. The small decrease of size and fluorescence emission intensity during the size increasing period (from peak compres-

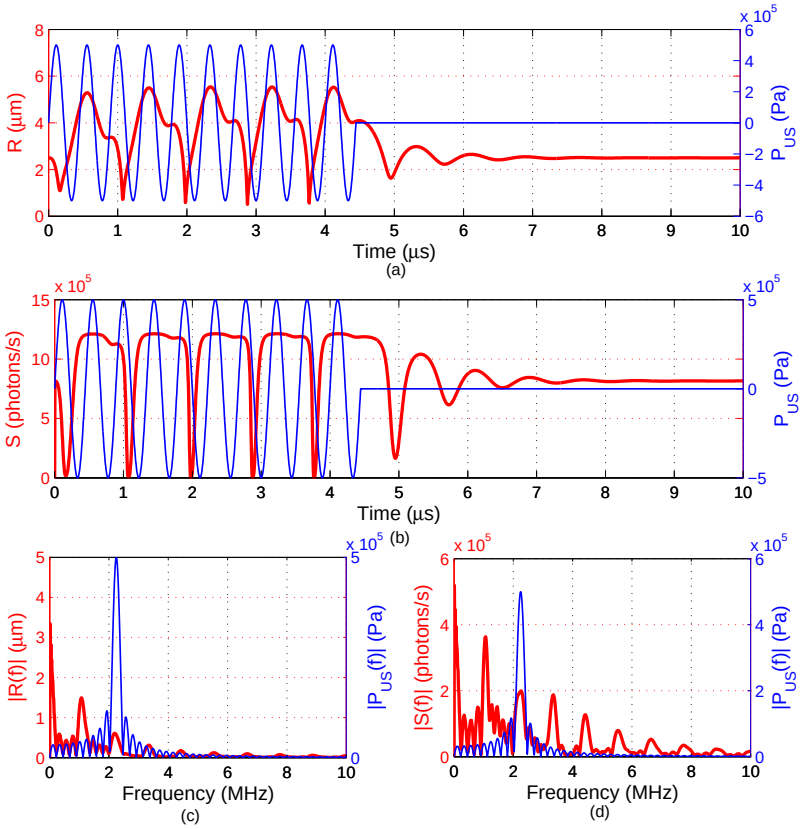


Figure 3.8: Oscillation of microbubble radius (R) and the fluorescence emission intensity (S) for $P_A = 500\,\text{kPa}$ and $R_0 = 2.5\,\mu\text{m}$. (a) Radius of microbubble (left y axis) and US pressure (right y axis) in time domain; (b) fluorescence emission intensity (left y axis) and US pressure (right y axis) in time domain; (c) radius of microbubble (left y axis) and US pressure (right y axis) in frequency domain; (d) fluorescence emission intensity (left y axis) and US pressure (right y axis) in frequency domain.

sional pressure to peak rarefactional pressure) is due to the damped oscillation at the previous cycle which has a size decreasing trend at the corresponding time duration (e.g. 0.61 µs to 0.70 µs). Compared with 2.5 µm microbubble at the same US pressures (Fig. 3.7), stronger harmonics were observed for 0.75 µm microbubble (Fig. 3.9). Similar simulations but with 1 and 50 pulses of US can be found in Fig. A.5 and Fig. A.6 in Appendix A.

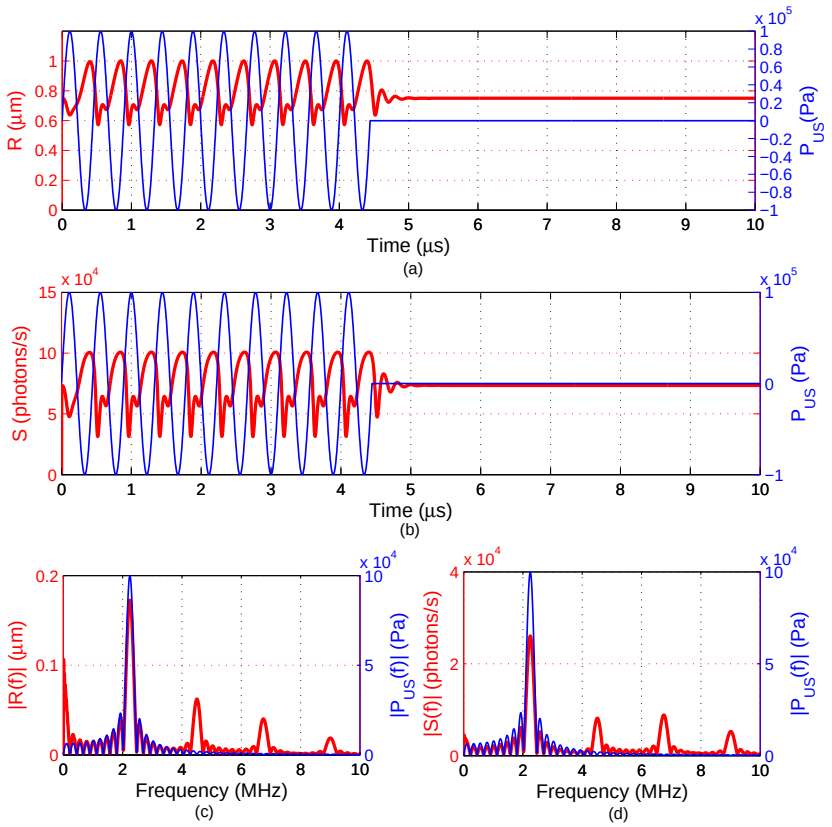


Figure 3.9: Oscillation of microbubble radius (R) and the fluorescence emission intensity (S) for $P_A = 100\,\text{kPa}$ and $R_0 = 0.75\,\mu\text{m}$. (a) Radius of microbubble (left y axis) and US pressure (right y axis) in time domain; (b) fluorescence emission intensity (left y axis) and US pressure (right y axis) in time domain; (c) radius of microbubble (left y axis) and US pressure (right y axis) in frequency domain; (d) fluorescence emission intensity (left y axis) and US pressure (right y axis) in frequency domain.

In conclusion, US can lead to a volumetric oscillation of fluorophore labelled microbubbles and a modulated fluorescent signal. For the same size, higher US pressure can lead to an increased non-linearity. For the same US pressure, non-linear oscillation is easier to occur for microbubbles with smaller size.

3.3.3 Influence of R_0, C, and P_A

In this section the influence of microbubble radius, DiI concentration, and US pressure on the fluorescence emission intensity of the fluorophore labelled microbubbles were studied. The single-sided amplitude spectrum of the emission intensity was calculated through FFT. The peak amplitudes at the fundamental US frequency, second harmonic frequency, sub-harmonic frequency, and ultra-harmonic frequency were then obtained from the amplitude spectrum by extracting the values at 2.25 MHz, 4.5 MHz, 1.125 MHz, and 3.375 MHz respectively.

Influence of R_0, C, and P_A on AC signal

Fig. 3.10 shows the peak amplitude of the emission intensity (AC signal) at fundamental frequency (2.25 MHz) while varying R_0 and C, with P_A fixed at 100 kPa, 200 kPa, 300 kPa, 400 kPa, 500 kPa, and 600 kPa. It can be seen from each subfigure of Fig. 3.10 that for a fixed R_0 and P_A, if increasing C further after the maximum AC signal is observed (horizontal direction), the AC amplitude decreases. This is because the self-quenching efficiency becomes very strong for higher C, leading to a lower emission intensity. Through comparison of the different subfigures, it can be seen that to obtain a higher AC signal for the higher C, a higher P_A is required.

It is also observed from Fig. 3.10 that AC signal is dependent on both C, R_0, and P_A, and it is difficult to decouple their effects. The region of R_0 where the maximum AC signal can be obtained can be different for different C and P_A. For example, at $P_A = 100$ kPa (Fig. 3.10a) and $C = 2$ mol% (vertical direction), maximum AC signal can be obtained with R_0 in the region of 1.5 µm - 5 µm. However, at $P_A = 100$ kPa and $C = 4$ mol%, with increase of R_0 the AC signal firstly increases and then decreases. The maximum AC signal is obtained only around $R_0 = 1.7$ µm. The optimum R_0 becomes less dependent on C when $C > 2.3$ mol%. Besides, it can be seen that at $P_A = 100$ kPa, the optimized C has little dependence on R_0, with only a slightly left shift with increase of R_0. For example, for the 4.5 µm microbubble, the optimized C is around 3.2 mol %, close to 4 mol % for 1.8 µm microbubble. At higher P_A the maximum AC signal is separated into two regions - one is at $R_0 \approx 1.7$ µm with relatively higher C, the other is at $C \in$

$(2\,\text{mol\%} - 5\,\text{mol\%})$ with relatively higher R_0. Inspecting all the US pressures studied, it can be concluded that generally the maximum AC signal can be obtained within the region $C \in (2\,\text{mol\%}\ 5\,\text{mol\%})$ and $R_0 \in (1.5\,\mu\text{m}\ 5\,\mu\text{m})$.

Inspecting different subfigures of Fig.3.10 at a fixed radius and concentration, it can also be seen that the AC emission signal decreases if P_A increases after the maximum peak amplitude has been reached. This is due to a more significant increase of the non-linearity. Fig. 3.11, Fig. 3.12, and Fig. 3.13 show AC signal at the second harmonic (4.5 MHz), sub-harmonic (1.125 MHz), ultra-harmonic (3.375 MHz) US frequency respectively. The region where the maximum signal is obtained can be seen clearly in these figures. During the decrease process of the AC signal at 2.25 MHz, an increase of the AC emission signals at the second harmonic frequency, sub-harmonic frequency or ultra-harmonic frequency can be observed. For example, for $R_0 = 2.5\,\mu\text{m}$ and $C = 2$ mol%, the AC emission signal at 2.25 MHz for $P_A = 300\,\text{kPa}$ (Fig.3.10c, 1.4×10^5 photons/s) is lower than that for $P_A = 200\,\text{kPa}$ (Fig.3.10a, 2.7×10^5 photons/s). However, the AC emission signal at 1.125 MHz for $P_A = 300\,\text{kPa}$ (Fig.3.12c, 4.0×10^5 photons/s) is much higher than for $P_A = 200\,\text{kPa}$ (Fig.3.12a, 1.2×10^5 photons/s). The AC emission signal at 3.375 MHz for $P_A = 300\,\text{kPa}$ (Fig.3.13c, 1.5×10^5 photons/s) is also much higher than for $P_A = 200\,\text{kPa}$ (Fig.3.13a, 9.4×10^4 photons/s).

The positions (R_0, C) for the maximum AC signals for the four frequency components are summarized in Table 3.3, Table 3.4, Table 3.5, and Table 3.6 respectively. It can be concluded that for the US pressure investigated, the optimum radius (the radius where the maximum AC signal can be obtained) is roughly independent of the applied US pressure. The optimum radius is around 1.7 µm for fundamental and second harmonic components and around 2.5 µm for sub-harmonic and ultra-harmonic components. However, with increase of US pressure, both the optimum concentration (the DiI concentration where maximum AC signal can be obtained) and the maximum AC signal increase. This suggests again that for higher concentration, higher US pressure is required to obtain an optimum AC signal. This is because higher concentration requires higher pressure to separate the closely packed fluorophores on the shell of the microbubble. It needs to be noted that in Table 3.3, C has been 10.0 mol% at 500 kPa,

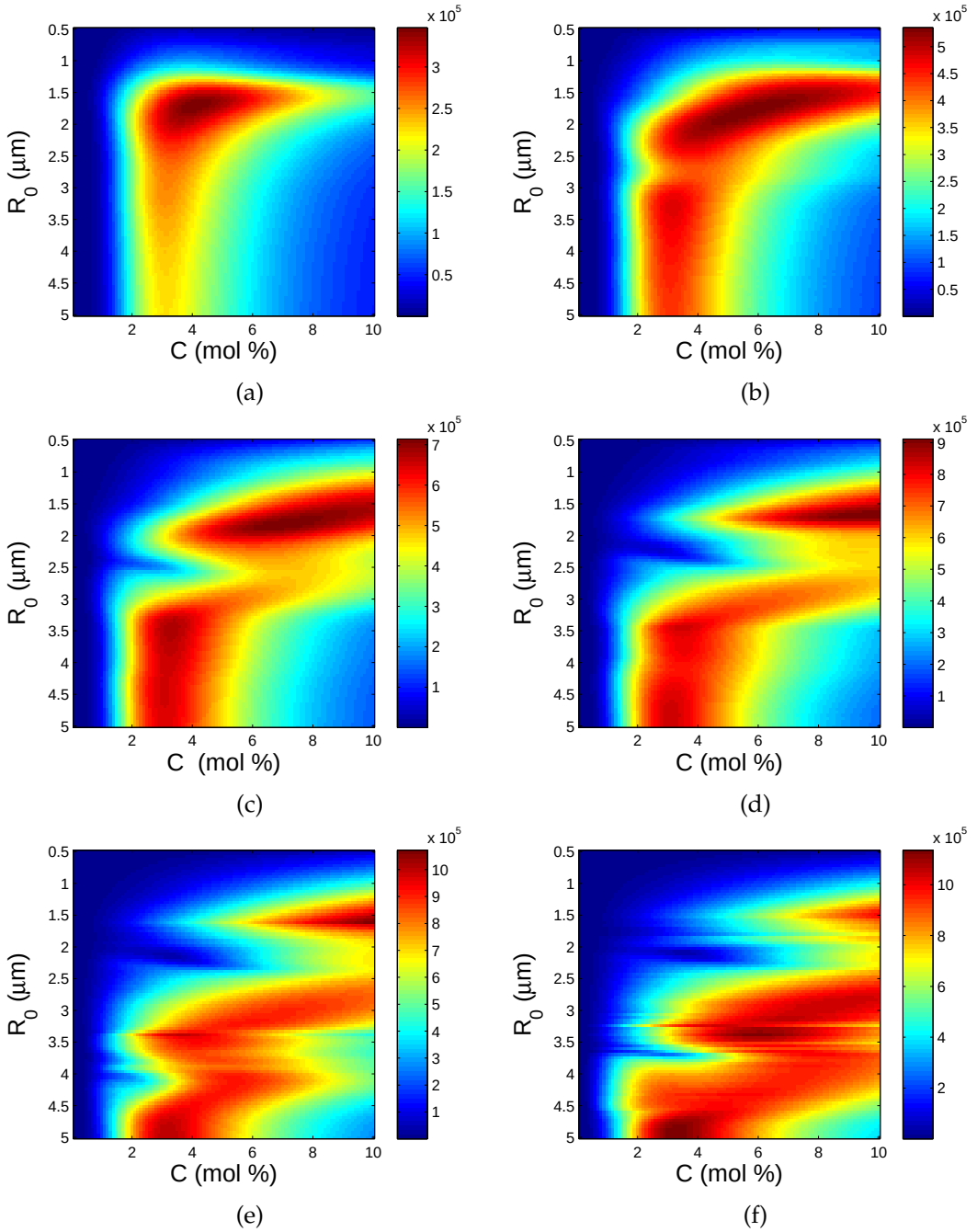


Figure 3.10: Peak amplitude of the fluorescence emission intensity at the fundamental frequency (2.25 MHz) against microbubble radius (R_0) and DiI labeling concentration (C). The amplitude of US (P_A) is (a) 100 kPa, (b) 200 kPa, (c) 300 kPa, (d) 400 kPa, (e) 500 kPa, and (f) 600 kPa.

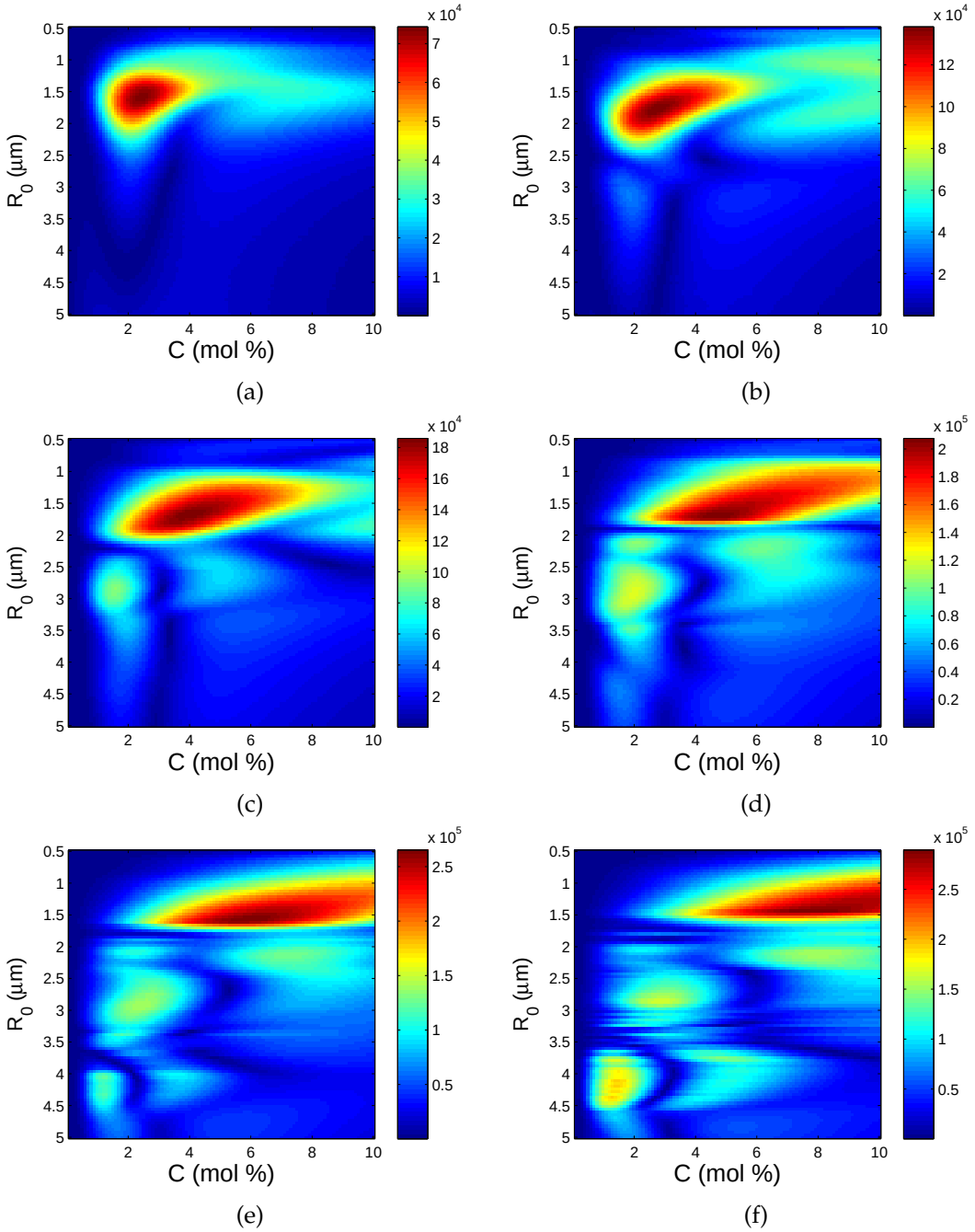


Figure 3.11: Peak amplitude of the fluorescence emission intensity at the second harmonic frequency (4.5 MHz) against microbubble radius (R_0) and DiI labeling concentration (C). The amplitude of US (P_A) is (a) 100 kPa, (b) 200 kPa, (c) 300 kPa, (d) 400 kPa, (e) 500 kPa, and (f) 600 kPa.

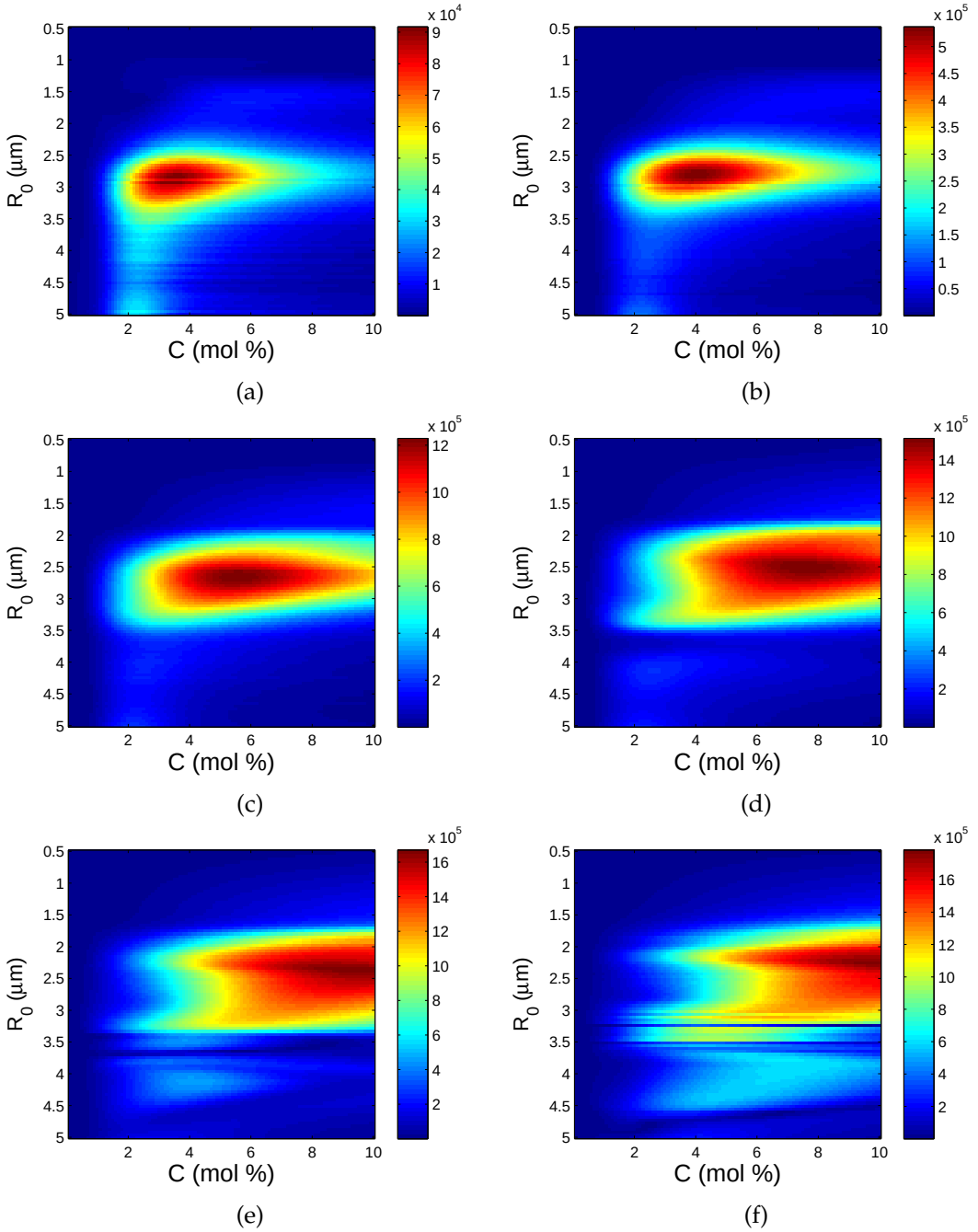


Figure 3.12: Peak amplitude of the fluorescence emission intensity at the sub-harmonic frequency (1.125 MHz) against microbubble radius (R_0) and DiI labeling concentration (C). The amplitude of US (P_A) is (a) 100 kPa, (b) 200 kPa, (c) 300 kPa, (d) 400 kPa, (e) 500 kPa, and (f) 600 kPa.

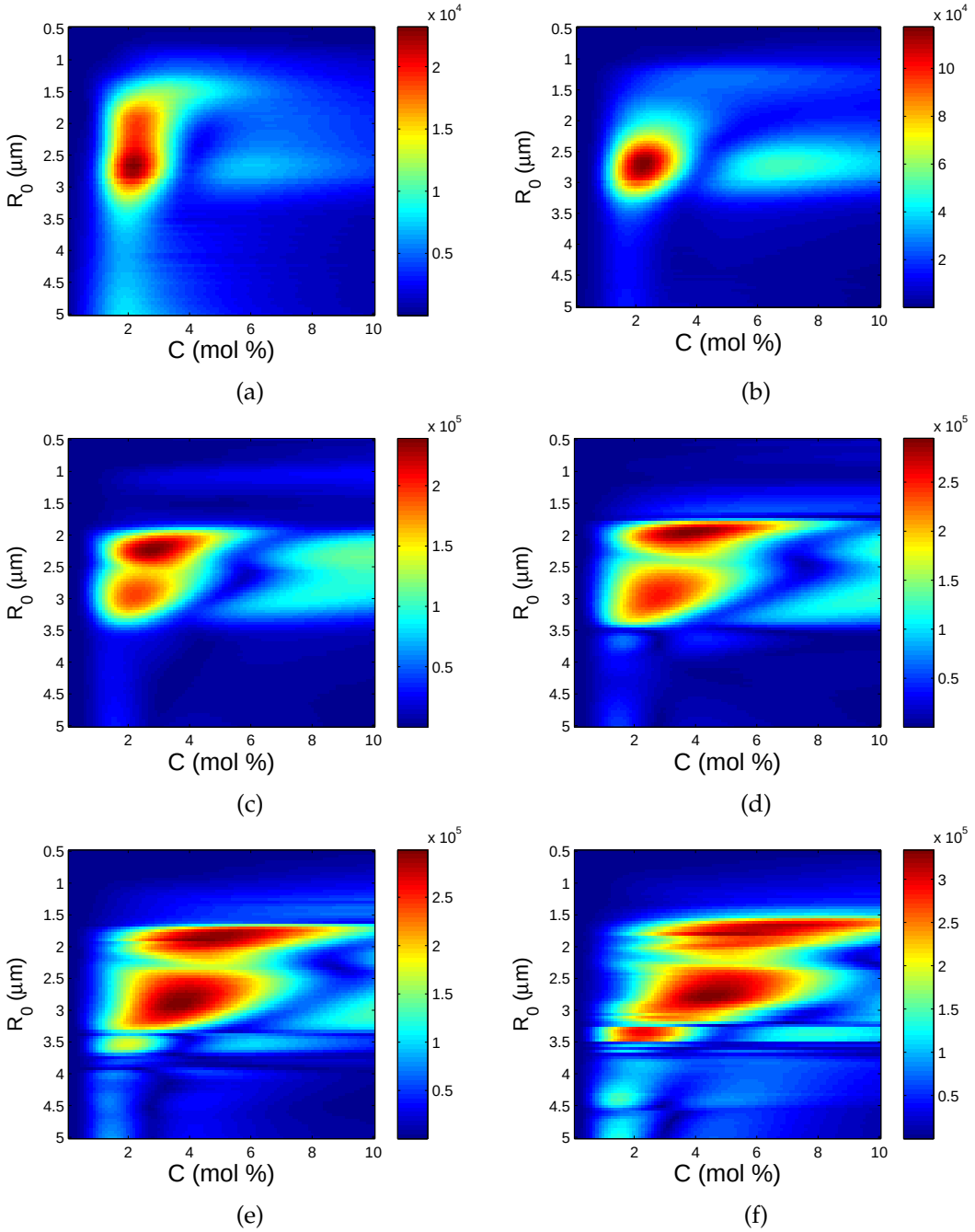


Figure 3.13: Peak amplitude of the fluorescence emission intensity at the ultra-harmonic frequency (3.375 MHz) against microbubble radius (R_0) and DiI labeling concentration (C). The amplitude of US (P_A) is (a) 100 kPa, (b) 200 kPa, (c) 300 kPa, (d) 400 kPa, (e) 500 kPa, and (f) 600 kPa.

therefore for the higher amplitude of US 600 kPa, (R_0, C) for the maximum AC signal is located at (4.9 µm, 3.3 mol%) and doesn't follow the trend as other pressures.

Table 3.3: (R_0, C) for the maximum AC signal at 2.25 MHz ($AC_{|2.25}$) at different US pressures.[1]

P_A	(R_0, C)	$AC_{\|2.25}$
100 kPa	(1.7 µm, 4.1 mol %)	3.5×10^5 photons/s
200 kPa	(1.8 µm, 5.6 mol %)	5.5×10^5 photons/s
300 kPa	(1.9 µm, 6.8 mol %)	7.0×10^5 photons/s
400 kPa	(1.7 µm, 9.8 mol %)	9.0×10^5 photons/s
500 kPa	(1.6 µm, 10.0 mol %)	1.1×10^6 photons/s
600 kPa	(4.9 µm, 3.3 mol %)	1.2×10^6 photons/s

[1] Data taken from Fig. 3.10.

Table 3.4: (R_0, C) for the maximum AC signal at 4.5 MHz ($AC_{|4.5}$) at different US pressures.[1]

P_A	(R_0, C)	$AC_{\|4.5}$
100 kPa	(1.6 µm, 2.4 mol %)	7.5×10^4 photons/s
200 kPa	(1.8 µm, 2.8 mol %)	1.4×10^5 photons/s
300 kPa	(1.7 µm, 4.1 mol %)	1.8×10^5 photons/s
400 kPa	(1.7 µm, 4.8 mol %)	2.1×10^5 photons/s
500 kPa	(1.6 µm, 5.9 mol %)	2.6×10^5 photons/s
600 kPa	(1.4 µm, 7.9 mol %)	2.9×10^5 photons/s

[1] Data taken from Fig. 3.11.

Table 3.5: (R_0, C) for the maximum AC signal at 1.125 MHz ($AC_{|1.125}$) at different US pressures.[1]

P_A	(R_0, C)	$AC_{\|1.125}$
100 kPa	(2.9 µm, 3.4 mol %)	9.0×10^4 photons/s
200 kPa	(2.8 µm, 4.0 mol %)	5.0×10^5 photons/s
300 kPa	(2.7 µm, 5.6 mol %)	1.2×10^6 photons/s
400 kPa	(2.5 µm, 7.6 mol %)	1.5×10^6 photons/s
500 kPa	(2.3 µm, 9.1 mol %)	1.6×10^6 photons/s
600 kPa	(2.3 µm, 10.0 mol %)	1.8×10^6 photons/s

[1] Data taken from Fig. 3.12.

Influence of R_0, C, and P_A on modulation depth

The modulation depth is a criteria for optimization of fluorophore labelled microbubble contrast agent. The modulation depth is calculated as:

$$Modulation\,depth = I_{AC}/I_{DC} \tag{3.3.1}$$

where I_{AC} is the peak amplitude of the AC emission intensity (modulated signal). It is

Table 3.6: (R_0, C) for the maximum AC signal at 3.375 MHz ($AC_{|3.375}$) at different US pressures.[1]

P_A	(R_0, C)	$AC_{\|3.375}$
100 kPa	(2.7 µm, 2.2 mol %)	2.3×10^4 photons/s
200 kPa	(2.7 µm, 2.3 mol %)	1.6×10^5 photons/s
300 kPa	(2.2 µm, 2.8 mol %)	2.4×10^5 photons/s
400 kPa	(1.9 µm, 3.9 mol %)	2.9×10^5 photons/s
500 kPa	(2.9 µm, 3.7 mol %)	3.0×10^5 photons/s
600 kPa	(2.8 µm, 4.5 mol %)	3.4×10^5 photons/s

[1] Data taken from Fig. 3.13.

obtained through an FFT method by calculating the single-sided amplitude spectrum and extracting the amplitude at the fundamental frequency. I_{DC} is the DC emission intensity (unmodulated signal). In this section modulation depth was calculated using Eq. 3.3.1 while varying R_0 and C, with P_A fixed at 100 kPa, 200 kPa, 300 kPa, 400 kPa, 500 kPa, and 600 kPa, as shown in Fig. 3.14. It should be noted that both of the AC and DC emission intensity are from only one microbubble, and no light propagation is considered. Practically there will be some microbubbles excited but located outside the US focal zone, and thus contribute to the unmodulated light leading to a lower modulation depth. This will be simulated in the next Section 3.3.4.

Fig. 3.14 indicates that the modulation depth is highly dependent on C. With increase of C (along horizontal direction), the modulation depth increases until reaching the maximum value. It was observed that for $C \geq 2$ mol %, modulation depth is above 2%. Compared with C, the influence of R_0 on modulation depth is relatively smaller. But a clear dependance of modulation depth on R_0 can still be observed: with increase of R_0 (along vertical direction), the modulation depth firstly increases, and then decreases. The highest modulation depth is around 3300% and it was obtained through several combinations of R_0, C, and P_A (e.g, $R_0 = 0.6$ µm, $C = 10$ mol%, and $P_A = 300$ kPa). This modulation depth is much higher than 10^{-6} - 10^{-4} for the traditional USMFT without applying contrast agents [64].

Curves showing the dependance of the modulation depth on P_A can be seen in Fig. 3.15. Fig. 3.15a shows modulation depth at six different C covering the range of 0.1 mol% - 10 mol% with R_0 fixed at 2.5 µm. Fig. 3.15b shows modulation depth at six different R_0 covering the range of 0.5 µm - 5 µm with C fixed at 2 mol%. It can be seen from

Fig. 3.15a that the modulation depth increases with increase of P_A until it becomes almost constant. The P_A where the modulation depth becomes flat increases with increase of C. The modulation depth for 2 mol% is almost constant when increasing P_A from 100 kPa to 600 kPa, suggesting $P_A = 100$ kPa is sufficient to obtain the maximum modulation depth. Fig. 3.15b shows generally the optimized P_A where the maximum modulation depth can be obtained increases with increase of R_0. For example, the optimized P_A for R_0 = 1.4 µm, 2.3 µm, 3.2 µm, 4.1 µm, and 5 µm is 100 kPa, 220 kPa, 300 kPa, 450 kPa, and 600 kPa respectively. This indicates that microbubble with bigger radius requires higher US pressure to reach a size that the maximum AC signal can be obtained. It should also be noted that the modulation depth decrease after the first peak is due to an increased nonlinear oscillation. It was also observed in Fig. 3.15 that in most cases with further increase of US pressure, the modulation depth increases again (e.g. at $R_0 = 4.1$ µm and $C = 2$ mol%). This should be due to a different peak position for the oscillations at the fundamental and sub-harmonic frequencies. At the US pressure range where the modulation depth increases, a decrease of the oscillation at sub-harmonic frequency is observed.

3.3.4 Modulation depth and SNR in a scattering phantom

If considering a large population of fluorophore labelled microbubbles injected inside a tube buried in the scattering phantom, both the excitation and emission light will be scattered in the medium. Therefore the fluorescence detected will decrease. Besides, the fluorophores on the microbubbles located outside the US focal zone will also be excited, therefore there will be more unmodulated fluorescence. The modulation depth will be greatly reduced due to the decreased modulated fluorescence and increased unmodulated fluorescence background.

In this section the fluorescence emission intensity at the detector when fluorophore labelled microbubbles are injected inside a tube in a scattering medium is calculated. The simulation geometry is shown earlier in Fig. 3.3. The fluorescence propagated to the detector from all the microbubbles located in the intersect of the US focal zone and the tube are integrated using Eq. 3.2.22. The modulated signal at the US frequency

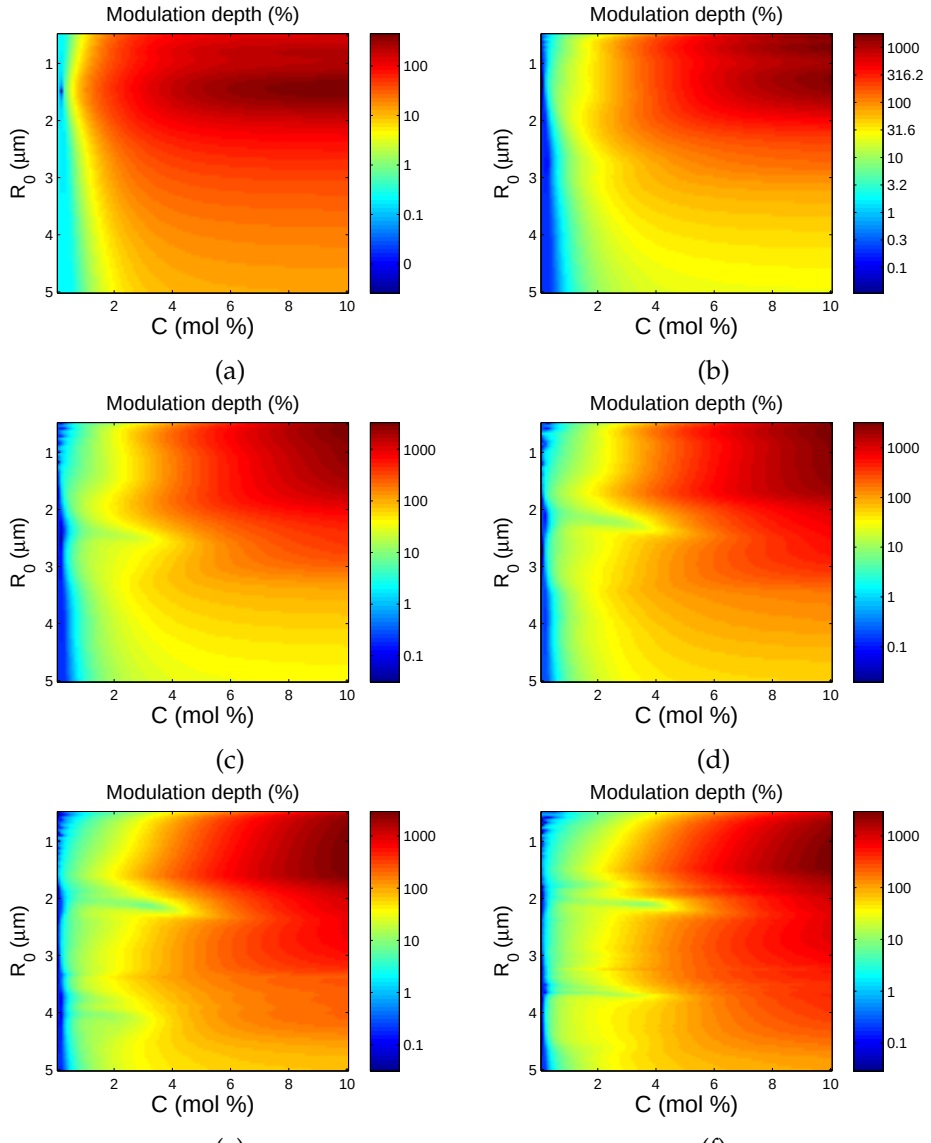
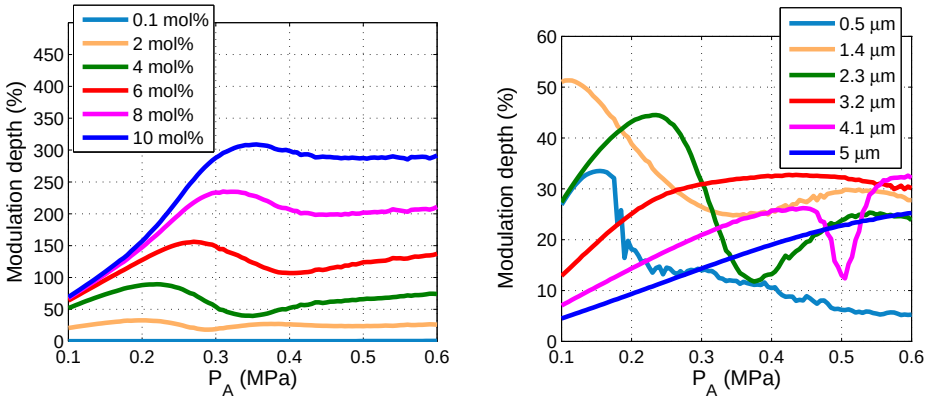


Figure 3.14: Influence of microbubble radius (R_0) and concentration (C) on modulation depth. The amplitude of the US pressure (P_A) is (a) 100 kPa, (b) 200 kPa, (c) 300 kPa, (d) 400 kPa, (e) 500 kPa, and (f) 600 kPa.



(a) (b)

Figure 3.15: Influence of US pressure (P_A) on modulation depth (a) at different C with $R_0 = 2.5\,\mu m$; (b) at different R_0 with $C = 2$ mol %.

is then calculated using the FFT method the same as described in Section 3.3.3. The unmodulated signal is calculated by integrating the fluorescence emission intensity over the tube region which is assumed to be a cylinder with 3 mm diameter and 30 mm height located with the height direction along the y axis. The modulation depth is then calculated using Eq. 3.3.1. The SNR is calculated using the method described in Section 2.2.4 of Chapter 2 with parameters of the detecting system shown in Table 2.2. The influence of the microbubble radius R_0, DiI labeling concentration C, amplitude of the US pressure P_A, microbubble concentration N_B, and thickness of the scattering medium r_{sd} are investigated. The values of the parameters can be found in Table 3.1 and Table 3.2 in Section 3.2.

Fig. 3.16 shows the modulated signal, unmodulated signal, modulation depth, and SNR while varying R_0 from 0.5 µm to 5 µm and C from 0.1 mol% to 10.1 mol%. Here $P_A = 100$ kPa and the 2D maps for the other US pressures can be found in Appendix B. It can be seen that the dependance of the modulated signal, unmodulated signal and modulation depth on R_0 and C are all similar to the situation when only one microbubble is considered (Fig. 3.10a, Fig. 3.6a, and Fig. 3.14a respectively). The highest modulation depth obtained is 20.5% by $R_0 = 1.4\,\mu m$, $C = 10.1$ mol%. The highest SNR obtained is 29.5 dB by $R_0 = 1.4\,\mu m$, $C = 6.1$ mol%. The modulation depth and SNR for $R_0 = 2.5\,\mu m$, $C = 2.0$ mol% are 1.3% and 18.2 dB respectively. These modulation depths are much smaller compared with the case when only one microbubble is considered (e.g., 21.2% for $R_0 = 2.5\,\mu m$, $C = 2.0$ mol%). However, application of fluorophore

labelled microbubbles can still increase significantly the detectability of the modulated fluorescence signal in the scattering medium, compared with the case when no contrast agents are used.

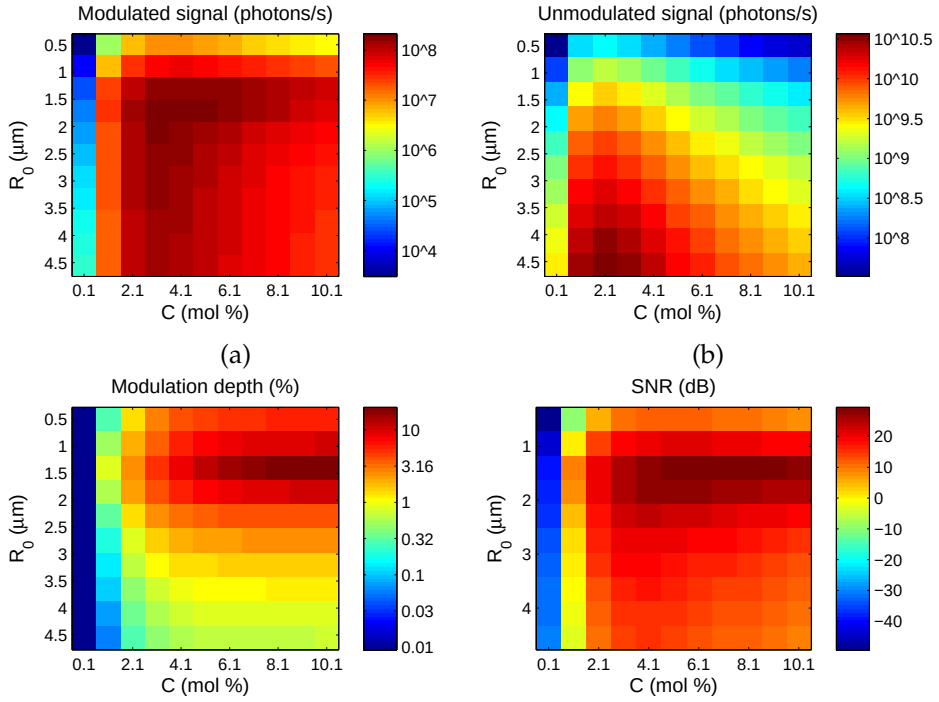


Figure 3.16: Influence of R_0 and C on (a) modulated signal; (b) unmodulated signal; (c) modulation depth; and (d) SNR. $P_A = 100\,\text{kPa}$.

Fig. 3.17 shows the modulated signal, unmodulated signal, modulation depth, and SNR while varying P_A from 100 kPa to 600 kPa with $R_0 = 2.5\,\mu\text{m}$ and $C = 2\,\text{mol\%}$. It can be seen that the modulated signal increases slightly when increasing P_A from 100 kPa to 300 kPa. With further increase of the US pressure the modulated signal vibrates as a result of non-linear volumeric oscillation. The unmodulated signal is independent on the US and is thus a constant. At 300 kPa the highest modulation depth (1.1%) and SNR (19 dB) are obtained.

Fig. 3.18 shows similar quantities while varying the thickness of the medium from 1 cm to 10 cm. It can be seen with increase of the thickness the modulated signal and unmodulated signal decrease logarithmically. This is because the photons are scattered and absorbed more in a thicker medium. Above around 2.3 cm the SNR becomes lower than 0 dB and the modulated signal is too weak to be detected.

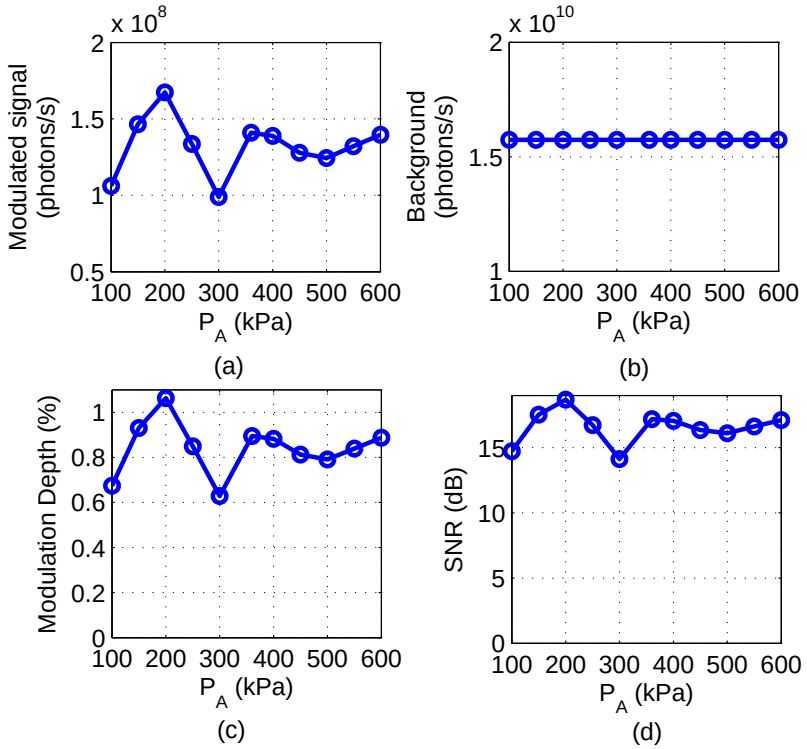


Figure 3.17: Influence of P_A on (a) modulated signal; (b) unmodulated signal; (c) modulation depth; and (d) SNR.

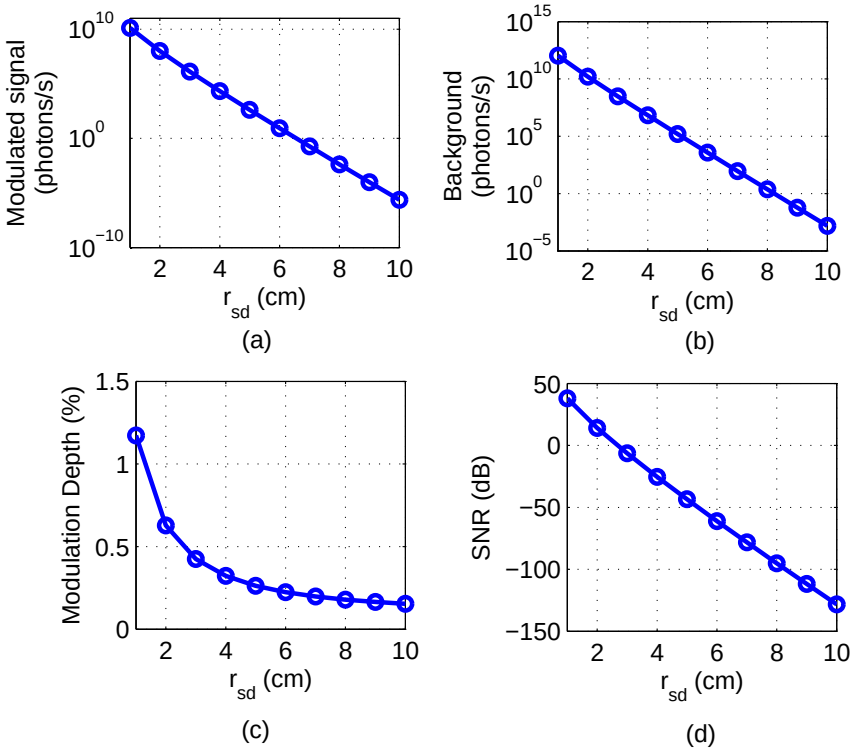


Figure 3.18: Influence of r_{sd} on (a) modulated signal; (b) unmodulated signal; (c) modulation depth; and (d) SNR.

Fig. 3.19 shows similar quantities while varying N_B from 2×10^5 particles/ml to 2×10^{12} particles/ml. It was observed that both of the modulated and unmodulated signal increase with increase of the microbubble concentration linearly at the same rate. Therefore the modulation depth is a constant 0.63%, independent of the microbubble concentration. However, the SNR increases with increase of the microbubble concentration. This indicates that for a thicker medium in which case the SNR tends to be lower, a higher concentration of microbubbles can be used to improve the SNR.

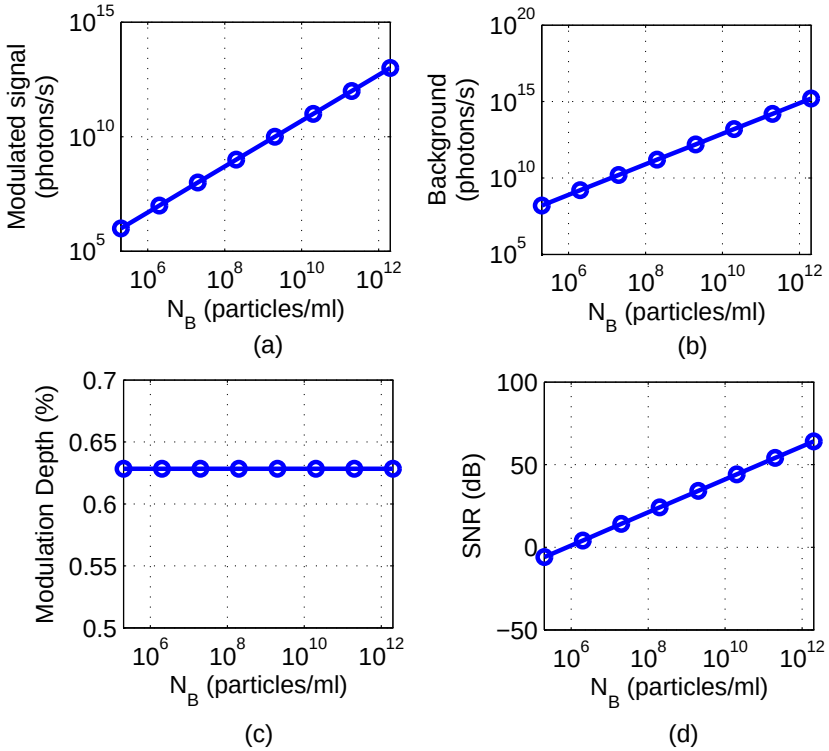


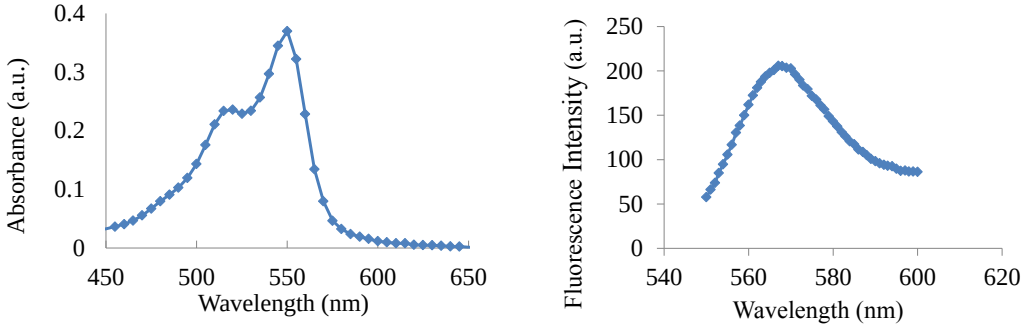
Figure 3.19: Influence of N_B on (a) modulated signal; (b) unmodulated signal; (c) modulation depth; and (d) SNR.

3.4 Experiment

To demonstrate the effect of fluorophore labelled microbubbles on the modulation depth of USMFT, a DiI labelled microbubble solution was produced and its scattered excitation light and fluorescence emission intensity when applying US were detected and analysed.

3.4.1 Preparation of fluorophore labelled microbubbles

In this study the lipophilic dye DiI [1] (DiIC18(3), Life Technologies Ltd, Paisley, UK) was used as the fluorophore to label microbubble. The overlap between its absorption and emission spectrum (shown in Fig. 3.20) makes it a good candidate to achieve fluorescence self-quenching with Förster distance around 45 Å [141].



(a) (b)

Figure 3.20: Spectrum of fluorophore-labelled microbubble. (a) Absorbance spectrum; (b) emission spectrum.

The fluorophore labelled microbubbles were prepared as follows: stock solutions of chemicals were prepared by dissolving the dry powder in chloroform. The concentration of DSPC [2] (#850365, Avanti Polar Lipids Inc, AL, USA), DPPG [3] (#840475, Avanti Polar Lipids Inc, AL, USA), palmitic acid (#900400, Avanti Polar Lipids Inc, AL, USA) and DiI are 10 mg/ml, 10 mg/ml, 1 mg/ml, and 1 mg/ml respectively. 80 µl DSPC, 10 µl DPPG, 80 µl palmitic acid, 25 µl DiI and 49.1 mg polyethylene glycol 4000 were mixed and dissolved in methanol and chloroform in the volume ratio 1:4. The mixed solution was then dried using rotationary vapor to evaporate all of the methanol and chloroform and create a dried-lipid film. The lipid film was rehydrated with 10 ml deionized water. The solution was vortexed using whirlimixer (Fisher Scientific UK Ltd, Bishop Meadow Road, Loughborough, UK) and repeatable pipetting to make the dried lipid completely redissolve in water. The amounts of materials used in the preparation procedure were calculated to produce a labeling concentration of DiI of 2 mol%. This concentration was used for all the subsequent experiments. The prepared mi-

[1] 1,1′-Dioctadecyl-3,3,3′,3′-Tetramethylindocarbocyanine Perchlorate
[2] 1,2-distearoyl-sn-glycero-3-phosphocholine
[3] 1,2-dioleoyl-sn-glycero-3-phospho-(1′-rac-glycerol)

crobubble solution was kept in the refrigerator at 5 °C and tested within three days of production. The solution was agitated violently before use to produce microbubbles. The size distribution was tested using Zetasizer ZEN3600 (Malvern Instruments Ltd, Enigma Business Park, Grovewood Road, Malvern, UK). There were 65 % - 80 % microbubbles located in the diameter range of 3 - 6 µm.

It needs to be mentioned that the gas inside the microbubble can be air (e.g. Albunex) or high-molecular-weight gas such as perfluorocarbon, perfluoropropane (C_3F_8; e.g. Optison and Definity), or sulfur hexafluoride (SF_6; e.g. Sonovue). Air may rapidly diffuse through the lipid shell depending on the concentration difference inside and outside of the shell, while the shell is largely resistant to the diffusion of gas of high molecular weight [154]. The stability of the microbubble is an important factor for *in vivo* imaging because it influences the circulation time [155]. In this study the microbubbles were used *in vitro* therefore an air core was used as it is easy to handle.

3.4.2 Experimental setup

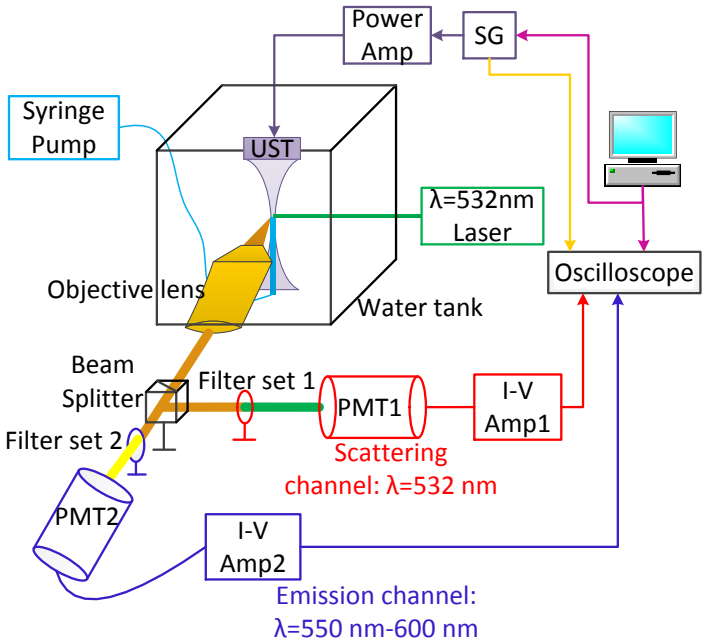


Figure 3.21: Setup for characterization of microbubble dynamics. SG: signal generator; I-V amp: transimpedance amplifier; PMT: photomultiplier tube.

The experimental setup is shown in Fig. 3.21. A signal generator (Tektronix AFG3022B,

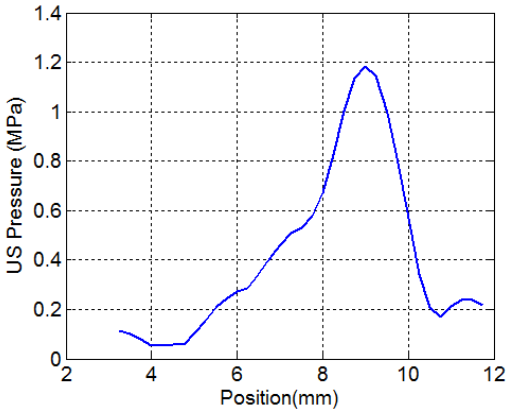


Figure 3.22: Measured pressure distribution at the US focal zone of the US transducer.

Beaverton, USA) and a RF power amplifier (Amplifier Research 75A250A, Souderton, USA) were employed to provide pulsed wave excitation of a focused 2.25 MHz US transducer (Olympus A304-SU, Massachusetts, USA) with 17 mm focal zone length. The lateral pressure distribution at the US focal zone was measured using a needle hydrophone (SN1700, Precision Acoustics Ltd, Dorset, UK) with an active diameter of 0.2 mm, followed by 65 mV excitation of the signal generator, as shown in Fig.3.22. The full width half maximum (FWHM) is ∼2.1 mm.

The microbubble solution was injected into a water tank (11 cm × 11 cm × 11 cm) through an open end tube (Z611239-250EA, Sigma-Aldrich Company Ltd., Dorset, UK) with 300 µm diameter by a syringe pump. The tube was located perpendicular to the λ = 532 nm laser light (Oxxius 532S-50-COL-PP, power = 50 mW, Lannion, France) and in line with the US propagation direction, which was also perpendicular to laser beam. The tip of the tube was at a position close to, but not at the US focus zone to avoid the distortion of the US region. Microbubbles can flow to the focus region by buoyancy and thus compensate the small separation. The scattered light by the microbubble was collected by an objective lens at 65 °to 115 °(90 +/- arcsinNA) to the laser light, which includes the angle 97 °, supplementary angle of the critical scattering angle ($\theta_c = 83°$ for air bubbles in water [156]. The schematic of the detection angle and critical scattering angle is shown in Fig. 3.23. This geometry of laser light and objective lens is important for the maximum detection of the scattered light. The light collected was split into two paths using a beam splitter. One path goes through filter set 1 which is

a high performance single-band bandpass filter with central wavelength 532 nm and bandpass 3 nm (FF01-532/3-25, Semrock, Rochester, New York) and then into the optical detector PMT1 (H5783-20, Hamamatsu, Hamamatsu City, Japan). The fluorescence emission was detected by passing the collected light from the second channel through filter set 2 to achieve a high rejection ratio of the excitation light and only allow the fluorescence emission to reach PMT2 (the module as PMT1). Filter set 2 includes a high performance 532 nm notch filter (#67-119, Edmund Optics, York, UK) and a high performance bandpass filter with central wavelength 575 nm and bandpass 25 nm (FF02-575/25-25, Semrock, Rochester, New York). The signals from the two PMTs were fed into two transimpedance amplifiers respectively (Stanford Research Systems SR445A, Souderton, USA), followed by a digital Phosphor oscilloscope (DPO2024, Tektronix, Beaverton, USA) for instantaneous measurements. The gain of SR445A is 10× and the input resistance was set to be 500 Ω. 'AC' and 'DC' coupling were used for the oscillascope when detecting the modulated and unmodulated signal respectively.

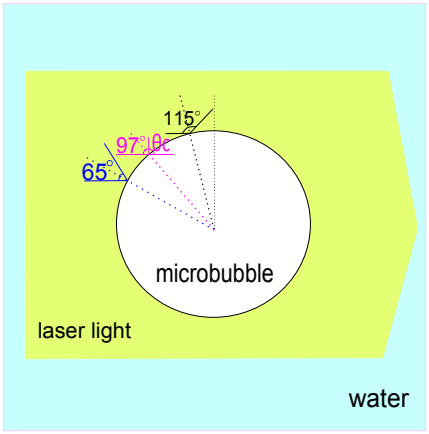
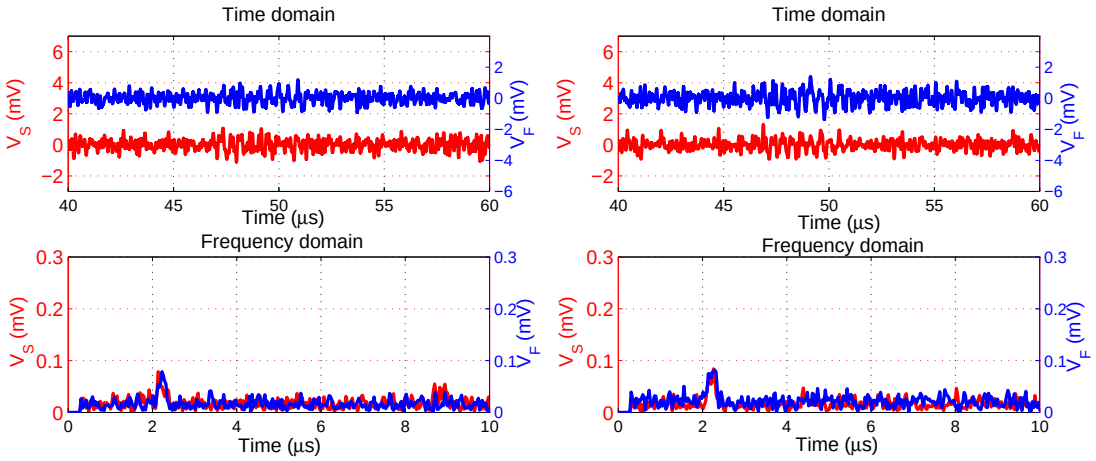


Figure 3.23: Schematic of the detection angle (65 °to 115 °) and critical scattering angle (θ_c).

3.4.3 Scattered and fluorescence signal from fluorophore-labelled microbubble

In this section the scattered excitation light signal (V_S, unit: mV) and the fluorescence emission signal (V_F, unit: mV) from fluorophore-labelled microbubbles were detected using the scattering and emission channel of the setup shown in Fig. 3.21 respectively.

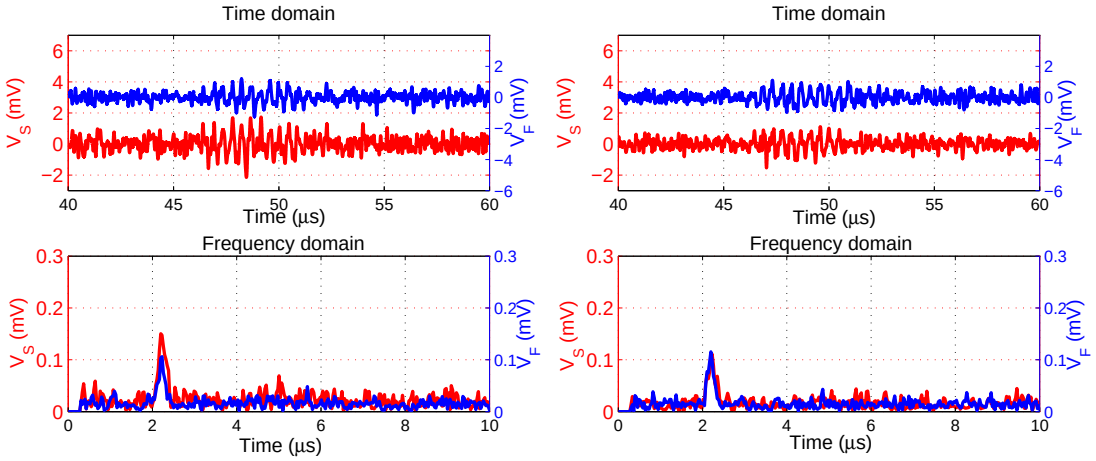
The signal generator outputs pulses at 2.25 MHz frequency, with number of cycles 10 and pulse repetition frequency 1 Hz. The US pressure at the focal zone was varied from 0.45 MPa to 1.27 MPa. The signals were extracted from the detected signals by removing any baseline trend from the original signal, followed by digital filtering in the frequency domain (band pass filter from 1 MHz to 10 MHz), and Inverse FFT. The extracted signals in the time domain and frequency domain are shown in Fig. 3.24. Modulation of the fluorescence emission intensity at US frequency was observed for all the pressures applied, and it is in phase with the scattered light, which indicates volumetric oscillation of microbubbles. For pressures from 0.45 MPa (a) to 0.82 MPa (e) modulated fluorescence signal only at fundamental frequency (2.25 MHz) was observed. However with increase of US pressure it can be seen that the modulated fluorescence signal becomes stronger. For pressures from 0.91 MPa (f) to 1.27 MPa (j) there were second harmonics at 4.5 MHz observed indicating non-linear oscillation.


Time domain
V_S (mV)
V_F (mV)
Time (µs)
Frequency domain
V_S (mV)
V_F (mV)
Time (µs)

(a)

Time domain
V_S (mV)
V_F (mV)
Time (µs)
Frequency domain
V_S (mV)
V_F (mV)
Time (µs)

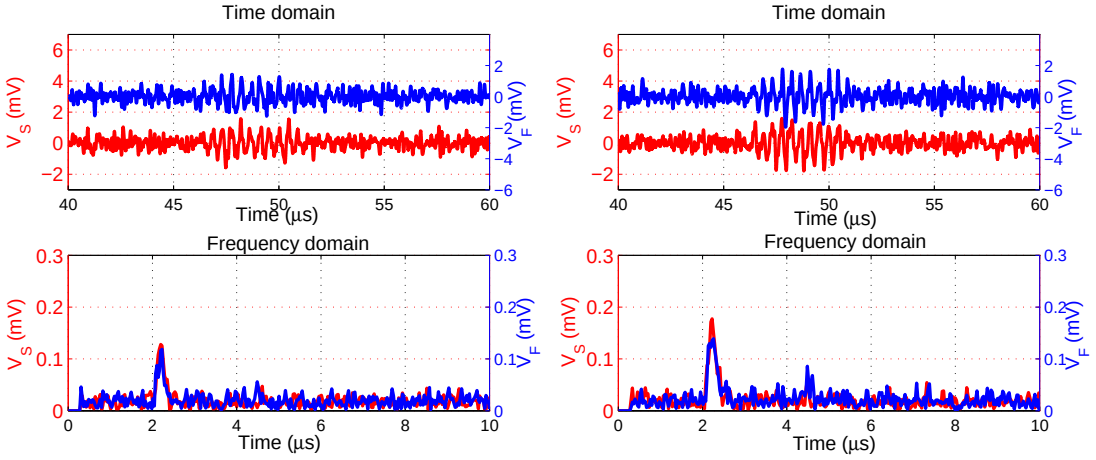
(b)


Time domain
V_S (mV)
V_F (mV)
Time (µs)
Frequency domain
V_S (mV)
V_F (mV)
Time (µs)

(c)

Time domain
V_S (mV)
V_F (mV)
Time (µs)
Frequency domain
V_S (mV)
V_F (mV)
Time (µs)

(d)


Time domain
V_S (mV)
V_F (mV)
Time (µs)
Frequency domain
V_S (mV)
V_F (mV)
Time (µs)

(e)

Time domain
V_S (mV)
V_F (mV)
Time (µs)
Frequency domain
V_S (mV)
V_F (mV)
Time (µs)

(f)

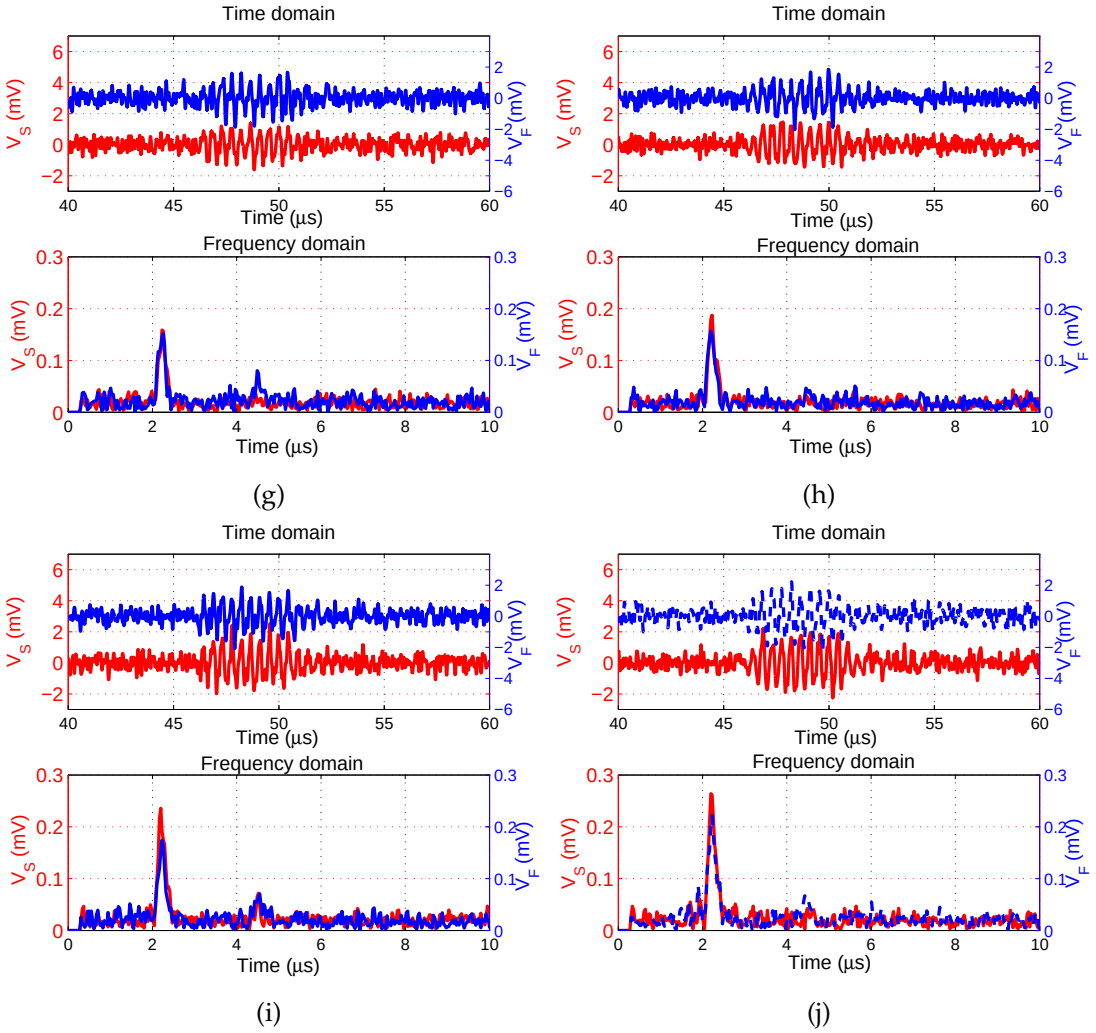


Figure 3.24: Modulated fluorescence emission intensity from fluorophore labelled microbubbles in time domain and frequency domain. (a) 0.45 MPa; (b) 0.54 MPa; (c) 0.63 MPa; (d) 0.73 MPa; (e) 0.82 MPa; (f) 0.91 MPa; (g) 1.00 MPa; (h) 1.09 MPa; (i) 1.18 MPa; (j) 1.27 MPa. V_S: scattered excitation light signal; V_F: fluorescence emission signal.

The amplitude of the modulated fluorescence signal (AC) and modulation depth for all the pressures studied are then calculated and shown in Fig. 3.25. Here the modulation depth is calculated by dividing the amplitude of the AC signal with the unmodulated signal, which was obtained from the oscilloscope using DC coupling. It can be seen that the amplitude of the AC signal and modulation depth increased with increase of the US pressure. The lowest modulation depth is 0.8% (0.45 MPa) and highest modulation depth is around 1.6% (1.27 MPa). It should be mentioned here that the microbubbles can undergo both volume and position oscillation, however, the contribution of the latter to the observed oscillation of fluorescence, especially the second harmonic, is

very small compared with the contribution of the volume oscillation and thus can be ignored. The position oscillation would result as a modulation depth only $10^{-6} - 10^{-4}$.

The modulation depth obtained from the experiment (1.6%) is much lower than the simulated modulation depth of 24% for 2 mol% DiI (Fig.3.15a yellow curve). There are several reasons for this. The most likely reason is an undesirable labelling of DiI on the shell of microbubbles. In the theoretical model DiI is assumed to distribute evenly on the shell. However, in practice different shell species can form concentrated lipid islands [142]. Fluorophores located in these islands might not be able to expand sufficiently to generate a detectable modulated signal. It has been demonstrated that 'rapid-cooled' temperature treatment can lead to a ten-fold increase in the generation of the US modulated fluorescence signal [142]. Secondly, the fluorophores on microbubbles located outside the US focal zone can also be excited and thus contribute only to the unmodulated signal. Thirdly, as suggested by Fig.3.15 the optimized US pressure is dependent on the microbubble size. The microbubble suspension produced in this thesis has a wide size distribution of 3 - 6 µm (65 % - 80 %). At a specific US pressure, microbubbles with relatively small size may have a strong non-linear oscillation, while microbubbles with relatively big size may be still intact. Fourthly, the distributed fluorophore labelled microbubbles at different sizes can oscillate at different phases (can be observed from the intensity oscillations in Fig. 3.7-3.9) that may cancel out some of the energy. Nevertheless, the modulation depth obtained with application of fluorophore labelled microbubbles is much higher than values without using contrast agents ($10^{-6} - 10^{-4}$). A more explicit investigation of the effect of the fluorophore labelled microbubbles can be achieved through comparison of the fluorophore labelled microbubbles with mixed solution of fluorophores and microbubbles as well as solution with only fluorophores.

3.5 Discussion and conclusions

In this chapter the volumetric oscillations of unlabelled and fluorophore-labelled microbubble were firstly modeled. The emission intensity of the fluorophore-labelled

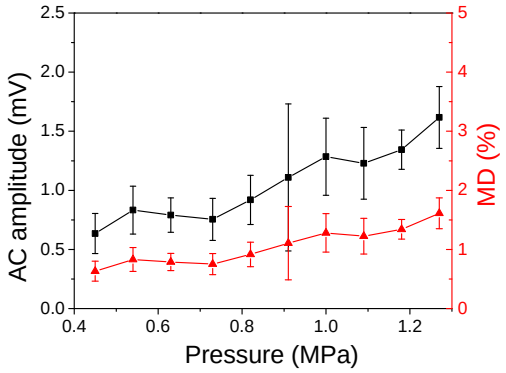


Figure 3.25: Amplitude of the AC signal and the corresponding modulation depth (MD) against US pressure for fluorophore labelled microbubble.

microbubble in the absence and presence of an US field was then simulated. The influence of parameters of the microbubbles (radius, fluorophore labeling concentration, microbubble concentration), US (US pressure) and the scattering medium (thickness) on the emission intensity were investigated. The modulated depth and SNR for a population of microbubbles in a scattering medium were calculated. In the experimental section DiI labelled microbubbles were produced by a simple agitation method and the modulated fluorescent signal when applied US was demonstrated.

The simulation results show that the fluorescence emission intensity both in the absence and presence of an US field is highly dependent on the concentration of DiI. This is due to the dependance of FRET efficiency on intermolecular distance of DiI molecules which is a function of the concentration. The fluorescence emission intensity is the maximum at the concentration of 2 mol % in the absence of US. This is in agreement with the experimental results in [141] where a range of DiI labelled microbubbles with different concentrations were produced and the curve of fluorescence emission intenstiy vs. DiI concentration was plotted. The simulation also shows that microbubble radius has no influence on the concentration of maximum fluorescence emission intensity for the case without applying US. This is because the microbubble radius only works as a scaling factor determining the number of fluorophores in the microbubble (Eq. 3.2.4) and has no influence on the quenching efficiency (Eq. 3.2.7).

In the presence of US the fluorescence emission intensity is modulated at the US frequency. At higher US pressure harmonic components can also occur. The simulation

result in Fig. 3.10 shows that the effects of C, R_0, and P_A on the maximum AC signal are highly relevant with each other, and it is difficult to decouple their effects. Generally the maximum AC signal can be obtained within the region $C \in (2\,\text{mol\%}\ 5\,\text{mol\%})$ and $R_0 \in (1.5\,\mu\text{m}\ 5\,\mu\text{m})$. However microbubbles with different size may have different optimum concentration. Also microbubble with a higher fluorophore labelling concentration or a bigger radius requires higher US pressure to obtain its maximum volumeric oscillation and the highest AC signal. These findings emphasize the importance of size, fluorophore concentration, and US pressure to allow the production of a microbubble specifically designed for optimum performance with USMFT. For the manufacture of microbubbles, it would be useful to refine the microbubble size to a smaller range, so that most of the microbubbles can be labelled by an optimized concentration and exposed by an appropriate US pressure.

Overall, the results show that the fluorophore-labelled microbubble can improve significantly the modulation depth and the SNR of USMFT in a scattering medium. One of the current challenges for application of the fluorophore-labelled microbubbles in tissue imaging is that microbbbles are not stable and tend to rupture easily when exposed to US [157, 158]. Therefore an appropriate US pressure needs to be identified to maximize the modulated fluorescence signal, and also to avoid the rupture of microbubbles. For quantitative imaging the relationship between the parameters of the US and the response of the microbubbles must be fully characterized. Therefore further calibration need to be performed to relate the observed modulated fluorescence signal to the actual parameters of the microbubble such as its size for specific US parameters.

CHAPTER 4

Characterization of pyrene-labelled liposomes contrast agent

4.1 Introduction

In Chapter 3 the use of microbubbles as acoustic-optical contrast agent was discussed. In this chapter another contrast agent is investigated which is based on the use of nanoscale liposomes containing lipids labelled with the excimer producing fluorophore pyrene.

Despite the advantages mentioned in Chapter 3 about using fluorophore labelled microbubbles as a contrast agent for USMFT, using liposomes has the following advantages. Firstly, liposomes are more stable and can stay inside the body for a longer circulation time (on the order of hours or days [159]). The pharmacokinetic properties of liposomes have been extensively studied [160] and the pharmacokinetic lifetimes of liposomes within a human circulatory system can be increased through surface modifications [161]. In comparison, microbubbles have a short circulation time (on the order of 10 mins [162, 163]) and might only survive a few US pulses. Secondly, the nanoscale size means that the liposomes can pass through vascular walls to potentially overcome the formidable blood brain barrier and make extra-vascular targeting possible, while the microscale size of the microbubbles restricts the use to the circulatory system.

Thirdly, liposomes can be manufactured with defined monodisperse size distribution and high reproducibility, however this is much more difficult to achieve for microbubbles. The size distribution of microbubbles produced by sonification, the most commonly used method for microbubble preparation, is generally very wide [164]. There are some advanced techniques such as microfluidic flow-focusing [165] which are able to prepare microbubbles with a high degree of control over their size. Such devices usually have slow microbubble yield and require careful handling to avoid clogging of fine channels (several micrometres). Fourthly, due to the liquid core compared with gas for microbubble, liposomes can reflect US much less than microbubble and thus produce less perturbation of the US field. This is beneficial for imaging resolution because less reflection and scattering means that the US can be more localized.

The fluorophore used in this Chapter is pyrene. Excimer formation of pyrene is a well-known concentration-dependent phenomenon. Excimers are dimers in the excited state and they are formed by collision between an excited molecule and an identical unexcited molecule through sharing the excitation energy [166]. The excimer formation rate, defined as the excimers formed in unit time, is dependent on the concentration of the fluorophore molecules and their lateral diffusivity [167]. When the two aromatic rings of an excited state pyrene molecule and a ground state pyrene molecule are facing at a distance of 3.37 Å, pyrene excimers form producing a substantially red-shifted fluorescent emission in the excimer band ($\lambda = 430\,\text{nm} - 590\,\text{nm}$) in contrast to the monomer band ($\lambda = 370\,\text{nm} - 400\,\text{nm}$) [166]. The unusually long lifetime of pyrene emission (>100 ns) allows this excited state reaction to occur [168]. Excimers are formed when one of the dimer components is in the excited state. When the excimer returns to the ground state, its components dissociate and often repel each other [169]. Since the wavelength of an excimer's emission is longer (lower energy) than that of the excited monomer's emission, the two emissions can be separately detected.

Due to the concentration dependent spectral features of pyrene which is also sensitive to tissue microenvironment, it has a wide range of applications such as monitoring protein conformation [170, 171], investigating the transmembrane dynamics of lipids [172], and used as fluorosensor for oxygen [173], iron [174], or cyanide concentration [175].

Here this work describes the preparation and characterization of nanoscale liposomes containing pyrene labelled lipids (see Fig. 4.1) as USMFT contrast agents based on US mediated variation of the excimer fluorescence. Liposomes are dynamic systems. The lipids in the lipid bilayers will not remain in a fixed position but will move in various ways including lateral diffusion, lipid rotation around its axis, tail wagging and flip-flop (see Section 4.5.1 for detailed explanation of these motions). These motions will lead to the collision of two pyrene molecules and formation of pyrene excimers. In this study the pyrene labelled liposomes were exposed to an US field which can change the dynamic characteristics of the liposomes and further change the collision rate of the pyrene molecules and hence induce a variation of the excimer fluorescence. Liposomes containing different molar concentrations of lipids with pyrene labelled on the phospholipid fatty acid tail (tail labelled liposomes) and also lipids with pyrene labelled on the phospholipid head group (head labelled liposomes) were studied. This methodology was chosen for identification of a suitable contrast agent formulation and to enable an initial investigation of the underlying mechanisms. It needs to be noted that the rationale for using pyrene labelled lipids is based on pyrene being a well-established and widely used fluorophore whose excimer producing behavior has been extensively studied [170]. The excitation and excimer emission wavelengths of pyrene are however short in respect to tissue imaging and thus downstream applications for tissue imaging will need to utilize the emerging range of excimer producing fluorophores that can be excited and emit at longer wavelengths (e.g: BODIPY [176]).

The preparation of pyrene labelled liposomes is firstly described in Section 4.2. Section 4.3 shows the measurements of the emission spectra of tail labelled liposomes and head labelled liposomes. The acousto-fluorescence experimental system used to characterise the pyrene labelled liposomes is discussed in Section 4.4. The fluorescence emission intensity of tail labelled liposomes and head labelled liposomes in the absence and presence of US were then detected and are compared in Section 4.5. Possible US mediated mechanisms are also discussed in this section. Section 4.6 shows analysis of the size and concentration of liposomes after US exposure. The influence of temperature on fluorescence emission intensity is studied in Section 4.6, followed by discussion

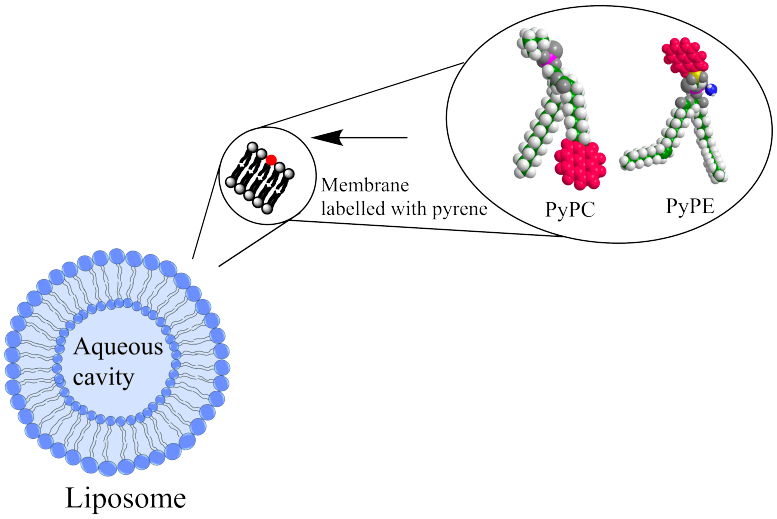


Figure 4.1: Schematic showing liposome containing pyrene labelled phospholipids, expanded section depicts tail and headgroup labelled lipids.

and conclusions in Section 4.8.

4.2 Preparation of pyrene labelled liposomes

Liposomes can be classified into two categories based on the number of bilayers: (1) unilamellar vesicles and (2) multilamellar vesicles. Unilamellar liposomes have a single phospholipid bilayer sphere enclosing the aqueous solution, while multilamellar liposomes have a structure of concentric phospholipid spheres separated by layers of water [87]. Unilamellar liposomes were produced in this study due to its relatively simple structure, which benefits the mechanism investigation later in Section 4.5.3. Freeze-thaw pressure extrusion process is a well-established and reliable protocol for producing unilamellar model membrane systems of diameter 50 nm to 180 nm [177]. In the freeze-thaw cycle liposomes are frozen rapidly and thawed slowly. During this procedure the lamellarity of liposomes is reduced through fusion. The liposomal bilayer is also disrupted which is considered to be due to ice crystals formed during the freezing process [178]. This breaks apart the closely spaced lamellae of the vesicles thereby raising the trapping efficiency by increasing the ratio of aqueous solute to lipid, as well as to allow drug molecules to diffuse into the liposome, promoting encapsulation [179]. The repetitive extrusion after freeze-thaw through filters with a 100 nm pore size results

in the straightforward production of homogeneously sized large unilamellar vesicles systems [177, 180].

In this project liposomes were prepared using the above mentioned freeze-thaw pressure extrusion process. The detailed preparation procedure is: the phosphocholine phospholipids with pyrene labelled on the tail group [1](β-Py-C10-HPC or PyPC; Life Technologies Ltd, CA, USA) were reconstituted at 1 mg/ml in methanol and chloroform in the volume ratio 5:1. PyPC was mixed with DPPC [2] phospholipids (#850355, Avanti Polar Lipids Inc, AL, USA) and the solvent was evaporated with oxygen-free nitrogen gas (BOC Group plc, Manchester, UK). The dried lipids were resuspended in PBS buffer (BR0014, Oxoid Limited, Hampshire, UK) to a final total lipid concentration of 12.8 mM. The buffer was made with deionised water, and filtered with 0.2 µm pore filters (EMD Millipore, MA, USA) before use. The buffered lipids underwent 5 freeze-thaw cycles using liquid nitrogen (-196 °C) and hot water (45 °C). The solution was then extruded 10 times through track-etched membranes with 100 nm pore size (Whatman Plc, Bucks, UK) using a barrel extruder (Northern Lipids Inc, Burnaby, Canada) at 45 °C. The aforedescribed PBS buffer was used for all subsequent dilutions. The liposome stock solution was sealed and stored in a refrigerator at 5 °C, and didn't show visible signs of oxidation (become yellow in colour).

For the lipids with pyrene labelled on the head group, 18:1 Pyrene PE [3] (PyPE; Avanti Polar lipids Inc, AL, USA) was used and mixed with DPPC at 0.5 mol%. It needs to be mentioned that PyPE contains unsaturated bonds (dioleoyl) and is 18 carbon atoms long, while PyPC is saturated (dipalmitoyl) and the acyl chains are 10 carbon atoms long. The behaviour of a pyrene lipid can strongly depend on the length of the labelled chain, which is explained as the pyrene moiety attached to a long acyl chain perturbs less the packing of the matrix lipid [181]. In fact it has been suggested that lipids containing a short pyrene labelled chain resemble unsaturated natural lipids, while those with a long pyrene-labelled chain resemble natural lipids with saturated chains [182]. Therefore, fortunately, although the PyPC has a shorter chain than the PyPE this can

[1] 1-Hexadecanoyl-2-(1-Pyrenedecanoyl)-sn-Glycero-3-Phosphocholine
[2] 1,2-dipalmitoyl-sn-glycero-3-phosphocholine
[3] 1,2-dioleoyl-sn-glycero-3-phosphoethanolamine-N-(1-pyrenesulfonyl)

perhaps compensate for the difference in saturation of the two lipids. The liposome concentration is $3 - 13 \times 10^8$ particles/ml, tested using a Nanosight LM14 (Malvern Instruments Ltd, Malvern, UK).

4.3 Fluorescence spectrum measurements

Different pyrene concentrations were utilised to identify a suitable concentration at which fluorescence variation induced by US is expected to be obtained. It has been observed that when the molar percentage of pyrene to phospholipid is higher than 1:120 (0.83 mol%) excimer formation occurs [183]. In this study a threshold pyrene concentration that is sufficient for excimer formation in the presence of US and that also displays minimal excimer formation in the absence of US, to minimise the background signal as well as the perturbation to the lipid bilayer, was sought. In this section pyrene tail labelled lipids (PyPC) with concentrations close to 0.83 mol% were selected (0.5 mol%, 0.75 mol% and 1.5 mol%) to identify a suitable concentration for the experiments of US mediated fluorescence variation. The concentration is the molar percentage of pyrene labelled lipid to total lipids used.

The fluorescence emission spectra of these tail labelled liposomes in the absence of US were obtained using a spectrofluorometer (Fluoromax-4, Horiba Scientific, Kyoto, Japan), as shown in Fig. 4.2. Samples were excited at $\lambda = 337$ nm with a 2 nm bandwidth. The emission was observed between $\lambda = 370$ nm and 600 nm with a 2 nm bandwidth.

The spectrum is characterised by two monomer bands that peak at $\lambda =\sim 375$ nm and $\lambda =\sim 395$ nm and a broad excimer band that peaks at $\lambda =\sim 470$ nm. It can be seen that at higher pyrene concentration there are more excimers formed. The extent of excimer formation is conventionally assessed by the ratio of the intensity of the excimer band at $\lambda = 470$ nm (I_E) and monomer band at $\lambda = 375$ nm (I_M) [166]. Therefore I_E/I_M is calculated and shown in the inset graph of Fig. 4.2. At 0.5 mol%, there is some excimer emission, although it is very low in comparison to the monomer emission with I_E/I_M being 0.12. With increase of the pyrene concentration, I_E/I_M increases. At 1.5 mol%,

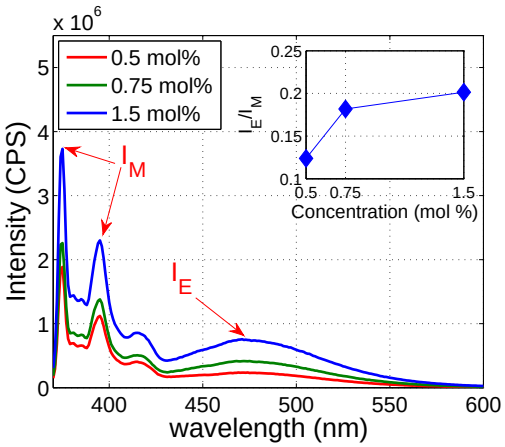


Figure 4.2: Emission spectra of liposomes containing 0.5 mol%, 0.75 mol%, and 1.5 mol% PyPC. The total lipid concentration for each sample is the same (1.28 mM). The intensity ratio of excimer and monomer (I_E / I_M, λ = 470 nm: 375 nm) for each concentration is shown in the inset graph. CPS: counts per second.

I_E / I_M is 0.20 and there is a clear peak at the wavelength range of 450 nm - 500 nm. Therefore the concentration of 0.5 mol% can be regarded as the threshold for excimer formation. To minimise excimer formation at equilibrium state (without application of US), liposomes with a 0.5 mol% concentration of pyrene labelled lipids were selected as the most suitable concentration and used in all subsequent experiments.

A comparison was also made of the emission spectra from liposomes containing PyPC and PyPE to determine the effect the position of the pyrene moiety has on the equilibrium state of the excimer formation. To check repeatability three PyPC based liposome samples and three PyPE based liposome samples were made and their spectra are shown in Fig. 4.3. It can be seen that the spectra are similar and there are no clear differences found for the excimer formation of PyPC based liposomes and PyPE based liposomes. This observation can be explained considering the orientation of PyPC and PyPE in lipid bilayer. The pyrene moiety located at the head group of PyPE can lead to a rotation of the molecule owing to the hydrophobic characteristics of pyrene [184]. This rotation has negative effect on excimer emission, because a stacked orientation of two pyrene rings is critical for excimer formation [185]. However, the rotation can also generate more voids in the lipid bilayer which can facilitate quicker lateral diffusion, causing a positive effect on excimer formation [186]. For the PyPC labelled liposomes, pyrene is attached on the tail group which is already hydrophilic therefore no rota-

tion is expected. The spectra shown in Fig. 4.3 suggest these two effects compensate, therefore a similar excimer formation of PyPC labelled liposomes and PyPE labelled liposomes were observed.

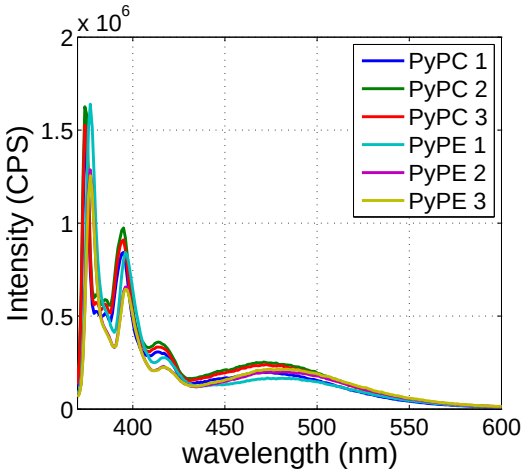


Figure 4.3: Emission spectra of liposomes containing 0.5 mol% PyPC or PyPE. Three PyPC based liposome samples ('PyPC 1', 'PyPC 2', 'PyPC 3') and three PyPE based liposome samples ('PyPE 1', 'PyPE 2', 'PyPE 3') were made and there spectra were measured. Total lipid concentration is the same for all the samples (1.28 mM).

The influence of lipid concentration on excimer formation was also studied. PyPC containing liposomes (0.5 mol%) were diluted into solutions with different total lipid concentrations (unit: µM) and the spectra were measured. I_E and I_M were then obtained from the spectra and I_E/I_M was calculated. To check repeatability three PyPC based liposome samples made separately ('PyPC 1', 'PyPC 2', 'PyPC 3') were used for this investigation. Fig. 4.4 shows with increase of the lipid concentration, both monomer intensity and excimer intensity increase. The nonlinear relationship of intensity with lipid concentration is due to the inner filter effect - the light emitted is scattered by the particles inside the cuvette, and this effect is more intense at higher concentration [187]. Fig. 4.4c shows that I_E/I_M is almost the same for all the lipid concentrations studied. This result, in combination with Fig. 4.2, demonstrates that the excimer formation capability is determined by the pyrene labelled lipid to total lipids ratio but not by the total lipid concentration.

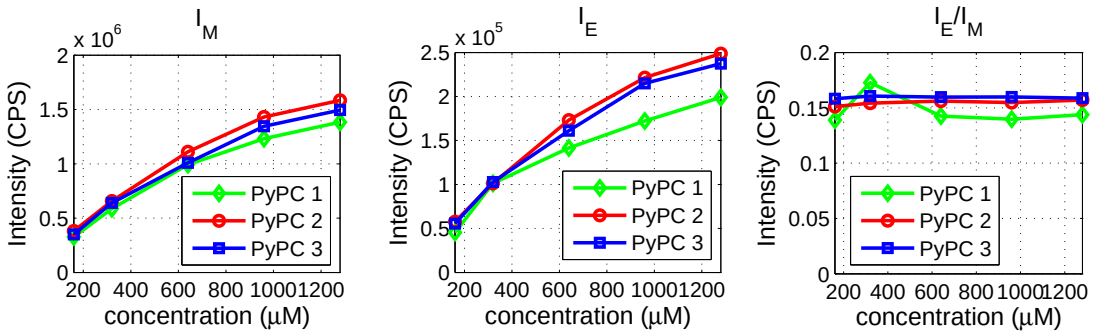


Figure 4.4: Influence of lipid concentration on excimer formation. I_M: monomer intensity; I_E: excimer intensity. Three PyPC based liposome samples ('PyPC 1', 'PyPC 2', 'PyPC 3') were used for this investigation.

4.4 Acousto-fluorescence system

4.4.1 Experimental setup

The acousto-fluorescence detection setup is shown in Fig. 4.5. The excitation light source is a LED (LED341W, Thorlabs, Ely, UK) with the spectrum shown in Fig. 4.6, measured using a spectrometer (HR4000, Ocean Optics, Dunedin, USA). The central wavelength is at $\lambda = 337$ nm, which matches the peak excitation wavelength of pyrene. The LED driver used was the ITC8000 series module mounted on the PRO8000 8-slot chassis (Thorlabs, Ely, UK). The LED was mounted inside the TCLDM9 (Thorlabs, Ely, UK) laser mount, and the light was guided by an optical fiber (1 mm diameter) to the US focal zone. An excitation filter with 337 nm central wavelength and 10 nm Bandpass (#65-128, Edmund Optics, York, UK) was located between the laser mount and the fiber through a C-mount tube to minimise the light at other wavelengths. A diluted solution of pyrene-labelled liposomes (1:10 in phosphate buffered saline (PBS) buffer) with an approximate 1.28 mM lipid concentration and $3 - 13 \times 10^7$ particles/ml concentrational liposomes was injected through an open ended tube (inner diameter: 400 µm) by a syringe pump at a flowing speed of 0.015 ml/min. The buffer tank was filled with the PBS buffer that was used to make the liposomes, in order to maintain the osmotic pressure in the liposomes. The end of the tube was positioned in the US focal zone with the tip of the optical fiber placed in close proximity (less than 2 mm) to maximise delivery of the excitation light to the sample. To prevent cross-contamination between samples,

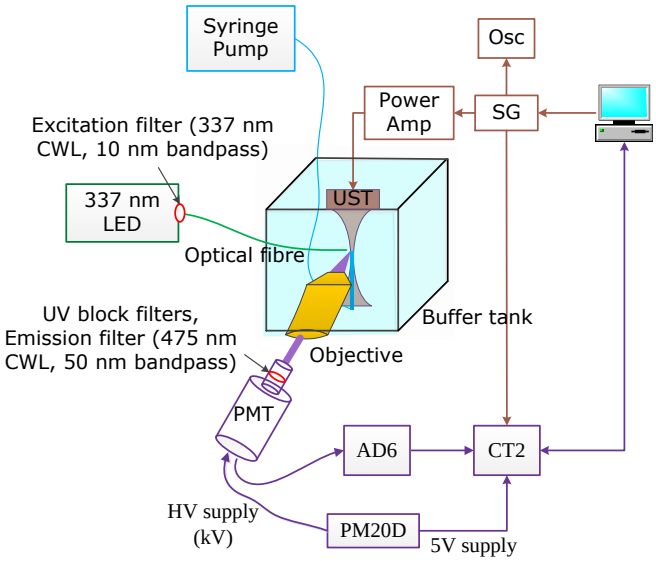


Figure 4.5: Schematic of the experimental setup. OSC: oscilloscope; SG: signal generator; PMT: photomultiplier tube; AD6: amplifier-discriminator; CT2: counter/timer module; PM20D: power supply; CWL: centre wavelength.

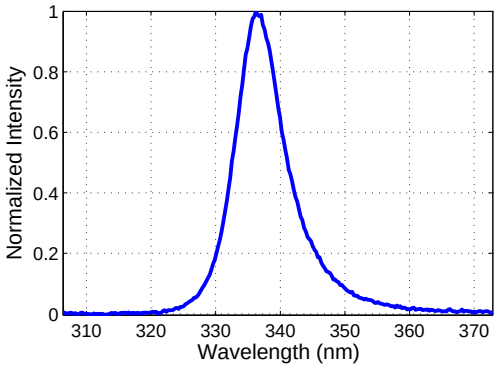


Figure 4.6: Measured spectrum of the LED.

the buffer tank was washed with detergent and acetone, and rinsed with deionised water in between measurements.

A signal generator (AFG 3022, Tektronix, Beaverton, USA) and a radio frequency power amplifier (Amplifier Research 75A250A, Souderton, USA) were employed to drive a focused 2.25 MHz US transducer (Olympus A304-SU, Massachusetts, USA). The emission light was collected by a long working distance objective lens (Mitutoyo M Plan Apo 20, Numerical aperture (NA) 0.42, Japan). To achieve a field of view with height 2 mm, the objective lens was adjusted to be $\frac{1\,\text{mm}}{tan(arcsinNA)} = 2.16\,\text{mm}$ away from its focal plane, as shown in Fig. 4.7. A high performance filter with central wavelength 475 nm and 50 nm bandpass (#86-962, Edmund Optics, York, UK) and two UV block-

ing filters (UVK-2510, UQG, Cambridge, UK) were mounted in front of the detector to achieve a high rejection ratio of the excitation light and monomer emission. The detector was a photon counting system (ET Enterprises Ltd, Uxbridge, UK) consisting of a PMT (9108B), AD6 (amplifier-discriminator), CT2 (counter/timer module) and PM20 (power supply). The photon counting system and the signal generator were controlled and synchronised using Labview. The whole system was located inside a light-tight black box in a dark room to avoid capture of room light. It should be noted that in this chapter the fluorescence is detected at DC with the PMT operated at the photon counting mode rather than detecting the modulated signal with PMT operated at the analogue mode in Chapter 3. This is advantageous as it does not require detectors and electronics to demodulate signals in the MHz range. Alternatively, full field fluorescence images could be obtained with a CCD camera while scanning the US focus to enhance fluorescence at different regions of interest in the sample. Detection at DC would also allow long CCD integration times to be employed where necessary.

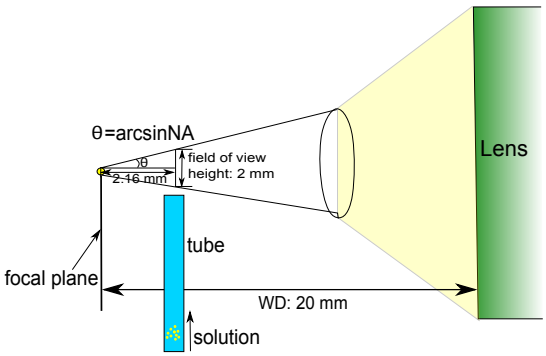


Figure 4.7: Schematic for calculation of the height of the field of view. WD: working distance; NA: Numerical Aperture.

The sample and PBS solution were left outside of the refrigerator for around half an hour prior the measurements to avoid change of temperature and oxygen concentration of the solution. This is because fluorescence emission from pyrene can be quenched by oxygen [188] and the oxygen concentration in the solution is dependent on temperature. It should also be noted that although the pyrene labelled liposomes were extruded and had the potential problem of losing pyrene lipids and lipids, it has been tested that the percentage loss of the two were similar [189]. Therefore the PyPC (or PyPE) to DPPC ratio should remain similar as the ratio prior to extrusion and the lipids losses

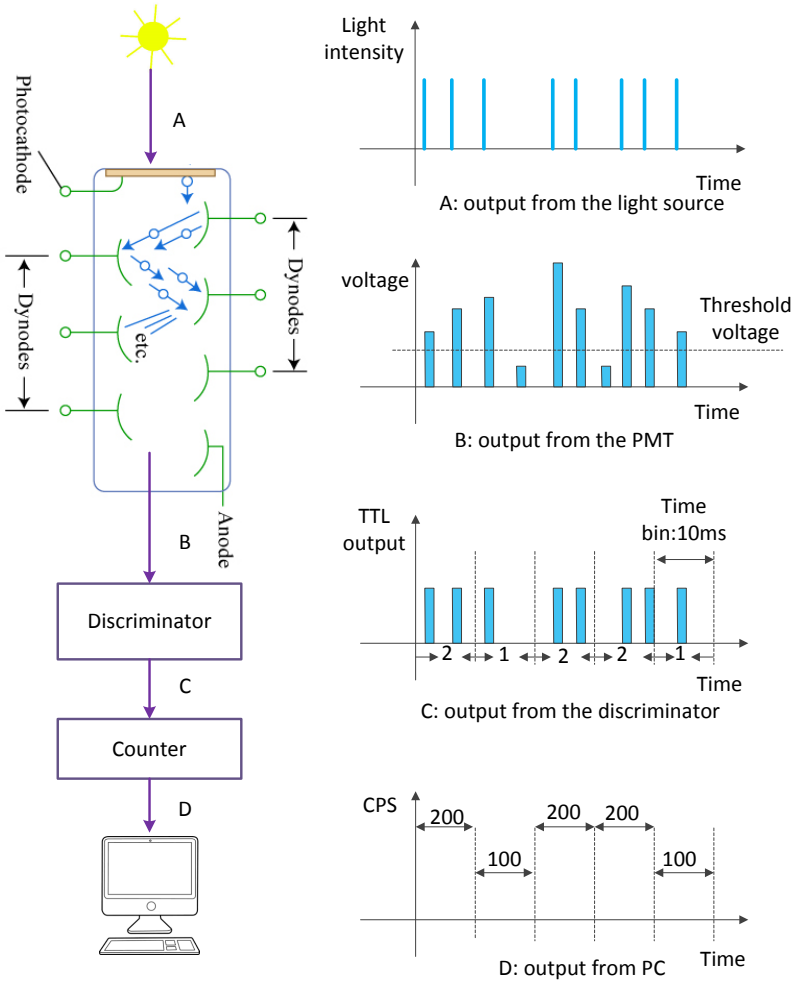


Figure 4.8: Schematic of the photon counting system.

were not considered in this study.

4.4.2 Calculation of the maximum counting rate

The excimer emission is very weak ($\sim 10^6$ photons/s), therefore a PMT working in photon counting mode was used as the detecting system to improve the SNR of the system. The photon counting system is shown in Fig. 4.8. To make sure the system was operated in its linear range, and also to avoid damage of the system by high light exposure, it is necessary to calculate the maximum counting rate.

Photoelectrons are generated when photons (A, Fig. 4.8) are exposed on photocathodes of the PMT. The number of generated photoelectrons during a measuring time T

follows a Poisson random process. The average percentage of incident photons that is converted to photoelectrons at wavelength λ is defined as the quantum efficiency ($\eta(\lambda)$). The generated photoelectrons are accelerated and multiplied by the dynodes, and collected by the anode of the PMT. The output pulses (B, Fig. 4.8) from the PMT vary in magnitude which follows a Poisson random process because of the statistical nature of the gain process. The mean peak pulse voltage at B is $V_B = RGe/t_{PMT}$, where R is the input impedance of the discriminator AD6, e is the electron charge, G and t_{PMT} are gain and the anode pulse width of the PMT respectively. Using the parameters of the photon counting system shown in Table 4.1, V_B is calculated as 35 mV. The AD6 amplifier-discriminator outputs a TTL pulse (C, Fig. 4.8) for each photomultiplier input pulse that exceeds a threshold level of -2 mV. The output TTL pulses are counted by the counter CT2 connected to a PC.

Table 4.1: Parameters of the photon counting system (PMT: 9108B).

Symbol	Meaning	Value
R	input impedance of AD6	50 Ω
G	PMT gain	2.2×10^7
t_{PMT}	anode pulse width of the PMT	5 ns
$\eta(\lambda)$	quantum efficiency	25% ($\lambda = 475$ nm)
I_{max}	maximum anode current limitation	100 µA
T	count rate correction factor	2.4×10^{-8}

Limitation from the maximum anode current:

Radiant sensitivity $E(\lambda)$ (mA/W) at the photocathode of the PMT can be calculated as [190]:

$$E(\lambda) = \frac{\lambda \eta(\lambda)}{1.24} \tag{4.4.1}$$

where λ is the central wavelength of the excimer emission, and $\eta(\lambda)$ is the quantum efficiency of the PMT. Radiant sensitivity at the anode is then calculated as $E(\lambda)G = 1.94 \times 10^6$ A/W. The anode current should not exceed I_{max}, therefore the light exposed to the PMT should not exceed $P_{max} = I_{max}/[E(\lambda)G\eta(\lambda)hf] = 4.96 \times 10^8$ photons/s.

Limitation from the maximum counting rate:

The maximum counting rate of the photon counting system depends on pulse-pair resolution, which is the minimum time interval at which each pulse can be separated [190].

The reciprocal of this pulse pair resolution is the maximum count rate. The pulse pair resolutions of CT2 and AD6 are 8.3 ns and 20 ns respectively. So the pulse pair resolution of the system is 20 ns. The maximum counting rate is thus $1/(20\,\text{ns}) = 5 \times 10^7$ counts/s. Considering the possibility of pulse overlap, the actual maximum counting rate is around one-tenth of the calculated above. However the maximum counting rate can be expanded using the counting rate correction formula which is [190]:

$$N = n/(1 - nT) \tag{4.4.2}$$

where n is the measured counting rate, T is the count rate correction factor, and N is the true counting rate. Therefore, the maximum counting rate can still be regarded as 5×10^7 counts/s. The corresponding light level at $\lambda = 475\,\text{nm}$ is $5 \times 10^7/\eta(\lambda) = 2 \times 10^8$ photons/s.

Comparing this value with the light intensity limited by the maximum anode current of the PMT, the overall light level that can be exposed on the photon counting system is limited by the counting rate of AD6. The maximum light level and maximum counting rate of the photon counting system are 2×10^8 photons/s and 5×10^7 counts/s respectively. If the light exposed to the PMT is between 2×10^8 photons/s and 4.96×10^8 photons/s, the reading of the photon counting system is nonlinear. If the light exposed to the PMT goes beyond 4.96×10^8 photons/s, the PMT might be damaged permanently.

4.4.3 Calculation of the concentration distribution

The liposomes in the PBS solution experience four forces - buoyancy, gravity, viscous force induced by the solution, and driving force caused by the incoming sample via flow. Since the density of the liposome and PBS solution are the same, the buoyancy and gravity are balanced and can be ignored. The liposome solution injected by the syringe pump has an initial flowing speed v_0 of $\frac{0.015\,\text{ml/min}}{\pi {r_t}^2} = 0.20\,\text{cm/s}$ and thus has an initial momentum, where $r_t = 200\,\mu\text{m}$ is the radius of the tube used to inject the solution.

Momentum relaxation time τ_{mr}

If only considering viscous force $f\vec{v}(t)$, with $f = 6\pi\eta r_0$ being friction factor and $\vec{v}(t)$ being the particle instantaneous velocity at time t, by integrating Newton's second law:

$$\frac{d\vec{p}}{dt} = -f\vec{v}(t) \tag{4.4.3}$$

with $\vec{p}$ being momentum, the instantaneous velocity $\vec{v}(t)$ can be expressed as:

$$\vec{v}(t) = v_0 exp(-t/\tau_{mr}) \tag{4.4.4}$$

where $\tau_{mr} = m/f = \frac{2\rho {r_0}^2}{9\eta}$ is defined as momentum relaxation time and it describes the time over which the particle loses all its momentum [191].

The distance travelled by the particle during the time t is:

$$l(t) = \int_0^t v(t')dt' = v_0\tau_{mr}[1 - exp(-t/\tau_{mr})] \tag{4.4.5}$$

Table 4.2: Particle parameters.

Symbol	Meaning	Value
r_0	particle (liposome) radius	50 nm
ρ	particle density	1 g/cm^3
η	water viscosity	10^{-3} Pa sec
T	temperature	298 K

The parameters of the particle (liposome) are shown in Table 4.2. The calculated values of the momentum relaxation time and the corresponding distance travelled by the particle during the momentum relaxation time are $\tau_{mr} = 6.24 \times 10^{-10}$ s and $l(\tau_{mr}) = 7.89 \times 10^{-13}$ m respectively. It can be seen that the momentum relaxation time and the corresponding distance travelled are extremely short. Therefore this mechanism can be reasonably ignored and the initial flowing speed can be regarded as zero.

Concentration distribution

The diffusion of the particles in the area of interest can be calculated by Fick's second law:

$$\frac{dc(x,t)}{dt} = D\frac{d^2c(x,t)}{dx^2} \tag{4.4.6}$$

Before the diffusion, there are no liposomes distributed in the area of interest. Following injection the concentration at the position where the liposome solution is injected is the same as the liposome solution. Therefore the following boundary condition is employed:

$$\begin{cases} \text{for } t = 0,\ c = 0 \text{ at } 0 \leqslant x \leqslant +\infty \\ \text{for } t > 0,\ c = C_0 \text{ at } x = 0 \\ c = 0 \text{ at } x = \infty \end{cases} \tag{4.4.7}$$

where $c(x,t)$ is the concentration distribution at time t and a distance x from the position where the solution is injected from the open end tube. $C_0 = 10^8$ particles/ml, D is the diffusion coefficient and it is a function of the temperature T and friction factor f such that $D = kT/f = 4.9075 \times 10^{-12}\text{m}^2/\text{s}$, where k is Boltzmann's constant. The solution of Eq. 4.4.6 and Eq. 4.4.7 is $c(x,t) = C_0(1 - erf(x/(2\sqrt{Dt})))$, where $erf(z) = \frac{2}{\sqrt{\pi}} \int_0^z e^{-\xi^2} d\xi$. The calculated concentration distribution is shown in Fig. 4.9 and Fig. 4.10.

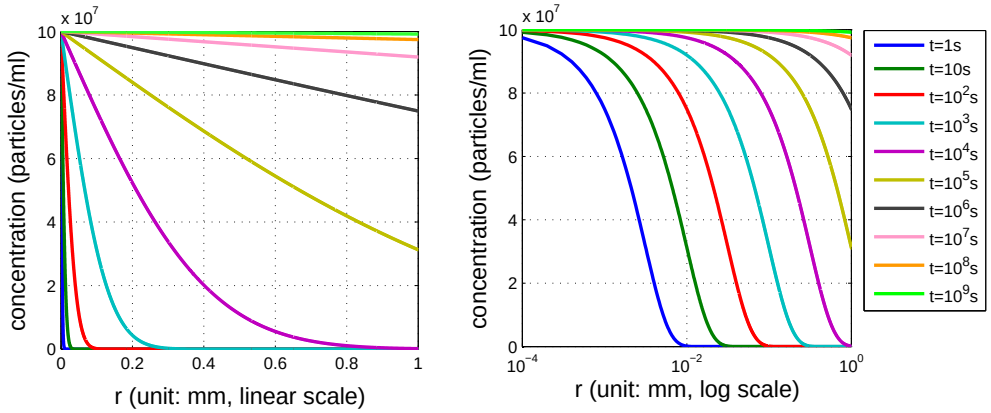


Figure 4.9: Concentration distribution along distance at different time points.

Fig. 4.9 and Fig. 4.10 show that if only considering particle diffusion, the time required for liposomes to reach $r = 1\,\text{mm}$ is at the time scale of 10^4 s (purple line in Fig. 4.9 and dark green line in Fig. 4.10). The time taken for the concentration gradient to become constant is at the time scale of 10^5 s (yellow line in Fig. 4.9). The time taken for the concentration at $r = 1\,\text{mm}$ to be constant is at the time scale of 10^8 s (orange line in Fig. 4.9). These time scales are much larger than the experimental measuring time period which is less than 100 s, therefore diffusion induced by a concentration gradient

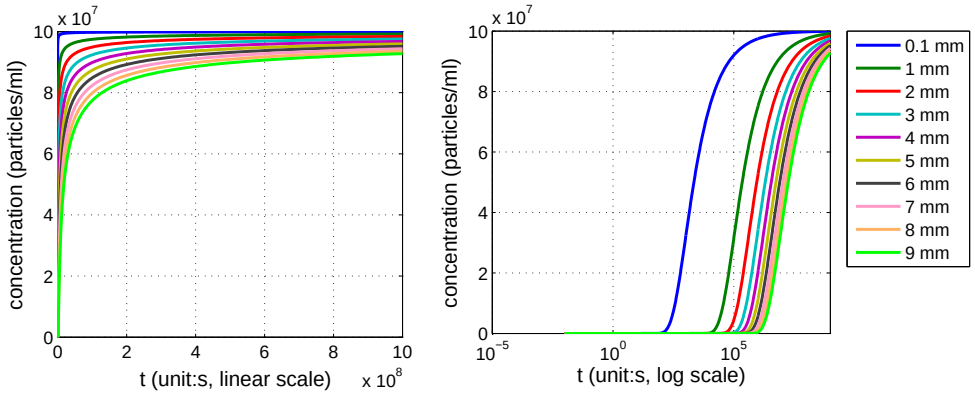


Figure 4.10: Concentration distribution with time at different positions.

is not the dominant reason for the liposome movement in the US focal zone.

Actually considering the area of interest as a cylinder with the diameter determined by the optical field of capture (2 mm) and the height determined by the US focal zone (2.1 mm), with a flowing speed 0.015 ml/min, the time taken to fill in the area of interest is around 26 s (without considering the diffusion). This is much closer to the measured time for the detected intensity to become constant ($\sim$ 60 s). Therefore the liposome movement in the US focal zone should be: as some new solution enters, to keep the overall volume the same (incompressible solution), some solution is ejected. When all the field of interest has been filled, the liposome concentration at this region is the same as the solution injected, so the ejected solution has the same contribution to the measured light level as the injected solution. This is the time when the detected intensity becomes constant. The measured time of 60 s is longer than the calculated value of 26 s since some of the newly injected solution will also be ejected during this procedure.

4.5 Acousto-fluorescence measurements

In this section the US mediated fluorescence variation is investigated by performing the acousto-fluorescence measurements. PyPC based liposomes and PyPE based liposomes were exposed to both long and short duration CW US and the fluorescence was monitored. Possible mechanisms are discussed.

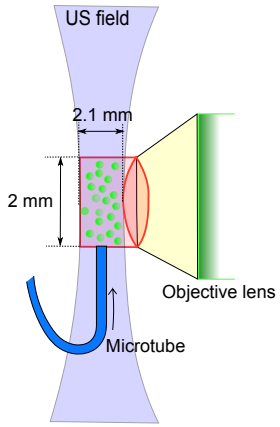


Figure 4.11: Schematic of the setup at the area of interest, which is regarded as a cylinder with the bottom (2 mm diameter) decided by the optical field of capture and the height (2.1 mm) decided by the US focal zone.

4.5.1 Movement of lipids in labelled liposomes

The movement of lipids (e.g. DPPC, PyPC, PyPE) in labelled liposomes includes lipid lateral diffusion [192], flapping of the acyl chains, and transbilayer movement [172].

Lateral diffusion (also known as lateral translocation) refers to the lateral movement of lipids in the membrane. Membrane lipids are generally free to move laterally if they are not restricted by certain interactions. Lateral diffusion is a fairly quick and spontaneous process with a diffusion rate around 2 mm/s. Without influence of US, excimer formation is believed to be diffusion controlled and I_E/I_M is proportional to the diffusion rate [193]. The lateral mobility of a molecule was proved to be directly related to the frequency with which a vacancy of sufficient size (free volume) is created in its neighborhood [186]. It can be expected that if US can perturb the liposomes and produce more free volume in the lipid bilayers, the lateral diffusion rate can be changed which can lead to a change of the excimer fluorescence.

The host lipid used to produce the liposomes in this study is DPPC which has 16 carbon atoms in both of the two fatty acyl chains. Relating this number of carbon atoms with [194], the liposome should be between phase $L_{\beta'}$ and $P_{\beta'}$, meaning that the lipid bilayer is in gel state but there is a certain extent of mobility of the phosphate head group and a considerable reduction in the tilt of the acyl chains to the bilayer normal. In other words there is lateral movement of the DPPC and also flapping movement of the acyl chains (also know as tail wagging). It should be mentioned that the influence

of PyPC on the phase state of the lipid bilayer is ignored in this study due to the very low molar fraction of PyPC (0.5 mol%). This assumption is quite reasonable comparing the data shown in [195], in which 2.4 mol% pyrene phospholipid induces a decrease of the phase transition temperature of DPPC liposomes from 41.4 °C to 40.7 °C only.

Transbilayer moment (also known as translocation or flip-flop) involves the movement of a lipid from one half of the bilayer to the other half of the bilayer. The rate of transbilayer movement is believed to be very slow, with half-times in the order of days in the absence of protein-mediated processes [196]. The reason is the thermodynamically unfavourable transfer of the hydrophilic head-group of a lipid molecule through the hydrophobic core of the lipid bilayer [197]. However, the transbilayer movement speed can be increased using some membrane active pepitides such as melittin and magainin 2 amide [172]. Also transbilayer movement is dependent on the temperature. A dramatic increase of transbilayer movement was observed at the phase transition temperature of the lipid, of the order of several minutes [196, 197]. The reason for the increased transbilayer movement is assumed to be perturbations of the bilayer structure by the peptides or the molecular packing defects at the phase transition. The perturbations or membrane defects induced by US might lead to a similar increased transbilayer movement.

4.5.2 Comparison of tail labelled liposome with head labelled liposome

In this section the excimer emissions from tail labelled liposomes (PyPC based liposomes) and head labelled liposomes (PyPE based liposomes) when exposed to long duration CW US were detected and compared.

The excimer emission intensity was detected using the setup shown in Fig. 4.5 and described in Section 4.4. The photon counting system recorded the excimer emission intensity (unit: CPS) during the measuring period of 18 s with a sampling period of 10 ms. The signal generator was turned on at 4 s by Labview for 14 s. The US pressure is over a range of 360 kPa to 1.45 MPa, measured using a needle hydrophone with 0.2 mm active diameter. This pressure is relevant to the typical values used in clinical diagnostic and therapeutic applications (0.3 MPa - 10 MPa [198]). The detected excimer

emission intensity was normalized according to the excimer emission intensity prior to US sonication. 50 consecutive data points corresponding to 500 ms measurement time were averaged and the mean and standard deviation were plotted.

Fig. 4.12 displays the normalised excimer emission intensity for both PyPC and PyPE containing liposomes. It can be seen that US exposure causes an increase in excimer emission intensity for all cases studied with the rate and increased intensity of emission being different for the PyPC and PyPE systems. Of note is the higher rate and maximum intensity of excimer emission intensity from PyPC containing liposomes at lower US pressures (360 kPa, 380 kPa, and 450 kPa) as compared to PyPE systems. This behavior changed at higher US pressures (530 kPa, 640 kPa, and 1.45 MPa) with the PyPE systems displaying the highest rate of excimer emission. Fig. 4.12 also shows after prolonged sonication of samples, the excimer emission decreased to the background level. This effect is more prevalent at higher US pressures and PyPE systems and may be due to the rupture of liposomes caused by the cavitation of pre-existing bubbles in the surrounding media or in the lipid bilayer. This is verified later in Section 4.6.

To quantify the differences in the temporal and pressure dependent variation of excimer emission intensity for the PyPC and PyPE based liposomes observed in Fig. 4.12, the On-to-Off ratio of the fluorescence intensity (in %) and rise rate (in s^{-1}) were calculated at each pressure studied, results shown in Fig. 4.13. Here the On-to-Off ratio is calculated by dividing the increased fluorescence intensity with US on to the intensity prior to sonication, shown in Fig. 4.13a. The rise rate is calculated from dividing the On-to-Off ratio by the sonication time interval for the emission to reach a maximum, shown in Fig. 4.13b.

Over the pressure range studied the On-to-Off ratio of the PyPE based system was relatively invariant ranging from approximately 20 % to 40 %. The PyPC system, however, showed a significant dependence on pressure with a variation from approximately 20 % to 130 % with larger On-to-Off ratio occurring at the lower end of the pressure range studied (360 kPa, 380 kPa, and 450 kPa) as noted in Fig. 4.13a. Although On-to-Off ratio for the PyPE system is relatively invariant with pressure, the rise rate displays strong pressure dependence. With reference to Fig. 4.13b the rise rate was found to notably

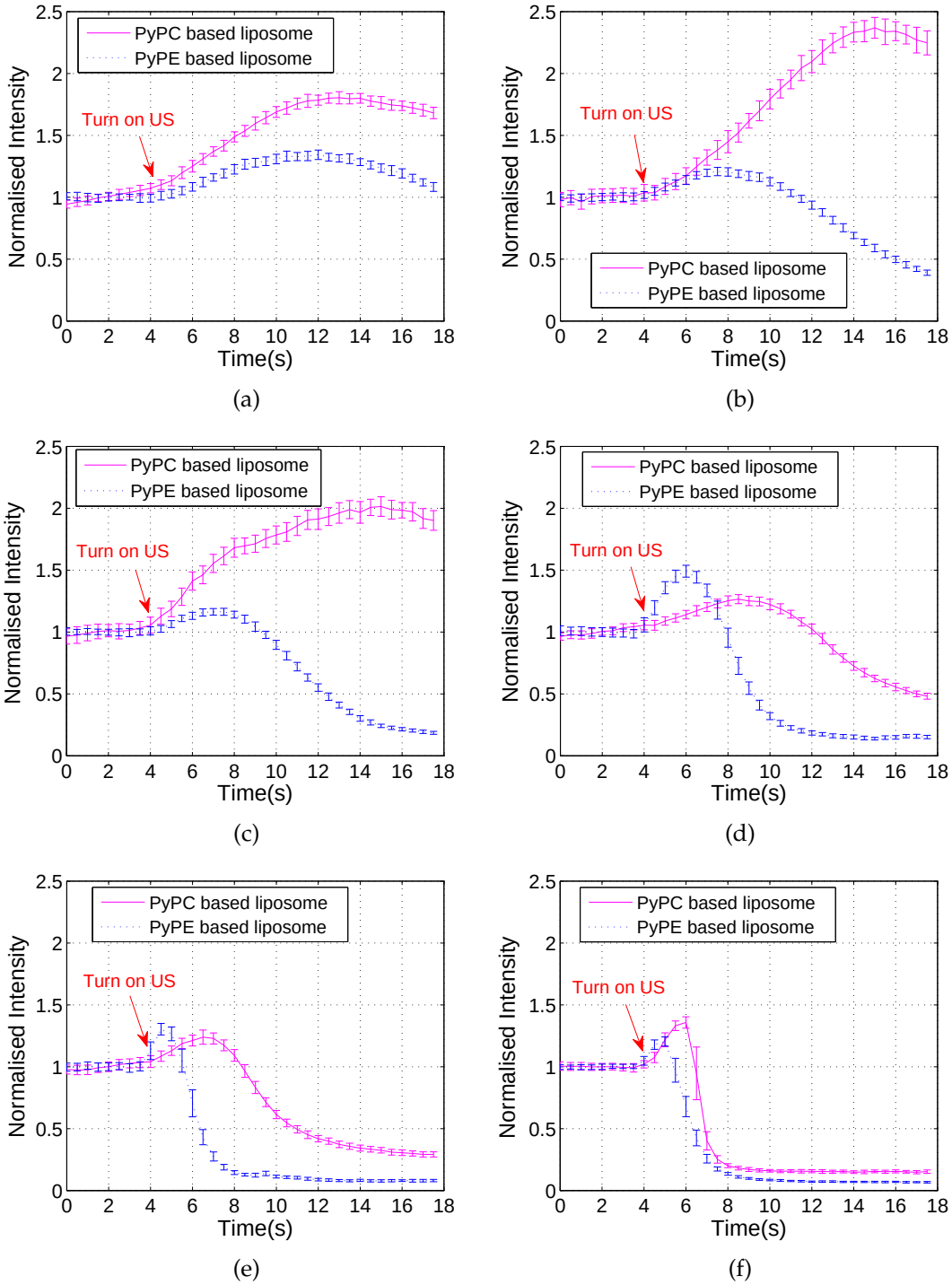
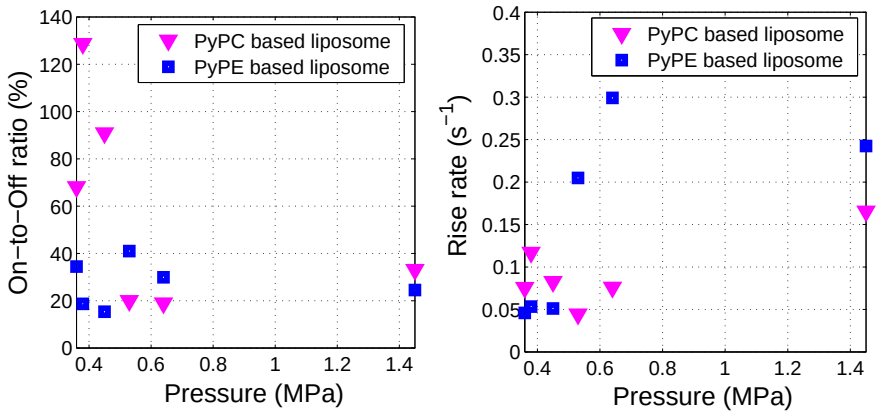


Figure 4.12: Acousto-fluorescence measurements with CW US turned on at 4 s at different US pressures (a) 360 kPa (b) 380 kPa (c) 450 kPa (d) 530 kPa (e) 640 kPa (f) 1.45 MPa for PyPC and PyPE containing liposomes. The data were recorded continuously for 18 s with sampling period of 10 ms. 50 measurements (corresponding to 500 ms time window) are averaged to obtain mean and standard deviation.



(a) (b)

Figure 4.13: Comparison of PyPC and PyPE based liposomes. (a) On-to-Off ratio against US pressure; (b) rise rate against US pressure.

vary with pressure only for the PyPE containing liposomes. It is relatively invariant for PyPC containing liposomes ranging from approximately $0.05\,s^{-1}$ to $0.15\,s^{-1}$.

4.5.3 Possible mechanisms for the US mediated fluorescence variation

The significant differences shown in Fig. 4.12 and Fig. 4.13 between the US mediated excimer emission from pyrene tail and head labelled systems can be understood by considering the possible mechanisms. US at mega pascal pressure and megahertz frequency has long been found to induce noninertial cavitation [199]. The noninertial cativation refers to a class of cavitation in which a violent collapse does not occur [67]. During the noninertial cativation process the gas bubbles pre-existing in the fluid contract and expand due to the compression and rarefaction of US. In the current work the CW US may lead to occurrence of noninertial cavitation, which may generate small cavities and create free volume in the lipid bilayer. The increased free volume can facilitate quicker lateral diffusion of the pyrene labelled lipids [200] and thus increase the collision rate of the pyrene moieties and the excimer emission intensity for both PyPC and PyPE based liposomes.

Furthermore, for the PyPC based liposomes, the mechanism of the observed variation of the excimer emission intensity induced by US might also relate to the wagging of the acyl chains. In Section 4.5 it was mentioned that the lipids are in $L_{\beta'}$ and $P_{\beta'}$ phase

therefore the acyl chains are tilting with each other. The tilting of the acyl chains could hamper juxtaposition of the pyrene moieties [195], which is critical for excimer formation. US might make acyl chains less tilted and the wagging motion stronger, which increases the possibility that two neighboring pyrene aromatic rings are brought to a planar arrangement to form excimer. Crucially, this mechanism of excimer emission is absent in the PyPE based liposomes because the pyrene moiety is attached on the head group of the phospholipid. The mechanism by which US affects the acyl chains is not clear. One possible explanation might relate to the embedded bubbles that nucleated in the bilayer during the US exposure process [201].

As indicated in Fig. 4.13 at lower US pressure (360 kPa, 380 kPa, 450 kPa) both the On-to-Off ratio and the rise rate are lower for PyPE based liposomes compared with PyPC based liposomes. At higher US pressure (530 kPa, 640 kPa, 1.45 MPa) PyPE based liposomes have similar On-to-Off ratio as PyPC based liposomes, but the rise rate of PyPE based liposomes is significantly higher. Based on the above discussions this observation might be explained as: for PyPC based liposomes both (1) the US increased wagging motion and (2) the US increased lateral diffusion contribute to the increased intensity, while for PyPE based liposomes only the US increased lateral diffusion is present. Since the wagging motion of a lipid is generally considered at a faster time scale compared with lateral diffusion [202, 203], PyPC based liposomes have low activation energy (refers to the minimum energy required for excimer formation) and involve fast kinetic process (refers to the excimer formation process). Therefore at lower US pressure the first mechanism dominates while at higher US pressure the second mechanism dominates. It should be noted that since excimer formation is extremely sensitive to proximity (angstrom level) and orientation of the pyrene moieties, a slight change of the lateral diffusivity of the pyrene labelled lipids or wagging motion of the pyrene attached acyl chains (for PyPC system) can cause variation of the excimer emission intensity.

In addition to the lateral diffusion, transbilayer movement might be another mechanism for PyPE based liposomes at higher US pressure. The hydrophobic nature of pyrene [184] promotes lipid transbilayer movement in which lipids 'flip' between the

two bilayer leaflets. In the equilibrium state this effect averages out as the lipids in both leaflets are equally likely to flip, however, the application of US may cause non-uniform transbilayer movement in addition to lateral diffusion. In comparison, the pyrene moiety of PyPC lipids is already in a hydrophobic environment and thus there is no intrinsic tendency for transbilayer movement.

In conclusion, the results in Fig. 4.12 and Fig. 4.13 imply that US might lead to three variations: (1) wagging motion of the acyl chains; (2) lateral diffusion of pyrene labelled lipids; (3) transbilayer movement of pyrene labelled lipids. The main mechanism at low pressure is the increased wagging motion of the acyl chains (PyPC based liposomes only) owing to the relatively low activation energy of this degree of freedom. At high pressure lateral diffusion is dominant for both the PyPC and the PyPE based liposomes. Owing to the hydrophobic nature of the pyrene, PyPE based liposomes might also undergo transbilayer movement. The comparison of PyPC containing liposomes and PyPE containing liposomes and the proposed mechanisms for the observed US mediated fluorescence variation are summarised in Table 4.3.

Table 4.3: Comparison of PyPC containing liposomes and PyPE containing liposomes.

	PyPC containing liposomes	PyPE containing liposomes
Location of pyrene moiety	acyl chain	head
Equilibrium state	homogeneous distribution	disordered distribution
US mediated mechanisms	flapping of acyl chains lateral diffusion	lateral diffusion transbilayer movement

4.5.4 Short exposure measurements

The results in the previous section demonstrate the increased excimer fluorescence signal from pyrene labelled nanoscale liposomes following long duration CW US. To minimize the cavitation based liposome rupture induced by long duration US at high pressures as described above, the response of pyrene labelled liposomes to US with short duration (quasi CW exposure mode) was studied. Here the excimer emission intensity from both PyPC and PyPE systems was studied at three different combina-

tions of pressure and exposure times (430 kPa, 3 s; 570 kPa, 0.8 s; 850 kPa, 0.3 s). These were representative of pressures that elicited large increased fluorescence with appropriate exposure times to minimise the occurrence of cavitation based liposome rupture. Results are shown in Fig. 4.14 with the fits to the data based on a combination of exponential rise functions ($y = A_1 exp(-t/t_r) + y_1$) and exponential decay functions ($y = A_2 exp(-t/t_d) + y_2$).), where y and t are the normalized intensity and time respectively, A_1, A_2, t_r, t_d, y_1, and y_2 are fitting parameters. Specifically t_r and t_d are exponential rise and decay time constants. Table. 4.4 summarises the exposure regime, t_r, t_d and On-to-Off ratio.

Table 4.4: Data obtained from PyPC and PyPE containing liposomes using short duration US.

Liposome system	Pressure (kPa)	Exposure time (s)	t_r (s)	t_d (s)	On-to-Off ratio (%)
PyPC	430	3.0	2.20	2.91	50
PyPE	430	3.0	4.07	2.11	39
PyPC	570	0.8	0.88	2.38	26
PyPE	570	0.8	0.96	2.61	24
PyPC	850	0.3	0.33	2.36	15
PyPE	850	0.3	0.80	2.53	20

Fig. 4.14 shows a clear increase in excimer emission intensity when US is turned on for all systems and at all US pressure and exposure times studied. It can be seen that the On-to-Off ratio, t_r, and t_d are all dependent on the applied US pressure and the exposure time. Here the pressure dependence and emission rise time constants are attributed to the activation energy and kinetics of mechanisms related to increased collision rate of pyrene labelled lipids, which are possibly due to increased lateral diffusion and 'wagging' of the pyrene attached acyl chains (PyPC based liposomes only). The decay time constant can be linked to the relaxation times intrinsic to the mechanisms underlying excimer emission. The rise time constant is lower for the PyPC system compared to the PyPE system for all exposure regimes studied suggesting the kinetics here are dominated by the increased collision of pyrene moieties via the fast 'wagging' motions of the fatty acyl tails. In contrast the decay time constant is relatively invariant for the different liposome systems and the different US exposure regimes. Here excimer decay will be dominated by the characteristic times for the lipid distribution to return

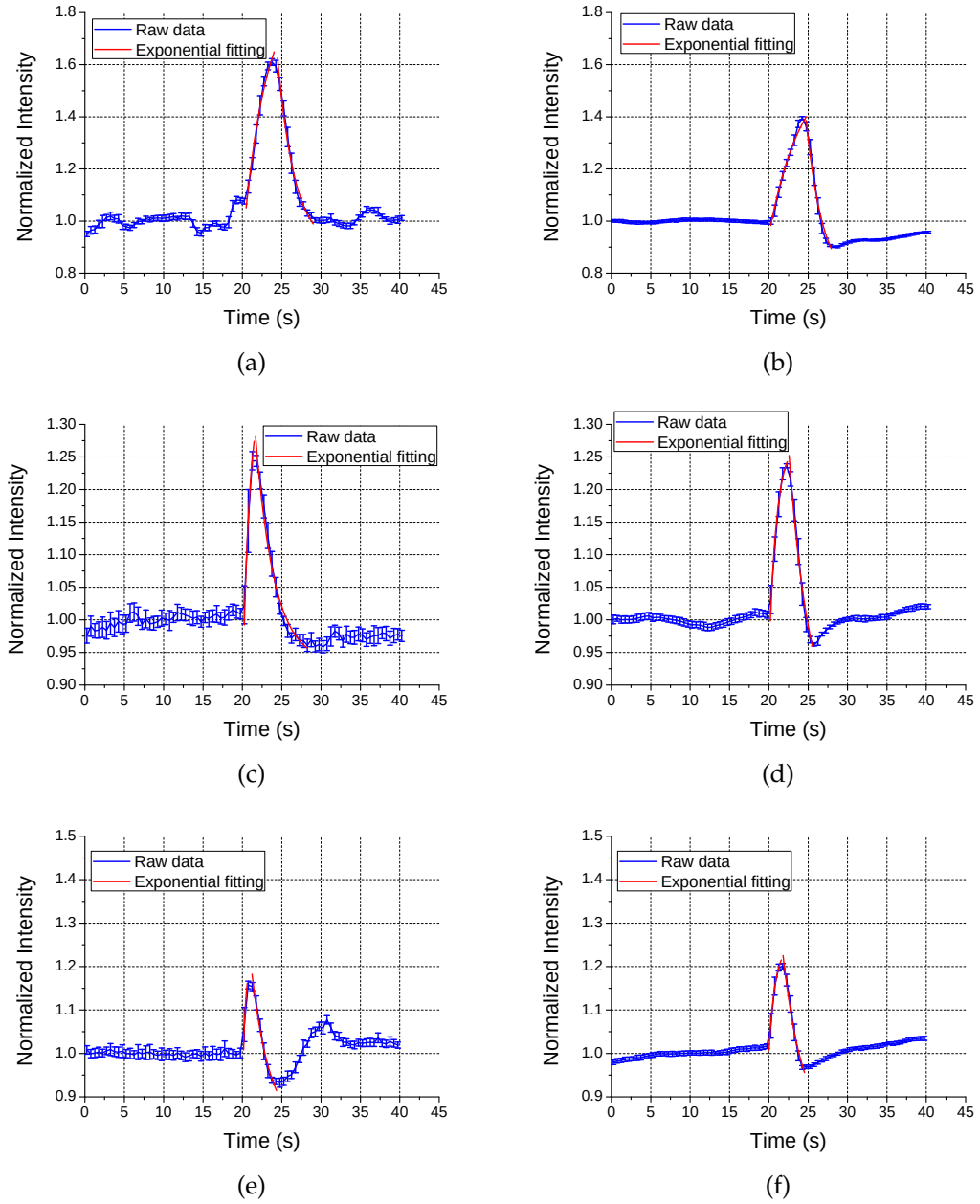


Figure 4.14: Intensity change induced by short duration US for (a) PyPC containing liposomes at 430 kPa for 3 s; (b) PyPE containing liposomes at 430 kPa for 3 s; (c) PyPC containing liposomes at 570 kPa for 0.8 s; (d) PyPE containing liposomes at 570 kPa for 0.8 s; (e)PyPC containing liposomes at 850 kPa for 0.3 s; (f) PyPE containing liposomes at 850 kPa for 0.3 s. The data were recorded with sampling period of 10 ms. Three repeating experiments were performed with the sample replenished in between and the averaged values were calculated. Mean and standard deviation of 50 consecutive values (corresponding to 500 ms measurement time) are shown.

to its equilibrium state rather than the effects of increased collision.

It should be noted that the On-to-Off ratio as well as the rise rate of excimer emission depends both on the US pressure and exposure time. Although it is difficult to decouple the effects of pressure and exposure time on the On-to-Off ratio, the results indicate that greater fluorescence variation can be obtained with a combination of lower US pressure with longer exposure time. Thus the selection of a suitable US pressure needs to balance the achievable On-to-Off ratio with the rise time constant. The selection of US duration needs to balance the requirement for exposure times that are sufficiently long to elicit large fluorescence enhancement with the desire to avoid loss of liposomes due to rupture.

4.6 Cavitation effects at high pressure

Fig. 4.12 shows that prolonged sonication of samples leads to a reduction in excimer emission to the background level. This effect is more prevalent at higher US pressures and for PyPE based liposomes. The reduction in excimer emission may be due to the rupture of liposomes caused by the cavitation of bubbles in the surrounding media or in the bilayer itself. To investigate this further size analysis of the liposomes before and after exposure to US was carried out in this section.

The geometry to collect insonified liposomes is shown in Fig. 4.15. A cellulose tube (#132294, Spectrum Laboratories, Rancho Dominques, USA) which has an inner diameter of 200 µm and outer diameter of 216 µm was connected to a 1 mm outer diameter tube by a tube adapter (F-183, MicroTight, Kinesis, Cambridgeshire, UK). The cellulose tube was located inside the US focal zone, which was monitored by a needle hydrophone with 0.2 mm active diameter. The tail labelled liposomes solution was injected into the cellulose tube by a syringe pump. During the collection procedure US was maintained at 850 kPa. The size of the collected insonified sample was then measured by the Nanosight LM14.

The measured results showed a reduction of the liposome mean size (74 nm compared to 128 nm) and an increase in the mean liposome concentration (1.00×10^9 particles/ml

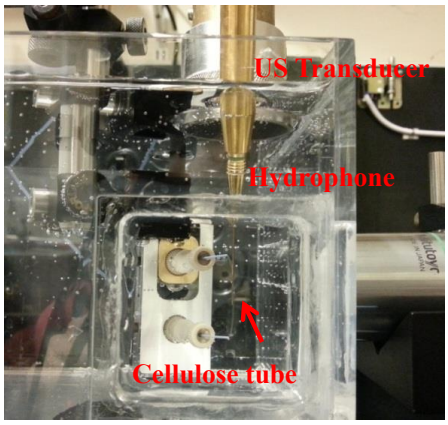


Figure 4.15: Geometry to collect insonified liposome.

compared to 2.70×10^8 particles/ml) after sonication providing support for the cavitation hypothesis. The values were calculated by averaging six different regions of interest of the Nanosight microscope. The size distribution of one region is shown in Fig. 4.16.

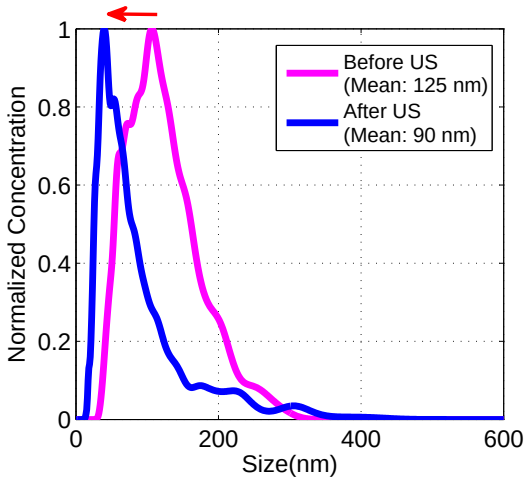


Figure 4.16: Size distribution of PyPC labelled liposome before and after 850 kPa US exposure. Tested using Nanosight LM14.

During the cavitation process, larger liposomes were shattered into smaller discoid sections called bilayer phospholipid fragments which fold up into thermodynamically stable smaller liposomes [204]. Several mechanisms might coexist to lead to the cavitation. The first mechanism is the unstable cavitation (inertial cavitation). In detail, gas-filled microscopic bubbles already in the solution are expanded and contracted by the US field. Bubbles whose size is near the resonant size of the applied US oscillate nonlinearly and eventually collapse, which results in violent implosion that produces a

shockwave that can cause damage of the liposome bilayer. Further, the bubbles whose size is far from the US frequency would oscillate continuously without implosion and undergoes stable cavitation. Such stable cavitation can also have large effects on the liposome. The stable oscillation of gas bubbles can induce acoustic microstreaming, which is the collection of convective flow patterns developed near the surface of an oscillating bubble. It is proposed that such acoustic microstreaming can cause high shear elongation forces on the liposome, create unstable cylinders and then break them into smaller liposomes [204]. Another cavitation process involves the nucleation of microscale gas bubbles in the hydrophobic region of lipid bilayers. These bubbles grow, and their interaction with the US field can also cause bilayer disruption. Unstable cavitation is not thought to commonly occur at therapeutic levels of US [199]. The stable cavitation and bubble nucleation in the lipid bilayer are thus more likely to be the mechanisms for the liposome rupture observed in this section. Note that Fig. 4.12 shows excimer emission from PyPE containing liposomes decreases earlier than PyPC containing liposomes. This suggests that PyPE containing liposomes are less stable than PyPC containing liposomes. This might be due to the more severe disturbance of the pyrene on the lipid bilayer for PyPE compared with PyPC and the more disordered distribution that PyPE containing liposomes possessed of [205].

4.7 Influence of temperature on excimer formation

Temperature was claimed to have influence on the excimer formation rate [206–208]. There is an intermediate temperature at which there is a maximum rate of the excimer to monomer, since temperature can influence the viscosity of lipid bilayer and the dissociation rate of excimer [207]. In this section the influence of temperature on PyPC containing liposomes and PyPE containing liposomes at 0.5 mol% were studied by detecting the excimer and monomer emission at various temperatures using a spectrofluorometer (Fluoromax-4, Horiba Scientific, Kyoto, Japan). Ice was put inside the immersion thermostats bath (TC120, Grant Instruments, Shepreth, UK) which is equipped with the spectrofluorometer to reduce the temperature to 15 °C. The increase

of the temperature was controlled by the thermostats bath directly.

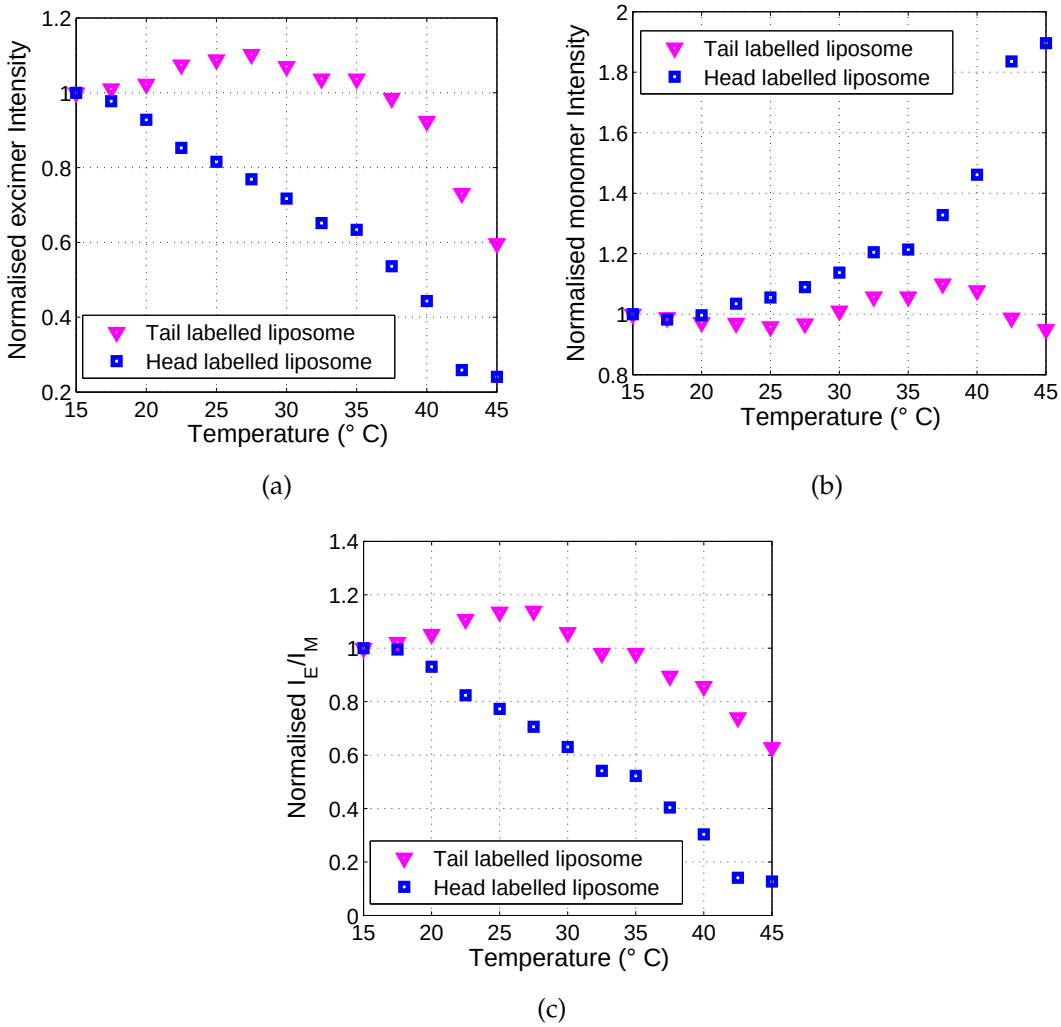
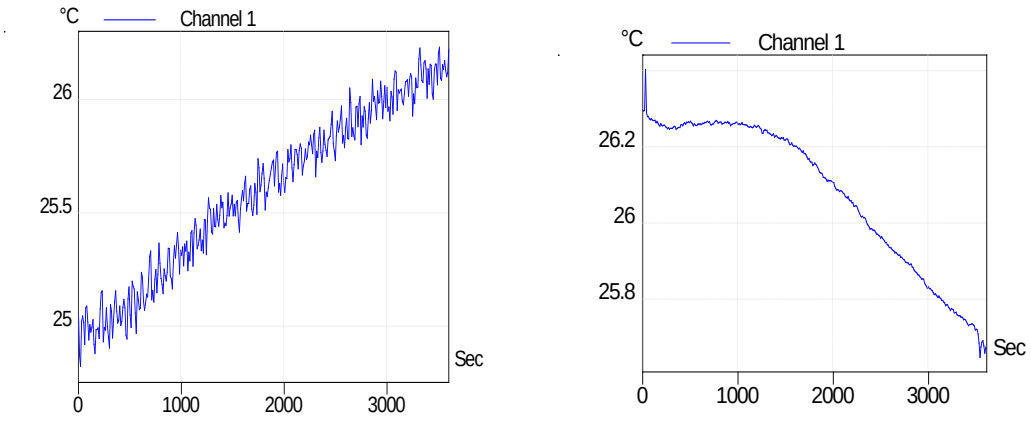


Figure 4.17: Influence of temperature on excimer formation. The excimer intensity is normalized according to the starting temperature of 15 °C. (a) Normalized excimer intensity; (b) Normalized monomer intensity; (c) Normalized ratio of excimer and monomer.

Fig. 4.17 shows that for tail labelled liposomes, from 15 °C to 27 °C the excimer intensity increased slowly, and from 27 °C to 35 °C the intensity decreased slowly. After 35 °C the excimer intensity decreased quicker and undergoes a sudden drop above around 40 °C. This excimer intensity change is in accordance with the phase state of liposomes. At lower temperature range, the excimer formation increases with the increase of the viscosity of the lipid bilayer. At high temperature, especially above the gel to liquid phase transition temperature of DPPC (41 °C), however, the excimer emission is suppressed by the high dissociation rate of the excimer [207]. The relationship of excimer intensity

with temperature for tail labelled liposomes was observed to be different from head labelled liposomes. For the latter, the excimer intensity keeps decreasing with increase of temperature. The intensity decrease becomes more significant above 40 °C. The 1 °C difference with the phase transition temperature of DPPC is due to the 2.5 °C temperature step which was chosen considering the temperature accuracy of the thermostats bath and experimental time.

For tail labelled liposomes, there is only a maximum 10% change of excimer intensity in 20 °C change of a wide room temperature range from 15 °C to 35 °C, while the US transducer heating was measured to be around only 1 °C in an hour (shown in Fig. 4.18a). So the tail labelled liposomes can be regarded as temperature stable from 15 °C to 35 °C. For head labelled liposomes, the maximum change is 39% from 15 °C to 35 °C. However, for the 1 °C change which might be induced by the US transducer, there is only 1.95% change of the excimer intensity. This is much lower than the fluorescence variation that was measured in Section 4.5. So head labelled liposomes can also be regarded as temperature stable during the acousto-fluorescence measurements.



(a) (b)

Figure 4.18: Change of buffer temperature with time at the focal zone induced by US. (a) Turn on US continuously for 3600 s; (b) Turn off US. The temperature was monitored using a datalogger (Pico TC-08, Pico Technology, St Neots, UK) located at the US focal zone and immersed in PBS buffer. There were no liposomes injected during the temperature measurement as the liposomes are not considered to affect the temperature due to its liquid core.

4.8 Discussion and conclusions

In conclusion, a new approach to enhancement of US mediated fluorescent signals based on the use of nanoscale excimer labelled liposomes has been proposed and demonstrated the first time and the possible mechanisms are analysed. An increase in excimer emission intensity following exposure to US was observed for all cases studied with the On-to-Off ratio of excimer intensity and rise rate being different for the PyPC and PyPE systems, and dependent on the applied US pressure and exposure time. The greatest On-to-Off ratio (130 %) and fastest rise time constant (0.33 s) are achieved through the use of the PyPC system. The possible mechanisms are related to the US induced inertial cavitation causing variation of the collision rate of pyrene molecules. In the PyPC system the main factor underlying the observed excimer fluorescence variation is considered to arise from the wagging of acyl chains which requires low energy and involves fast kinetic process. This is accompanied with lipid lateral diffusion, mechanisms also active in the PyPE system.

The use of PyPC and PyPE to prepare liposome make the depth and orientation of the fluorophore well defined. This makes it possible to study the influence of wagging of the acyl chains on the increased excimer intensity. It should be noted that this approach avoids high background fluorescence signals associated with imperfect quenching, characteristic of techniques based on fluorescent SQ and FRET. Further the use of excimer emissions avoids any background signal caused by direct transmission of the excitation signal due to the large red-shift of the excimer emission with no overlap with the monomer absorption band. This peak separation also avoids SQ of the excimer even at high particle and labelling concentrations [209].

A clinically valuable application of this contrast agent is the optical detection of tissue microenvironment such as oxygen concentration, pH, ion concentration and other properties which can indicate diseases. Since pyrene and its derivatives have a long excited state lifetime and are efficiently quenched by oxygen [210, 211], pyrene-labelled liposomes as an optical oxygen sensor to monitor tissue oxygen concentrations is a promising application. The linear regression curve obtained for emission intensity ra-

tio of excimer and monomer intensity with Cu^{2+} concentration [212] also suggests the possibility of using pyrene-labelled liposomes as a fluorosensor for detecting Cu^{2+} ions in living cells. Furthermore, there are other oxygen sensitive dyes (e.g. $Ru(phen)_3$ [213], $Ir(C_s)_2acac$, PdTPTBP [214]) or pH sensitive dyes (e.g. fluorescein, BCECF [215], 5,6-CF [216]) that may be encapsulated inside the liposome bilayer, and tuned for US sensitivity for use as contrast agents for high-resolution imaging of oxygen or pH.

Finally, it needs to be mentioned that applications of pyrene labelled liposomes are limited to superficial surface due to the short wavelength of the excitation light and pyrene excimer emission. For imaging at deeper tissue, excimers operating at longer wavelength need to be used. BODIPY-FL has been found to have excimer formation characteristics (excitation maximum around $\lambda = 500\,\text{nm}$, excimer emission maximum around $\lambda = 620\,\text{nm}$ [176, 217]). It has demonstrated several applications such as to study membrane traffic in living cells [218]. In addition, there are long-wavelength (650 nm - 900 nm) BODIPY fluorophores are being synthesized [19]. The use of such wavelengths can extend the applicability of the presented contrast agent to the investigation of deep tissue fluorescent imaging.

CHAPTER 5

US mediated near infrared fluorescence imaging in scattering phantom using FRET based nanoscale liposomes

5.1 Introduction

In Chapter 4 pyrene is used to help investigate the possibility of using excimer labelled liposomes as contrast agents for USMFT. However, the approach using pyrene as the excimer has some disadvantages in particular the excitation and emission wavelengths are too short for deep tissue imaging. Although there are a few new fluorophores that are able to form excimers at longer excitation and emission wavelengths such as BODIPY-FL (excitation maximum: $\lambda =\sim 500\,\text{nm}$, excimer emission maximum: $\lambda =\sim 620\,\text{nm}$) [176, 217] from the BODIPY family, perylene-3,4:9,10-bis(dicarboximide) (PDI) and its derivatives (excitation maximum: $\lambda =\sim 490\,\text{nm}$, excimer emission maximum: $\lambda =\sim 742\,\text{nm}$) [219], their availabilities are relatively limited. In this chapter another candidate contrast agent, i.e., the donor-acceptor labelled lipsomes, is investigated based on the FRET mechanism.

FRET (Fluorescence Resonance Energy Transfer) is a distance dependent transfer of energy from an excited donor fluorophore to a suitable acceptor fluorophore in a non-radiative way through long-range dipole-dipole interactions [137]. Different from radiative energy transfer, FRET occurs without the appearance of a photon. The theory supporting FRET is based on the concept of treating an excited fluorophore as an oscillating dipole that can undergo an energy exchange with a second dipole having a similar resonance frequency [220]. The donor fluorophore undergoes deexcitation from its excited electronic state by transferring energy to the acceptor [221]. There are a few criteria that must be satisfied in order for FRET to occur [222]. These are: (i) the emission spectrum of one fluorophore (donor) molecule must significantly overlap with the absorption spectrum of another fluorophore (acceptor), (ii) the donor and acceptor must be in close proximity to each other (typically 1 to 10 nanometer), (iii) the transition dipole moments of the donor and acceptor must not be perpendicular - otherwise the transfer efficiency is zero, irrespective of the donor-acceptor distance or the spectral overlap [31]. In fact the transition dipole orientation of the donor and acceptor must be approximately parallel to each other so that the acceptor dipole can be induced by the donor, (iv) the fluorescence lifetime of the donor molecule must be of sufficient duration to allow FRET to occur, (v) the donor should have a high quantum yield. Since FRET is highly sensitive to distance, it is one of the few tools available for measuring nanometer scale distances well below the optical resolution limit both *in vitro* and *in vivo* [223]. Application areas include structural analysis of macromolecules such as DNA [224, 225], proteins [226]), optical imaging of pH [227], proteases [227], hypoxia [228] in tumor microenvironment, fluorescence based chemical sensors and biosensors [222], monitoring of cellular events, molecular level interactions and drug release [229].

Considerable effort is focused on the search for new energy donor/acceptor pairs. Traditional FRET organic dyes (e.g. fluorescein, rhodamine, Cy3, and Cy5), as well as newer nanomaterials, such as semiconductor-based QDs, rare-earth doped nanocrystals and gold nanoparticles (AuNPs) [229], and genetically encoded dyes such as green fluorescent protein [230], can be used as FRET donors or acceptors. Therefore extend-

ing fluorophores from excimer to FRET pairs could expand greatly the choice of fluorophores to label the carrier of the contrast agent, since there are fewer fluorophores which have been found to have excimer formation characteristics than fluorophores which can form FRET pairs. Furthermore, similar to excimers, there is a large gap between the excitation maxima of the donor and the emission maxima of the acceptor for FRET. Therefore background induced by break-through of the excitation light and also autofluorescence can be greatly reduced. This is an advantage over techniques based on fluorescence self-quenching.

The carbocyanine dyes DiIC18(5) [1] (DiD; Life Technologies Ltd, CA, USA) and DiIC18(7) [2] (DiR; Life Technologies Ltd, CA, USA) have been used for FRET imaging to investigate *in vivo* drug release kinetics [231]. DiD (donor) and DiR (acceptor) were individually encapsulated into poly(ethyleneoxide)-b-polystyrene nanoparticles and the nanoparticles were coincubated with cancer cells. Increased FRET signals were observed suggesting release of DiD and DiR to cell membranes [231]. Compared with excimers such as pyrene, the spectral regions of DiD and DiR are largely red shifted to close or within the NIR window, with the excitation maximum of DiD and DiR at $\lambda =\sim 648\,\text{nm}$ and $\lambda =\sim 750\,\text{nm}$ respectively, emission maximum of DiD and DiR at $\lambda =\sim 670\,\text{nm}$ and $\lambda =\sim 780\,\text{nm}$ respectively, as shown in Fig. 5.1. As discussed in Chapter 1, light wavelengths located in the NIR window are very beneficial for deep tissue imaging due to reduced absorption, scattering, and tissue autofluorescence. Another point needs to be mentioned is that DiD or DiR has been used largely to track cells in live mice [232] and has not been reported to cause serious cytotoxicity at concentrations that provide strong, uniform staining [233].

In this chapter DiD and DiR are chosen as the FRET pair for a liposome contrast agent. DiD and DiR dyes are composed of two long hydrocarbon chains and a charged fluorophore head group, structure shown in Fig. 5.2. The two chains of DiD or DiR insert into lipid bilayers, while the fluorophore head is located at the bilayer surface and parallel to each other, as indicated by Fig 13.2.1 in literature [235]. This satisfies the orientation requirement of FRET. Once the chains are inserted into the bilayer, the dyes

[1] 1,1′-Dioctadecyl-3,3,3′,3′-Tetramethylindodicarbocyanine, 4-Chlorobenzenesulfonate Salt
[2] 1,1′-Dioctadecyl-3,3,3′,3′-Tetramethylindotricarbocyanine Iodide

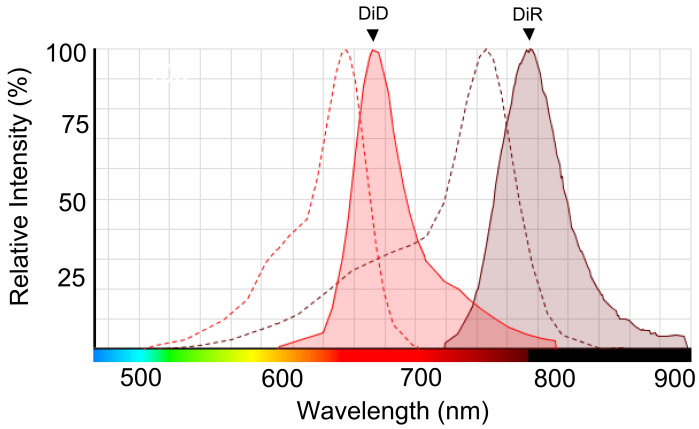
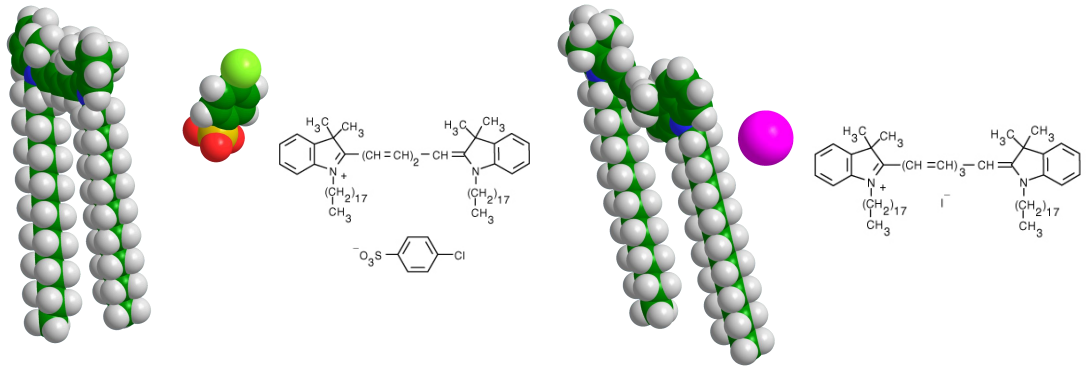


Figure 5.1: Fluorescence spectra of DiD and DiR. Excitation: dashed lines; Emission: straight lines (From 'Fluorescence SpectroViewer' of Life Technologies [234]).



(a) (b)

Figure 5.2: Molecule structures of (a) DiD and (b) DiR.

are rapidly and homogeneously distributed throughout the whole bilayer surface via lateral diffusion [231]. Therefore DiD and DiR are assumed to be evenly distributed inside the lipid bilayer at the equilibrium state (without application of US).

The schematic diagram of DiD-DiR labelled liposomes is shown in Fig. 5.3. Depending on the concentration there are likely four types of mechanisms existing in the lipid bilayer of the DiD-DiR labelled liposomes apart from the direct excitation and fluorescence emission of DiD or DiR, as shown in Fig. 5.3: 1) FRET from DiD to DiR; 2) self-quenching of DiD; 3) self-quenching of DiR; 4) FRET from DiD to DiR, and subsequent self-quenching of DiR. In 4) the energy transfers from DiD to DiR, and then to DiR dimers. Fluorescence self-quenching is a complex phenomenon and the mechanism is still not well understood. There are three fluorophore self-quenching mechanisms that have been discussed in literature and self-quenching is thought to be due to one or a combination of them [75]: 1) dye molecules form nonfluorescent dimers (dimerization); 2) FRET between monomers and eventually to nonfluorescent dimers (referred to as *transfer extinction* [75]); 3) collisional quenching by dye-dye interaction during the excited state lifetime. Since lateral diffusion of dyes is probably too slow to permit collisional quenching during the lifetime of the probes [236], self-quenching of DiD or DiR should be due mainly to the first two reasons.

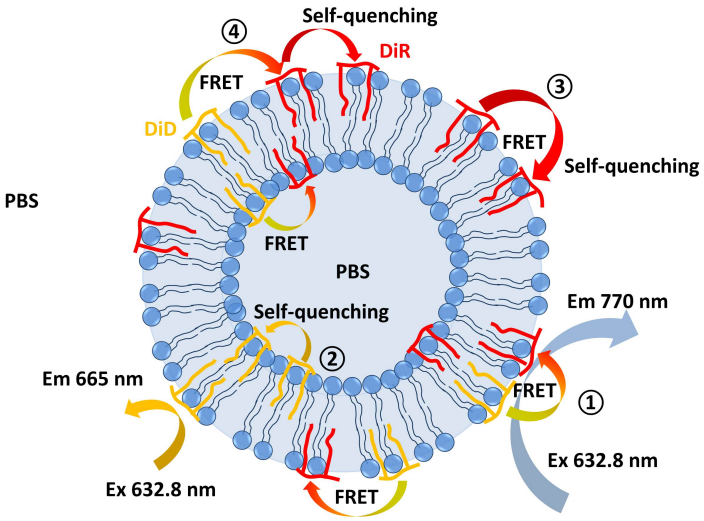


Figure 5.3: Schematic diagram of DiD-DiR labelled liposomes. Ex: excitation wavelength; Em: emission wavelength; PBS: Phosphate Buffered Saline; FRET: Fluorescence Resonance Energy Transfer.

In this chapter the emission spectra from liposomes labelled at a range of DiD and DiR concentrations are firstly measured to obtain information at equilibrium state (without applying US). The US dynamic characteristics are then studied by measuring and analyzing the time dependent fluorescence emission when applying US. The influence of US on the fluorescence variation is studied by varying US pressure and exposure time. Finally line scanning images of a tube buried deep inside a scattering phantom are obtained. Possible US mediated mechanisms are also discussed.

5.2 Preparation of DiD, DiD-DiR or DiR labelled liposomes

There are two methods to make DiD or DiR labelled liposomes described in the literature. The first is to introduce DiD or DiR at the time of formation of liposomes [237]. The other one is post addition of DiD or DiR after the liposomes have been formed [238, 239]. The second method is based on the extreme lipophilic characteristics of carbocyanine dyes and can be advantageous when liposomes have been manufactured [238]. However, due to the low speed of transbilayer movement (half-times in the order of days [196]), the DiD and DiR are probably only located in the outer layer which is not as efficient as labelling the fluorophores on both of the layers. From this consideration the first method is adopted in this study.

DiD, DiD-DiR or DiR labelled liposomes were produced based on the freeze-thaw extrusion method used in Chapter 4. DiD and DiR were reconstituted at 2 mg/ml in ethanol respectively to prepare stock solutions. The prepared DiD or DiR solution was mixed with DPPC phospholipids and the solvent was evaporated with oxygen-free nitrogen gas (BOC Group plc, Manchester, UK). The other procedures are the same as described previously in Section 4.2 of Chapter 4. Three types of sample were made in this study: DiD-DiR labelled liposomes (various concentrations, various ratios of DiD to DiR), DiD only liposomes (various concentrations), and DiR labelled liposomes (various concentrations). DiD only liposomes and DiR labelled liposomes were made as donor-only controls and acceptor-only controls respectively to indicate fluorescence intensity without FRET and monitor direct excitation of the acceptor fluorophore. For

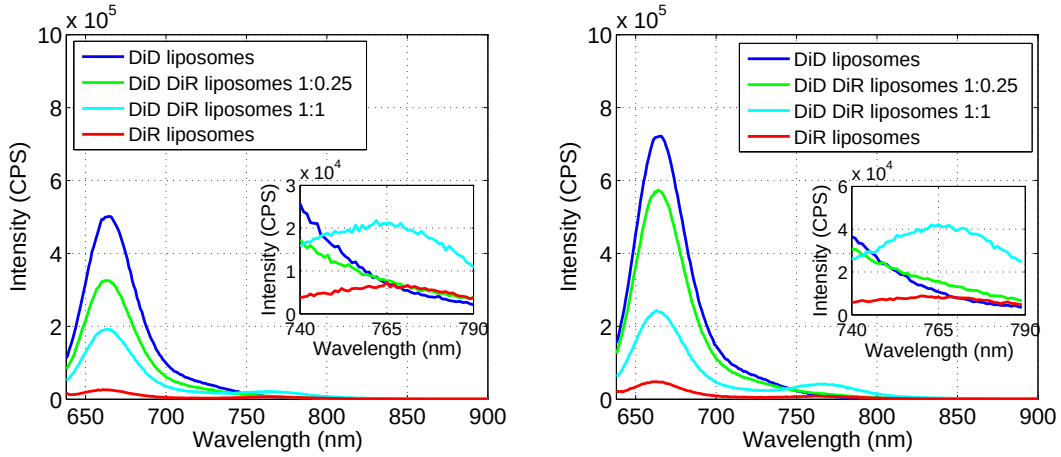
all the measurements the lipid concentration was 1.28 mM which was 10 times dilution of the prepared liposome solution.

5.3 Measurements of emission spectra

Liposomes with six different DiD labelling concentrations (0.05 mol%, 0.1 mol%, 0.25 mol%, 0.5 mol%, 0.75 mol%, and 1 mol%) at four different ratios of DiD and DiR (1:0, 1:0.25, 1:1, and 0:1) were made using the method described in Section 5.2. The concentration is the molar percentage of the amount of DiD or DiR to total amount of materials used (sum of DiD, DiR and DPPC). These concentrations were chosen based on the investigation of dose dependency of liposomal stability, in which the suggested concentration to minimize the disruptive effects caused by integration of the carbocyanine dyes on the liposomal membrane is around 10 ug/ml dye to 2.5 mg/ml liposomal-lipid [238], corresponding to a concentration in molar percentage of 0.3 mol%. To obtain information at the equilibrium state, the spectra of these liposomes were measured using a spectrofluorometer (Fluoromax-4, Horiba Scientific, Kyoto, Japan) following excitation at $\lambda = 633$ nm with a 2 nm slit width, results are shown in Fig. 5.4. The emission was collected from $\lambda = 638$ nm to $\lambda = 900$ nm, using a 2 nm slit width. The emission spectrum of each sample was measured repetitively for five times. The spectra are essentially the same therefore no average was performed.

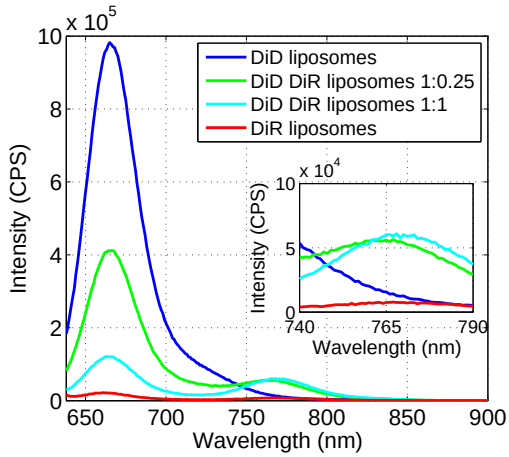
The detected fluorescence from these liposomes can be considered as from fluorophores incorporated in the lipid bilayer of the liposomes only, rather than from the surrounding buffer for two reasons. First, DiD and DiR have the characteristic that they are highly fluorescent in lipid environments but are weakly fluorescent in water. Second, the lipid can be regarded to be only distributed in the lipid bilayer of the unilamellar liposomes and there is very limited self aggregation of polar lipid molecules in other structures in the buffer. This is benefited from the freeze-thaw extrusion liposome preparation method, as suggested by the freeze-fracture electron micrographs in literature [177].

Fig. 5.4 shows that in the DiD only liposomes strong peaks are seen spanning the DiD

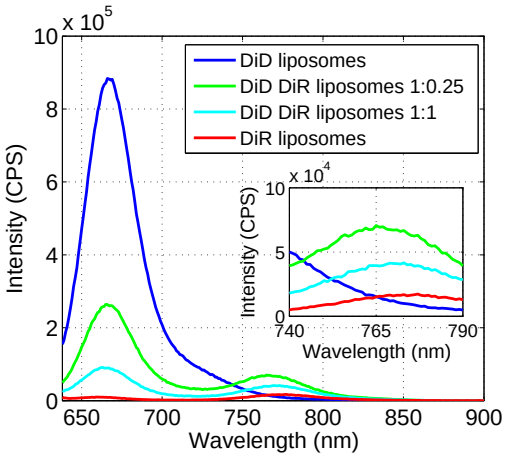


(a) 0.05 mol%

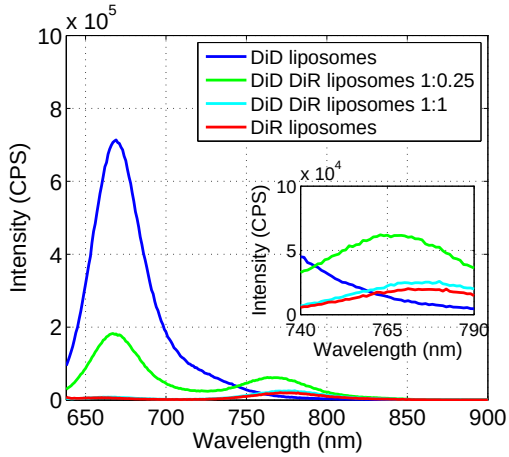
(b) 0.1 mol%



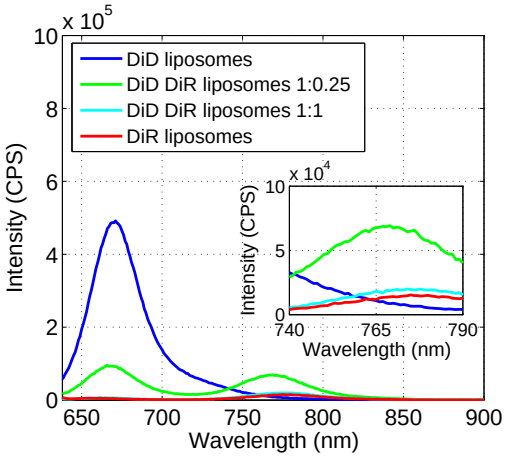
(c) 0.25 mol%



(d) 0.5 mol%



(e) 0.75 mol%



(f) 1 mol%

Figure 5.4: Emission spectrums of DiD only liposomes, DiD-DiR labelled liposomes with DiD to DiR ratio 1 to 1, DiD-DiR labelled liposomes with DiD to DiR ratio 1 to 0.25, and DiR labelled liposomes at six different DiD labelling concentrations. The inset graphs show spectra at DiR emission wavelength between 740 nm and 790 nm. Excitation wavelength: $\lambda = 633$ nm. CPS: counts per second.

emission wavelength band (around 640 nm - 690 nm, center wavelength: ∼664 nm). Due to the overlap of the DiD excitation wavelength with the absorption spectrum of DiR, there is also low emission at DiR wavelength (around 740 nm - 790 nm, center wavelength: ∼766 nm) arising from the DiR only liposomes. This cross-talk is expected to exist in any liposomes containing DiR and was corrected later through calculation of N_{FRET} (see Eq. 5.4.9 and Eq. 5.4.13 in Section 5.4.2). The spectra of DiD-DiR labelled liposomes show clear intensity decrease at the DiD emission band compared with DiD only liposomes. This decrease of DiD is known as *donor quenching*. The donor quenching of DiD-DiR labelled liposomes with DiD to DiR ratio 1:1 is bigger than that of liposomes with ratio 1:0.25, suggesting higher FRET for the former as a result of a higher concentration of the acceptor.

Comparing DiD-DiR labelled liposomes 1:1 with DiR labelled liposomes that have the same amount of DiR, Fig. 5.4b, Fig. 5.4c, and Fig. 5.4d show the fluorescence emission at DiR wavelength ($\lambda \approx 766$ nm) from liposomes with a DiD to DiR ratio 1:1 is higher. The increased acceptor emission (known as *sensitized emission*) is because DiR in DiD-DiR labelled liposomes receives more energy than DiR in DiR only liposomes due to FRET. For the cases of higher DiR concentration of 0.75 mol% and 1 mol%, Fig. 5.4e and Fig. 5.4f show very close amount of fluorescence emission at DiR wavelength from the two types of liposomes, suggesting strong self-quenching of DiR at higher concentrations.

Comparing DiD-DiR labelled liposomes 1:1 with DiD-DiR labelled liposomes 1:0.25, Fig. 5.4a and Fig. 5.4b show that the sensitized emission ($\lambda \approx 766$ nm) from the former is higher than the latter. This is straightforward since there are higher amounts of DiR for the former. However, with increase of concentration it was observed that the sensitized emission from DiD-DiR labelled liposomes 1:0.25 is approaching DiD-DiR labelled liposomes 1:1 and even goes beyond the latter, as shown in Fig. 5.4c-f. This suggests again a stronger self-quenching of DiR at higher DiR concentrations. It is interesting to see that at 0.5 mol% (Fig. 5.4d), 0.75 mol% (Fig. 5.4e) and 1 mol % (Fig. 5.4f), fluorescence emissions both at DiD and DiR wavelength bands from DiD-DiR labelled liposomes with a ratio of 1:1 are much lower than that from DiD-DiR labelled liposomes

with a ratio of 1:0.25. As discussed in Section 5.1 self-quenching of DiR should be due to a combination of dimer formation and resonance energy transfer to nonfluorescent dimers.

To further understand the concentration dependence of energy transfer in the fluorophore labelled liposomes, fluorescence emission intensity at DiD wavelength (658 nm - 695 nm) and DiR wavelength (755 nm - 816 nm) were extracted from the spectra and plotted against labelling concentration. Fig. 5.5a, b, c, and d show fluorescence emission intensity at DiD wavelength from DiD only liposomes, DiR wavelength from DiR only liposomes, DiD wavelength from DiD-DiR labelled lipsomes, and DiR wavelength from DiD-DiR labelled liposomes respectively. For the DiD-DiR labelled liposomes the two ratios of 1:1 and 1:0.25 were used. The integrated wavelength ranges are based on the spectral characteristics of the optical filters used in the acousto-fluorescence setup which will be described later in Section 5.5.

A similar trend was observed for these cases: the fluorescence emission decreased following an initial increase with increase of labelling concentration, suggesting stronger self-quenching at higher concentration. An exception is that in Fig. 5.5d the DiR emission is almost a constant when the DiD concentration reaches 0.5 mol%. This suggests self-quenching of DiR from DiD-DiR liposomes with ratio 1:0.25 is less severe due to the lower concentration of DiR compared with DiD-DiR liposomes with the ratio 1:1. Interestingly it was found that the peak concentration for detection at DiD emission wavelength of DiD-DiR labelled liposomes ($\sim$0.1 mol%) is smaller than that for DiD only liposomes ($\sim$0.25 mol%). Similarly the peak concentration for detection at DiR emission wavelength of DiD-DiR labelled liposomes ($\sim$0.25 mol%) is smaller than that for DiR only liposomes ($\sim$0.75 mol%). This suggests the coexistence of FRET and self-quenching in DiD-DiR liposomes. It should be mentioned here that the peak concentration of DiR is found to be around three times bigger than the peak concentration of DiD. This suggests that self-quenching is more likely for DiD compared with DiR. This might be due to longer Förster distance, or easier dimerization of DiD-DiD compared with dimerization of DiR-DiR. The Förster distance of DiI-DiO [3] was determined to be

[3] DiOC16(3) (3,3′-Dihexadecyloxacarbocyanine Perchlorate)

57 Å [240], which can provide an approximate reference to Förster distances of DiD-DiD and DiR-DiR due to similar structures of the four carbocyanine dyes.

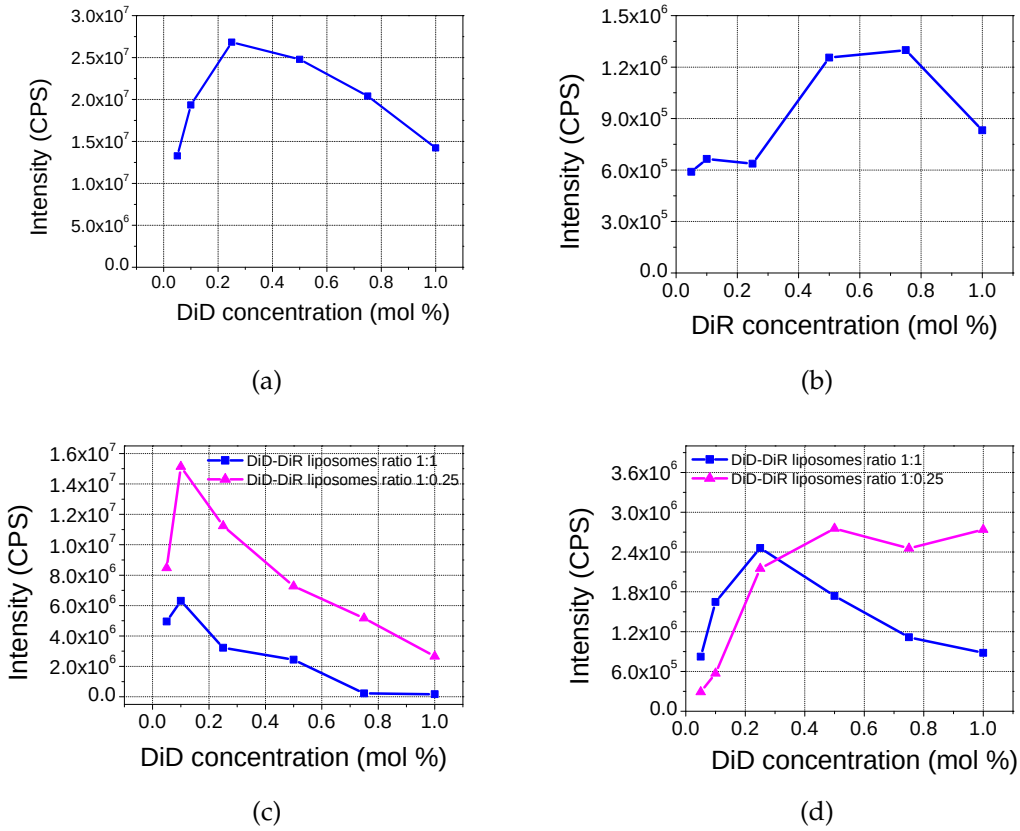


Figure 5.5: Influence of concentration on fluorescence emission intensity at (a) DiD emission wavelength of DiD only liposomes; (b) DiR emission wavelength of DiR only liposomes; (c) DiD emission wavelength of DiD-DiR labelled liposomes; (d) DiR emission wavelength of DiD-DiR labelled liposomes. Excitation wavelength for (a), (c), and (d) is at $\lambda = 633\,\text{nm}$; for (b) is at $\lambda = 710\,\text{nm}$. DiD emission wavelength: 658 nm - 695 nm; DiR emission wavelength: 755 nm - 816 nm. CPS: counts per second.

5.4 Quantitative study of FRET and self-quenching

5.4.1 Calculation of FRET and self-quenching efficiency

To investigate FRET and self-quenching quantitatively a 'normalized intensity' is defined as the averaged fluorescence emission intensity per unit labelling concentration of the fluorophore. It is calculated as the ratio of the measured fluorescence intensity with the labelling concentration of the corresponding fluorophore (intensity/labelling concentration, unit: CPS/mol %). Dividing the normalized intensity by the molar amount

of the lipids used, the denominator of the defined normalized intensity only leaves the total amount of the fluorophores. Since the same amount of lipids was used in all cases, the defined normalized intensity indicates the averaged fluorescence emission intensity per unit fluorophore.

DiD based FRET and self-quenching efficiency

The normalized intensity at DiD emission wavelength from the DiD only liposomes and DiD-DiR labelled liposomes were calculated and shown in Fig. 5.6. The green auxiliary line is an extension of the normalized intensity at DiD wavelength from DiD only liposomes with 0.05 mol% DiD concentration ($\bar{I}_{DiD|DiD0.05mol\%}$) along concentration axis. It can be seen that with increase of concentration, the normalized DiD emission intensity from the DiD only liposomes decreases. This suggests that self-quenching of DiD exists even at the lowest studied concentration of 0.05 mol% and becomes more significant at higher concentration.

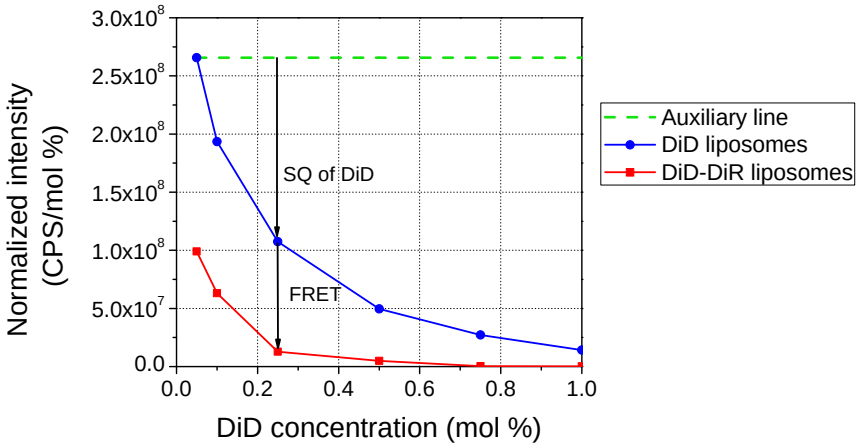


Figure 5.6: Normalized fluorescence emission intensity at DiD wavelength (658 nm - 695 nm). CPS: counts per second.

Without self-quenching of DiD the normalized intensity of DiD emission from DiD only liposomes is expected to be a straight line parallel with the concentration axis as indicated by the green auxiliary line in Fig. 5.6. This is because in this case the fluorescence emission intensity from a unit fluorophore is independent of concentration. However due to the existence of self-quenching the normalized intensity decreases. Therefore the decreasing percentage can be used to estimate the self-quenching effi-

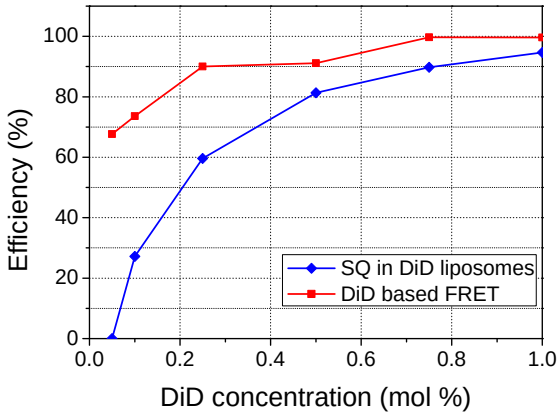


Figure 5.7: SQ and FRET efficiency calculated based on fluorescence intensity at DiD emission wavelength.

ciency of DiD in DiD only liposomes (SQ_{DiD}), namely:

$$SQ_{DiD} = \frac{\overline{I}_{DiD|DiD0.05mol\%} - \overline{I}_{DiD|DiD}}{\overline{I}_{DiD|DiD0.05mol\%}} \tag{5.4.1}$$

where $\overline{I}_{DiD|DiD}$ represents the same quantity as $\overline{I}_{DiD|DiD0.05mol\%}$ but for other DiD concentrations.

The normalized intensity can also help analyzing the FRET efficiency. Due to FRET the emission intensity at the DiD wavelength range from DiD-DiR labelled liposomes is reduced compared with that from DiD only liposomes. Therefore the DiD based FRET efficiency ($FRET_{DiD}$) can be estimated from the fractional decrease, namely:

$$FRET_{DiD} = \frac{\overline{I}_{DiD|DiD} - \overline{I}_{DiD|DiD-DiR} + \overline{I}_{DiD|DiR}}{\overline{I}_{DiD|DiD}} \tag{5.4.2}$$

where $\overline{I}_{DiD|DiD-DiR}$ and $\overline{I}_{DiD|DiR}$ are the normalized intensity at DiD emission wavelength from DiD-DiR labelled liposomes and DiR only liposomes respectively. $\overline{I}_{DiD|DiR}$ in Eq. 5.4.2 is used for correction of the fluorescence at donor emission band from the acceptor. This FRET metric has long been in use in biomembrane FRET studies [240]. The calculated self-quenching efficiency and DiD based FRET efficiency are shown in Fig. 5.7. As expected both of the two increase with increase of concentration. At 1 mol% the FRET and self-quenching efficiency are 99.6 % and 94.6 % respectively, suggesting occurrence of high levels of FRET and self-quenching.

It should be noted that it is assumed that no self-quenching exists in liposomes with the lowest concentration of 0.05 mol% for estimation of the self-quenching efficiency of DiD. The auxiliary line indicating fluorescence emission intensity from a unit fluorophore was calculated using 0.05 mol% as a reference. As self-quenching was detected at 0.05 mol% the real fluorescence emission intensity from a unit fluorophore is predicted to be higher than that used in this analysis. The effect of this on efficiency calculations would be a systematic shift in the self-quenching efficiency to higher values than those in Fig.5.7. It should also be noted that the assumption of the flat auxiliary line is based on a linear process occurring with factors such as the reabsorption by the sample, sample thickness, sample scattering all being ignored. In addition, it is assumed that self-quenching efficiencies of DiD in DiD-DiR labelled liposomes and DiD only liposomes are the same. The existence of DiR fluorophores might change the distribution of DiD fluorophores in the lipid bilayer but its influence on self-quenching efficiency might be averaged out therefore is not considered in this analysis.

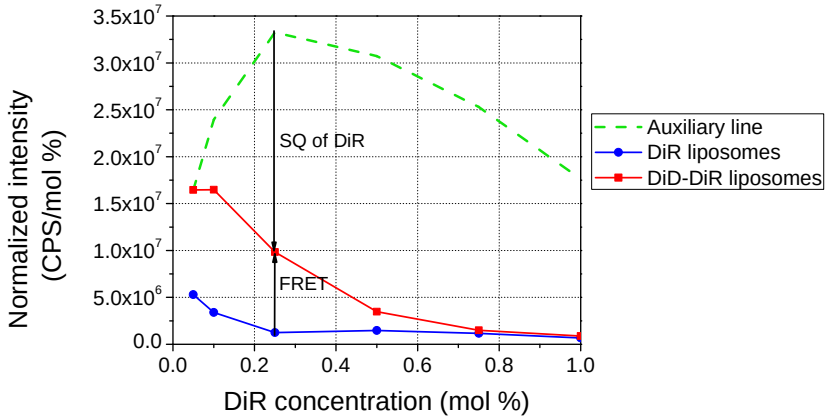


Figure 5.8: Normalized fluorescence emission intensity at DiR wavelength (755 nm - 816 nm). CPS: counts per second.

DiR based FRET and self-quenching efficiency

In this section acceptor (DiR) based FRET and self-quenching efficiency are calculated to evaluate energy transfer efficiency at equilibrium state. The normalized intensity at DiR emission wavelength from the DiR only liposomes and DiD-DiR labelled liposomes following excitation at $\lambda = 633$ nm was firstly calculated and shown in Fig. 5.8. The green baseline is based on experimentally measured DiD emission intensity from

DiD only liposomes. Without self-quenching of DiR and DiD the normalized intensity for DiR emission from DiD-DiR liposomes should increase when the concentration increases. This is because with closer proximity the fluorescence emission intensity from unit DiR is expected to increase due to stronger FRET in this case. However, it was observed in Fig. 5.8 (red curve) that the normalized DiR emission intensity from DiD-DiR liposomes decreases. This must be due to self-quenching of DiR, to directly reduce DiR emission, and self-quenching of DiD, to indirectly reduce DiR emission via reduction in FRET. Note also that the normalized intensity at 0.05 mol% and 0.1 mol% is similar to each other. This is likely to be a consequence of the interactions of self-quenching and FRET: self-quenching of DiD and DiR has a negative effect on the DiR emission intensity, however this is compensated by FRET which has a positive effect on the DiR emission intensity. To calculate self-quenching of DiR the auxiliary baseline was plotted and it is based on the assumption that the effect of DiD to DiR is similar to excitation light. Therefore the baseline ($\overline{I}_{baseline}$) is scaled by considering the dependence of DiD emission intensity on concentration, as calculated below:

$$\overline{I}_{baseline} = \frac{\overline{I}_{DiR|DiD-DiR0.05mol\%} I_{DiD|DiD}}{I_{DiD|DiD0.05mol\%}} \tag{5.4.3}$$

where $\overline{I}_{DiR|DiD-DiR0.05mol\%}$ is the normalized DiR emission intensity from DiD-DiR liposomes at 0.05 mol%, $I_{DiD|DiD}$ is the absolute DiD emission intensity from DiD liposomes, and $I_{DiD|DiD0.05mol\%}$ is the absolute DiD emission intensity from DiD liposomes at 0.05 mol%. The self-quenching efficiency of DiR (SQ_{DiR}) is then calculated as:

$$SQ_{DiR} = \frac{\overline{I}_{baseline} - \overline{I}_{DiR|DiD-DiR}}{\overline{I}_{baseline}} \tag{5.4.4}$$

The increase of the normalized intensity at DiR emission wavelength from DiD-DiR liposomes as compared to that from DiR only liposomes is owing to the existence of DiD providing energy for DiR through FRET. The DiR based FRET efficiency ($FRET_{DiR}$) can be estimated from the increased percentage of the normalized intensity, namely [241]:

$$FRET_{DiR} = \frac{\epsilon_{DiRat633nm}}{\epsilon_{DiDat633nm}} \frac{\overline{I}_{DiR|DiD-DiR} - \overline{I}_{DiR|DiR} - \overline{I}_{DiR|DiD}}{\overline{I}_{DiR|DiR}} \tag{5.4.5}$$

where $\epsilon_{DiRat633nm}/\epsilon_{DiDat633nm}$ is the ratio of the extinction coefficient of DiR only liposomes ($\epsilon_{DiRat633nm}$) and DiD only liposomes ($\epsilon_{DiDat633nm}$) respectively at $\lambda = 633\,\text{nm}$. Based on Lambert-Beer's Law for the same amount of samples and path length of the radiation beam used for recording the absorption spectrum, $\epsilon_{DiRat633nm}/\epsilon_{DiDat633nm} = A_{DiR}/A_{DiD}$, where A_{DiR} and A_{DiD} are the absorbance of DiR only liposomes and DiD only liposomes respectively at $\lambda = 633\,\text{nm}$. Therefore $\epsilon_{DiRat633nm}/\epsilon_{DiDat633nm}$ can be obtained from absorbance measurements of A_{DiR} and A_{DiD} (The measured absorbance spectra at various concentrations can be found in Appendix D). $\bar{I}_{DiR|DiD-DiR}$, $\bar{I}_{DiR|DiR}$, and $\bar{I}_{DiR|DiD}$ are the normalized DiR emission intensity from DiD-DiR labelled liposomes, DiR only liposomes, and DiD only liposomes respectively. $\bar{I}_{DiR|DiD}$ is included in Eq. 5.4.5 for correction of the fluorescence emission of donor at acceptor wavelength. The calculated self-quenching efficiency of DiR in DiD-DiR labelled liposomes and DiR based FRET efficiency are shown in Fig. 5.9.

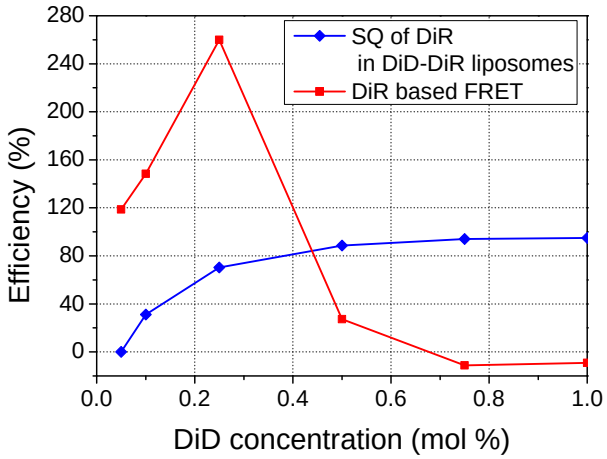


Figure 5.9: self-quenching and FRET efficiency calculated based on fluorescence intensity at DiR emission wavelength.

The self-quenching efficiency of DiR in DiR only liposomes was also calculated using a similar method as Eq. 5.4.1, as shown in Fig. 5.10. The self-quenching efficiency of DiR in DiD-DiR liposomes was also plotted in Fig. 5.10. It can be seen that the two self-quenching efficiencies are close to each other but not exactly the same (less than 12.4 % difference). Different activities exist in the two types of liposomes. For DiR only liposomes the excitation wavelength is 710 nm and there exists self-quenching of DiR only. For DiD-DiR liposomes the excitation wavelength is 633 nm, and the energy transfer in-

volved is more complicated - there exists FRET, self-quenching of DiD, self-quenching of DiR following FRET, and self-quenching of DiR following direct excitation.

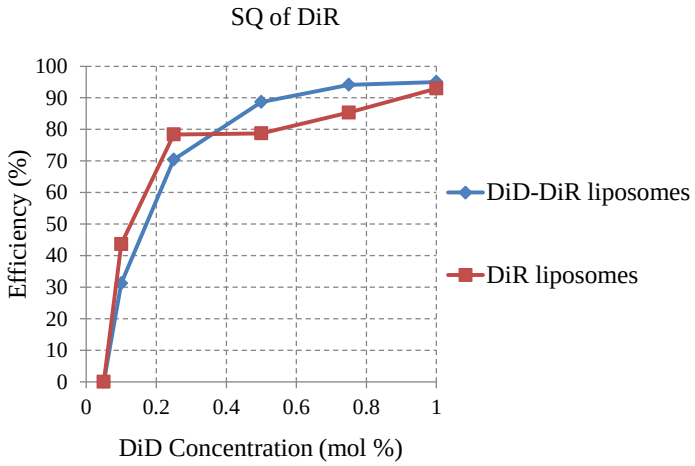


Figure 5.10: Comparison of self-quenching of DiR for DiD-DiR liposomes with DiR only lipsomes.

5.4.2 Calculation of $FRET1$ and N_{FRET}

In the spectrum measurements there are detection of donor fluorescence with the acceptor emission filter and detection of acceptor fluorescence with the donor emission filter (e.g. the fluorescence emission at the DiD emission wavelength peak at around $\lambda = 667\,\text{nm}$ from DiR labelled liposomes, seen in Fig. 5.4). To correct this cross-talk, $FRET1$ [242] for DiD-DiR labelled liposomes is defined as:

$$FRET1 = \frac{Ff - (Fd/Dd)Df - A\bar{f}a[(Fa/Aa) - (Fd/Dd)(Da/Aa)]}{G[1 - (Da/Fa)(Fd/Dd)]} \tag{5.4.6}$$

where

$$A\bar{f}a = \frac{Af - (Ad/Fd)/Ff}{1 - (Fa/Aa)(Ad/Ff)} \tag{5.4.7}$$

G is a constant and can be assigned as $G = 1$ [242]. Ff, Fd, Dd, Df, $A\bar{f}a$, Af, Fa, Aa, and Da are symbols showing the fluorescence emission intensity from a specific sample (DiD only liposomes, DiR only liposomes, or DiD-DiR labelled liposomes) at a specific detection wavelength range (DiD emission band or DiR emission band) excited

by either $\lambda = 633\,\text{nm}$ or $\lambda = 710\,\text{nm}$. To express these terms more clearly in the context of this work they are renamed and explained in Table 5.1. Since Ad was measured to be zero in this work, Eq. 5.4.7 can be simplified as:

$$\bar{Afa} = Af \tag{5.4.8}$$

Table 5.1: Symbols and their interpretation.

Symbols	Re-named symbols	Meaning
Ff	$I_{DiR\|DiD-DiR(\lambda_{633nm})}$	Emission at DiR wavelength from DiD-DiR labelled liposomes excited at $\lambda = 633\,\text{nm}$
Fd	$I_{DiR\|DiD(\lambda_{633nm})}$	Emission at DiR wavelength from DiD only liposomes excited at $\lambda = 633\,\text{nm}$
Dd	$I_{DiD\|DiD(\lambda_{633nm})}$	Emission at DiD wavelength from DiD only liposomes excited at $\lambda = 633\,\text{nm}$
Df	$I_{DiD\|DiD-DiR(\lambda_{633nm})}$	Emission at DiD wavelength from DiD-DiR labelled liposomes excited at $\lambda = 633\,\text{nm}$
Af	$I_{DiR\|DiD-DiR(\lambda_{710nm})}$	Emission at DiR wavelength from DiD-DiR labelled liposomes excited at $\lambda = 710\,\text{nm}$
Fa	$I_{DiR\|DiR(\lambda_{633nm})}$	Emission at DiR wavelength from DiR only liposomes excited at $\lambda = 633\,\text{nm}$
Aa	$I_{DiR\|DiR(\lambda_{633nm})}$	Emission at DiR wavelength from DiR only liposomes excited at $\lambda = 633\,\text{nm}$
Da	$I_{DiD\|DiR(\lambda_{633nm})}$	Emission at DiD wavelength from DiR only liposomes excited at $\lambda = 633\,\text{nm}$
Ad	$I_{DiR\|DiD(\lambda_{710nm})}$	Emission at DiR wavelength from DiD only liposomes excited at $\lambda = 710\,\text{nm}$

Although all types of cross-talk are corrected in $FRET1$, it needs to be normalized for the concentrations of donor and acceptor to make it comparable among different measurements. N_{FRET} has therefore been defined as a reliable and global calculation method for FRET quantification [243]. It is a normalized quantity only dependent on the FRET efficiency and complex percentage P [243]. Here a complex means an interacting pair of donor and acceptor and P is calculated as two-fold of the percentage of complexes exhibiting FRET to total donors and acceptors. With the DiD to DiR ratio 1:1, it is a reasonable assumption that P is the same constant for all the samples studied. Therefore N_{FRET} is only dependant on the FRET efficiency and can be used to compare

different samples with different concentrations. N_{FRET} was calculated as:

$$N_{FRET} = \frac{FRET1}{\sqrt{I_{DiR|DiD-DiR(\lambda_{710nm})} \times I_{DiD|DiD-DiR(\lambda_{633nm})}}} \tag{5.4.9}$$

In the literature it is usually supposed that $Da = 0$ because of the low emission at donor wavelength from the acceptor, $FRET1$ defined in Eq. 5.4.6 can thus be simplified as follows with a new symbol $nFRET$:

$$nFRET = I_{DiR|DiD-DiR(\lambda_{633nm})} - I_{DiD|DiD-DiR(\lambda_{633nm})} \times a - I_{DiR|DiD-DiR(\lambda_{710nm})} \times b \tag{5.4.10}$$

This quantity is always referred to as *net FRET* [244]. a and b are correction coefficients of the percentage of DiD and DiR bleed-through respectively and are calculated as:

$$a = \frac{I_{DiR|DiD(\lambda_{633nm})}}{I_{DiD|DiD(\lambda_{633nm})}} \tag{5.4.11}$$

$$b = \frac{I_{DiR|DiR(\lambda_{633nm})}}{I_{DiR|DiR(\lambda_{710nm})}} \tag{5.4.12}$$

Therefore N_{FRET} can also be simplified with the new symbol N_{FRETs}:

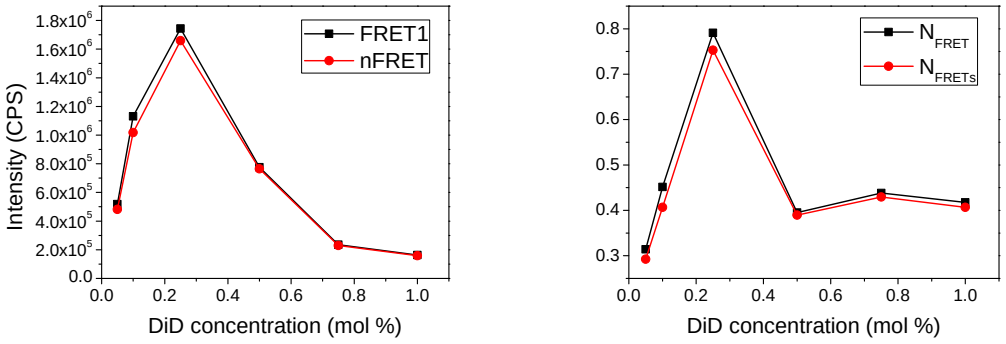
$$N_{FRETs} = \frac{nFRET}{\sqrt{I_{DiR|DiD-DiR(\lambda_{710nm})} \times I_{DiD|DiD-DiR(\lambda_{633nm})}}} \tag{5.4.13}$$

$FRET1$, N_{FRET}, a, b, $nFRET$ and N_{FRETs} are thus calculated for all of the concentrations studied and listed in Table 5.2. It can be seen both a (bleed-through of DiD) and b (bleed-through of DiR) increase with increase of the concentration. The bleed-through of DiD is very low ($a \in [0.019\ 0.026]$). This is because DiD produces very low fluorescence emission at $\lambda = 766\,\text{nm}$. However, the bleed-through of DiR is much higher ($b \in [0.448\ 0.801]$), which is due to the wide absorption spectrum of DiR. The quantities expressing FRET corrected for cross-talk are also shown in Fig. 5.11. It can be seen that $FRET1$, $nFRET$, $NFRET$ and N_{FRETs} are all the highest at concentration 0.25 mol%. $nFRET$ and N_{FRET} are close with $FRET1$ and N_{FRETs} respectively suggesting the assumption $Da = 0$ is reasonable - fluorescence emission intensity from DiR at

DiD emission band when excited at 633 nm is very low and can be ignored.

Table 5.2: Measurements of FRET for DiD-DiR labelled liposomes.

Concentration (mol%)	$FRET1$	N_{FRET}	a	b	$nFRET$	N_{FRETs}
0.05	5.18×10^5	0.31	0.019	0.448	4.82×10^5	0.29
0.1	1.13×10^6	0.45	0.019	0.511	1.02×10^6	0.41
0.25	1.74×10^6	0.79	0.020	0.489	1.66×10^6	0.75
0.5	7.76×10^5	0.40	0.021	0.583	7.65×10^5	0.39
0.75	2.35×10^5	0.44	0.024	0.677	2.30×10^5	0.43
1	1.62×10^5	0.42	0.026	0.801	1.58×10^5	0.41



(a) (b)

Figure 5.11: Quantities corrected for cross-talk. (a) $FRET1$ and $nFRET$; (b) N_{FRET} and N_{FRETs}. CPS: counts per second.

It should be noted that the normalized emission intensity at DiD wavelength from DiD-DiR labelled liposomes shown as the red curve in Fig.5.6 is the result of both FRET and self-quenching of DiD. Similarly the normalized DiR emission intensity from DiD-DiR labelled liposomes shown as the red curve in Fig.5.8 is the result of both FRET, self-quenching of DiR, and self-quenching of DiD. Therefore these two curves can indicate the dependence of the intensity from unit fluorophore on concentration. In Section 5.5 these two curves are used to help analyse the intensity change induced by US.

5.5 Characterization of fluorophores labelled liposomes

5.5.1 Measurements of US mediated fluorescence variation

In this section the fluorophore labelled liposomes are characterized in an enclosed tube located inside deionized water. 0.1 mol% DiD-DiR labelled liposomes, 0.1 mol% DiD only liposomes, 0.5 mol% DiD-DiR labelled liposomes, 0.5 mol% DiD only liposomes

are chosen for characterization based on the calculation of FRET and SQ in Section 5.4. US might not be able to induce a detectable fluorescence variation if the concentration is too high or too low. For the former case FRET and self-quenching might be too strong to be reduced, while for the latter case FRET and self-quenching might be too weak to be induced. From Fig. 5.6 and Fig. 5.8 it can be seen 0.1 mol % and 0.5 mol % are concentrations suitable for detection at both DiD emission wavelength and DiR emission wavelength.

The setup is shown in Fig. 5.12. A syringe pump (KD Scientific Inc. Holliston, MA, USA) was used to inject the sample solution through a light transparent Fluorinated Ethylene Propylene (FEP, Adtech Polymer Engineering Ltd., Glos, UK) tube with inner diameter 1.1 mm, and 0.2 mm wall thickness. The solution was kept static during measurements. A focused US transducer (2.25 MHz) was used and it was driven by a signal generator (AFG 3022, Tektronix, Beaverton, USA) and a radio frequency power amplifier (Amplifier Research 75A250A, Souderton, USA). The US focal zone and the laser light were aligned to overlap the tube at the same position using a 0.2 mm diameter needle hydrophone (SN1700, Precision acoustics Ltd. Dorchester, UK). The beam from a $\lambda = 632.8$ nm red laser (5 mW power, Melles Griot, Carlsbad, CA, USA) was expanded 10 times (original diameter 1 mm) by a beam expander to expose more liposomes to the light. To reduce bleed-through of the excitation light, its direction was adjusted by two mirrors so that it is not directly detected. The detection system is similar to that used in Fig. 4.5 of Chapter 4. The difference is that PMT9107B is replaced by PMT9136B (ET Enterprises Ltd, Uxbridge, UK), which has an extended infrared sensitivity. The emission filters are also changed according to wavelength - for detection at DiD wavelength, a bandpass filter with a central wavelength of 676 nm (FF01-676/37-25, Semrock, New York, USA, transmission band: 658 nm-695 nm) was used; for detection at DiR wavelength a bandpass filter with a central wavelength of 764 nm (#87-759, Edmund Optics, York, UK, transmission band: 754 nm-816 nm) was used. Apart from these two filters a notch filter with a center wavelength of 632 nm (NT63-347, Edmund Optics, York, UK, reflection band: 623 nm-639 nm) was used to reject more excitation light. The spectra of the filters can be found in Appendix C.

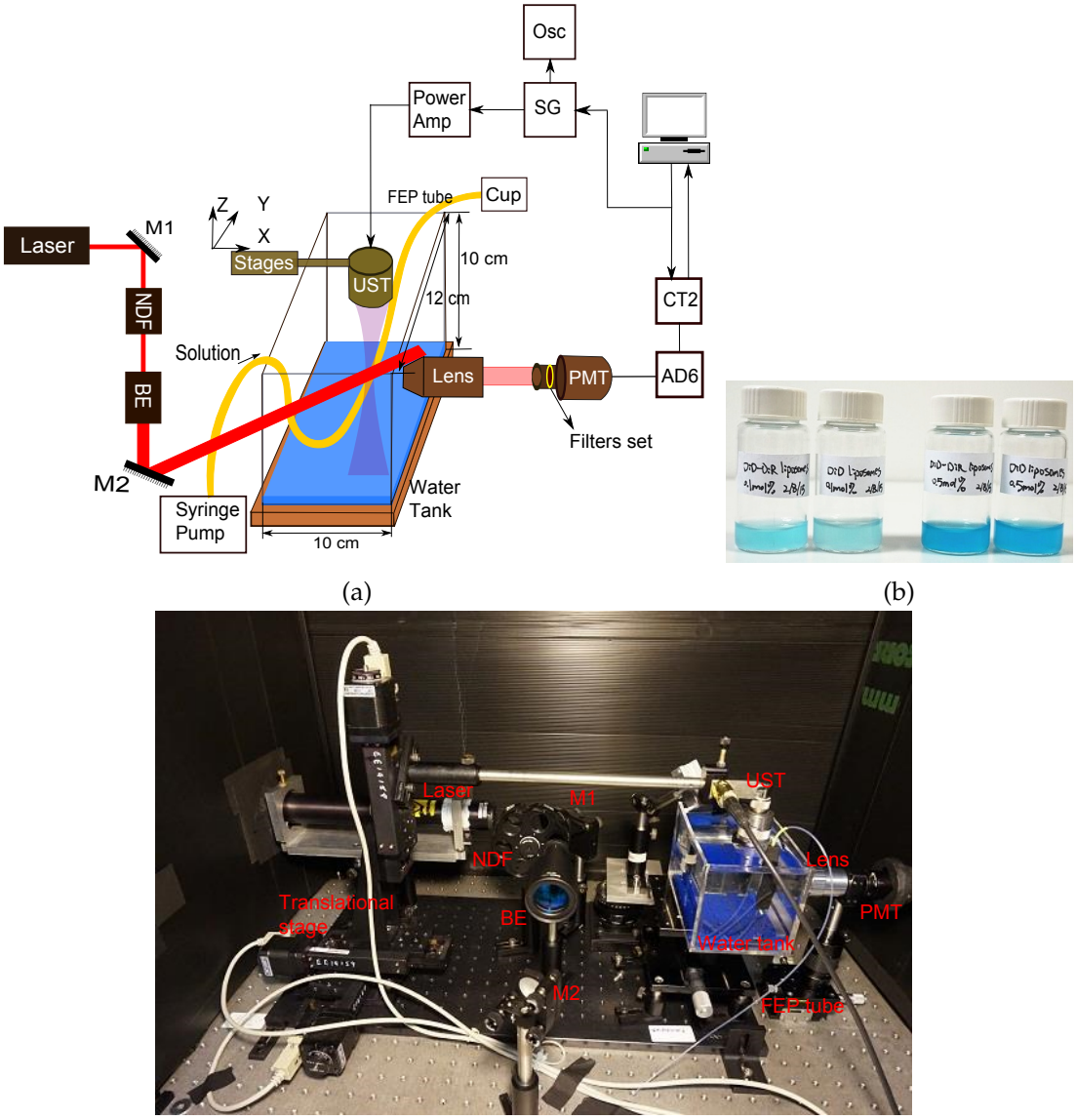


Figure 5.12: Setup for characterization of fluorophore labelled liposomes. (a) Schematic diagram; (b) photo of the samples used; (c) photo of the experimental system. M1: mirror 1; NDF: neutral density filter; BE: beam expander; M2: mirror 2; UST: ultrasound transducer; FEP: Fluorinated Ethylene Propylene; Osc: oscilloscope; SG: signal generator; PMT: photomultiplier tube; CT2: counter/timer module; AD6: amplifier-discriminator.

The US transmission efficiency of the FEP tube was measured to be 67.8 %. The schematic of the setup is shown in Fig. 5.13. The US transducer and the needle hydrophone were situated inside a container filled with water for US transmission. The tube was located perpendicular to the US transmission direction so that the needle hydrophone can be inserted into the tube. The US transmission efficiency was measured as the percentage of the pressures when the needle hydrophone was located inside of the tube and when no tube was present. The US pressure measured when the hydrophone is enclosed by the tube is the sum of transmission through the first wall and reflection of the second wall. The reflection of the second wall was ignored in this simplified test. The US pressures were measured using a similar setup as Fig. 5.13 but the hydrophone was located in line with the US propagation direction, at which the needle hydrophone has the maximum sensitivity.

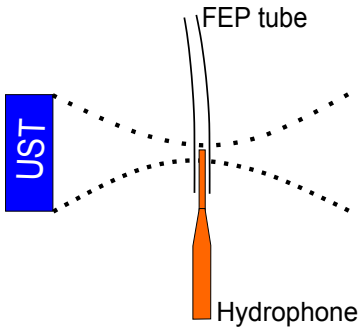


Figure 5.13: Schematic of the setup to measure US transmission efficiency of the FEP tube. FEP: Fluorinated Ethylene Propylene; UST: ultrasound transducer.

The fluorescence emission intensity when applying US with 1.2 MPa peak pressure is shown in Fig. 5.14. The US was turned on at 4 s for 4 s, and then turned off for 15 s. Six repeats were performed to check the repeatability of the dynamics of the liposomes. The intensity was recorded with a sampling period (time window of CT2) of 100 ms. 10 consecutive values (corresponding to 1000 ms) are averaged and the mean values are plotted. Fig. 5.14 shows that the US induced responses in the samples are dependant on detection wavelength (DiD emission or DiR emission wavelength), fluorophore concentration (0.1 mol% or 0.5 mol%) as well as labelled fluorphores (DiD only or both DiD and DiR). The emission intensity is observed to increase for detection at DiD emission wavelength from DiD-DiR labelled liposomes 0.5 mol% (Fig. 5.14e); decrease at DiR emission wavelength from DiD-DiR labelled liposomes 0.1 mol% (Fig. 5.14b), and de-

crease for all DiD only liposomes (Fig. 5.14c, Fig. 5.14d, Fig. 5.14g, and Fig. 5.14h). It was also observed that the fluorescence emission increased following an initial slight decrease for detection at the DiD emission wavelength from DiD-DiR labelled liposomes 0.1 mol% (Fig. 5.14a) and DiR emission wavelength from DiD-DiR labelled liposomes 0.5 mol% (Fig. 5.14f). It is worth mentioning that the detected fluorescence emission intensity in the DiR emission band from DiD only liposomes is due to the long tail end of the emission spectrum of DiD fluorophore. The US induced change trends are summarized in Table 5.3.

Table 5.3: Intensity change trend of liposomes (↑: increase, ↓: decrease).

Sample	DiD-DiR liposomes	DiD-DiR liposomes	DiD liposomes	DiD liposomes
Detection wavelength	DiD wavelength	DiR wavelength	DiD wavelength	DiR wavelength
0.1 mol%	↓↑	↓	↓	↓
0.5 mol%	↑	↓↑	↓	↓

5.5.2 Proposed mechanisms of the US mediated fluorescence variation

In this section possible mechanisms of the observed US mediated variation of the fluorescence emission intensity are discussed. US is assumed to have two effects that influence the fluorescence emission intensity: (1) US increases the lateral mobility (e.g: lateral diffusion) of dye molecules and lipids; (2) US leads to size expansion of liposomes. The origin of these two effects might be due to US induced noninertial cavitation [67]. As described in Section 4.5.3 of Chapter 4, during the noninertial cavitation, gas bubbles pre-existing in the fluid can oscillate or move, which generates small cavities and creates free volume in the lipid bilayer. The increased free volume can facilitate quicker lateral diffusion of the lipids [186] and thus lead to effect (1). Noninertial cavitation also involves the nucleation of gas bubbles in the hydrophobic region of lipid bilayers, which might be the reason for effect (2). A rectified diffusion can also increase the size [67]. To explain the different change trends observed in Fig. 5.14, there are three points that need to be noted.

Firstly, the increased lateral mobility increases the likelihood that fluorophore molecules get close enough for non-radiative energy transfer, therefore has the function of in-

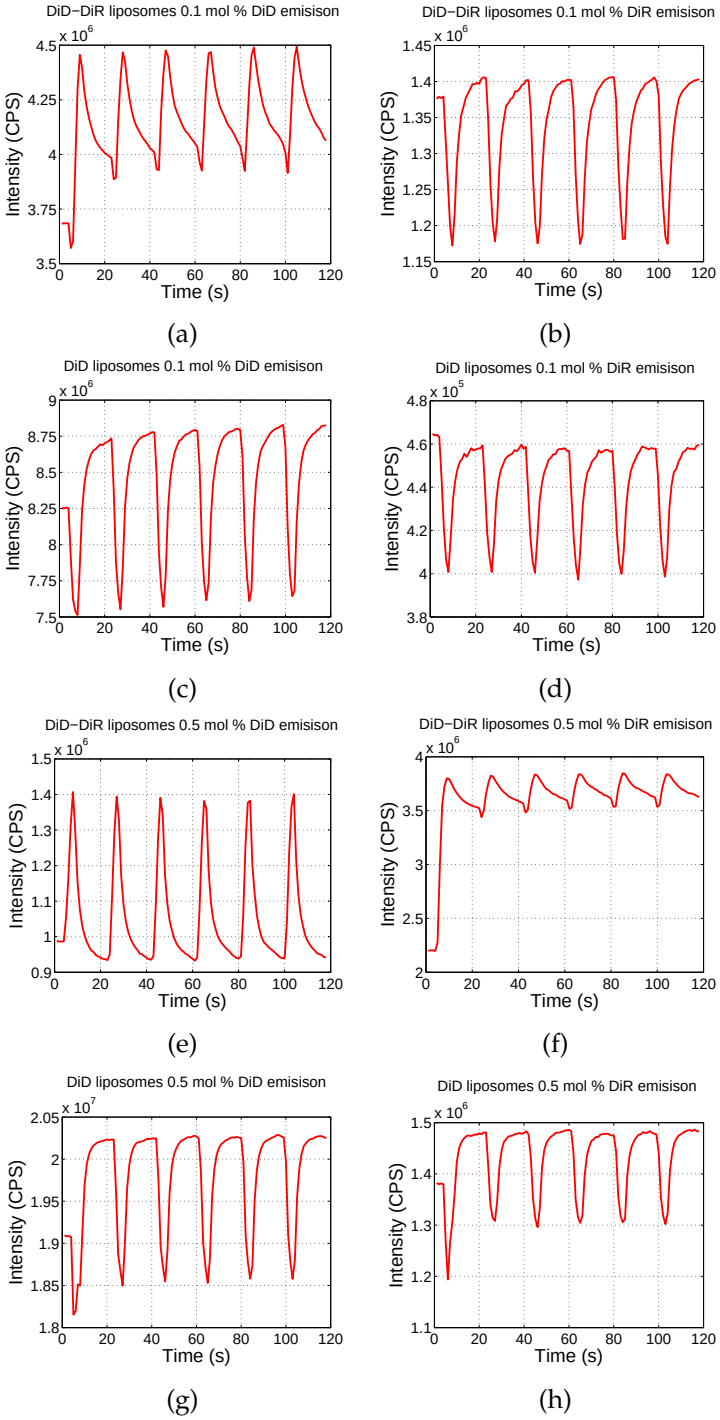


Figure 5.14: US mediated variation of fluorescence emission intensity when detecting at (a) DiD wavelength from DiD-DiR labelled liposomes 0.1 mol%; (b) DiR wavelength from DiD-DiR labelled liposomes 0.1 mol%; (c) DiD wavelength from DiD only liposomes 0.1 mol%; (d) DiR wavelength from DiD only liposomes 0.1 mol%; (e) DiD wavelength from DiD-DiR labelled liposomes 0.5 mol%; (f) DiR wavelength from DiD-DiR labelled liposomes 0.5 mol%; (g) DiD wavelength from DiD only liposomes 0.5 mol%; (h) DiR wavelength from DiD only liposomes 0.5 mol%. CPS: counts per second.

creasing FRET and self-quenching. This effect is thus similar as increasing fluorophore concentration. On the other hand, size expansion decreases the concentration of fluorophores located inside the lipid bilayer. This leads to a decrease of the intermolecular distances of fluorophores d including DiD-DiR distance (d_{FRET}), DiD-DiD distance (d_{DiD}), and DiR-DiR distance (d_{DiR}). Due to the sixth power law dependance of energy transfer efficiency on distance [137], FRET and self-quenching are reduced and the fluorescence emission intensity at DiD or DiR emission wavelength can be changed. The normalized intensity defined in Section 5.4.1 can therefore be changed by both the increased mobility and the size expansion. It needs to be mentioned that since FRET is effective over a very short distance ranging from 1 nm to 10 nm, a slight change in molecule mobility or size might lead to a detectable fluorescence variation.

Secondly, for detection at DiD emission wavelengths the effects of self-quenching and FRET are always the same - decrease of either effect leads to increased intensity while increase of either effect leads to decreased intensity. However, for detection at DiR emission wavelengths, the effects of FRET and self-quenching conflict with each other - increase of FRET leads to increase of DiR emission intensity, while increase of self-quenching of DiR leads to decrease of DiR emission intensity. In addition, increase of self-quenching of DiD leads to an indirect decrease of the DiR emission intensity via reduction of FRET.

Thirdly, relating effect (1) and effect (2) with the detected fluorescence variation shown in Fig. 5.14, both effects should be at a time scale of millisecond to second. However, the evolving process of size expansion should be slower than the perturbation of lipid bilayer.

Proposed US mediated mechanisms for each of the labelled liposomes are discussed in the following.

DiD emission from** 0.1 mol% **DiD-DiR liposomes:

The fluorescence emission intensity at DiD wavelength from DiD-DiR liposomes with 0.1 mol% DiD concentration (DiD to DiR ratio: 1:1) was observed to decrease slightly upon application of US, followed with a more significant increase in the second stage,

as seen in Fig. 5.14a. The initial signal decrease should be due to the increased mobility, which makes FRET and self-quenching stronger. The evolving size expansion reduces FRET and self-quenching, therefore leads to increase of the donor emission in the second stage. The more significant signal increase suggests that size expansion is the dominant factor to determine the fluorescence variation.

DiD emission from** 0.5 mol% **DiD-DiR liposomes:

DiD emission intensity from 0.5 mol% DiD-DiR liposomes was observed to increase with application of US (Fig. 5.14e). This difference with the previous case of 0.1 mol% DiD-DiR liposomes is likely to be due to the increased FRET and self-quenching efficiency at equilibrium state, as seen in Fig. 5.7. Since the FRET efficiency (90.2%) and self-quenching efficiency (81.3%) have already been extremely high, the increased mobility has little influence on the donor emission intensity. The size expansion which reduces the FRET and self-quenching efficiency and increases the fluorescence emission intensity makes more contribution to the fluorescence variation.

DiR emission from** 0.1 mol% **DiD-DiR liposomes:

DiR emission intensity from 0.1 mol% DiD-DiR liposomes was observed to decrease with application of US (Fig. 5.14b). Referring back to the red curve in Fig. 5.8 which describes the relationship of the normalized intensity at DiR emission wavelength from DiD-DiR labelled liposomes with concentration of fluorophores, it can be seen that at 0.1 mol%, further increase of DiD concentration leads to decrease of the intensity, while further decrease of DiD concentration has no influence on the intensity. This observation indicates that the increased mobility is the dominant factor to determine the variation of the intensity, and the effect of size expansion can be ignored. With increase of concentration, FRET (increase DiR emission), self-quenching of DiD (decrease DiR emission), and self-quenching of DiR (decrease DiR emission) increase. The fluorescence decrease in Fig. 5.8 indicates that self-quenching of DiD and DiR makes more contribution to the overall fluorescence variation. The increased mobility of dye molecules increases FRET, self-quenching of DiD, and self-quenching of DiR. The observed change trend of DiR emission from 0.1 mol% DiD-DiR liposomes in Fig. 5.14b suggests that the increased self-quenching of DiD and DiR makes more contribution

to the fluorescence variation than the increased FRET. This is in accordance with the observation in Fig. 5.8.

DiR emission from** 0.5 mol% **DiD-DiR liposomes:

Fig. 5.14f shows that DiR emission intensity from 0.5 mol% DiD-DiR liposomes decreases slightly with application of US, followed by a more significant increase. The signal decrease in the first stage is due to the same reason as the previous case. However, referring back to the normalized intensity of DiD-DiR liposomes in Fig. 5.8, it can be seen that at 0.5 mol%, the fluorescence changes either increasing or decreasing the fluorophore concentration. Therefore the influence of size expansion should be considered in this case. Size expansion decreases self-quenching of DiD and self-quenching of DiR. however, it should be noted that size expansion increases FRET for 0.5 mol% DiD-DiR liposomes, different from the previous case. This is because as suggested by Fig. 5.9, above 0.25 mol% FRET decreases with increase of concentration, which is probably due to the very high self-quenching effect of both DiD and DiR. Because all of the three effects of size expansion lead to increase of the fluorescence emission at the DiR emission wavelength range, in the second stage a signal increase was observed.

Fluorescence emission from DiD only liposomes:

It was observed from Fig. 5.14c, Fig. 5.14d, Fig. 5.14g, and Fig. 5.14h that the fluorescence emission intensity (both DiD and DiR emission) from DiD only liposomes (both at 0.1 mol% and 0.5 mol% DiD concentration) always decreases when US is applied. As both of the concentrations 0.1 mol% and 0.5 mol% are relatively low for DiD only liposomes, increased mobility which increases self-quenching of DiD always makes a greater contribution to the fluorescence intensity.

Permanent baseline shift:

It was shown in Fig. 5.14 that the response of fluorescence emission from the liposomes to US is highly repeatable except for the first US exposure. This is more obvious for detection at DiD wavelengths for 0.1 mol% DiD-DiR labelled liposomes (Fig. 5.14a), DiD wavelength from 0.1 mol% DiD only liposomes (Fig. 5.14c), DiR wavelength from 0.5 mol% DiD-DiR labelled liposomes (Fig. 5.14f), DiD and DiR wavelength from 0.5 mol%

DiD liposomes (Fig. 5.14g and Fig. 5.14h). It can be seen for these cases after the first US exposure the equilibrium state is shifted higher than the initial state permanently. This indicates that a slight size expansion might be induced by US and the liposomes failed to recover within the time the next US sequence is applied.

In conclusion, the US mediated variation of the fluorescence emission intensity is different for the eight cases studied. Possible mechanisms are summarized in Table 5.4. The increased mobility of dye molecules and US induced size expansion are the two factors that might lead to the fluorescence variation. The increased mobility decreases the fluorescent signal. The size expansion increases the fluorescent signal. Both effects exist for detection of DiD emission from DiD-DiR labelled liposomes with 0.1 mol% DiD concentration and DiR emission from DiD-DiR labelled liposomes with 0.5 mol% DiD concentration, therefore a bimodal fluorescence variation was observed. For detection of DiD emission from DiD-DiR labelled liposomes with 0.5 mol% DiD concentration, only the size expansion contributes to the fluorescence intensity due to high FRET and self-quenching efficiency, therefore only signal increase is observed. For detection of DiR emission from DiD-DiR labelled liposomes with 0.1 mol% DiR concentration, only the increased mobility contributes to the fluorescence intensity, therefore only signal decrease is observed. The DiD concentration of 0.1 mol% can therefore be regarded as the threshold for detection at DiD emission wavelengths from DiD-DiR labelled liposomes: below this concentration US leads to decrease of the fluorescence intensity; above this concentration US leads to increase of the fluorescence intensity; around this concentration a bimodal change is observed. Similarly the DiR concentration of 0.1 mol% can be regarded as the threshold for detection at DiR emission wavelengths from DiD-DiR labelled liposomes. DiR has a higher threshold than DiD which is likely to be due to the opposite effect of FRET and self-quenching. Since there is only self-quenching in the DiD only liposomes, the threshold is higher than 0.5 mol% therefore no signal increase was observed. Finally it needs to be noted that a threshold concentration for excimer formation was used in Chapter 4. Size expansion which further reduces the excimer is thereby not considered as a mechanism for the observed increase of the excimer emission intensity.

Table 5.4: Proposed mechanisms for US mediated fluorescence variation of DiD-DiR labelled liposomes (↑: increase, ↓: decrease).

Effects of US	Fluorescence variation trend induced			
	$DiD_{0.1}$ [1]	$DiD_{0.5}$ [2]	$DiR_{0.1}$ [3]	$DiR_{0.5}$ [4]
Increased mobility	↓	–	↓	↓
Size expansion	↑	↑	–	↑

[1] Detection at DiD emission wavelength for DiD concentration of 0.1 mol%.
[2] Detection at DiD emission wavelength for DiD concentration of 0.5 mol%.
[3] Detection at DiR emission wavelength for DiR concentration of 0.1 mol%.
[4] Detection at DiR emission wavelength for DiR concentration of 0.5 mol%.

5.5.3 Influence of US pressure and exposure time

In this section the influence of US on the variation of the fluorescence emission intensity is investigated by applying various US pressures and exposure times. The same experimental system shown in Fig. 5.12 is used. Fig. 5.15 shows the intensity difference of DiD emission and the corresponding On-to-Off ratio (%) for DiD-DiR labelled liposomes at 0.1 mol%, DiD only liposomes at 0.1 mol%, DiD-DiR labelled liposomes at 0.5 mol%, and DiD only liposomes at 0.5 mol%. The intensity difference is the subtraction of the highest intensity and the lowest intensity. The On-to-Off ratio is defined as the ratio of the intensity difference with the intensity baseline prior sonification. The samples were static inside the tube and were exposed to US six times without being replenished in between. Mean and standard deviation were calculated and presented, as shown in Fig. 5.15 and Fig. 5.16 for detection at DiD and DiR wavelength respectively. The first US exposure leads to a change of the intensity very different from the latter five therefore is not included for calculation. The US mediated variation of the fluorescence emission intensity at the individual US pressure and exposure time investigated can be found in Appendix E.

It can be seen from Fig. 5.15a and Fig. 5.15b that at the lower end of US pressure or exposure time, the intensity difference and On-to-Off ratio are very low. With further increase of US pressure or exposure time, the intensity difference and On-to-Off ratio also increase. This should be due to bigger changes in size of the liposomes and increased mobility of lipids and DiD molecules in the lipid membrane at higher US pressure or longer exposure times.

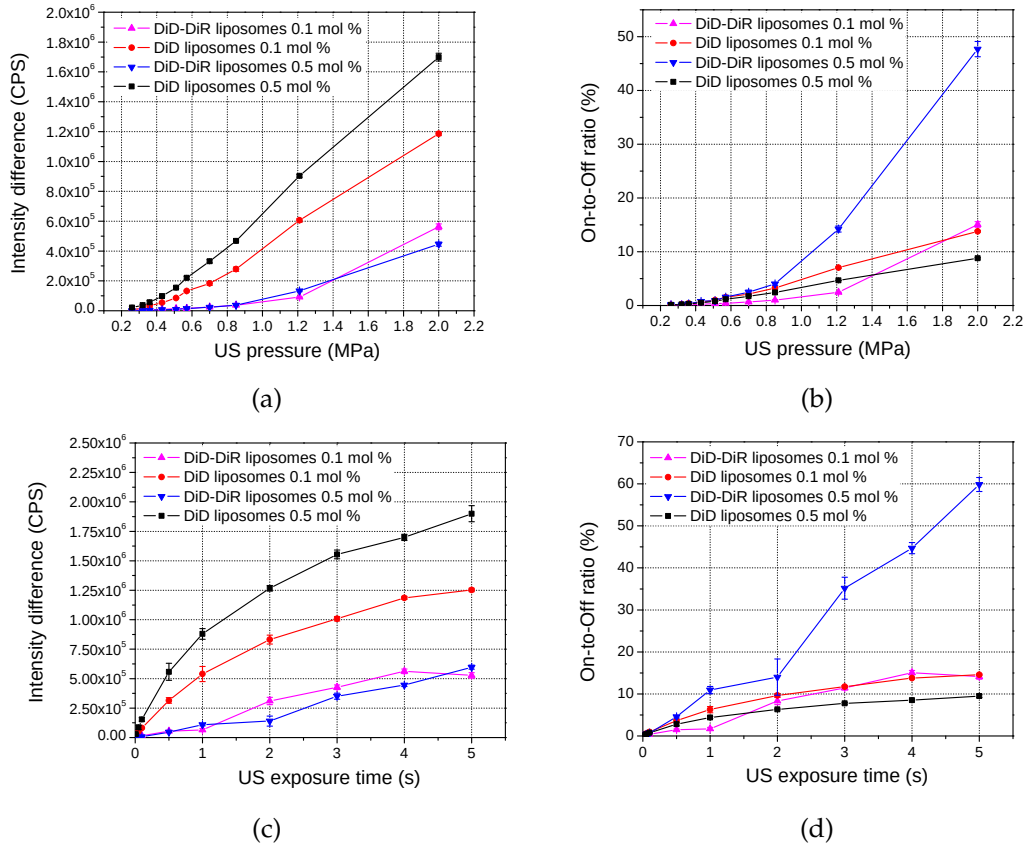


Figure 5.15: Influence of US on fluorescence emission intensity at DiD emission band by varying US pressure or exposure time for DiD-DiR labelled liposomes at 0.1 mol%, DiD only liposomes at 0.1 mol%, DiD-DiR labelled liposomes at 0.5 mol%, and DiD only liposomes at 0.5 mol%. (a) Intensity difference varying US pressure at US exposure time 4 s; (b) On-to-Off ratio varying US pressure at US exposure time 4 s; (c) intensity difference varying US exposure time at US pressure 2 MPa; (d) On-to-Off ratio varying US exposure time at US pressure 2 MPa. CPS: counts per second.

It was observed from Fig. 5.15 that the intensity difference obtained from DiD only liposomes are higher than DiD-DiR labelled liposomes for both of the two concentrations for all the pressure and exposure times studied. However the On-to-Off ratio obtained from the DiD-DiR labelled liposomes was much higher at the higher concentration of 0.5 mol% (Fig. 5.15b and Fig. 5.15d). The maximum On-to-Off ratio of 60% was obtained with 2 MPa and 5 s US exposure using DiD-DiR labelled liposomes at 0.5 mol% concentration. These results suggest that US can induce fluorescence variation from both DiD only liposomes and DiD-DiR labelled liposomes. Benefiting from FRET, DiD-DiR labelled liposomes with 0.5 mol% has the highest sensitivity.

Fig. 5.16 shows the influence of US pressure and exposure time on the intensity difference of emission at DiR wavelength and the corresponding On-to-Off ratio for the above mentioned four samples. Again with increase of US pressure or exposure time both the intensity difference and the On-to-Off ratio increase. Liposomes labelled by both DiD and DiR were among those to obtain higher intensity difference due to FRET for all the US pressures and exposure times studied. At 0.1 mol% the On-to-Off ratio obtained from DiD-DiR labelled liposomes are also higher than that from DiD only liposomes. However, at 0.5 mol% the On-to-Off ratio obtained from DiD-DiR labelled liposomes are lower than DiD only liposomes because the former has much higher intensity baseline at DiR emission wavelength.

5.6 Line scanning imaging in heavily scattering phantom

5.6.1 Line scanning imaging

In this section line scanning imaging was performed using the DiD-DiR labelled liposomes (DiD to DiR ratio: 1:1) as contrast agent because of the high US mediated fluorescence variation as observed in the last section. DiD only liposomes were used as a donor only control. DiD concentrations at both 0.1 mol% and 0.5 mol% were measured. Fluorescence emission at both the DiD and DiR wavelength was captured. The setup is similar to the one used in the previous Section 5.5 and is shown in Fig. 5.17. The main difference is that the FEP tube was buried along x direction in a scattering

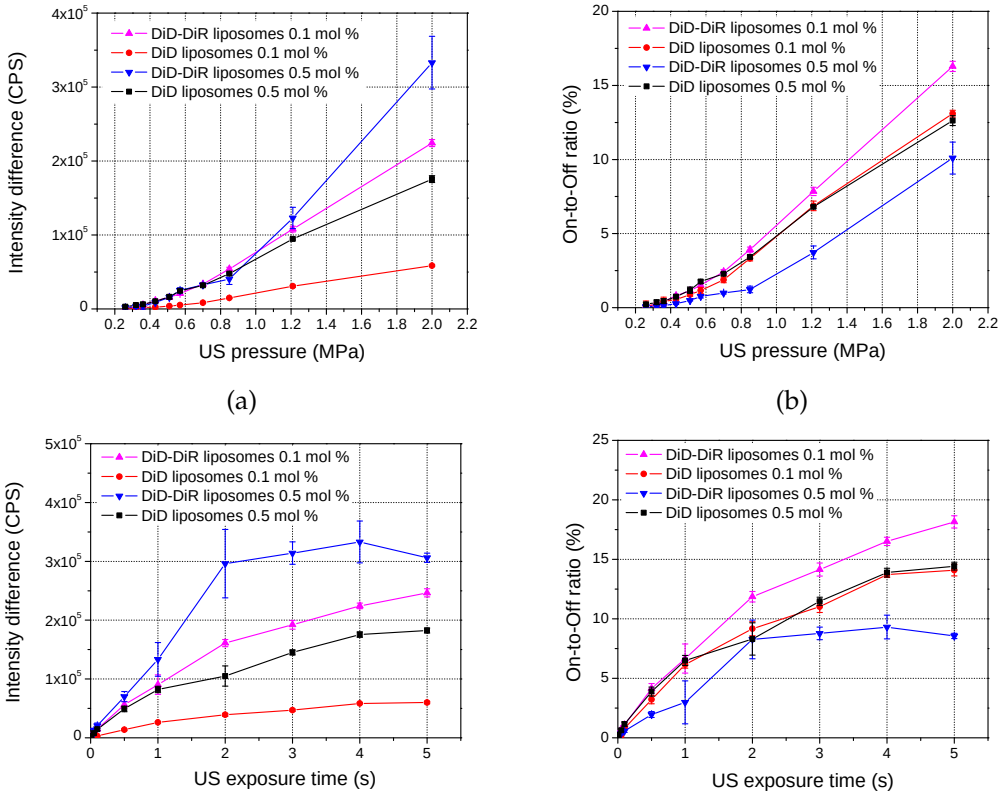
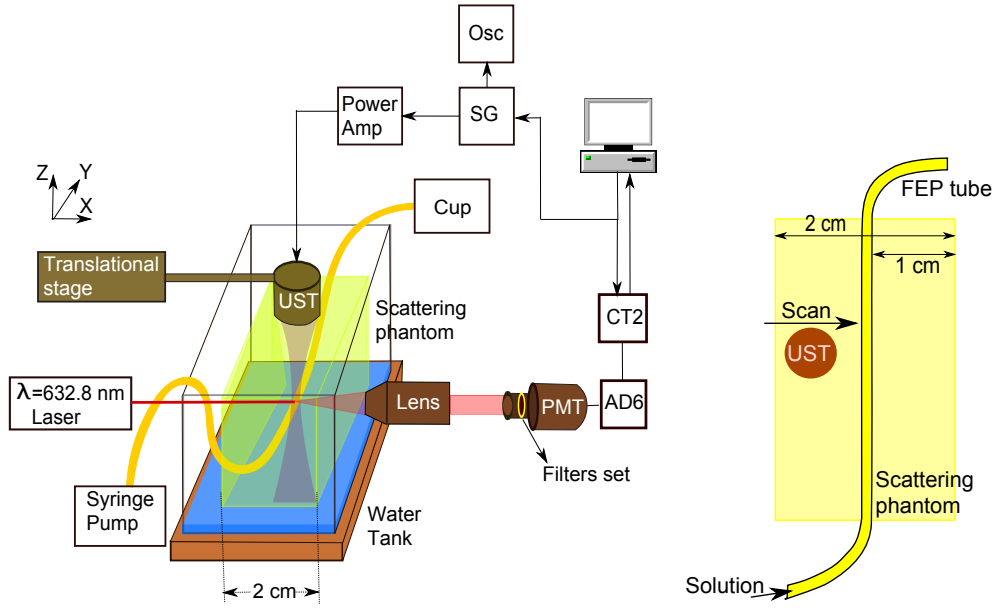


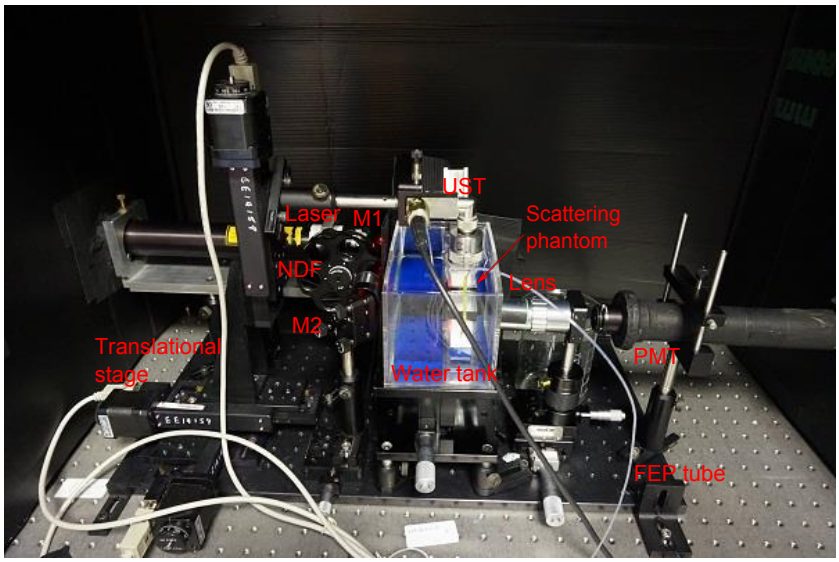
Figure 5.16: Influence of US on fluorescence emission intensity at DiR emission band by varying US pressure or exposure time for DiD-DiR labelled liposomes at 0.1 mol%, DiD only liposomes at 0.1 mol%, DiD-DiR labelled liposomes at 0.5 mol%, and DiD only liposomes at 0.5 mol%. (a) Intensity difference varying US pressure at US exposure time 4 s; (b) On-to-Off ratio varying US pressure at US exposure time 4 s; (c) intensity difference varying US exposure time at US pressure 2 MPa; (d) On-to-Off ratio varying US exposure time at US pressure 2 MPa. CPS: counts per second.

phantom ($2 \times 7.7 \times 5$ cm, x-y-z) at depth of 1 cm, as shown in Fig. 5.17b. Also distinct from the setup shown in Fig. 5.12, the laser light illuminates the scattering phantom directly and perpendicularly. This is because the excitation laser light is heavily scattered in the scattering phantom and the light transmitted through is divergent with a relatively low light level already. The US transducer was controlled by a translational stage (Standa, 8SMC1-USBhF, Vilnius, Lithuania) to move along x direction. The translational stage, signal generator, and counter were synchronized by the computer. After the initialization of the SG and counter, the translational stage moves 100 steps (1 step is 2.5 µm). Then the US is turned on for 4 s and off for 15 s repeating six times. At the same time the fluorescence emission intensity is detected by the photon counting system and recorded by the computer. After this the translational stage moves to the next position and the US and photon counting system are operated again. This procedure is repeated until the translational stage reaches the pre-set final position. The mean and standard deviation of the intensity difference or the On-to-Off ratio as defined in Section 5.5 were calculated at each position and plotted. The scanning procedures were performed both when the samples were flowing inside the tube with a speed of 0.01 ml/min and when the samples were static. For the latter case the samples were scanned twice without being updated in between to test whether US can still induce fluorescence variation after the first scan. Scans were also obtained without applying US. In this case the sample was kept static inside the tube and the water tank was scanned along z direction for 24 mm with a step of 250 µm. At each position 1000 values of the intensity was recorded with a time window of 100 ms. Mean and standard deviation for each position can thus be calculated.

The scattering phantom is prepared according to the method described in Ref. [245]. Briefly, the agarose powder was stirred and dissolved in distilled water in a beaker. The solution was then heated in a microwave oven until bubbles appeared. The solution was removed from the microwave oven and stirred again to resuspend any settled power and gel pieces, then reheated until boiling. Polystyrene microparticles (1.5 µm diameter) which have been dissolved in distilled water using an ultrasonic bath, were mixed with the agarose solution. The size of the scattering phantom was $77 \times 20 \times$

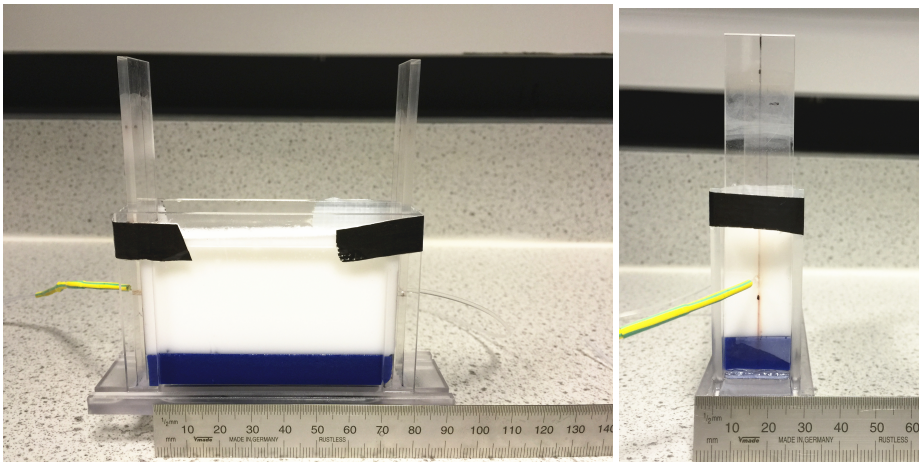


(a) (b)



(c)

Figure 5.17: Setup for line scanning imaging. (a) Schematic; (b) top view of the schematic; (c) photo of the experimental system. UST: ultrasound transducer; Osc: oscilloscope; SG: signal generator; PMT: photomultiplier tube; CT2: counter/timer module; AD6: amplifier-discriminator; FEP: Fluorinated Ethylene Propylene; M1: mirror 1; NDF: neutral density filter; M2: mirror 2.



(a) (b)

Figure 5.18: Scattering phantom with a FEP tube embedded.

50 mm controlled using a mould (as shown in Fig. 5.18). The FEP tube was fixed in the mould before casting the mixture. The final weight concentration of agarose is 2 %. The scattering phantom has a reduced scattering coefficient (μ_s') around 1 mm^{-1}. The reduced scattering coefficient of biological tissue is dependent on wavelength and specific organs. $\mu_s' = 1\,mm^{-1}$ is a typical value for the wavelength range of 600 nm - 1000 nm [127]. No additional absorption is added so the absorption coefficient (μ_a) is comparable to that of water ($\mu_a = 0.0003\,mm^{-1}$ at $\lambda = 633$ nm; $\mu_a = 0.0004\,mm^{-1}$ at $\lambda = 665$ nm; $\mu_a = 0.003\,mm^{-1}$ at $\lambda = 766$ nm [246]). The parameters of the scattering phantom are summarized in Table 5.5.

Scans of the tube filled with DiD-DiR labelled liposomes or DiD only liposomes by detecting at DiD or DiR emission wavelength were obtained. The fluorescence emission intensity (unit: CPS) when the fluorophore labelled liposomes were injected inside the tube was summarised in Table 5.6. FRET from DiD to DiR is suggested by the lower fluorescence intensity of DiD-DiR labelled liposomes at DiD emission wavelength compared with that of DiD only liposomes, and the higher fluorescence intensity of DiD-DiR labelled liposomes at DiR emission wavelength compared with that of DiD only liposomes.

Fig. 5.19 - Fig. 5.26 show the scanned images. x axis indicates position of the US transducer. Left y axis indicates either intensity difference ((a) and (b) of each figure) or On-to-Off ratio ((c) and (d) of each figure) for the scans obtained with applying US.

Table 5.5: Parameters of the scattering phantom.

Symbol	Meaning	Value
μ_s'	reduced scattering coefficient	$1\,\mathrm{mm}^{-1}$
g	asymmetric coefficient	0.938
$\mu_s = \mu_s'/(1-g)$	scattering coefficient	$16\,\mathrm{mm}^{-1}$
μ_a	absorption coefficient	$0.0003\,\mathrm{mm}^{-1}$ at $\lambda = 633\,\mathrm{nm}$ $0.0004\,\mathrm{mm}^{-1}$ at $\lambda = 665\,\mathrm{nm}$ $0.003\,\mathrm{mm}^{-1}$ at $\lambda = 766\,\mathrm{nm}$ [246]
d	diameter of polystyrene microparticles	$1.5\,\mu\mathrm{m}$
P	density of polystyrene	1.05
$A = \pi(d/2)^2$	physical cross section area of the particle	$1.7671 \times 10^{-6}\,\mathrm{mm}^2$
Q_s	efficiency factor	3.373
$\sigma_s = Q_s A$	effective scattering area	$5.9604 \times 10^{-6}\,\mathrm{mm}^2$
$\rho_s = \mu_s/\sigma_s$	number of particles per volume	$2.68 \times 10^{6}\,\mathrm{mm}^3$
$W = \frac{3.14Pd^3\rho_s}{6\times10^{12}}$	weight of scattering particles	$4.98 \times 10^{-6}\,\mathrm{g\,cm}^{-3}$

Table 5.6: The fluorescence emission intensity detected by the photon counting system.

Sample	**Light intensity**	**Sample**	**Light intensity**
DiD-DiR labelled liposomes 0.1 mol% DiD emission	3×10^6 CPS	DiD-DiR labelled liposomes 0.1 mol% DiR emission	7×10^5 CPS
DiD only liposomes 0.1 mol% DiD emission	5×10^6 CPS	DiD only liposomes 0.1 mol% DiR emission	4×10^5 CPS
DiD-DiR labelled liposomes 0.5 mol% DiD emission	1×10^6 CPS	DiD-DiR labelled liposomes 0.5 mol% DiR emission	1×10^6 CPS
DiD only liposomes 0.5 mol% DiD emission	1.4×10^7 CPS	DiD only liposomes 0.5 mol% DiR emission	7×10^5 CPS

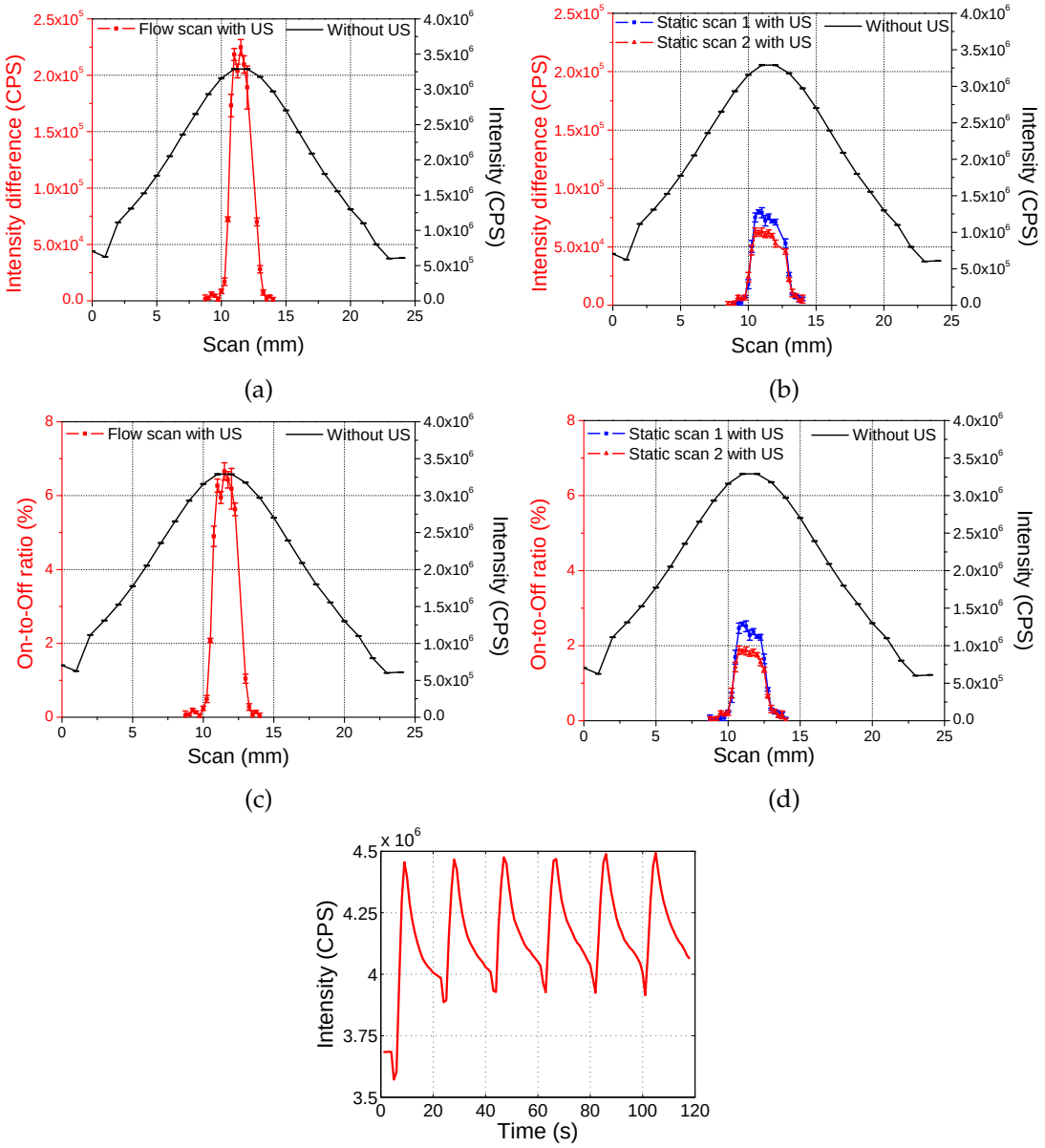


Figure 5.19: Scan of a tube filled with DiD-DiR labelled liposomes (0.1 mol%) at the mid-plane of a scattering phantom through detection at DiD emission wavelength. (a) and (c): The sample was flowing at a speed of 0.01 ml/min; (b) and (d): the sample was static and scanned twice without updating the sample in between. The corresponding fluorescence variation (from Fig. 5.14a) is shown in (e). CPS: counts per second.

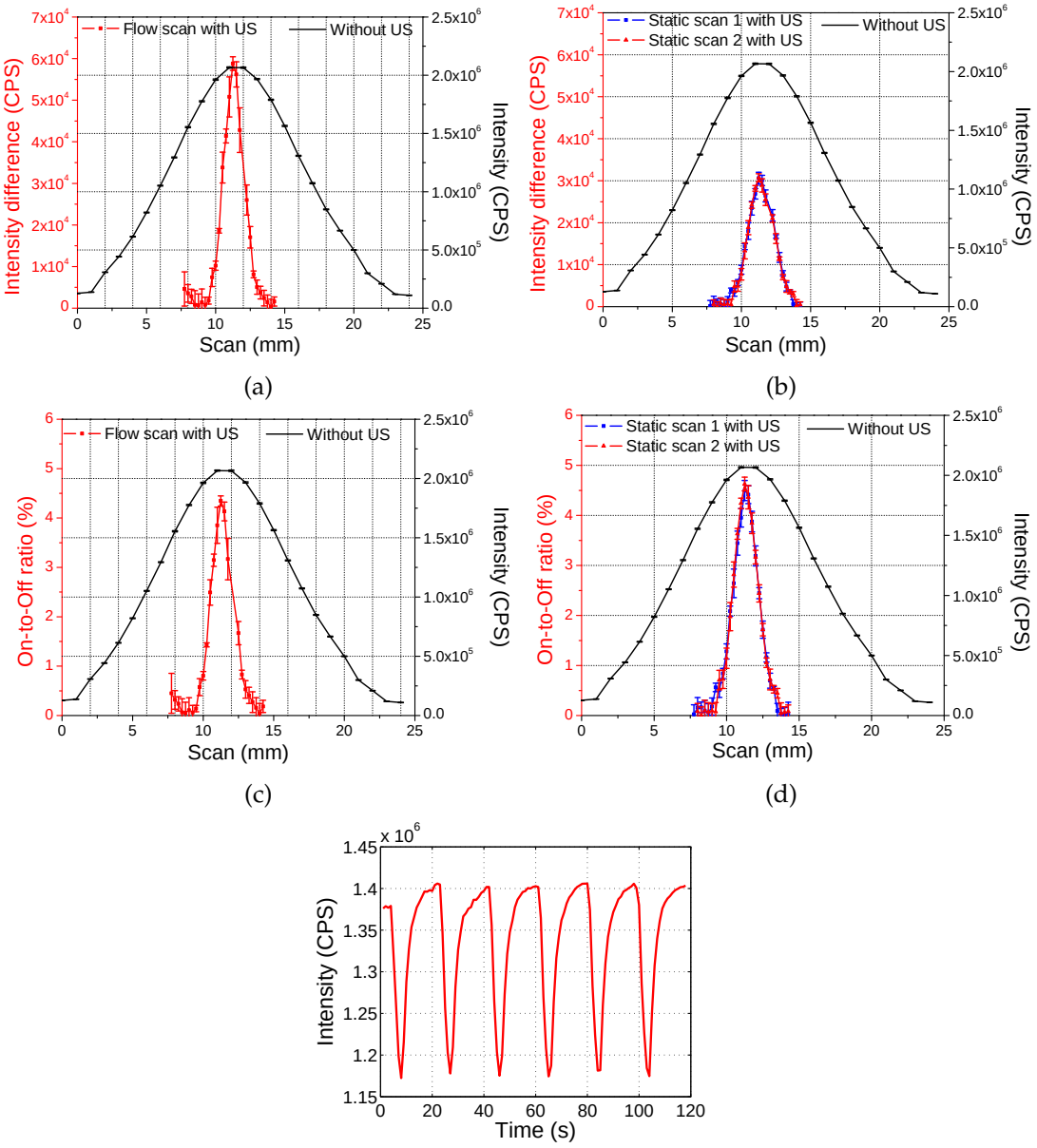


Figure 5.20: Scan of a tube filled with DiD-DiR labelled liposomes (0.1 mol%) at the mid-plane of a scattering phantom through detection at DiR emission wavelength. (a) and (c): The sample was flowing at a speed of 0.01 ml/min; (b) and (d): the sample was static and scanned twice without updating the sample in between. The curves for the two static scans overlapped. The corresponding fluorescence variation (from Fig. 5.14b) is shown in (e). CPS: counts per second.

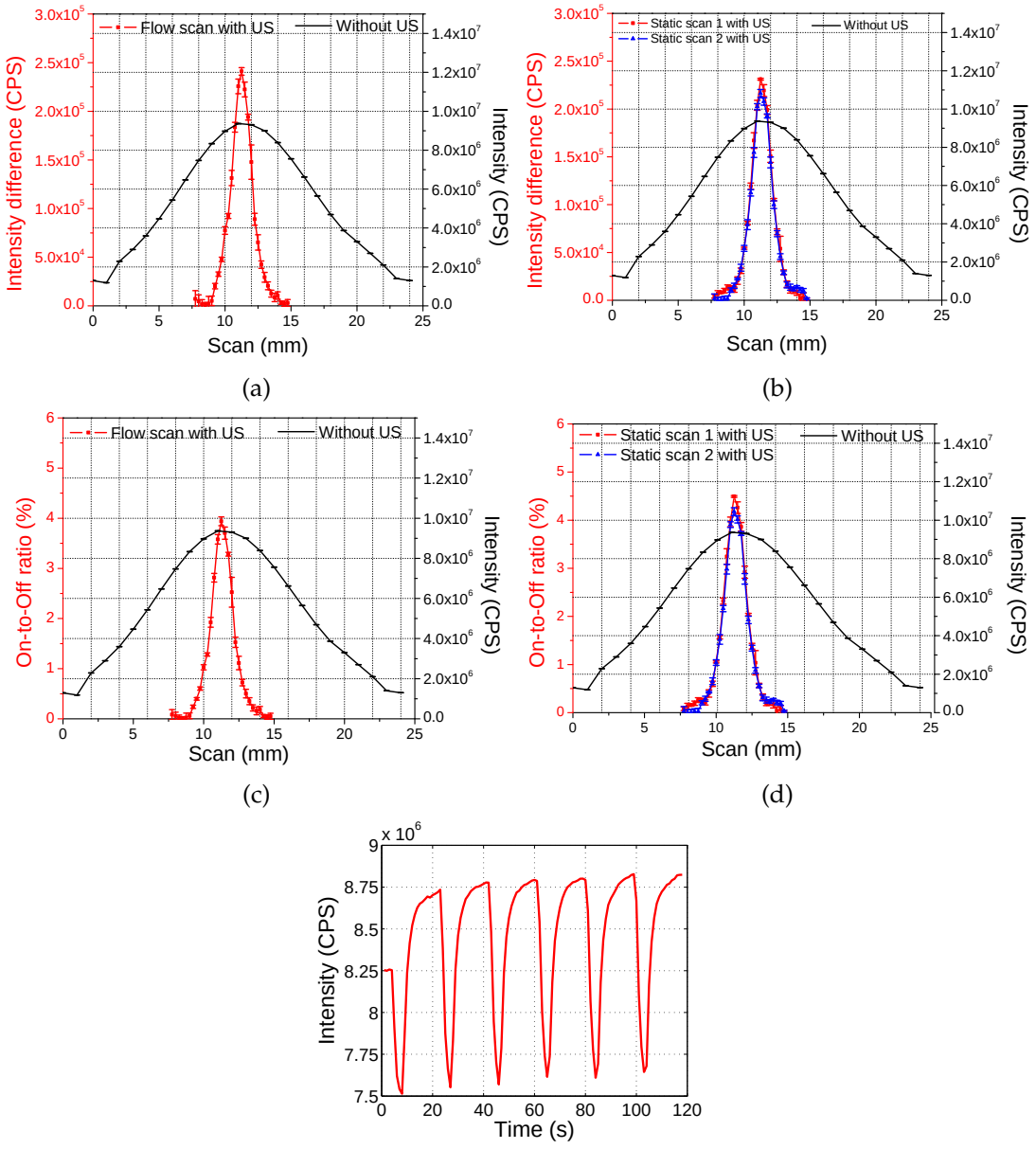


Figure 5.21: Scan of a tube filled with DiD only liposomes (0.1 mol%) at the mid-plane of a scattering phantom through detection at DiD emission wavelength. (a) and (c): The sample was flowing at a speed of 0.01 ml/min; (b) and (d): the sample was static and scanned twice without updating the sample in between. The corresponding fluorescence variation (from Fig. 5.14c) is shown in (e). CPS: counts per second.

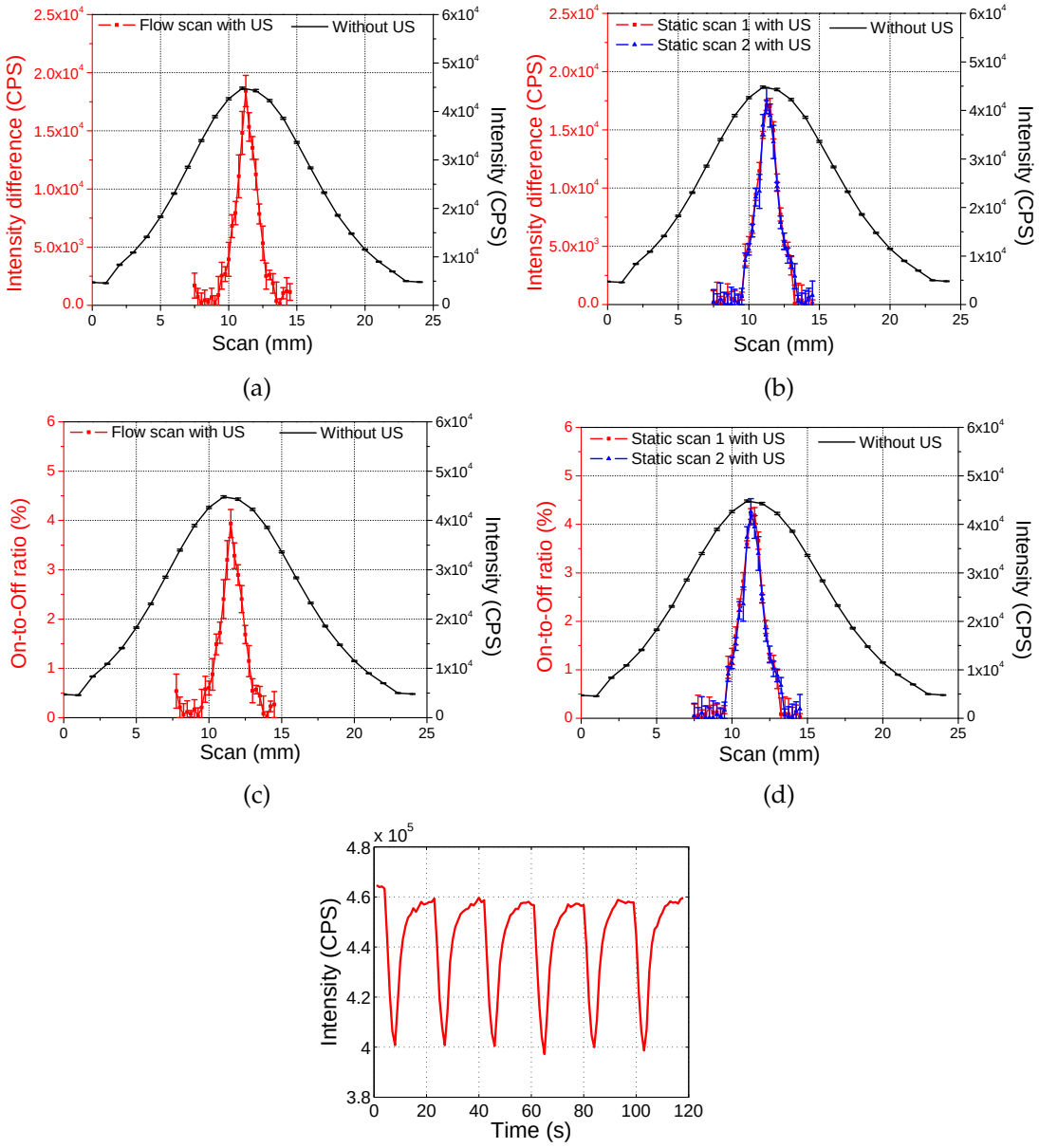


Figure 5.22: Scan of a tube filled with DiD only liposomes (0.1 mol%) at the mid-plane of a scattering phantom through detection at DiR emission wavelength. (a) and (c): The sample was flowing at a speed of 0.01 ml/min; (b) and (d): the sample was static and scanned twice without updating the sample in between. The curves for the two static scans overlapped. The corresponding fluorescence variation (from Fig. 5.14d) is shown in (e). CPS: counts per second.

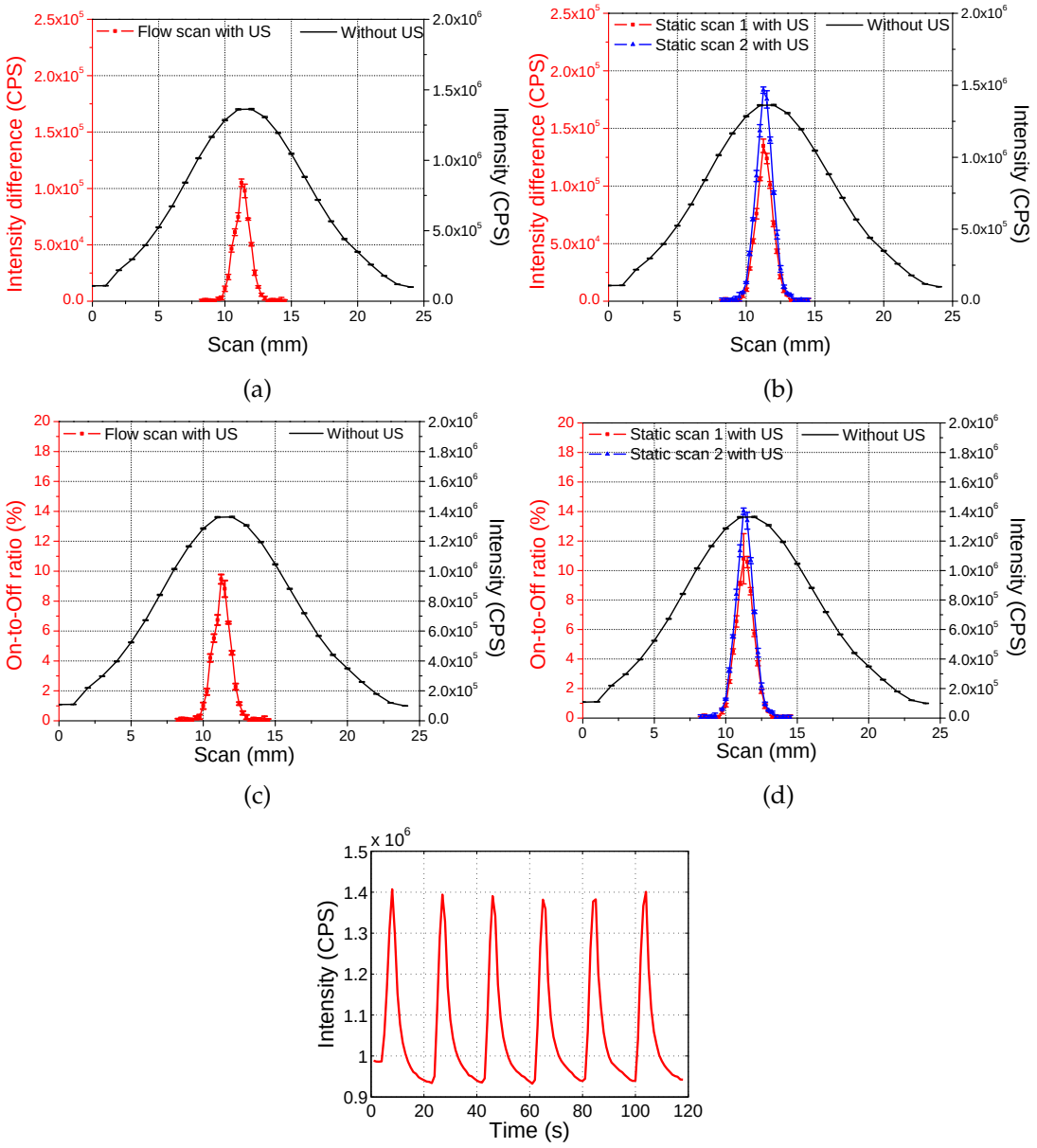


Figure 5.23: Scan of a tube filled with DiD-DiR labelled liposomes (0.5 mol%) at the mid-plane of a scattering phantom through detection at DiD emission wavelength. (a) and (c): The sample was flowing at a speed of 0.01 ml/min; (b) and (d): the sample was static and scanned twice without updating the sample in between. The corresponding fluorescence variation (from Fig. 5.14e) is shown in (e). CPS: counts per second.

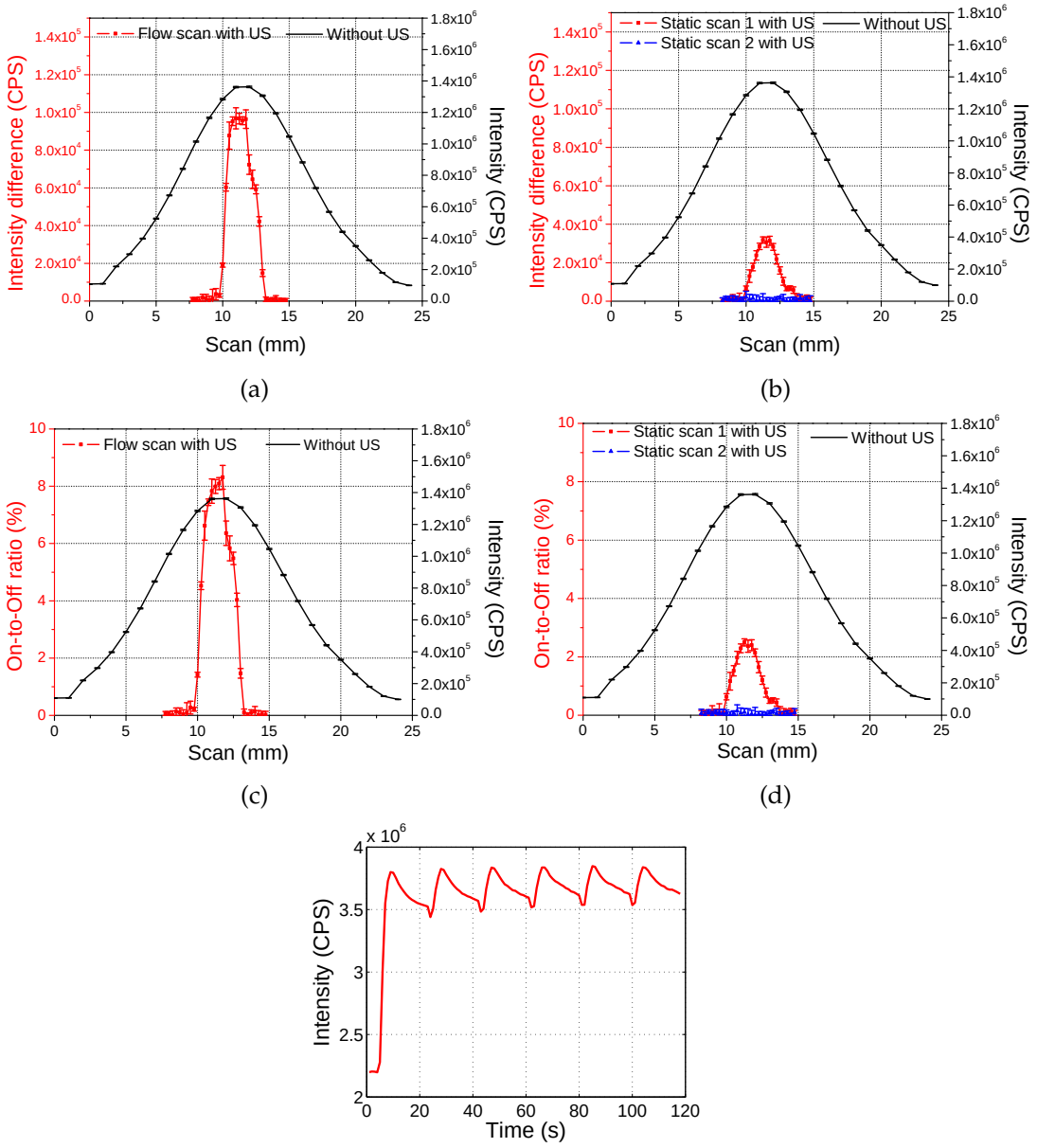


Figure 5.24: Scan of a tube filled with DiD-DiR labelled liposomes (0.5 mol%) at the mid-plane of a scattering phantom through detection at DiR emission wavelength. (a) and (c): The sample was flowing at a speed of 0.01 ml/min; (b) and (d): the sample was static and scanned twice without updating the sample in between. The corresponding fluorescence variation (from Fig. 5.14f) is shown in (e). CPS: counts per second.

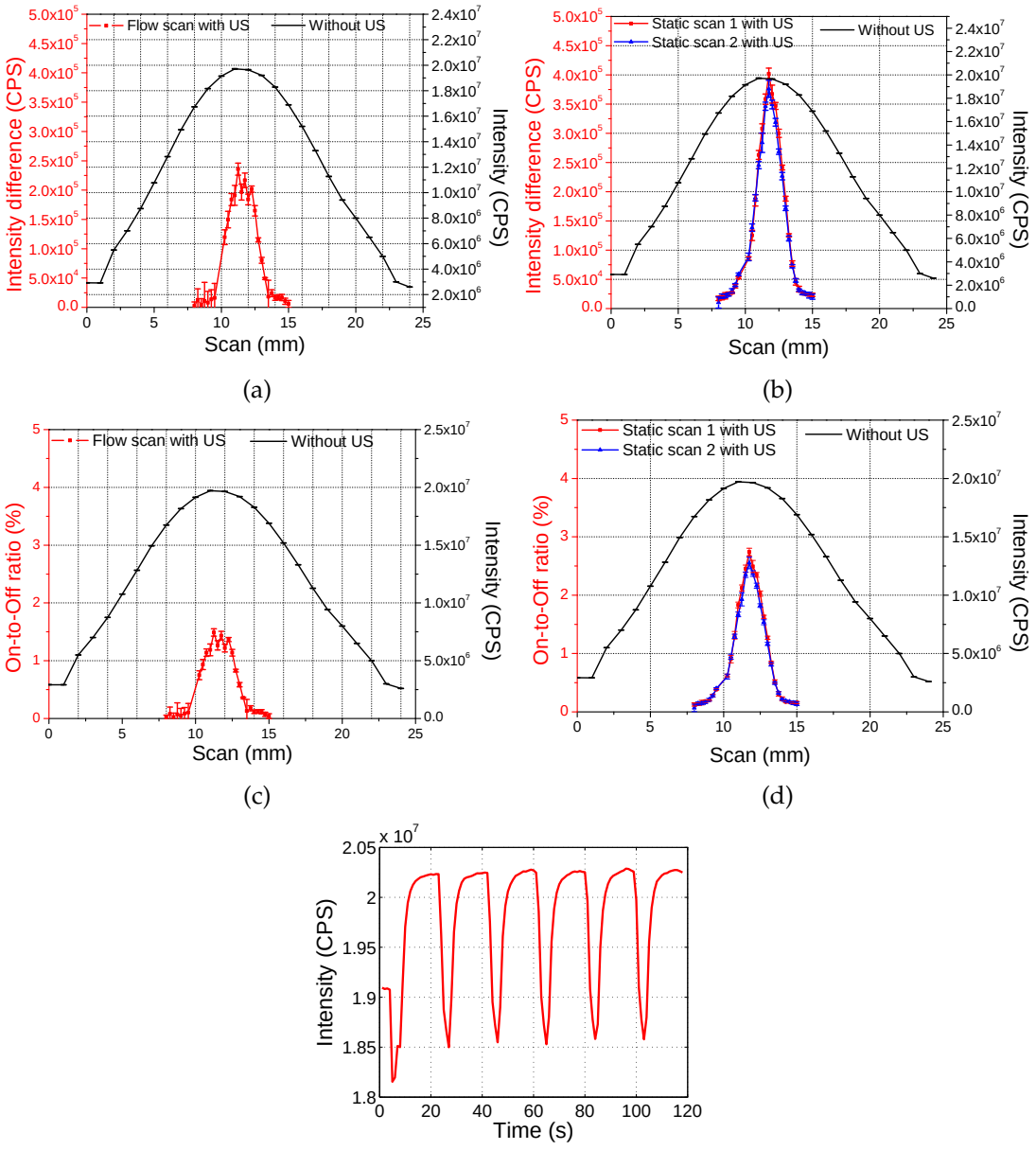


Figure 5.25: Scan of a tube filled with DiD only liposomes (0.5 mol%) at the mid-plane of a scattering phantom through detection at DiD emission wavelength. (a) and (c): The sample was flowing at a speed of 0.01 ml/min; (b) and (d): the sample was static and scanned twice without updating the sample in between. The corresponding fluorescence variation (from Fig. 5.14g) is shown in (e). CPS: counts per second.

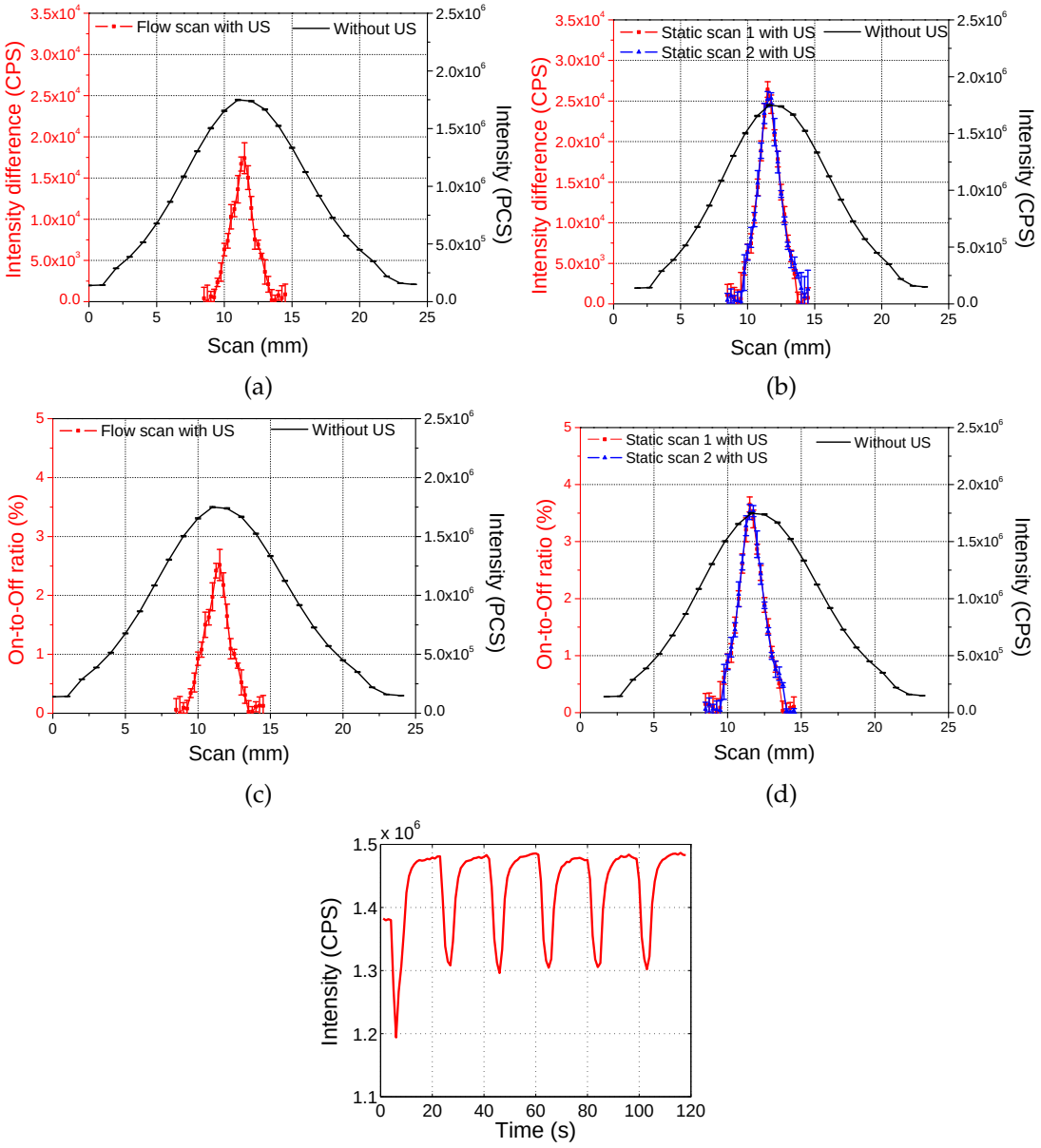


Figure 5.26: Scan of a tube filled with DiD only liposomes (0.5 mol%) at the mid-plane of a scattering phantom through detection at DiR emission wavelength. (a) and (c): The sample was flowing at a speed of 0.01 ml/min; (b) and (d): the sample was static and scanned twice without updating the sample in between. The curves for the two static scans overlapped. The corresponding fluorescence variation (from Fig. 5.14h) is shown in (e). CPS: counts per second.

The intensity for scans without applying US is indicated by right y axis.

To quantitatively compare different cases the contrast of the line scanning image is defined as the difference of the highest On-to-Off ratio with the lowest On-to-Off ratio. It was observed that in most cases the contrast obtained when the samples were static is slightly higher than the situation when the samples were flowing. This is because for the flowing case some of the liposomes were ejected out from the US focal zone during the 4 s US exposure therefore the average US exposure time is shorter. For a flowing speed of 0.01 ml/min (0.17 mm/s), the distance traveled during the 4 s US duration is 0.68 mm. Liposomes located within 0.68 mm from the edge of the US focal zone will be ejected out from the US focal zone, while the fluorescence variation of the new liposomes injected is smaller due to shorter time of US exposure.

In most cases the repeated static scanning was observed to overlap the original. This indicates that in these cases the perturbed liposomes were able to recover to its original state. It was also observed that when the solution was flowing, there is an occasional intensity drift both in the absence and presence of US, which could be due to an uneven distribution of liposomes inside the tube. Since the intensity difference and On-to-Off ratio are all relative values the intensity drift has little influence on the obtained scans but leads to a slightly higher standard deviation for the flowing cases. For Fig. 5.19 and Fig. 5.24 the highest intensity difference and On-to-Off ratio obtained were lower for the static case compared with the flowing case, and the second static scan has lower values compared with the first static scan. This might be because longer time is required for the 'perturbed' liposomes to return to its equilibrium state for these two cases. The bimodel observed in Fig. 5.19e and Fig. 5.24e also suggests that the US perturbations for these two cases might be more severe than the other cases.

It can be seen from Fig. 5.19 - Fig. 5.26 that the intensity differences obtained through detection at DiD emission wavelength are higher for DiD only liposomes compared with DiD-DiR labelled liposomes for all the cases studied. However, when detecting at DiR emission wavelength, DiD-DiR labelled liposomes produce a higher intensity difference compared with DiD liposomes (both at 0.1 mol% and 0.5 mol%, flowing case). The spatial resolution obtained from applying US is also greatly improved compared

with the resolution obtained without applying US for all the cases studied. Here the resolution is defined as the FWHM of the line scan image. The contrast and resolution of the line scan images for the flowing case are summarized in Table 5.7. The contrasts obtained from DiD-DiR labelled liposomes are higher than DiD only liposomes, indicating the important role FRET plays in enhancement of the US mediated fluorescence variation. The highest contrast is 9.0 %, obtained from DiD-DiR liposomes at 0.5 mol% through detecting at DiD emission wavelength. For tissue imaging fluorescence imaging at DiR wavelength is preferred. The contrast achieved through detecting at this wavelength is 8.5 % using DiD-DiR labelled liposomes with 0.5 mol% DiR concentration. The profile of the line scanned image is dependent on the overlapped region of the US field and the tube and also the sensitivity of the samples to US. The resolution is therefore determined by several factors including (1) the US focal zone (FWHM: 2.1 mm) (2) the size of the tube (inner diameter: 1.1 mm) and (3) the threshold for US to induce a detectable fluorescence variation for each of the cases studied. The resolution differences among the eight cases shown in Table 5.7 should be due to the third reason. The average resolution is 1.87 mm and the improvement compared with the case without using US is by a factor of 6.3.

Table 5.7: Resolution and contrast of the line scan images.

Sample	Detection wavelength	Resolution			Contrast
		With US (mm)	Without US (mm)	Improvement	
0.1 mol% DiD-DiR liposomes	DiD	1.79	11.81	6.6	7.8%
0.1 mol% DiD liposomes	DiD	1.63	11.61	7.1	3.3%
0.1 mol% DiD-DiR liposomes	DiR	1.70	10.67	6.3	5.8%
0.1 mol% DiD liposomes	DiR	1.55	12.27	7.0	4.6%
0.5 mol% DiD-DiR liposomes	DiD	1.46	10.85	7.4	9.0%
0.5 mol% DiD liposomes	DiD	2.59	13.34	5.2	1.3%
0.5 mol% DiD-DiR liposomes	DiR	2.38	11.84	5.0	8.5%
0.5 mol% DiD liposomes	DiR	1.93	11.12	5.8	2.5%

5.7 Discussion and conclusions

In this chapter nanoscale DiD-DiR labelled liposomes with NIR fluorescence emission were investigated as potential contrast agents for USMFT. The measurements of emission spectra show that strong FRET and self-quenching exist in the DiD-DiR labelled liposomes, with the efficiencies dependent on the fluorophore concentrations. Fluorescence variations were observed when the DiD-DiR labelled liposomes were exposed to US. The specific change trend depends on the fluorophore concentration and the detection wavelength. The concentrations of 0.1 mol% and 0.5 mol% were found to be thresholds for detection at DiD and DiR emission wavelength respectively for DiD-DiR labelled liposomes. On application of US, below this threshold an intensity decrease can be observed, above this threshold an intensity increase can be observed, while at this threshold the intensity was observed to firstly decrease followed by an increase. One useful application of these results is to quantitative determine the fluorophore concentration.

Line scanning of a tube with 1 mm inner diameter buried at a depth of 1 cm in a scattering phantom shows that the resolution can be improved around 6.3 times compared with its no US counterpart and a contrast of 9 % can be obtained. The important role FRET plays in enhancement of the US mediated fluorescence variation is seen from the much greater contrast achieved with the DiD-DiR system as compared to the case when DiD only liposomes were used. These results demonstrate that DiD-DiR labelled liposomes have potential to be used as contrast agent for fluorescence imaging at deep tissue to increase resolution.

The proposed mechanisms for US mediated fluorescence variation are the increased mobility of dye molecules and a size expansion during the US exposure. These mechanisms explain well the instantaneous responses of DiD-DiR labelled liposomes to US at various fluorophore concentrations. Due to the observation of a bimodel variation for some detection, it is also necessary to involve two mechanisms and compare their dominance. However, further experiments need to be performed to verify these mechanisms. Theoretical modeling of the dynamics of liposomes in US field is also desirable

to perform quantitative study. The imaging resolution (1.87 mm) obtained in this study is limited by the size of US focal zone (FWHM: 2.1 mm). An US transducer with higher frequency might be involved in the future to reduce the focal size and further improve the resolution. Despite the significantly improved resolution in a heavily scattering phantom, for *in vivo* imaging factors such as stability, pharmacokinetics, and biocompatibility need to be considered. Besides, the contrast agent would need to be attached with ligands for specific targeting. These would be the future work.

CHAPTER 6

Conclusions and future work

USMLT using various contrast agents has been presented in this thesis. This chapter provides conclusions of the research findings and suggests possible future work.

6.1 Conclusions

Fluorescence/bioluminescence imaging in deep biological tissue is a novel field developed only in recent years. In the first chapter of this thesis the challenges of FLI and BLI, which are mainly due to high tissue scattering and absorption, were highlighted. Several FLI and BLI techniques including fluorescence microscopy, FDOT, FLIM, and BLT were discussed. These techniques are limited either to superficial surface (fluorescence microscopy, FLIM) or by low resolution (FDOT, BLT). To get high resolution (< 1 mm) fluorescence or bioluminescence images in deep tissue (> 1 cm), several hybrid techniques combining fluorescence with US have been developed in recent years. Hybrid techniques including USMFT, TMFT, and TRUE based methods were reviewed in Chapter 1. All of these techniques have the potential to obtain high resolution fluorescence images in deep tissue, but they have drawbacks for further *in vivo* application. TMFT requires the contrast agent used has extremely high thermo-sensitivity. TRUE based fluorescence technique is limited in the speed at which it can operate to dynamic system, and it can not be used for BLI. USMFT faces the challenges of very low modulation depth which leads to low SNR.

As a result, all of the work presented in this thesis aims to increase modulation depth or On-to-Off ratio of USMLT and to analyze the underlying mechanisms, through application of contrast agents, including fluorophore labelled microbubbles and liposomes.

In the second chapter, the mechanisms of USMBLT were studied numerically by modification of NIRFAST, a package for modeling diffusely propagating light in tissue. The influences of US on the optical properties (reduced scattering coefficient, absorption coefficient, and refractive index) and concentration of source particles were firstly analysed. The US modulated bioluminescence fluence rate was then simulated. Effects of the optical properties, source particle concentration, US pressure, and US position on the modulation depth were investigated. The SNR for *in vivo* detection was also calculated to explore the feasibility of applying USMBLT for pre-clinical imaging. It was demonstrated that the dominant effect in generation of USMBL signal is US induced variation in the concentration of the source particles, and this effect is at least two orders of magnitude greater than that caused by changes in the optical properties. It is also found that modulation depth increases linearly with increase of US pressure. The maximum modulation depth can be obtained when the US focal zone overlaps the bioluminescence source region. The modulated fluence rate increases linearly with increase of the concentration but the modulation depth is independent of the concentration. Further, it can be concluded that the compressibility of the source particles is an important factor for the modulation depth, indicating application of contrast agents such as microbubbles can increase the modulation depth. Results for SNR calculation confirm the feasibility of applying USMBLT in preclinical imaging of mice to improve the spatial resolution of BLI.

In the third chapter, the application of fluorophore labelled microbubbles in USMFT was theoretically investigated. Initial experiments were also performed to demonstrate the increased modulation depth. The fluorophores were labelled on the shell of the microbubbles, which were tuned to be self-quenched. Upon application of US the microbubbles oscillate changing the intermolecular distances of the fluorophores resulting in a modulated fluorescence signal. The volumetric oscillation of fluorophore labelled microbubble and its fluorescence emission intensity with or without applica-

tion of US were simulated. The influences of factors including microbubble radius, fluorophore concentration, and US pressure on the US modulated fluorescence signal were studied. The modulation depth and SNR with fluorophore labelled microbubbles located inside a scattering medium were simulated. It was shown that the effects of the three factors are closely related to each other, and it is difficult to decouple their effects. Generally the maximum modulated signal can be obtained within the region $C \in (2\,\text{mol\%}\ 5\,\text{mol\%})$ and $R_0 \in (1.5\,\mu\text{m}\ 5\,\mu\text{m})$. However microbubbles with different size may have different optimum concentration. Also microbubbles with a higher fluorophore labelling concentration or a bigger radius require higher US pressure to obtain its maximum volumeric oscillation and obtain the highest modulated signal. Therefore it is desirable to produce microbubble suspensions having narrow size distribution, so that most of the microbubbles can be labelled by an optimized concentration and exposed to an appropriate US pressure. This might be achieved using the newly emerged microbubble preparation technologies such as membrane emulsification, electrohydrodynamic atomisation and microfluidic processing [164].

In the fourth and fifth chapters a new approach to enhancement of fluorescent signals by US based on the use of nanoscale fluorophore labelled liposomes was demonstrated experimentally. Liposomes can be manufactured routinely with a defined size. In addition, compared with microbubbles, liposomes have advantages such as they have much better stability, less US scattering and nanoscale size. In the fourth chapter liposomes containing lipids labelled with the fluorophore pyrene were optically excited and the excimer fluorescence emission intensity was detected in the absence and presence of an US field. The acousto-fluorescence dynamics of liposomes containing lipids with pyrene labelled on the fatty acid tail group (PyPC) and the head group (PyPE) were compared. An increase in excimer emission intensity following exposure to US was observed for both cases studied. The increased intensity and time constants were found to be different for the PyPC and PyPE labelled liposomes, and dependent on the applied US pressure and exposure time. The greatest US On-to-Off ratio (130%) and smallest rise time constant (0.33 s) are achieved through the use of the PyPC labelled liposomes. Possible mechanisms underlying the observed increase of the excimer emis-

sion intensity in the PyPC labelled liposomes is considered to arise from the 'wagging' of acyl chains which involves fast response and requires lower US pressure. This is accompanied with the increased lipid lateral diffusivity, mechanisms also active in the PyPE labelled liposomes.

However, the excitation and emission wavelengths of pyrene are too short for deep tissue imaging. In the fifth chapter DiD-DiR labelled liposomes based on FRET were studied with the excitation and emission spectra located close or within the NIR window (650 nm-1000 nm), where the penetration depth can get up to several centimeters. It was observed that strong FRET and SQ exist in the donor-acceptor pair labelled liposomes. The fluorescence emission intensity is very sensitive to the applied US, with the specific change trend dependent on types of fluorophores (DiD only liposomes, DiR only liposomes, or DiD-DiR labelled liposomes), detecting wavelength (DiD emission wavelength or DiR emission wavelength), and fluorophore concentration (0.1 mol% or 0.5 mol%). The concentrations of 0.1 mol% and 0.5 mol% were found to be thresholds for detection at DiD and DiR emission wavelengths respectively for DiD-DiR labelled liposomes. Below this threshold an intensity decrease can be observed, above this threshold an intensity increase can be observed, while at this threshold the intensity was observed to firstly decrease followed by an increase. Line scanning of a tube buried at a depth of 1 cm in a heavily scattering phantom shows a contrast of 8.5% can be obtained using 0.5 mol% DiD-DiR labelled liposomes through detection at DiR emission wavelength (around 740 nm - 790 nm). The resolution can be improved by a factor of 6.3 compared with its no US counterpart. These results demonstrate that DiD-DiR labelled liposome has potential to be used as enhancement agent for *in vivo* deep tissue or whole-body small animal imaging with high resolution.

6.2 Future work

Current development of USMLT and the work carried out in this thesis have demonstrated that USMLT is a promising technique to increase the resolution and imaging depth of FLI and BLI. However, there is still much research to be done before it can be

used as a routine preclinical imaging method. This section outlines several proposals for the future work in terms of the contrast agents in USMLT.

6.2.1 Experimental demonstration of USMBLT

Theoretical modeling in Chapter 2 suggests that using an US with frequency 1 MHz and peak pressure 1 MPa, a modulation depth of 6.1×10^{-5} can be obtained for USMBLT. The corresponding SNR is 5.3 dB with the same setup used in [55] for a surface radiance of 10^9 photons $s^{-1}\,cm^{-2}\,sr^{-1}$. This suggest that the experimental demonstration of USMBLT is promising. The challenge is still the very low modulation depth. To improve the axial resolution US needs to be operated at pulsed mode. This can further decrease modulation depth because less source particles are exposed to US. One method to address this is to increase the compressibility of the luciferase-luciferin solution, which might be achieved through application of microbubbles. Another method might be to modulate or enhance the BRET efficiency. In BRET, the donor fluorophore of the FRET technique is replaced by a luciferase. In the presence of a substrate, bioluminescence from the luciferase excites the acceptor fluorophore through the same FRET mechanisms [247]. Therefore a luciferase-fluorophore labelled microbubble/liposome system might be developed to improve the spatial resolution of BLI. The advantage of this scenario is that no external light source is used, therefore the high sensitivity of BLI is maintained. Also due to the application of fluorophores, the light level is improved compared with pure bioluminescence, which can result of a higher SNR.

6.2.2 Further optimization of fluorophore labelled liposomes

Further optimization of the fluorophore labelled liposomes can be performed by evaluating several factors, including sensitivity, resolution and stability.

Echogenic liposomes are being investigated intensively in recent years. For example, they are being developed as multifunctional theranostic agents for detection of atherosclerotic plaques and for image-guided US-mediated delivery of therapeutics to treat cardiovascular diseases [248]. By enclosing small gas bubbles inside the lipid bi-

layer, echogenic liposomes are able to scatter US more effectively. It would be very interesting to develop echogenic liposomes labelled by donor-acceptor or fluorophores that have excimer formation characteristic. The aim of this investigation is to increase the sensitivity of the contrast agent to US and potentially reduce the required US pressure and exposure time based on the work carried out in this thesis. This is desirable considering the possible side-effect to biological tissue caused by high pressure US exposure for a long duration. This is also beneficial to reduce the acquisition time of imaging.

Imaging resolution of USMFT is determined by the US focal zone, the lateral size of which is dependant on the US frequency. In this thesis a 2.25 MHz US transducer was used and scanning images were obtained with an average FWHM resolution of 1.87 mm. The lateral resolution might be further reduced through application of US transducer with a higher US frequency and a smaller lateral size. The axial size of the US focal zone is much bigger - around 20 mm. To achieve a high axial resolution short US pulses in combination with strobing illumination for time-gating might be employed in the future. Another possible method to improve the axial resolution is to use two US transducers with an angle of 90 degree. The intersectional volume of the two US focal zone can have a much shorter axial size compared with the axial size when only one US transducer is used. This method has been used for TRUE and a 2.5 times improvement of axial resolution is achieved [249]. Other techniques developed to improve axial resolution of US modulated optical tomography (e.g frequency-swept [250], random phase jumps [251]) might also be used.

It has been established that liposomal stability *in vivo* is directly related to vesicle half-life in the blood circulation - the more stable the vesicles are, the longer they circulate in the blood [159]. For imaging and diagnosis purposes a short circulation time of a few hours might be enough. However, for longitudinal monitoring of drugs loaded liposomes following the start of therapy, longer circulation time up to one month might be necessary. Therefore control over the physical stability of liposomes becomes an important prerequisite for their effective use. One method to increase the stability of liposomes is to add cholesterol to liposome bilayers. However, the influence of choles-

terol on the US induced fluorescence intensity variation needs to be characterized because its lipid condensing effect [236] might change the response of the liposomes upon sonification.

6.2.3 Further investigation of mechanisms

Another future work is to further investigate the mechanisms of the US induced fluorescence variation of the fluorophore labelled liposomes. In this thesis noninertial cavitation of gas bubbles pre-existing in the fluid is proposed as the original mechanism for US to stimulate a change of the lateral diffusion of the lipids. This might be demonstrated through degassing the suspension of fluorophore labelled liposomes. As a result of the liquid core, liposomes are relatively incompressible. However, since FRET occurs in the length scale of 1 nm to 10 nm, a small change of the volume might change the fluorescence emission intensity. To test whether the fluorophore labelled liposomes oscillate volumetrically in US field and whether this contributes to the fluorescence variation (a mechanism similar to fluorophore labelled microbubbles), comparison experiments involving planar lipid bilayer labelled with donor-acceptor can be performed.

It is also desirable to quantitatively measure lateral and transbilayer mobility of lipids with and without application of US, with different movements decoupled. Most of the methods to measure the lateral diffusion of membrane lipids, such as fluorescence recovery after photobleaching, fluorescence correlation spectroscopy, and single particle tracking [252], are restricted by the resolution of the optical microscope involved and can only work at micrometer length scale. It is therefore very challenging to measure the lateral diffusion of lipids in liposomes with only 100 nm diameter.

The transbilayer movement of lipids is often assessed using a dithionite-based assay. Dithionite can reduce the fluorescent Nitro-2,1,3-benzoxadiazol-4-yl (NBD) to non-fluorescent with a half-time of $\sim$ 20 s [197]. The schematic of the dithionite assay is shown in Fig. 6.1. When liposomes labelled with NBD-labelled analogs (e.g.: C6-NBD-PC) on both of its two leaflets are exposed to dithionite, the fluorescence intensity decreases and eventually plateaus at 50% of its original intensity. This is because

only fluorescence from the outer leaflet of the bilayer is quenched and the new plateau represents the analogs on the inner leaflet [197]. If the remaining NBD is exposed to dithionite through disruption of the membrane [253], or increase of transbilayer movement [197], the fluorescence emission intensity would be further reduced. A similar method can be employed for investigation of the influence of US on the transbilayer movement of PyPC and PyPE in liposomes. In this case iodide ions might be applied, which are quenchers for pyrene fluorescence through collisional quenching [254].

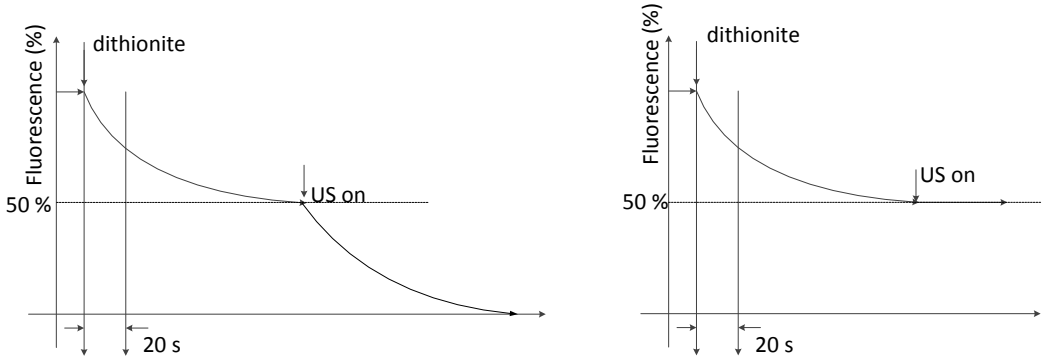


Figure 6.1: Schematic of the dithionite assay. (a) Transbilayer movement was induced by US; (b) no transbilayer movement induced.

Since the lifetime of the fluorophore is dependent on FRET efficiency, it would be interesting to study the influence of US on the lifetime of the fluorophores labelled in the liposomes. The advantage of time-resolved over intensity-based measurements is the ability to directly distinguish between effects due to FRET or probe concentration. For example, a low donor fluorescence intensity can be caused by either a low donor concentration or efficient quenching by FRET but only in the latter case is the fluorescence decay shortened. Furthermore, fluorescence lifetime based measurements can help determine SQ mechanisms. Nonfluorescent dimer formation alone would not change the lifetime [75]. Therefore if a change of lifetime was observed, SQ was due to either fluorescence energy transfer to dimers or collisional quenching. If no change of lifetime was observed, SQ was due only to nonfluorescent dimer formation.

6.2.4 Future applications of USMFT using fluorophore labelled liposomes

There are large amounts of potential applications that can be explored using USMFT with the developed fluorophore labelled liposomes. With USMFT the existing application of fluorescence imaging using exogenous fluorophores might be performed in intact and native physiological state. For example, biodistribution of liposomes is studied usually through examination of the removed organs after the mice are euthanized [255, 256]. With USMFT it is possible to noninvasively monitor the biodistribution (also targeting, uptaking, and therapeutic efficiency) of liposome-encapsulated drugs without having to excise the animals.

A clinically valuable application of USMFT using pyrene labelled liposomes is the optical detection of tissue microenvironment such as oxygen concentration, pH, iron concentration and other properties which can indicate diseases. Since pyrene and its derivatives have a long excited state lifetime and are efficiently quenched by oxygen [211], pyrene-labelled liposomes as an optical oxygen sensor to monitor tissue oxygen concentrations is a promising application. The linear regression curve obtained for emission intensity ratio of excimer and monomer intensity with Cu^{2+} concentration [212] also suggests the possibility of using pyrene-labelled liposomes as a fluorosensor for detecting Cu^{2+} ions in living cells. However, due to the short penetration depth of pyrene fluorescence, detection is limited to superficial tissue.

Excimer lablled liposomes at longer wavelength might be achieved using dyes from the difluoro-boraindacene family (4,4-difluoro-4-bora-3a,4a-diaza-s-indacene, abbreviated hereafter as BODIPY). BODIPY dyes have the emission wavelength maximum ranging from $\lambda = 510\,\text{nm}$ to 665 nm. Several BODIPY dyes, for example BODIPY-FL-ceramide, also has the concentration dependent excimer formation characteristic [217]. In addition, BODIPY dyes combine many advantages and have been developed for various biological applications. For example, the C16-BODIPY-FL was developed for detection of lipid peroxidation on red blood cells (RBC) using its excimer formation property [217]. Upon addition of cumene hydroperoxide or benzoyl peoxide to exadecanoyl-BODIPY-labelled RBC suspensions, the monomer emission peak initially increases, then de-

creases, while the excimer peaks continuously decrease. The ratio of the excimer to monomer ratio can thus be used to monitor the onset of lipid peroxidation [217]. Other applications include labels for biomolecules, indicators for proton and metal ions, stains for organelles and substrates for enzymes [257]. With application of BODIPY labelled liposomes as contrast agent of USMFT, it is promising to obtain this information in deeper tissue.

6.2.5 Concerns for *in vivo* imaging using the fluorophore labelled liposomes

There are some concerns for *in vivo* imaging using the fluorophore labelled liposomes. The effect of biological fluids, especially blood with which liposomes come into contact on injection, might change the properties of the liposomes. Interaction of liposomes with blood components such as plasma high density lipoproteins (HDL) might lead to leaky vesicles. It was claimed that phospholipid loss to HDL for liposomes made from 'high melting' phospholipid such as DPPC (used in this thesis) is reduced greatly [159]. Still chemical and physical processes such as hydrolysis of the ester bonds linking the fatty acids to the glycerol backbone, aggregation/flocculation and fusion/coalescence [258] might affect the performance of liposomes and need to be evaluated for effective *in vivo* imaging.

It was demonstrated that given intravenous injection liver, spleen, and bone marrow intercept most of the liposomes, while for subcutaneous injection much of the liposomes retained at the site of injection [159]. Therefore to obtain fluorescence images at other anatomical sites such as the kidney, heart and bladder, it might be more effective to modify the fluorophore labelled liposomes so that it can target a specific moiety such as a receptor. This could be done by attaching the liposomes to site-directing ligands that can bind and interact with specific cellular or tissue epitopes. Numerous approaches have been developed in the field of drug delivery for liposome targeting using site-directing ligands. For example, PGN635 is a human monoclonal antibody that specifically targets phosphatidylserine, which is normally constrained to the inner plasma membrane but becomes exposed on the surface of endothelial cells in tumor vasculature. Liposomes conjugated with PGN635 exhibited localization to tumor and

significantly reduced accumulations in liver or spleen [259]. One concern for modification of the fluorophore labelled liposomes is that the attached ligands might influence the US dynamics of the fluorophore labelled liposomes through change of the physical properties of lipid bilayer such as the lipid density. Therefore care should be taken to maintain the desirable properties of fluorophore labelled lipsomes when using ligand targeting.

References

[1] G. Choy, S. O'Connor, F. E. Diehn, N. Costouros, H. R. Alexander, P. Choyke, and S. K. Libutti, "Comparison of noninvasive fluorescent and bioluminescent small animal optical imaging," *Biotechniques*, vol. 35, no. 5, pp. 1022 – 1026, 2003.

[2] C. Balas, "Review of biomedical optical imaging - a powerful, non-invasive, non-ionizing technology for improving in vivo diagnosis," *Meas. Sci. Technol.*, vol. 20, no. 10, p. 104020, 2009.

[3] A. P. Dhawan, B. D'Alessandro, and X. Fu, "Optical imaging modalities for biomedical applications," *IEEE Rev. Biomed. Eng.*, vol. 3, pp. 69–92, 2010.

[4] M. Hassan and B. A. Klaunberg, "Biomedical applications of fluorescence imaging in vivo," *Comparative Med.*, vol. 54, no. 6, pp. 635 – 644, 2004.

[5] J. Rao, A. Dragulescu-Andrasi, and H. Yao, "Fluorescence imaging in vivo: recent advances," *Curr. Opin. Biotechnol.*, vol. 18, no. 1, pp. 17 – 25, 2007.

[6] F. Leblond, S. C. Davis, P. A. Valdés, and B. W. Pogue, "Pre-clinical whole-body fluorescence imaging: review of instruments, methods and applications," *J. Photoch. Photobio. B.*, vol. 98, no. 1, pp. 77 – 94, 2010.

[7] S. M. Marques and J. C. E. da Silva, "Firefly bioluminescence: a mechanistic approach of luciferase catalyzed reactions," *IUBMB Life*, vol. 61, no. 1, pp. 6 – 17, 2009.

[8] C. E. Badr and B. A. Tannous, "Bioluminescence imaging: progress and applications," *Trends Biotechnol.*, vol. 29, no. 12, pp. 624 – 633, 2011.

[9] A. Puaux, L. C. Ong, Y. Jin, I. Teh, M. Hong, P. K. H. Chow, X. Golay, and J. Abastado1, "A comparison of imaging techniques to monitor tumor growth and cancer progression in living animals," *Int. J. Mol. Imaging*, vol. 2001, no. 2011,

p. 321538, 2011.

[10] S. A. Hilderbrand and R. Weissleder, "Near-infrared fluorescence: application to in vivo molecular imaging," *Curr. Opin. Chem. Biol.*, vol. 14, no. 1, pp. 71 – 79, 2010.

[11] S. Vaezy and V. Zderic, *Image-Guided Therapy Systems*. Artech House engineering in medicine & biology series, Artech House, 2009.

[12] S. L. Jacques, "Optical properties of biological tissues: a review," *Phys. Med. Biol.*, vol. 58, no. 11, pp. R37–61, 2013.

[13] J. Escobedo, O. Rusin, S. Lim, and R. M. Strongin, "NIR dyes for bioimaging applications," *Curr. Opin. Chem. Biol.*, vol. 14, no. 1, pp. 64 – 70, 2010.

[14] V. J. Pansare, S. Hejazi, W. J. Faenza, and R. K. Prud'homme, "Review of long-wavelength optical and NIR imaging materials: contrast agents, fluorophores, and multifunctional nano carriers," *Chem. Mater.*, vol. 24, no. 5, pp. 812–827, 2012.

[15] M. L. Landsman, G. Kwant, G. A. Mook, and W. G. Zijlstra, "Light-absorbing properties, stability, and spectral stabilization of indocyanine green," *J. Appl. Physiol.*, vol. 40, no. 4, pp. 575–583, 1976.

[16] K. Kadish, K. Smith, and R. Guliard, *The Porphyrin Handbook*. Boston, USA: Academic Press, 2011.

[17] J. F. Lovell, C. S. Jin, E. Huynh, H. Jin, C. Kim, J. L. Rubinstein, W. C. W. Chan, W. Cao, L. Wang, and G. Zheng, "Porphysome nanovesicles generated by porphyrin bilayers for use as multimodal biophotonic contrast agents," *Nat. Mater.*, vol. 10, pp. 324–332, 2011.

[18] W. Stummer, A. Novotny, H. Stepp, C. Goetz, K. Bise, and H. J. Reulen, "Fluorescence-guided resection of glioblastoma multiforme utilizing 5-ALA-induced porphyrins: a prospective study in 52 consecutive patients," *J. Neurosurg.*, vol. 93, no. 6, pp. 1003–1013, 2000.

[19] X. Zhang, Y. Xiao, J. Qi, J. Qu, B. Kim, X. Yue, and K. D. Belfield, "Long-wavelength, photostable, two-photon excitable bodipy fluorophores readily modifiable for molecular probes," *J. Org. Chem.*, vol. 78, no. 18, pp. 9153–9160, 2013.

[20] A. P. Jathoul, H. Grounds, J. C. Anderson, and M. A. Pule, "A dual-color far-red to near-infrared firefly luciferin analogue designed for multiparametric bioluminescence imaging," *Angew. Chem. Int. Edit.*, vol. 53, no. 48, pp. 13059 – 13063, 2014.

[21] R. Weissleder, *Molecular Imaging: Principles and Practice*. People's Medical Publishing House, 2010.

[22] R. Alam, L. M. Karam, T. L. Doane, J. Zylstra, D. M. Fontaine, B. R. Branchini, and M. M. Maye, "Near infrared bioluminescence resonance energy transfer from firefly luciferase - quantum dot bionanoconjugates," *Nanotechnology*, vol. 25, no. 49, p. 495606, 2014.

[23] A. Diaspro, *Nanoscopy and Multidimensional Optical Fluorescence Microscopy*. CRC Press, 2010.

[24] B. O. Leung and K. C. Chou, "Review of super-resolution fluorescence microscopy for biology," *Appl. Spectrosc.*, vol. 65, no. 9, pp. 967 – 980, 2011.

[25] S. I. J. Ellenbroek and J. V. Rheenen, "Imaging hallmarks of cancer in living mice," *Nat. Rev. Cancer*, vol. 14, pp. 406 – 418, 2014.

[26] Y. Lin, H. Gao, O. Nalcioglu, and G. Gulsen, "Fluorescence diffuse optical tomography with functional and anatomical a priori information: feasibility study," *Phys. Med. Biol.*, vol. 52, no. 18, p. 5569, 2007.

[27] C. T. Xu, P. Svenmarker, H. Liu, X. Wu, M. E. Messing, L. R. Wallenberg, and S. Andersson-Engels, "High-resolution fluorescence diffuse optical tomography developed with nonlinear upconverting nanoparticles," *ACS Nano*, vol. 6, no. 6, pp. 4788 – 4795, 2012.

[28] N. Ducros, C. D'Andrea, A. Bassi, and F. Peyrin, "Fluorescence diffuse optical tomography: time-resolved versus continuous-wave in the reflectance configuration," *IRBM*, vol. 32, no. 4, pp. 243 – 250, 2011.

[29] P. Svenmarker, C. T. Xu, H. Liu, X. Wu, and S. Andersson-Engels, "Multispectral guided fluorescence diffuse optical tomography using upconverting nanoparticles," *Appl. Phys. Lett.*, vol. 104, no. 7, p. 073703, 2014.

[30] W. Becker, *Advanced Time-Correlated Single Photon Counting Applications*. Springer

Series in Chemical Physics, Springer International Publishing, 2015.

[31] K. Suhling, L. M. Hirvonen, J. A. Levitt, P. Chung, C. Tregidgo, A. L. Marois, D. A. Rusakov, K. Zheng, S. Ameer-Beg, S. Poland, S. Coelho, R. Henderson, and N. Krstajic, "Fluorescence lifetime imaging (FLIM): basic concepts and some recent developments," *Medical Photonics*, vol. 27, pp. 3 – 40, 2015.

[32] S. Rajoria, L. Zhao, X. Intes, and M. Barroso, "FLIM-FRET for cancer applications," *Curr. Mol. Imaging*, vol. 3, no. 2, pp. 144 – 161, 2014.

[33] W. L. Rice and A. T. N. Kumar, "Preclinical whole body time domain fluorescence lifetime multiplexing of fluorescent proteins," *J. Biomed. Opt.*, vol. 19, no. 4, p. 046005, 2014.

[34] W. L. Rice, D. M. Shcherbakova, V. V. Verkhusha, and A. T. N. Kumar, "In vivo tomographic imaging of deep-seated cancer using fluorescence lifetime contrast," *Cancer Research*, vol. 75, no. 7, pp. 1236–1243, 2015.

[35] A. Roda, P. Pasini, M. Mirasoli, E. Michelini, and M. Guardigli, "Biotechnological applications of bioluminescence and chemiluminescence," *Trends Biotechnol.*, vol. 22, no. 6, pp. 295 – 303, 2004.

[36] C. Qin, J. Feng, S. Zhu, X. Ma, J. Zhong, P. Wu, Z. Jin, and J. Tian, "Recent advances in bioluminescence tomography: methodology and system as well as application," *Laser Photonics Rev.*, vol. 8, no. 1, pp. 94 – 114, 2014.

[37] A. Roda and M. Guardigli, "Analytical chemiluminescence and bioluminescence: latest achievements and new horizons," *Anal. Bioanal. Chem.*, vol. 402, no. 1, pp. 69 – 76, 2012.

[38] A. Chaudhari, F. Darvas, J. R. Bading, R. A. Moats, P. S. Conti, D. J. Smith, S. R. Cherry, and R. M. Leahy, "Hyperspectral and multispectral bioluminescence optical tomography for small animal imaging," *Phys. Med. Biol.*, vol. 50, no. 23, p. 5421, 2005.

[39] H. Dehghani, S. C. Davis, and B. W. Pogue, "Spectrally resolved bioluminescence optical tomography," *Opt. Lett.*, vol. 31, no. 3, pp. 365 – 367, 2006.

[40] H. R. A. Basevi, K. M. Tichauer, F. Leblond, H. Dehghani, J. A. Guggenheim, R. W. Holt, and I. B. Styles, "Compressive sensing based reconstruction in biolumines-

cence tomography improves image resolution and robustness to noise," *Biomed. Opt. Express*, vol. 3, no. 9, pp. 2131–2141, 2012.

[41] D. M. Close, T. Xu, G. S. Sayler, and S. Ripp, "In vivo bioluminescent imaging (BLI): noninvasive visualization and interrogation of biological processes in living animals," *Sensors*, vol. 11, no. 1, p. 180, 2010.

[42] T. Ozawa, H. Yoshimura, and S. B. Kim, "Advances in fluorescence and bioluminescence imaging," *Anal. Chem.*, vol. 85, no. 2, pp. 590 – 609, 2013.

[43] J. Huang, Y. Li, J. Massague, A. Sicheneder, D. A. Vallera, and W. A. Hall, "Intracerebral infusion of the bispecific targeted toxin dtategf in a mouse xenograft model of a human metastatic non-small cell lung cancer," *J. Neuro-Oncol.*, vol. 109, no. 2, pp. 229 – 238, 2012.

[44] D. M. Barrett, A. E. Seif, and C. Carpenito, "Noninvasive bioluminescent imaging of primary patient acute lymphoblastic leukemia: a strategy for preclinical modeling," *Blood*, vol. 118, no. 15, pp. e112 – e117, 2011.

[45] F. Hiroya, N. Kenichi, A. Yasuo, K. Akio, S. Minoru, and T. Akihiko, "Increase in bioluminescence intensity of firefly luciferase using genetic modification," *Anal. Biochem.*, vol. 366, no. 2, pp. 131 – 136, 2007.

[46] K. Noda, T. Matsuno, H. Fujii, T. Kogure, M. Urata, Y. Asami, and A. Kuroda, "Single bacterial cell detection using a mutant luciferase," *Biotechnol. Lett.*, vol. 30, no. 6, pp. 1051 – 1054, 2008.

[47] Y. Nakajima, T. Yamazaki, S. Nishii, H. H. T. Noguchi, K. Niwa, V. R. Viviani, and Y. Ohmiya, "Enhanced beetle luciferase for highresolution bioluminescence imaging," *PLoS ONE*, vol. 5, no. 4, p. e10011, 2010.

[48] M. P. Hall, J. Unch, B. F. Binkowski, M. P. Valley, B. L. Butler, M. G. Wood, P. Otto, K. Zimmerman, G. Vidugiris, T. Machleidt, M. B. Robers, H. A. Benink, C. T. Eggers, M. R. Slater, P. L. Meisenheimer, D. H. Klaubert, F. Fan, L. P. Encell, and K. V. Wood, "Engineered luciferase reporter from a deep sea shrimp utilizing a novel imidazopyrazinone substrate," *ACS Chem. Biol.*, vol. 7, no. 11, pp. 1848 – 1857, 2012.

[49] K. Saito, Y. F. Chang, K. Horikawa, N. Hatsugai, Y. Higuchi, M. Hashida,

Y. Yoshida, T. Matsuda, Y. Arai, and T. Nagai, "Luminescent proteins for high-speed single-cell and whole-body imaging," *Nat. Commun.*, vol. 3, p. 1262, 2012.

[50] M. Keyaerts, V. Caveliers, and T. Lahoutte, "Bioluminescence imaging: looking beyond the light," *Trends Mol. Med.*, vol. 18, no. 3, pp. 164 – 172, 2012.

[51] K. Niwa, Y. Ichino, S. Kumata, Y. Nakajima, H. Y., D. Kato, V. R. Viviani, and O. Y., "Quantum yields and kinetics of the firefly bioluminescence reaction of beetle luciferases.," *Photochem. Photobiol.*, vol. 86, no. 5, pp. 1046 – 1049, 2010.

[52] S. G. Resink, A. C. Boccara, and W. Steenbergen, "State-of-the art of acousto-optic sensing and imaging of turbid media," *J. Biomed. Opt.*, vol. 17, no. 4, pp. 040901–1, 2012.

[53] M. Kobayashi, T. Mizumoto1, Y. Shibuya, M. Enomoto, and M. Takeda, "Fluorescence tomography in turbid media based on acousto-optic modulation imaging.," *Appl. Phys. Lett.*, vol. 89, no. 18, p. 181102, 2006.

[54] B. Yuan, "Ultrasound-modulated fluorescence based on a fluorophore-quencher-labeled microbubble system," *J. Biomed. Opt.*, vol. 14, no. 2, pp. 024043–11, 2009.

[55] N. T. Huynh, B. R. Hayes-Gill, F. Zhang, and S. P. Morgan, "Ultrasound modulated imaging of luminescence generated within a scattering medium.," *J. Biomed. Opt.*, vol. 18, no. 2, p. 020505, 2013.

[56] B. Yuan, S. Uchiyama, Y. Liu, K. T. Nguyen, and G. Alexandrakis, "High-resolution imaging in a deep turbid medium based on an ultrasound-switchable fluorescence technique," *Appl. Phys. Lett.*, vol. 101, no. 3, p. 033703, 2012.

[57] Y. Lin, L. Bolisay, M. Ghijsen, T. C. Kwong, and G. Gulsen, "Temperature-modulated fluorescence tomography in a turbid media," *Appl. Phys. Lett.*, vol. 100, no. 7, p. 073702, 2012.

[58] Y. Lin, T. C. Kwong, L. Bolisay, and G. Gulsen, "Temperature-modulated fluorescence tomography based on both concentration and lifetime contrast," *J. Biomed. Opt.*, vol. 17, no. 5, pp. 056007–1, 2012.

[59] Y. Pei, M. Wei, B. Cheng, Y. Liu, Z. Xie, K. Nguyen, and B. Yuan, "High resolution imaging beyond the acoustic diffraction limit in deep tissue via ultrasound-switchable NIR fluorescence," *Sci. Rep.*, vol. 4, p. 4690, 2014.

[60] B. Cheng, M. Y. Wei, Y. Liu, H. Pitta, Z. Xie, Y. Hong, K. T. Nguyen, and B. Yuan, "Development of ultrasound-switchable fluorescence imaging contrast agents based on thermosensitive polymers and nanoparticles," *IEEE J. Sel. Top. Quantum Electron.*, vol. 20, no. 3, pp. 67–80, 2014.

[61] Y. M. Wang, B. Judkewitz, C. A. DiMarzio, and C. Yang, "Deep-tissue focal fluorescence imaging with digitally time-reversed ultrasound-encoded light," *Nat. Commun.*, vol. 3, p. 928, 2012.

[62] K. Si, R. Fiolka, and M. Cui, "Fluorescence imaging beyond the ballistic regime by ultrasound-pulse-guided digital phase conjugation," *Nat. Photon.*, vol. 6, no. 10, pp. 657 – 661, 2012.

[63] P. Lai, Y. Suzuki, X. Xu, and L. V. Wang, "Focused fluorescence excitation with time-reversed ultrasonically encoded light and imaging in thick scattering media," *Laser Phys. Lett.*, vol. 10, no. 7, p. 075604, 2013.

[64] Y. Liu, B. Yuan, and J. Vignola, "Effect of fluorescent particle size on the modulation efficiency of ultrasound-modulated fluorescence.," *Int. J. Opt.*, vol. 2012, p. 260709, 2012.

[65] D. J. Hall, U. Sunar, and S. Farshchi-Heydari, "Quadrature detection of ultrasound-modulated photons with a gain-modulated, image-intensified, ccd camera," *The Open Optics Journal*, vol. 2, pp. 75 – 78, 2008.

[66] M. Kobayashi, N. Kikuchi, and A. Sato, "Optical tomography of fluorophores in dense scattering media based on ultrasound-enhanced chemiluminescence," *Appl. Phys. Lett.*, vol. 106, no. 2, p. 021103, 2015.

[67] A. I. of Ultrasound in Medicine, "Section 2 - definitions and description of nonthermal mechanisms," in *Mechanical Bioeffects From Diagnostic Ultrasound: AIUM Consensus Statements*, vol. 19, pp. 77–84, 2000.

[68] G. Bal and J. C. Schotland, "Ultrasound-modulated bioluminescence tomography," *Phys. Rev. E*, vol. 89, p. 031201, 2014.

[69] Q. Liu, S. Norton, and T. Vo-Dinh, "Modeling of nonphase mechanisms in ultrasonic modulation of light propagation.," *Appl. Opt.*, vol. 47, no. 20, pp. 3619 – 3630, 2008.

[70] T. Duc, S. Kaneta, and M. Kobayashi, "Study on mechanism of ultrasonic fluorescence modulation in light scattering medium based on diffusion approximation with varying refractive index," *Opt. Rev.*, vol. 19, no. 3, pp. 159 – 166, 2012.

[71] B. Yuan, J. Gamelin, and Q. Zhu, "Mechanisms of the ultrasonic modulation of fluorescence in turbid media," *J. Appl. Phys.*, vol. 104, no. 10, p. 103102, 2008.

[72] K. Vishwanath and M. Mycek, "Polystyrene microspheres in tissue-simulating phantoms can collisionally quench fluorescence," *J. Fluoresc.*, vol. 13, no. 1, pp. 105 – 108, 2003.

[73] M. Kobayashi, T. Mizumoto, T. Q. Duc, and M. Takeda, "Fluorescence tomography of biological tissue based on ultrasound tagging technique," in *Biophotonics 2007: Optics in Life Science*, pp. 6633 – 5, Optical Society of America, 2007.

[74] B. Yan, P. C. Martin, and J. Lee, "Single-bead fluorescence microspectroscopy: detection of self-quenching in fluorescence-labeled resin beads," *J. Comb. Chem.*, vol. 1, no. 1, pp. 78 – 81, 1999.

[75] R. F. Chen and J. R. Knutson, "Mechanism of fluorescence concentration quenching of carboxyfluorescein in liposomes: energy transfer to nonfluorescent dimers," *Anal. Biochem.*, vol. 172, no. 1, pp. 61 – 77, 1988.

[76] X. Xu, H. Liu, and L. V. Wang, "Time-reversed ultrasonically encoded optical focusing into scattering media," *Nat. Photon.*, vol. 5, no. 3, pp. 154 – 157, 2011.

[77] P. Lai, X. Xu, H. Liu, Y. Suzuki, and L. V. Wang, "Reflection-mode time-reversed ultrasonically encoded optical focusing into turbid media," *J. Biomed. Opt.*, vol. 16, no. 8, pp. 080505–3, 2011.

[78] H. Liu, X. Xu, P. Lai, and L. V. Wang, "Time-reversed ultrasonically encoded optical focusing into tissue-mimicking media with thickness up to 70 mean free paths," *J. Biomed. Opt.*, vol. 16, no. 8, pp. 086009–6, 2011.

[79] P. Lai, X. Xu, H. Liu, and L. V. Wang, "Time-reversed ultrasonically encoded optical focusing in biological tissue," *J. Biomed. Opt.*, vol. 17, no. 3, pp. 030506–1, 2012.

[80] Y. Suzuki, X. Xu, P. Lai, and L. V. Wang, "Energy enhancement in time-reversed ultrasonically encoded optical focusing using a photorefractive polymer," *J.*

Biomed. Opt., vol. 17, no. 8, pp. 080507–1, 2012.

[81] B. Jayet, J. P. Huignard, and F. Ramaz, "Optical phase conjugation in Nd:YVO4 for acousto-optic detection in scattering media," *Opt. Lett.*, vol. 38, no. 8, pp. 1256–1258, 2013.

[82] B. Jayet, J. P. Huignard, and F. Ramaz, "Fast wavefront adaptive holography in Nd:YVO4 for ultrasound optical tomography imaging," *Opt. Express*, vol. 22, no. 17, pp. 20622–20633, 2014.

[83] J. E. Rosen, S. Yoffe, A. Meerasa, M. Verma, and F. X. Gu, "Nanotechnology and diagnostic imaging: new advances in contrast agent technology," *J. Nanomed. Nanotechnol.*, vol. 2, no. 5, p. 1000115, 2011.

[84] D. Wu, L. Huang, M. S. Jiang, and H. Jiang, "Contrast agents for photoacoustic and thermoacoustic imaging: a review," *Int. J. Mol. Sci.*, vol. 15, pp. 23616–23639, 2014.

[85] M. X. Tang, H. Mulvana, T. Gauthier, A. K. P. Lim, D. O. Cosgrove, R. J. Eckersley, and E. Stride, "Quantitative contrast-enhanced ultrasound imaging: a review of sources of variability," *Interface Focus*, vol. 1, no. 4, pp. 520–539, 2011.

[86] N. Deshpande, A. Needles, and J. K. Willmann, "Molecular ultrasound imaging: current status and future directions," *Clin. Radiol.*, vol. 65, no. 7, pp. 567 – 581, 2010.

[87] A. Akbarzadeh, R. Rezaei-Sadabady, S. Davaran, S. Joo, N. Zarghami, Y. Hanifehpour, M. Samiei, M. Kouhi, and K. Nejati-Koshki, "Liposome: classification, preparation, and applications," *Nanoscale Res. Lett.*, vol. 8, no. 1, p. 102, 2013.

[88] S. R. Naik, S. K. Desai, P. D. Shah, and S. M. Wala, "Liposomes as potential carrier system for targeted delivery of polyene antibiotics," *Recent Pat. Inflamm. Allergy Drug Discov.*, vol. 7, no. 3, pp. 202 – 214, 2013.

[89] T. Oberholzer and P. L. Luisi, "The use of liposomes for constructing cell models," *J. Biol. Phys.*, vol. 28, no. 4, pp. 733 – 744, 2002.

[90] A. Samad, Y. Sultana, and M. Aqil, "Liposomal drug delivery systems: an update review," *Curr. Drug. Deliv.*, vol. 4, no. 4, pp. 297 – 305, 2007.

[91] T. M. Allen and P. R. Cullis, "Liposomal drug delivery systems: from concept to

clinical applications," *Adv. Drug Deliv. Rev.*, vol. 65, no. 1, pp. 36 – 48, 2013.

[92] M. Bally, K. Bailey, K. Sugihara, D. Grieshaber, J. Vörös, and B. Städler, "Liposome and lipid bilayer arrays towards biosensing applications," *Small*, vol. 6, no. 22, pp. 2481 – 2497, 2010.

[93] B. C. Roy, B. Chandra, D. Hromas, and S. Mallik, "Synthesis of new, pyrene-containing, metal-chelating lipids and sensing of cupric ions," *Org. Lett.*, vol. 5, no. 1, pp. 11 – 14, 2003.

[94] K. M. Hackman, B. S. Doddapaneni, C. W. Barth, I. H. Wierzbicki, A. W. G. Alani, and S. L. Gibbs, "Polymeric micelles as carriers for nerve-highlighting fluorescent probe delivery," *Mol. Pharm.*, vol. 12, no. 12, pp. 4386 – 4394, 2015.

[95] K. Miyata, R. J. Christie, and K. Kataoka, "Polymeric micelles for nano-scale drug delivery," *React. Funct. Polym.*, vol. 71, no. 3, pp. 227 – 234, 2011.

[96] M. Yokoyama, "Clinical applications of polymeric micelle carrier systems in chemotherapy and image diagnosis of solid tumors," *J. Exp. Clin. Med.*, vol. 3, no. 4, pp. 151 – 158, 2011.

[97] P. J. A. Frinking, A. Bouakaz, J. Kirkhorn, F. J. T. Cate, and N. D. Jong, "Ultrasound contrast imaging: current and new potential methods," *Ultrasound Med. Biol.*, vol. 26, no. 6, pp. 965 – 975, 2000.

[98] K. E. Morgan, J. S. Allen, P. A. Dayton, J. E. Chomas, A. L. Klibaov, and K. W. Ferrara, "Experimental and theoretical evaluation of microbubble behavior: effect of transmitted phase and bubble size," *IEEE T. Ultrason. Ferr.*, vol. 47, no. 6, pp. 1494 – 1509, 2000.

[99] P. Marmottant, S. Van der Meer, M. Emmer, M. Versluis, N. De Jong, S. Hilgenfeldt, and D. Lohse, "A model for large amplitude oscillations of coated bubbles accounting for buckling and rupture," *J. Acoust. Soc. Am.*, vol. 118, no. 6, pp. 3499 – 3505, 2005.

[100] V. Uhlendorf and C. Hoffmann, "Nonlinear acoustical response of coated microbubbles in diagnostic ultrasound," in *Ultrasonics Symposium*, vol. 3, pp. 1559 – 1562, 1994.

[101] W. Chen, A. A. Brayman, T. J. Matula, L. A. Crum, and M. W. Miller, "The pulse

length-dependence of inertial cavitation dose and hemolysis," *Ultrasound Med. Biol.*, vol. 29, no. 5, pp. 739 – 748, 2003.

[102] C. C. Church, "Frequency, pulse length, and the mechanical index," *Acoust. Res. Lett. Onl.*, vol. 6, no. 3, pp. 162 – 168, 2005.

[103] K. B. Bader and C. K. Holland, "Gauging the likelihood of stable cavitation from ultrasound contrast agents," *Phys. Med. Biol.*, vol. 58, no. 1, pp. 127 – 144, 2013.

[104] W. Chen, A. A. Brayman, T. J. Matula, and L. A. Crum, "Inertial cavitation dose and hemolysis produced in vitro with or without optison," *Ultrasound Med. Biol.*, vol. 29, no. 5, pp. 725 – 737, 2003.

[105] K. Chetty, E. Stride, C. A. Sennoga, J. V. Hajnal, and R. J. Eckersley, "High-speed optical observations and simulation results of sonovue microbubbles at low-pressure insonation," *IEEE T. Ultrason. Ferr.*, vol. 55, no. 6, pp. 1333 – 1342, 2008.

[106] P. A. Dayton, J. E. Chomas, A. F. H. Lum, J. S. Allen, J. R. Lindner, S. I. Simon, and K. W. Ferrara, "Optical and acoustical dynamics of microbubble contrast agents inside neutrophils," *Biophys. J.*, vol. 80, no. 3, pp. 1547 – 1556, 2001.

[107] J. E. Chomas, P. Dayton, D. May, and K. Ferrara, "Threshold of fragmentation for ultrasonic contrast agents," *J. Biomed. Opt.*, vol. 6, no. 2, pp. 141 – 150, 2001.

[108] A. Bouakaz, M. Versluis, and N. De Jong, "High speed optical observations of contrast agent dynamics and breakage," *AIP Conf. Proc.*, vol. 754, no. 1, pp. 204 – 207, 2005.

[109] S. H. Bloch, M. Wan, P. A. Dayton, and K. W. Ferrara, "Optical observation of lipid- and polymer-shelled ultrasound microbubble contrast agents," *Appl. Phys. Lett.*, vol. 84, no. 4, pp. 631 – 633, 2004.

[110] Y. Liu and B. Yuan, "An optical system for detecting 3D high-speed oscillation of a single ultrasound microbubble," *Biomed. Opt. Express*, vol. 4, no. 9, pp. 1559 – 1570, 2013.

[111] J. Guan and T. J. Matula, "Using light scattering tomeasure the response of individual ultrasound contrast microbubbles subjected to pulsed ultrasound in vitro," *J. Acoust. Soc. Am.*, vol. 116, pp. 2832 – 2842, 2004.

[112] J. Tu, J. Guan, Y. Qiu, and T. J. Matula, "Estimating the shell parameters of sonovue microbubbles using light scattering," *J. Acoust. Soc. Am.*, vol. 126, no. 6, pp. 2954 – 2962, 2009.

[113] M. J. Hsu, M. Eghtedari, A. P. Goodwin, D. J. Hall, R. F. Mattrey, and S. C. Esener, "Characterization of individual ultrasound microbubble dynamics with a light-scattering system," *J. Biomed. Opt.*, vol. 16, no. 6, pp. 067002–4, 2011.

[114] P. Rademeyer, D. Carugo, J. Lee, and E. Stride, "Microfluidic system for high throughput characterisation of echogenic particles," *Lab Chip*, vol. 15, pp. 417 – 428, 2015.

[115] H. J. Vos, *Single microbubble imaging*. PhD thesis, Erasmus Medical Center, 2009.

[116] B. Yuan, Y. Liu, P. M. Mehl, and J. Vignola, "Microbubble-enhanced ultrasound-modulated fluorescence in a turbid medium," *Appl. Phys. Lett.*, vol. 95, no. 18, p. 181113, 2009.

[117] Y. Liu, J. A. Feshitan, M. Wei, M. A. Borden, and B. Yuan, "Ultrasound-modulated fluorescence based on fluorescent microbubbles," *J. Biomed. Opt.*, vol. 19, no. 8, p. 085005, 2014.

[118] Y. Liu, J. A. Feshitan, M. Wei, M. A. Borden, and B. Yuan, "Ultrasound-modulated fluorescence based on donor-acceptor-labeled microbubbles," *J. Biomed. Opt.*, vol. 20, no. 3, p. 036012, 2015.

[119] C. J. H. Ho, G. Balasundaram, W. Driessen, R. McLaren, C. L. Wong, U. S. Dinish, A. B. E. Attia, V. Ntziachristos, and M. Olivo, "Multifunctional photosensitizer-based contrast agents for photoacoustic imaging," *Sci. Rep.*, vol. 4, p. 5342, 2014.

[120] B. W. Rice, M. D. Cable, and M. B. Nelson, "In vivo imaging of light-emitting probes," *J. Biomed. Opt.*, vol. 6, no. 4, pp. 432 – 440, 2001.

[121] L. Wang, S. L. Jacques, and L. Zheng, "MCML-monte carlo modeling of light transport in multi-layered tissues," *Comput. Methods. Programs. Biomed.*, vol. 47, no. 2, pp. 131 – 146, 1995.

[122] J. Lorenzo, *Principles of Diffuse Light Propagation: Light Propagation in Tissues with Applications in Biology and Medicine*. World Scientific, 2012.

[123] S. L. Jacques and B. W. Pogue, "Tutorial on diffuse light transport," *J. Biomed.*

Opt., vol. 13, no. 4, pp. 041302–19, 2008.

[124] H. Dehghani, M. E. Eames, P. K. Yalavarthy, S. C. Davis, S. Srinivasan, C. M. Carpenter, B. W. Pogue, and K. D. Paulsen, "Near infrared optical tomography using NIRFAST: algorithm for numerical model and image reconstruction.," *Numer. Methods Eng.*, vol. 25, no. 6, pp. 711 – 732, 2008.

[125] W. D. O'Brien, "Ultrasound-biophysics mechanisms.," *Prog. Biophys. Mol. Bio.*, vol. 93, no. 13, pp. 212 – 255, 2007.

[126] L. V. Wang, "Mechanisms of ultrasonic modulation of multiply scattered coherent light: an analytic model.," *Phys. Rev. Lett.*, vol. 87, no. 4, p. 043903, 2001.

[127] J. L. Sandell and T. C. Zhu., "A review of in-vivo optical properties of human tissues and its impact on pdt.," *J. Biophotonics.*, vol. 4, no. 11-12, pp. 773 – 787, 2011.

[128] H. Zhao, T. C. Doyle, O. Coquoz, F. Kalish, B. W. Rice, and C. H. Contag, "Emission spectra of bioluminescent reporters and interaction with mammalian tissue determine the sensitivity of detection in vivo.," *J. Biomed. Opt.*, vol. 10, no. 4, p. 041210, 2005.

[129] W. A. W. J. Kestin, M. Sokolov, "Viscosity of liquid water in the range -8°c to 150°c," *J. Phys. Chem. Ref. Data*, vol. 7, no. 3, pp. 941–948, 1978.

[130] M. Barry, S. May, and E. A. Weaver, "Imaging luciferase-expressing viruses," *Oncolytic Viruses, ser. Methods in Molecular Biology*, vol. 797, pp. 79 – 87, 2012.

[131] R. A. Fine and F. J. Millero, "Compressibility of water as a function of temperature and pressure," *J. Chem. Phys.*, vol. 59, no. 10, pp. 5529–5536, 1973.

[132] E. Conti, N. P. Franks, and P. Brick, "Crystal structure of firefly luciferase throws light on a superfamily of adenylate-forming enzymes.," *Structure*, vol. 4, no. 3, pp. 287 – 298, 1996.

[133] A. Käkinen, F. Ding, P. Chen, M. Mortimer, A. Kahru, and P. C. Ke, "Interaction of firefly luciferase and silver nanoparticles and its impact on enzyme activity," *Nanotechnology*, vol. 24, no. 34, p. 345101, 2013.

[134] C. W. Jarrett, C. F. Caskey, and J. C. Core, "Detection of a novel mechanism of acousto-optic modulation of incoherent light.," *PLoS ONE*, vol. 9, no. 8,

p. e104268, 2014.

[135] N. T. Huynh, H. Ruan, D. He, B. R. Hayes-Gill, and S. P. Morgan, "Effect of object size and acoustic wavelength on pulsed ultrasound modulated fluorescence signals.," *J. Biomed. Opt.*, vol. 17, no. 7, p. 076008, 2012.

[136] B. Yuan and Y. Liu., "Ultrasound-modulated fluorescence from rhodamine B aqueous solution.," *J. Biomed. Opt.*, vol. 15, no. 2, p. 021321, 2010.

[137] J. R. Lakowicz, *Principles of fluorescence spectroscopy*. Springer, 3rd ed., 2006.

[138] M. L. Foucault, L. Thomas, S. Goussard, B. R. Branchini, and C. Grillot-Courvalin, "In vivo bioluminescence imaging for the study of intestinal colonization by escherichia coli in mice," *Appl. Environ. Microbiol.*, vol. 76, no. 1, pp. 264–274, 2010.

[139] H. Fujii, K. Noda, Y. Asami, A. Kuroda, M. Sakata, and A. Tokida, "Increase in bioluminescence intensity of firefly luciferase using genetic modification," *Anal. Biochem.*, vol. 366, no. 2, pp. 131 – 136, 2007.

[140] B. E. Treeby and B. T. Cox, "K-wave: Matlab toolbox for the simulation and reconstruction of photoacoustic wave fields," *J. Biomed. Opt.*, vol. 15, no. 2, p. 021314, 2010.

[141] M. J. Benchimol, M. J. Hsu, C. E. Schutt, D. J. Hall, R. F. Mattrey, and S. C. Esener, "Phospholipid/carbocyanine dye-shelled microbubbles as ultrasound-modulated fluorescent contrast agents," *Soft Matter*, vol. 9, no. 8, pp. 2384 – 2388, 2013.

[142] C. E. Schutt, S. D. Ibsen, M. J. Benchimol, M. J. Hsu, and S. C. Esener, "Manipulating nanoscale features on the surface of dye-loaded microbubbles to increase their ultrasound-modulated fluorescence output," *Small*, vol. 10, no. 16, pp. 3316 – 3324, 2014.

[143] L. Hoff and P. C. Sontum, "Acoustic characterization of contrast agents for medical ultrasound imaging," *J. Acoust. Soc. Am.*, vol. 103, no. 5, p. 2960, 1998.

[144] A. Katiyar and K. Sarkar, "Excitation threshold for subharmonic generation from contrast microbubbles," *J. Acoust. Soc. Am.*, vol. 130, no. 5, pp. 3137 – 3147, 2011.

[145] K. Vokurka, "Comparison of Rayleigh's, Herring's, and Gilmore's models of gas bubbles," *Acustica*, vol. 59, pp. 214 – 219, 1986.

[146] E. Stride and N. Saffari, "Microbubble ultrasound contrast agents: a review," *Proc. Inst. Mech. Eng. H.*, vol. 217, no. 6, pp. 429 – 447, 2003.

[147] T. Sun, N. Jia, D. Zhang, and D. Xu, "Ambient pressure dependence of the ultraharmonic response from contrast microbubbles," *J. Acoust. Soc. Am.*, vol. 131, no. 6, pp. 4358 – 4364, 2012.

[148] S. M. Van der Meer, B. Dollet, M. M. Voormolen, C. T. Chin, A. Bouakaz, N. De Jong, M. Versluis, and D. Lohse, "Microbubble spectroscopy of ultrasound contrast agents," *J. Acoust. Soc. Am.*, vol. 121, no. 1, pp. 648 – 656, 2007.

[149] M. S. Patterson, B. Chance, and B. C. Wilson, "Time resolved reflectance and transmittance for the noninvasive measurement of tissue optical properties," *Appl. Opt.*, vol. 28, no. 12, pp. 2331–2336, 1989.

[150] X. Li, *Fluorescence and diffusive wave diffraction tomographic probes in turbid media*. PhD thesis, University of Pennsylvania, 1998.

[151] C. M. Ajo-Franklin, C. Yoshina-Ishii, and S. G. Boxer, "Probing the structure of supported membranes and tethered oligonucleotides by fluorescence interference contrast microscopy," *Langmuir*, vol. 21, no. 11, pp. 4976 – 4983, 2005.

[152] B. S. Packard and D. E. Wolf, "Fluorescence lifetimes of carbocyanine lipid analogs in phospholipid bilayers," *Biochemistry*, vol. 24, no. 19, pp. 5176 – 5181, 1985.

[153] T. Heimburg, "A model for the lipid pretransition: coupling of ripple formation with the chain-melting transition," *Biophys. J.*, vol. 78, no. 3, pp. 1154 – 1165, 2000.

[154] A. M. Chow and E. X. Wu, *Microbubbles*, pp. 321 – 334. John Wiley & Sons, Inc, 2014.

[155] J. Bulte and M. Modo, *Nanoparticles in Biomedical Imaging: Emerging Technologies and Applications*. Springer New York, 2007.

[156] P. L. Marston and S. C. Billette, "Scattering of light by a coated bubble in water near the critical and Brewster scattering angles," *J. Acoust. Soc. Am.*, vol. 80, no. S1, p. S59, 1986.

[157] J. Alter, C. A. Sennoga, D. Lopes, R. J. Eckersley, and D. J. Wells, "Microbubble stability is a major determinant of the efficiency of ultrasound and microbubble

mediated in vivo gene transfer," *Ultrasound Med. Biol.*, vol. 35, no. 6, pp. 976 – 984, 2009.

[158] S. Qin, C. F. Caskey, and K. W. Ferrara, "Ultrasound contrast microbubbles in imaging and therapy: physical principles and engineering," *Phys. Med. Biol.*, vol. 54, no. 6, p. R27, 2009.

[159] P. N. Shek, ed., *Liposomes in biomedical applications*. Harwood Academic Publishers GmbH., 1995.

[160] D. C. Drummond, O. Meyer, K. Hong, D. B. Kirpotin, and D. Papahadjopoulos, "Optimizing liposomes for delivery of chemotherapeutic agents to solid tumors," *Pharmacol. Rev.*, vol. 51, no. 4, pp. 691 – 744, 1999.

[161] S. Ait-Oudhia, D. E. Mager, and R. M. Straubinger, "Application of pharmacokinetic and pharmacodynamic analysis to the development of liposomal formulations for oncology," *Pharmaceutics*, vol. 6, no. 1, p. 137, 2014.

[162] S. Sirsi and M. Borden, "Microbubble compositions, properties and biomedical applications," *Bubble Sci. Eng. Technol.*, vol. 1, no. 1-2, pp. 3–17, 2009.

[163] L. Mullin, R. Gessner, J. Kwan, M. Kaya, M. A. Borden, and P. A. Dayton, "Effect of anesthesia carrier gas on in vivo circulation times of ultrasound microbubble contrast agents in rats," *Contrast. Media. Mol. Imaging.*, vol. 6, no. 3, pp. 126–131, 2011.

[164] E. Stride and M. Edirisinghe, "Novel microbubble preparation technologies," *Soft Matter*, vol. 4, pp. 2350–2359, 2008.

[165] K. Hettiarachchi, E. Talu, M. L. Longo, P. A. Dayton, and A. P. Lee, "On-chip generation of microbubbles as a practical technology for manufacturing contrast agents for ultrasonic imaging," *Lab Chip*, vol. 7, pp. 463 – 468, 2007.

[166] B. Valeur, *Effects of Intermolecular Photophysical Processes on Fluorescence Emission*, pp. 72 – 124. Wiley-VCH Verlag GmbH, 2001.

[167] M. Sassaroli, M. Vauhkonen, D. Perry, and J. Eisinger, "Lateral diffusivity of lipid analogue excimeric probes in dimyristoylphosphatidylcholine bilayers," *Biophys. J.*, vol. 57, no. 2, pp. 281–90, 1990.

[168] G. Bains, A. B. Patel, and V. Narayanaswami, "Pyrene: a probe to study pro-

tein conformation and conformational changes," *Molecules*, vol. 16, no. 9, p. 7909, 2011.

[169] A. Saha and N. Manna, *Optoelectronics and Optical Communication*. Laxmi Publications Pvt Limited, 2011.

[170] S. Lehrer, "Pyrene excimer fluorescence as a probe of protein conformational change," in *Proteins: Structure, Function, and Engineering* (B. B. Biswas and S. Roy, eds.), vol. 24 of *Subcellular Biochemistry*, pp. 115 – 132, Springer US, 1995.

[171] C. J. Yang, S. Jockusch, M. Vicens, N. J. Turro, and W. Tan, "Light-switching excimer probes for rapid protein monitoring in complex biological fluids," *P. Natl. Acad. Sci. USA*, vol. 102, no. 48, pp. 17278 – 17283, 2005.

[172] P. Müller, S. Schiller, T. Wieprecht, M. Dathe, and A. Herrmann, "Continuous measurement of rapid transbilayer movement of a pyrene-labeled phospholipid analogue," *Chem. Phys. Lipids*, vol. 106, no. 1, pp. 89 – 99, 2000.

[173] W. Xu, R. C. McDonough, B. Langsdorf, J. N. Demas, and B. A. DeGraff, "Oxygen sensors based on luminescence quenching: interactions of metal complexes with the polymer supports," *Anal. Chem.*, vol. 66, no. 23, pp. 4133 – 4141, 1994.

[174] G. Sivaraman, T. Anand, and D. Chellappa, "Pyrene based selective-ratiometric fluorescent sensing of zinc and pyrophosphate ions," *Anal. Methods*, vol. 6, pp. 2343 – 2348, 2014.

[175] M. Wang, J. Xu, X. Liu, and H. Wang, "A highly selective pyrene based 'off-on' fluorescent chemosensor for cyanide," *New J. Chem.*, vol. 37, pp. 3869 – 3872, 2013.

[176] D. L. Marks, R. Bittman, and R. E. Pagano, "Use of Bodipy-labeled sphingolipid and cholesterol analogs to examine membrane microdomains in cells," *Histochem. Cell. Biol.*, vol. 130, no. 5, pp. 819 – 832, 2008.

[177] L. D. Mayer, M. J. Hope, and P. R. Cullis, "Vesicles of variable sizes produced by a rapid extrusion procedure," *BBA - Biomembranes*, vol. 858, no. 1, pp. 161 – 168, 1986.

[178] J. D. Castile and K. M. G. T., "Factors affecting the size distribution of liposomes produced by freeze-thaw extrusion," *Int. J. Pharm.*, vol. 188, no. 1, pp. 87 – 95, 1999.

[179] A. P. Costa, X. Xu, and D. J. Burgess, "Freeze-anneal-thaw cycling of unilamellar liposomes: effect on encapsulation efficiency," *Pharmaceut. Res.*, vol. 31, no. 1, pp. 97 – 103, 2014.

[180] M. J. Hope, M. B. Bally, G. Webb, and P. R. Cullis, "Production of large unilamellar vesicles by a rapid extrusion procedure. characterization of size distribution, trapped volume and ability to maintain a membrane potential," *BBA - Biomembranes*, vol. 812, no. 1, pp. 55 – 65, 1985.

[181] M. Koivusalo, J. Alvesalo, J. A. Virtanen, and P. Somerharju, "Partitioning of pyrene-labeled phospho- and sphingolipids between ordered and disordered bilayer domains," *Biophys. J.*, vol. 86, no. 2, pp. 923 – 935, 2004.

[182] P. Somerharju, "Pyrene-labeled lipids as tools in membrane biophysics and cell biology," *Chem. Phys. Lipids*, vol. 116, no. 1-2, pp. 57 – 74, 2002.

[183] D. Daems, M. Van den Zegel, N. Boens, and F. C. De Schryver, "Fluorescence decay of pyrene in small and large unilamellar l, α-dipalmitoylphosphatidylcholine vesicles above and below the phase transition temperature," *Eur. Biophy. J.*, vol. 12, no. 2, pp. 97 – 105, 1985.

[184] L. Wang and X. Zhao, "Dynamic research of a potential carrier for hydrophobic compound model pyrene using amphiphilic peptide EYK," *Bull. Korean Chem. Soc*, vol. 32, no. 2, pp. 620 – 624, 2011.

[185] C. Shao, X. Shi, H. Wehbi, C. Zambonelli, J. F. Head, B. A. Seaton, and M. F. Roberts, "Dimer structure of an interfacially impaired phosphatidylinositol-specific phospholipase c," *J. Biol. Chem.*, vol. 282, no. 12, pp. 9228–9235, 2007.

[186] M. Vauhkonen, M. Sassaroli, P. Somerharju, and J. Eisinger, "Dipyrenylphosphatidylcholines as membrane fluidity probes. relationship between intramolecular and intermolecular excimer formation rates," *Biophys. J.*, vol. 57, no. 2, pp. 291 – 300, 1990.

[187] A. V. Fonin, A. I. Sulatskaya, I. M. Kuznetsova, and K. K. Turoverov, "Fluorescence of dyes in solutions with high absorbance. inner filter effect correction," *PLoS One*, vol. 9, no. 7, p. e103878, 2014.

[188] P. Somerharju, "Pyrene-labeled lipids as tools in membrane biophysics and cell

biology," *Chem. Phys. Lipids*, vol. 116, no. 1-2, pp. 57 – 74, 2002.

[189] M. You, E. Li, W. C. Wimley, and K. Hristova, "Förster resonance energy transfer in liposomes: measurements of transmembrane helix dimerization in the native bilayer environment," *Anal. Biochem.*, vol. 340, no. 1, pp. 154 – 164, 2005.

[190] H. Photonics, *Photomultiplier Tubes: Basics and Applications*. Hamamatsu Photonics, 3rd ed., 2006.

[191] A. P. Philipse, "Notes on Brownian motion." Unpublished. Available online at `http://userpages.umbc.edu/~dfrey1/ench630/philipse_notes_on_brownian_motion.pdf`, 2011.

[192] K. Tanhuanpää, J. Virtanen, and P. Somerharju, "Fluorescence imaging of pyrene-labeled lipids in living cells," *BBA - Mol. Cell Res.*, vol. 1497, no. 3, pp. 308 – 320, 2000.

[193] C. Cantrel, O. Caiveau, F. Moreau, and A. Zachowski, "Lipid lateral diffusion and local microviscosity in plant mitochondrial membranes with various length and unsaturation of fatty acids," *Physiol. Plant.*, vol. 110, no. 4, pp. 443 – 449, 2000.

[194] R. N. A. H. Lewis, N. Mak, and R. N. McElhaney, "A differential scanning calorimetric study of the thermotropic phase behavior of model membranes composed of phosphatidylcholines containing linear saturated fatty acyl chains," *Biochemistry*, vol. 26, no. 19, pp. 6118 – 6126, 1987.

[195] P. J. Somerharju, J. A. Virtanen, K. K. Eklund, P. Vainio, and P. K. J. Kinnunen, "1-palmitoyl-2-pyrenedecanoyl glycerophospholipids as membrane probes: evidence for regular distribution in liquid-crystalline phosphatidylcholine bilayers," *Biochemistry*, vol. 24, no. 11, pp. 2773 – 2781, 1985.

[196] J. Liu and J. C. Conboy, "Direct measurement of the transbilayer movement of phospholipids by sum-frequency vibrational spectroscopy," *J. Am. Chem. Soc.*, vol. 126, no. 27, pp. 8376–8377, 2004.

[197] K. John, S. Schreiber, J. Kubelt, A. Herrmann, and P. Müller, "Transbilayer movement of phospholipids at the main phase transition of lipid membranes: implications for rapid flip-flop in biological membranes," *Biophys. J.*, vol. 83, no. 6, pp. 3315 – 3323, 2002.

[198] U. Health Protection Agency, "Health effects of exposure to ultrasound and infrasound: Report of the independent advisory group on non-ionising radiation.," 2010. Available online at https://www.gov.uk/government/uploads/system/uploads/attachment_data/file/335014/RCE-14_for_web_with_security.pdf.

[199] L. D. Johns, "Nonthermal effects of therapeutic ultrasound: the frequency resonance hypothesis.," *J. Athl. Train.*, vol. 37, no. 3, pp. 293–299, 2002.

[200] M. Sassaroli, M. Vauhkonen, P. Somerharju, and S. Scarlata, "Dipyrenylphosphatidylcholines as membrane fluidity probes. pressure and temperature dependence of the intramolecular excimer formation rate.," *Biophys. J.*, vol. 64, no. 1, pp. 137–49, 1993.

[201] S. P. Wrenn, E. Small, and N. Dan, "Bubble nucleation in lipid bilayers: a mechanism for low frequency ultrasound disruption," *BBA - Biomembranes*, vol. 1828, no. 4, pp. 1192 – 1197, 2013.

[202] V. Sundararajan, S. Simon, D. Benos, and S. Feller, *Computational Modeling of Membrane Bilayers*. Current Topics in Membranes, Elsevier Science, 2011.

[203] J. Yang, C. Calero, and J. Martí, "Diffusion and spectroscopy of water and lipids in fully hydrated dimyristoylphosphatidylcholine bilayer membranes," *J. Chem. Phys.*, vol. 140, no. 10, p. 104901, 2014.

[204] E. S. Richardson, W. G. Pitt, and D. J. Woodbury, "The role of cavitation in liposome formation," *Biophys. J.*, vol. 93, no. 12, pp. 4100 – 4107, 2007.

[205] D. Huster, P. Müller, K. Arnold, and A. Herrmann, "Dynamics of membrane penetration of the fluorescent 7-nitrobenz-2-oxa-1,3-diazol-4-yl (nbd) group attached to an acyl chain of phosphatidylcholine," *Biophys. J.*, vol. 80, no. 2, pp. 822 – 831, 2001.

[206] N. J. Turro and P. L. Kuo, "Pyrene excimer formations in micelles of nonionic detergents and of water-soluble polymers," *Langmuir*, vol. 2, no. 4, pp. 438 – 442, 1986.

[207] A. Haplern and G. McBane, *Experimental Physical Chemistry: a laboratory textbook*. USA: W. H. Freeman., 2006.

[208] R. H. Templer, S. J. Castle, A. R. Curran, G. Rumbles, and K. D. R., "Sensing isothermal changes in the lateral pressure in model membranes using di-pyrenyl phosphatidylcholine," *Faraday Discuss.*, vol. 111, pp. 41 – 53, 1999.

[209] P. Conlon, C. J. Yang, Y. Wu, Y. Chen, K. Martinez, Y. Kim, N. Stevens, A. A. Marti, S. Jockusch, N. J. Turro, and W. Tan, "Pyrene excimer signaling molecular beacons for probing nucleic acids," *J. Am. Chem. Soc.*, vol. 130, no. 1, pp. 336 – 342, 2008.

[210] Y. Fujiwara and Y. Amao, "An oxygen sensor based on the fluorescence quenching of pyrene chemisorbed layer onto alumina plates," *Sensor Actuat. B-Chem.*, vol. 89, no. 1-2, pp. 187 – 191, 2003.

[211] B. J. Basu and K. S. Rajam, "Comparison of the oxygen sensor performance of some pyrene derivatives in silicone polymer matrix," *Sensor Actuat. B-Chem.*, vol. 99, no. 2-3, pp. 459 – 467, 2004.

[212] S. Sarkar, S. Roy, A. Sikdar, R. N. Saha, and S. S. Panja, "A pyrene-based simple but highly selective fluorescence sensor for Cu2+ ions via a static excimer mechanism," *Analyst*, vol. 138, pp. 7119 – 7126, 2013.

[213] K. P. McNamara, N. Rosenzweig, and Z. Rosenzweig, "Liposome-based optochemical nanosensors," *Microchim. Acta*, vol. 131, no. 1-2, pp. 57 – 64, 1999.

[214] X. Wang, J. A. Stolwijk, M. Sperber, R. J. Meier, J. Wegener, and O. S. Wolfbeis, "Ultra-small, highly stable, and membrane-impermeable fluorescent nanosensors for oxygen," *Methods Appl. Fluoresc.*, vol. 1, no. 3, p. 035002, 2013.

[215] M. Horie, H. Yanagisawa, and M. Sugawara, "Fluorometric immunoassay based on ph-sensitive dye-encapsulating liposomes and gramicidin channels," *Anal. Biochem.*, vol. 369, no. 2, pp. 192 – 201, 2007.

[216] S. Begu, S. Mordon, T. Desmettre, and J. M. Devoisselle, "Fluorescence imaging method for in vivo ph monitoring during liposomes uptake in rat liver using a ph-sensitive fluorescent dye," *J. Biomed. Opt.*, vol. 10, no. 2, pp. 024008–6, 2005.

[217] G. M. Makrigiorgos, "Detection of lipid peroxidation on erythrocytes using the excimer-forming property of a lipophilic BODIPY fluorescent dye," *J. Biochem. Bioph. Meth.*, vol. 35, no. 1, pp. 23 – 35, 1997.

[218] R. E. Pagano, O. C. Martin, H. C. Kang, and R. P. Haugland, "Diffusion and spectroscopy of water and lipids in fully hydrated dimyristoylphosphatidylcholine bilayer membranes," *J. Cell. Biol.*, vol. 113, no. 6, pp. 1267–1279, 1991.

[219] E. A. Margulies, L. E. Shoer, S. W. Eaton, and M. R. Wasielewski, "Excimer formation in cofacial and slip-stacked perylene-3,4:9,10-bis(dicarboximide) dimers on a redox-inactive triptycene scaffold," *Phys. Chem. Chem. Phys.*, vol. 16, pp. 23735 – 23742, 2014.

[220] R. M. Clegg, *Fluorescence imaging spectroscopy and microscopy*, ch. Fluorescence resonance energy transfer, pp. 179 – 252. John Wiley & Sons, 3rd ed., 1996.

[221] M. Beutler, K. Makrogianneli, R. Vermeij, M. Keppler, T. Ng, T. Jovin, and R. Heintzmann, "satFRET: estimation of Förster resonance energy transfer by acceptor saturation," *Eur. Biophy. J.*, vol. 38, no. 1, pp. 69 – 82, 2008.

[222] S. A. Hussain, D. Dey, S. Chakraborty, J. Saha, A. D. Roy, S. Chakraborty, P. Debnath, and D. Bhattacharjee, "Fluorescence resonance energy transfer (FRET) sensor," *Sci. Letts. J.*, vol. 4, no. 119, 2015.

[223] P. R. Selvin, "The renaissance of fluorescence resonance energy transfer," *Nat. Struct. Mol. Biol.*, vol. 7, no. 9, pp. 730 – 734, 2000.

[224] J. Liu and Y. Lu, "Multi-fluorophore fluorescence resonance energy transfer for probing nucleic acids structure and folding," in *Fluorescent Energy Transfer Nucleic Acid Probes* (V. Didenko, ed.), vol. 335 of *Methods in Molecular Biology*, pp. 257–271, Humana Press, 2006.

[225] R. M. Clegg, A. I. H. Murchie, A. Zechel, C. Carlberg, S. Diekmann, and D. M. J. Lilley, "Fluorescence resonance energy transfer analysis of the structure of the four-way DNA junction," *Biochemistry*, vol. 31, no. 20, pp. 4846 – 4856, 1992.

[226] I. L. Medintz, J. H. Konnert, A. R. Clapp, I. Stanish, M. E. Twigg, H. Mattoussi, J. M. Mauro, and J. R. Deschamps, "A fluorescence resonance energy transfer-derived structure of a quantum dot-protein bioconjugate nanoassembly," *Proc. Natl. Acad. Sci. USA*, vol. 101, no. 26, pp. 9612 – 7, 2004.

[227] Q. Cai, T. Yu, W. Zhu, Y. Xu, and X. Qian, "A turn-on fluorescent probe for tumor hypoxia imaging in living cells," *Chem. Commun.*, vol. 51, pp. 14739 – 14741, 2015.

[228] Y. Wu, W. Zhang, J. Li, and Y. Zhang, "Optical imaging of tumor microenvironment," *Am. J. Nucl. Med. Mol. Imaging*, vol. 3, no. 1, pp. 1 – 15, 2013.

[229] N. Chen, S. Cheng, C. Liu, J. S. Souris, C. Chen, C. Mou, and L. Lo, "Recent advances in nanoparticle-based Förster resonance energy transfer for biosensing, molecular imaging and drug release profiling," *Int. J. Mol. Sci.*, vol. 13, no. 12, p. 16598, 2012.

[230] R. Y. Tsien, "The green fluorescent protein," *Annu. Rev. Biochem.*, vol. 67, no. 1, pp. 509 – 544, 1998.

[231] P. Zou, H. Chen, H. J. Paholak, and D. Sun, "Noninvasive fluorescence resonance energy transfer imaging of in vivo premature drug release from polymeric nanoparticles," *Mol. Pharm.*, vol. 10, no. 11, pp. 4185 – 4194, 2013.

[232] V. Kalchenko, S. Shivtiel, V. Malina, K. Lapid, S. Haramati, T. Lapidot, A. Brill, and A. Harmelin, "Use of lipophilic near-infrared dye in whole-body optical imaging of hematopoietic cell homing," *J. Biomed. Opt.*, vol. 11, no. 5, pp. 050507–3, 2006.

[233] F. Progatzky, M. J. Dallman, and C. Lo Celso, "From seeing to believing: labelling strategies for in vivo cell-tracking experiments," *Interface Focus*, vol. 3, no. 3, p. 20130001, 2013.

[234] L. T. Ltd, "Fluorescence SpectraViewer." Available online at `https://www.thermofisher.com/uk/en/home/life-science/cell-analysis/labeling-chemistry/fluorescence-spectraviewer.html?ICID=svtool&UID=12731lip`.

[235] L. technologies, *The molecular probes handbook: a guide to fluorescent probes and labelling technologies*, ch. Probes for lipids and membranes, p. 549. Life Technologies Corporation, 11th ed., 2010.

[236] R. I. MacDonald, "Characteristics of self-quenching of the fluorescence of lipid-conjugated rhodamine in membranes," *J. Biol. Chem.*, vol. 265, no. 23, pp. 13533 – 9, 1990.

[237] B. P. Gray, M. J. McGuire, and K. C. Brown, "A liposomal drug platform overrides peptide ligand targeting to a cancer biomarker, irrespective of ligand affinity or

density," *PLoS ONE*, vol. 8, no. 8, p. e72938, 2013.

[238] E. Claassen, "Post-formation fluorescent labelling of liposomal membranes," *J. Immunol. Methods*, vol. 147, no. 2, pp. 231 – 240, 1992.

[239] N. M. Silva-Barcellos, F. Frézard, S. Caligiorne, and R. A. Santos, "Long-lasting cardiovascular effects of liposome-entrapped angiotensin-(1-7) at the rostral ventrolateral medulla," *Hypertension*, vol. 38, no. 6, pp. 1266 – 71, 2001.

[240] J. T. Buboltz, C. Bwalya, S. Reyes, and D. Kamburov, "Stern-volmer modeling of steady-state Förster energy transfer between dilute, freely diffusing membrane-bound fluorophores," *J. Chem. Phys.*, vol. 127, no. 21, 2007.

[241] R. Grünberg, T. S. Ferrar, A. M. van der Sloot, M. Constante, and L. Serrano, "Building blocks for protein interaction devices," *Nuc. Acids. Res.*, vol. 38, no. 8, pp. 2645–2662, 2010.

[242] G. W. Gordon, G. Berry, X. Liang, B. Levine, and B. Herman, "Quantitative fluorescence resonance energy transfer measurements using fluorescence microscopy," *Biophys. J.*, vol. 74, no. 5, pp. 2702 – 2713, 1998.

[243] Z. Xia and Y. Liu, "Reliable and global measurement of fluorescence resonance energy transfer using fluorescence microscopes," *Biophys. J.*, vol. 81, no. 4, pp. 2395 – 2402, 2001.

[244] A. Wagh, S. Y. Qian, and B. Law, "Development of biocompatible polymeric nanoparticles for in vivo NIR and FRET imaging," *Bioconjug. Chem.*, vol. 23, no. 5, pp. 981 – 992, 2012.

[245] H. Ruan, *Pulsed ultrasound modulated optical tomography with parallel speckle detection*. PhD thesis, University of Nottingham, 2012.

[246] W. S. Pegau, D. Gray, and J. R. V. Zaneveld, "Absorption and attenuation of visible and near-infrared light in water: dependence on temperature and salinity," *Appl. Opt.*, vol. 36, no. 24, pp. 6035–6046, 1997.

[247] Y. Xu, D. W. Piston, and C. H. Johnson, "A bioluminescence resonance energy transfer (bret) system: application to interacting circadian clock proteins," *Proceedings of the National Academy of Sciences*, vol. 96, no. 1, pp. 151–156, 1999.

[248] K. Radhakrishnan, K. J. Haworth, S. Huang, M. E. Klegerman, D. D. McPherson,

and C. K. Holland, "Stability of echogenic liposomes as a blood pool ultrasound contrast agent in a physiologic flow phantom," *Ultrasound Med. Biol.*, vol. 38, no. 11, pp. 1970 – 1981, 2012.

[249] Q. Yang, X. Xu, P. Lai, D. Xu, and L. Wang, "Time-reversed ultrasonically encoded optical focusing using two ultrasonic transducers for improved ultrasonic axial resolution," *Journal of Biomedical Optics*, vol. 18, no. 11, pp. 110502–110502, 2013.

[250] G. Yao, S. Jiao, and L. Wang, "Frequency-swept ultrasound-modulated optical tomography in biological tissue by use of parallel detection," *Opt. Lett.*, vol. 25, no. 10, pp. 734–736, 2000.

[251] M. Lesaffre, S. Farahi, M. Gross, P. Delaye, A. Boccara, and F. Ramaz, "Acousto-optical coherence tomography using random phase jumps on ultrasound and light," *Opt. Express*, vol. 17, no. 20, pp. 18211–18218, 2009.

[252] Y. Chen, B. C. Lagerholm, B. Yang, and K. Jacobson, "Methods to measure the lateral diffusion of membrane lipids and proteins," *Methods*, vol. 39, no. 2, pp. 147 – 153, 2006.

[253] J. C. McIntyre and R. G. Sleight, "Fluorescence assay for phospholipid membrane asymmetry," *Biochemistry*, vol. 30, no. 51, pp. 11819–11827, 1991.

[254] M. Langner and S. Hui, "Effect of free fatty acids on the permeability of 1,2-dimyristoyl-sn-glycero-3-phosphocholine bilayer at the main phase transition," *BBA - Biomembranes*, vol. 1463, no. 2, pp. 439 – 447, 2000.

[255] J. McCaskill, R. Singhania, M. Burgess, R. Allavena, S. Wu, A. Blumenthal, and N. A. J. McMillan, "Efficient biodistribution and gene silencing in the lung epithelium via intravenous liposomal delivery of siRNA," *Mol. Ther. Nucleic. Acids.*, vol. 2, p. e96, 2013.

[256] N. Mignet, Q. Chermont, T. Randrianarivelo, J. Seguin, C. Richard, M. Bessodes, and D. Scherman, "Liposome biodistribution by time resolved fluorimetry of lipophilic europium complexes," *Eur. Biophys. J.*, vol. 35, no. 2, pp. 155–161, 2006.

[257] T. K. Uppal, *Synthesis and characterization of red and near-infrared BODIPY-based fluorophores for various biological applications*. PhD thesis, Louisiana State University, 2012.

[258] M. L. Briuglia, C. Rotella, A. McFarlane, and D. A. Lamprou, "Influence of cholesterol on liposome stability and on in vitro drug release," *Drug Deliv. Transl. Res.*, vol. 5, no. 3, pp. 231–242, 2015.

[259] L. Zhang, H. Zhou, O. Belzile, P. Thorpe, and D. Zhao, "Phosphatidylserine-targeted bimodal liposomal nanoparticles for in vivo imaging of breast cancer in mice," *J. Control. Release*, vol. 183, pp. 114 – 123, 2014.

APPENDIX A

Simulation of microbubble radius and fluorescence emission intensity

Oscillation of radius and fluorescence emission intensity when using 10 cycles of US were shown in Section 3.3.2 of Chapter 3. Here similar simulations are provided, but with 1 cycle and 50 cycles of US.

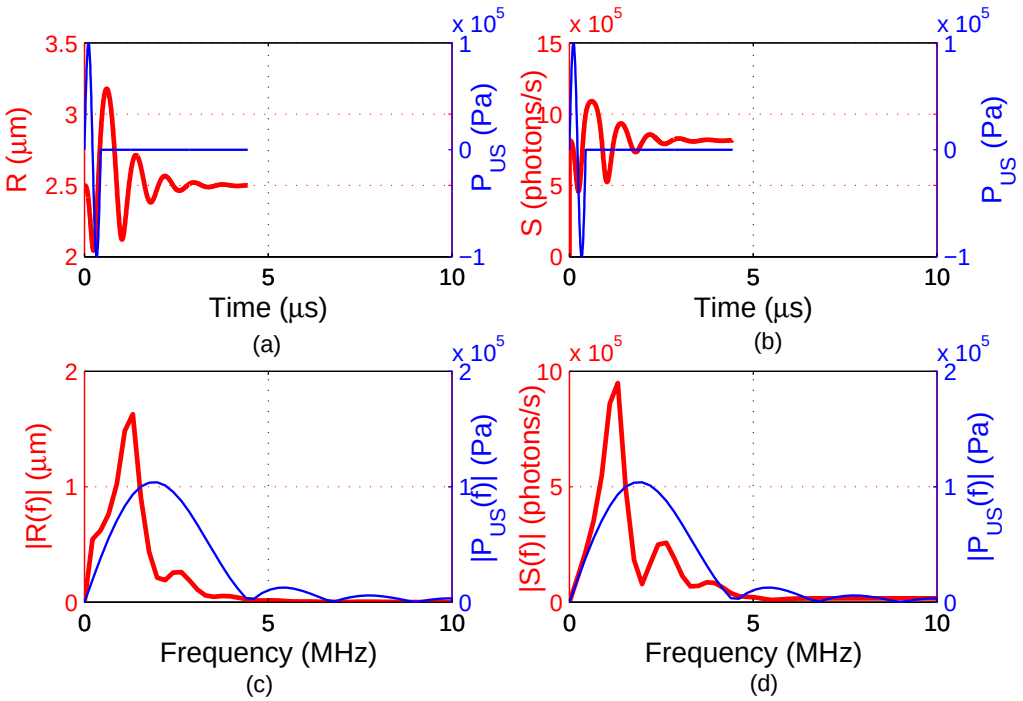


Figure A.1: Oscillation of microbubble radius (R) and fluorescence emission intensity (S) in time domain ((a) and (b)) and frequency domain ((c) and (d)). $N_C = 1$; $R_0 = 2.5\,\mu m$; $P_A = 100\,kPa$.

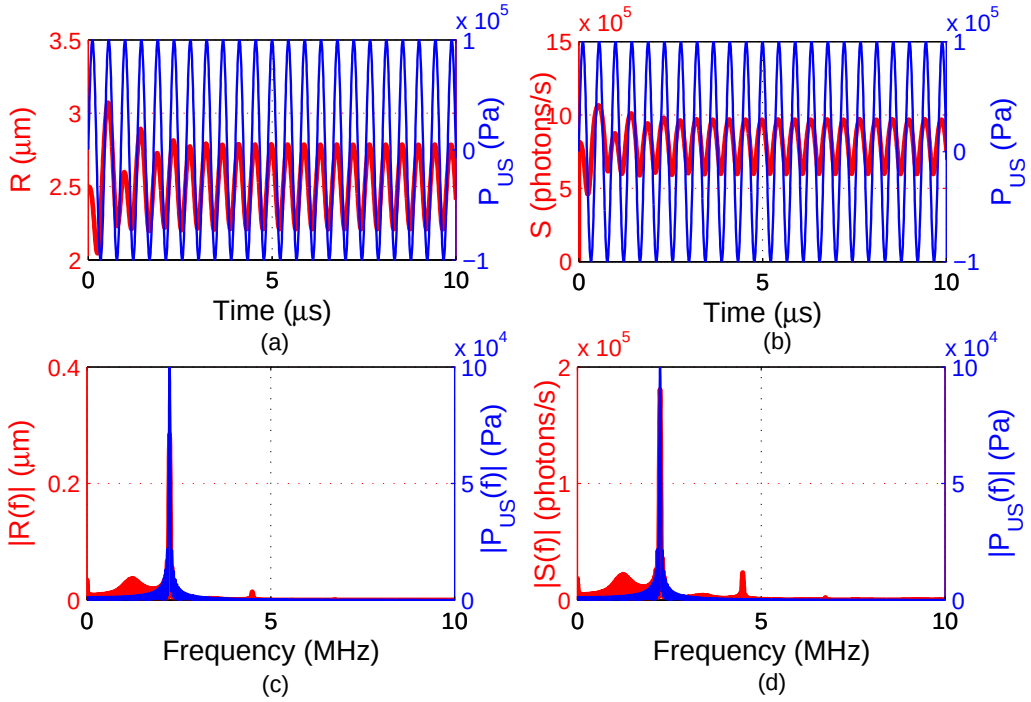


Figure A.2: Oscillation of microbubble radius (R) and the fluorescence emission intensity (S) in time domain ((a) and (b)) and frequency domain ((c) and (d)). $N_C = 50$; $R_0 = 2.5\,\mu m$; $P_A = 100\,kPa$. Signals only at the first 10 μs are shown in the time domain. The oscillation at the first four cycles is similar to Fig. 3.7 ($N_C = 10$). The peak amplitudes of the oscillation after the first four cycles are almost constant. With longer time of the signal, the frequency bandwidth becomes narrower. However the oscillation amplitudes are the same as the case for 10 pulses of US.

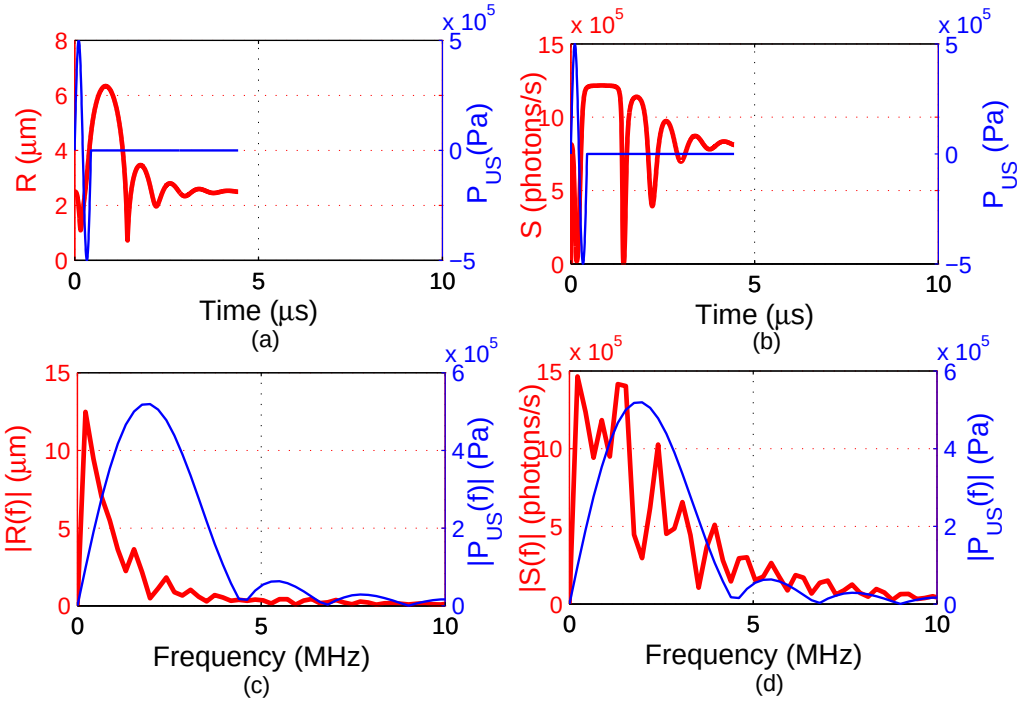


Figure A.3: Oscillation of microbubble radius (R) and fluorescence emission intensity (S) in time domain ((a) and (b)) and frequency domain ((c) and (d)). $N_C = 1$; $R_0 = 2.5\,\mu m$; $P_A = 500\,kPa$.

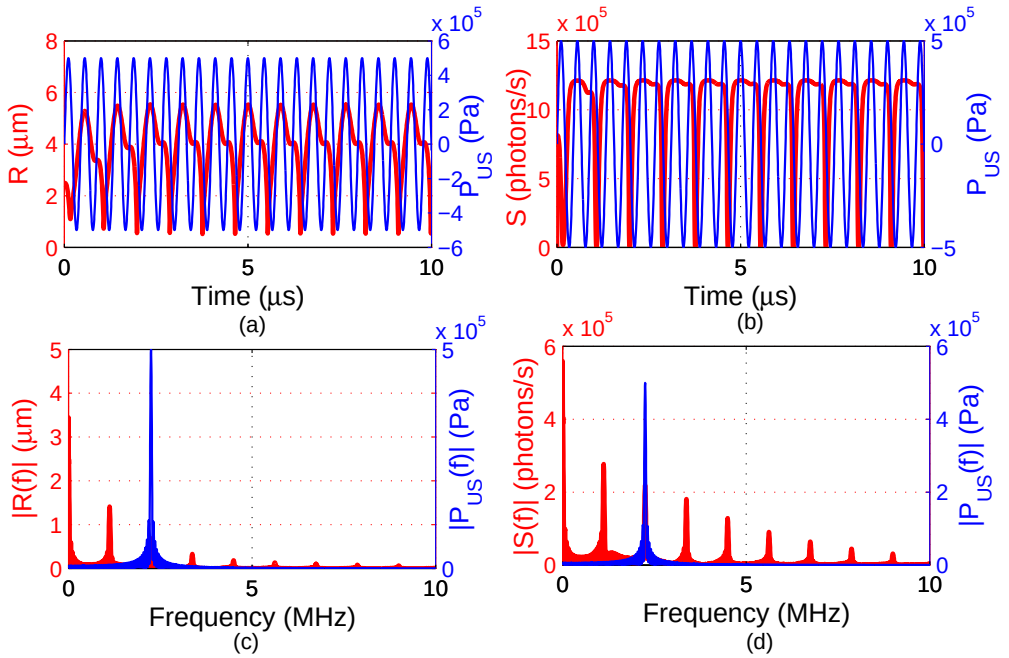


Figure A.4: Oscillation of microbubble radius (R) and fluorescence emission intensity (S) in time domain ((a) and (b)) and frequency domain ((c) and (d)). $N_C = 50$; $R_0 = 2.5\,\mu m$; $P_A = 500\,kPa$. It can be seen that the oscillation amplitudes are almost constant after the second cycle of oscillation.

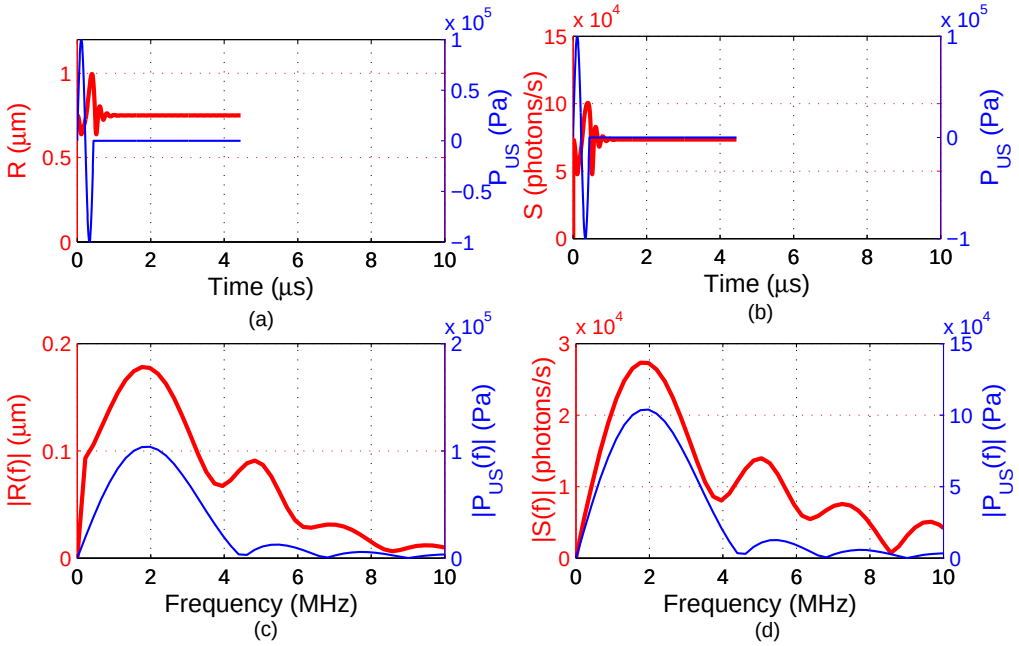


Figure A.5: Oscillation of microbubble radius (R) and fluorescence emission intensity (S) in time domain ((a) and (b)) and frequency domain ((c) and (d)). $N_C = 1$; $R_0 = 0.75\,\mu m$; $P_A = 100\,kPa$. The time periods of the oscillation for both the size and the emission intensity are shorter compared with $R_0 = 2.5\,\mu m$ microbubble shown in Fig. A.1. The time for 2.5 μm and 0.75 μm microbubble to undergo four cycles of oscillation (radius and emission intensity) are 3.1 μs and 1.0 μs respectively.

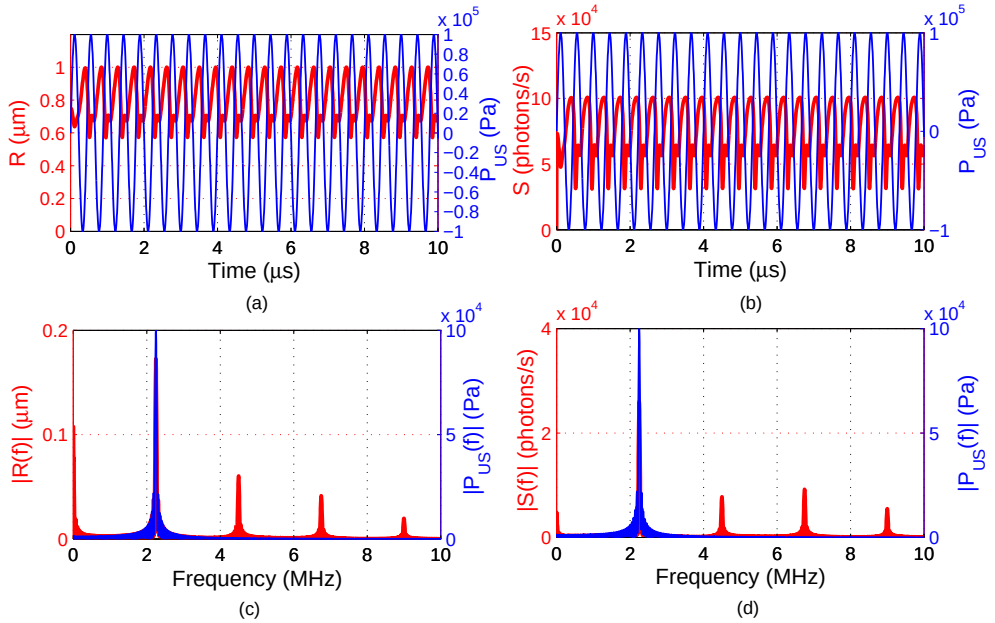
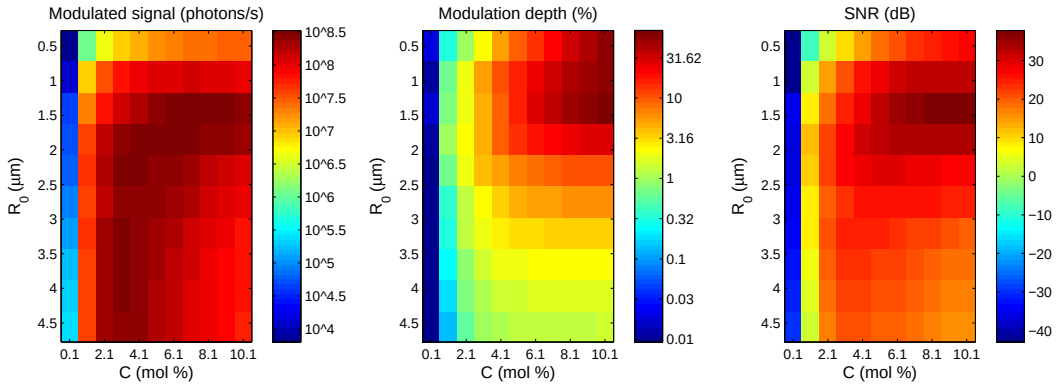


Figure A.6: Oscillation of microbubble radius (R) and fluorescence emission intensity (S) in time domain ((a) and (b)) and frequency domain ((c) and (d)). $N_C = 50$; $R_0 = 0.75\,\mu m$; $P_A = 100\,kPa$.

APPENDIX B

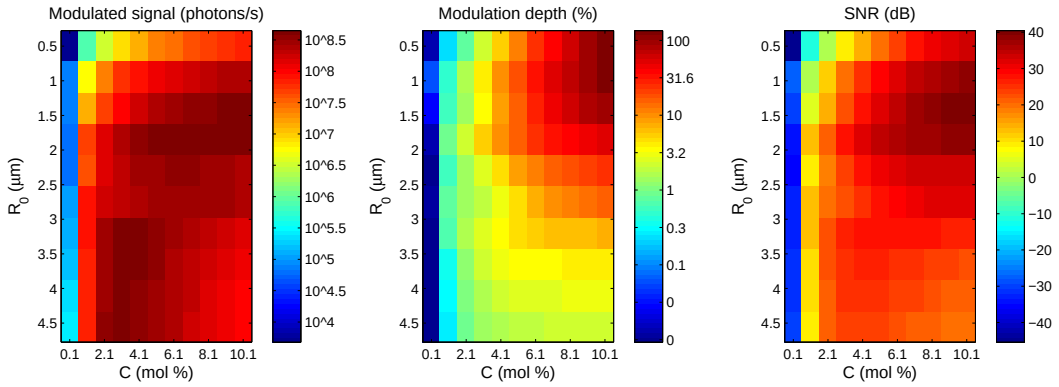
Modulation depth and SNR in a scattering phantom

Simulation results for the modulated signal, modulation depth, and SNR while varying R_0 and C in a scattering medium are shown in the following. The simulation is similar to that in Section 3.3.4 of Chapter 3, but at different US pressures (Fig. B.1: $P_A = 200\,\text{kPa}$; Fig. B.2: $P_A = 300\,\text{kPa}$; Fig. B.3: $P_A = 400\,\text{kPa}$; Fig. B.4: $P_A = 500\,\text{kPa}$; Fig. B.5: $P_A = 600\,\text{kPa}$). It can be seen that US does not change the dependance of the modulated signal, modulation depth, and SNR on R_0 and C.



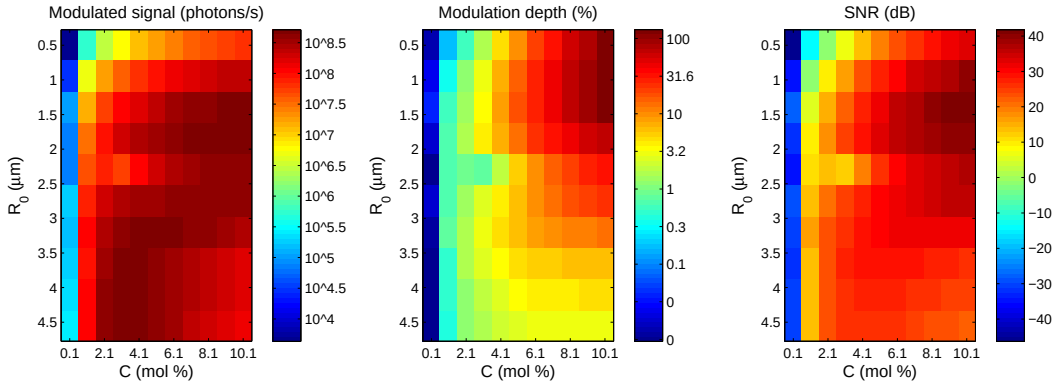
(a) (b) (c)

Figure B.1: Influence of R_0 and C on (a) modulated signal; (b) modulation depth; and (c) SNR. $P_A = 200\,\text{kPa}$.



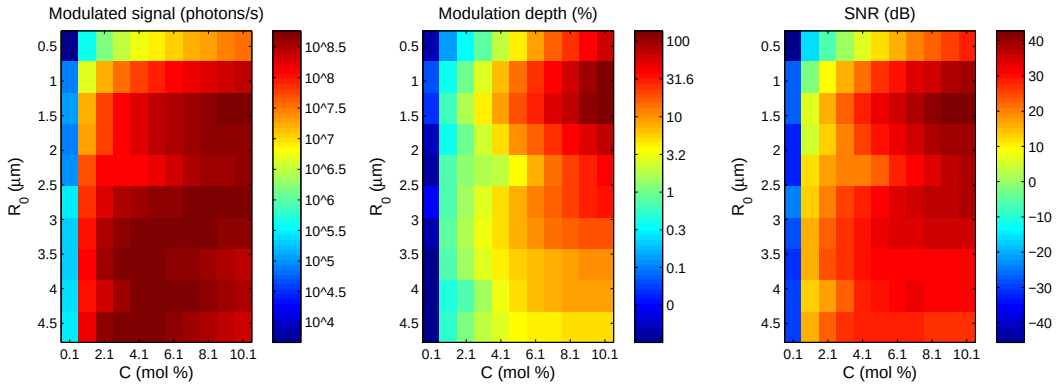
(a) (b) (c)

Figure B.2: Influence of R_0 and C on (a) modulated signal; (b) modulation depth; and (c) SNR. $P_A = 300\,\text{kPa}$.



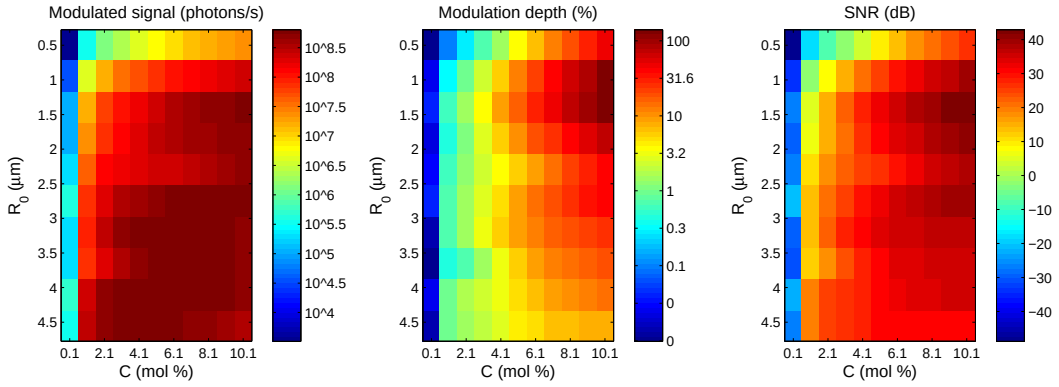
(a) (b) (c)

Figure B.3: Influence of R_0 and C on (a) modulated signal; (b) modulation depth; and (c) SNR. $P_A = 400\,\text{kPa}$.



(a) (b) (c)

Figure B.4: Influence of R_0 and C on (a) modulated signal; (b) modulation depth; and (c) SNR. $P_A = 500\,\text{kPa}$.



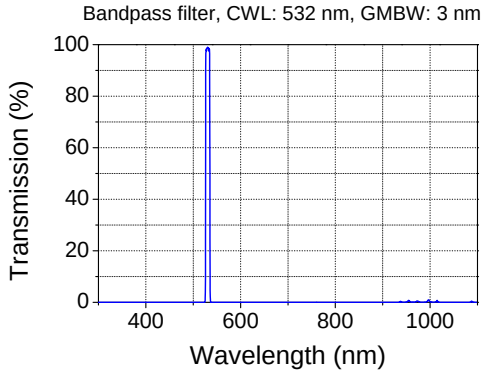
(a) (b) (c)

Figure B.5: Influence of R_0 and C on (a) modulated signal; (b) modulation depth; and (c) SNR. $P_A = 600\,\text{kPa}$.

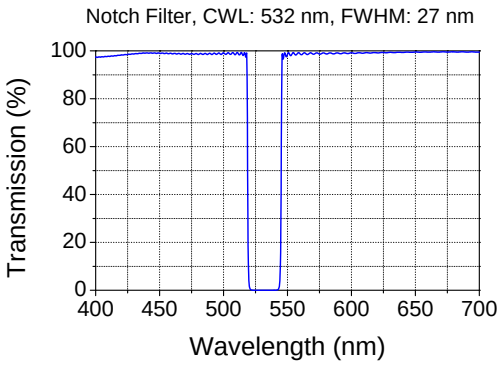
APPENDIX C

Spectra of the optical filters

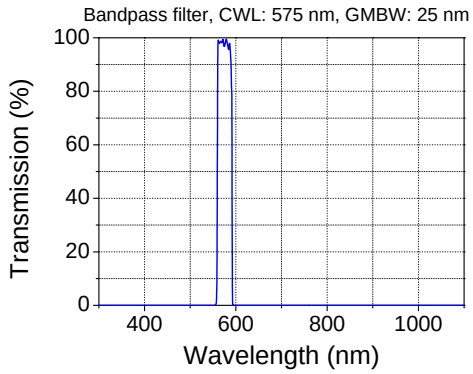
The spectra of the optical filters used in this thesis are provided in the following. Filters with spectra shown in Fig. C.1a, Fig. C.1b and Fig. C.1c are used in Chapter 3; filters with spectra shown in Fig. C.1d and Fig. C.1e are used in Chapter 4; filters with spectra shown in Fig. C.1f, Fig. C.1g and Fig. C.1h are used in Chapter 5.



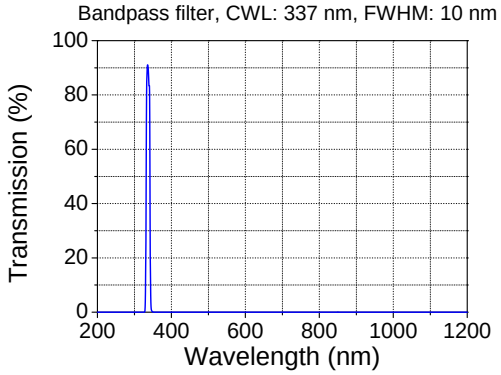
(a)



(b)



(c)



(d)

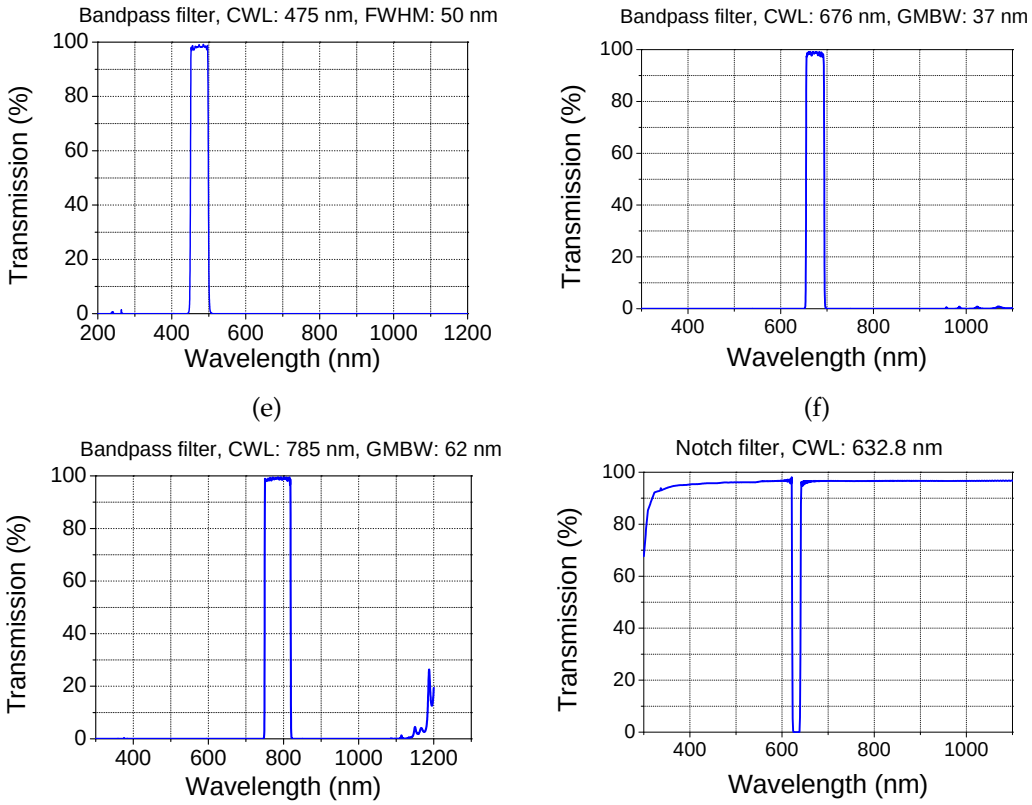


Figure C.1: Spectra of the optical filters. (a) FF01-532/3-25; (b) #67-119; (c) FF02-575/25-25; (d) #65-128; (e) #86-962; (f) FF01-676/37-25; (g) #87-759; (h) NT63-347. Data in (a), (c), (f) were provided by Semrock, New York, USA. Data in (b), (d), (e), (g), (h) were provided by Edmund Optics, York, UK.

APPENDIX D

Measurements of absorbance spectra

To obtain $\epsilon_{DiR}/\epsilon_{DiD}$ for calculation of DiR based FRET efficiency in Section 5.4.1 of Chapter 5, the absorbance spectra of DiD only liposomes and DiR only liposomes were measured using a spectrophotometer (Biochrom Libra S32 PC, Cambridge, UK). The prepared DiD and DiR only liposomes were diluted 10 times to have a lipid concentration of 1.28 mM, which is the same as that used for fluorescence emission spectrum measurements. DiD or DiR concentrations of 0.05 mol%, 0.1 mol%, 0.25 mol%, 0.5 mol%, 0.75 mol% and 1 mol% were measured. Wavelengths from 450 nm to 900 nm were scanned with a step of 1 nm and scan speed of 1856 nm/min. PBS buffer were used as a reference and the reference scan acted as a temporary baseline for the other samples. The measured results of DiD only liposomes, DiR only liposomes, and PBS buffer were shown in Fig. D.1, Fig. D.2, and Fig. D.3 respectively. The absorbance at 633 nm was extracted from the absorbance spectra and summarized in Table D.1.

Table D.1: Absorbance at 633 nm of DiD only liposomes and DiR only liposomes.

Concentration (mol%)	A_{DiD} [1]	A_{DiR} [2]	A_{DiR}/A_{DiD}
0.05	0.35	0.36	1.03
0.1	0.50	0.27	0.54
0.25	0.70	0.35	0.50
0.5	1.23	0.50	0.41
0.75	1.52	0.60	0.39
1	1.67	0.63	0.38

[1] Absorbance of DiD only liposomes
[2] Absorbance of DiR only liposomes

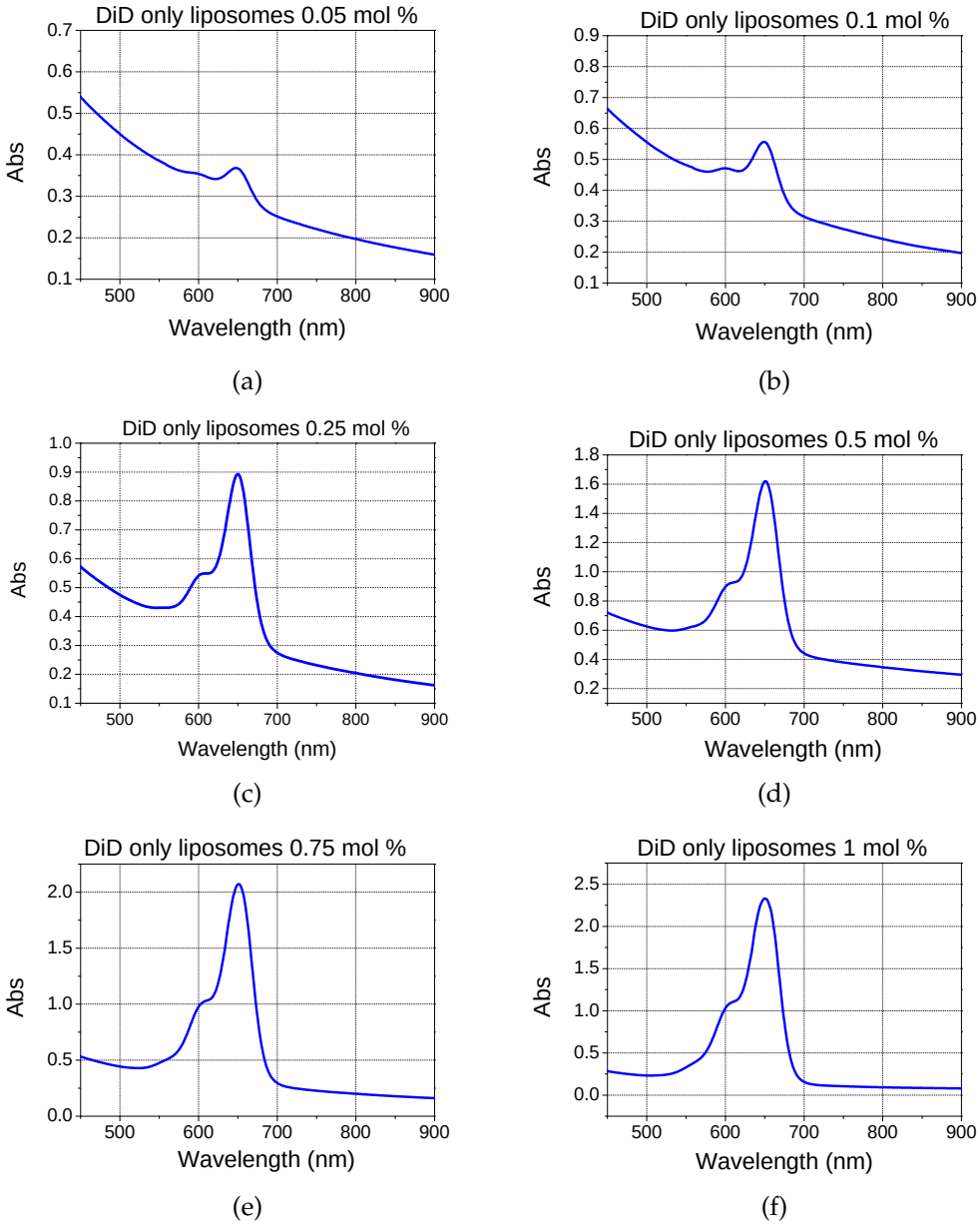


Figure D.1: Absorbance (Abs) spectra of DiD only liposomes at (a) 0.05 mol%; (b) 0.1 mol%; (c) 0.25 mol%; (d) 0.5 mol%; (e) 0.75 mol%; (f) 1 mol%.

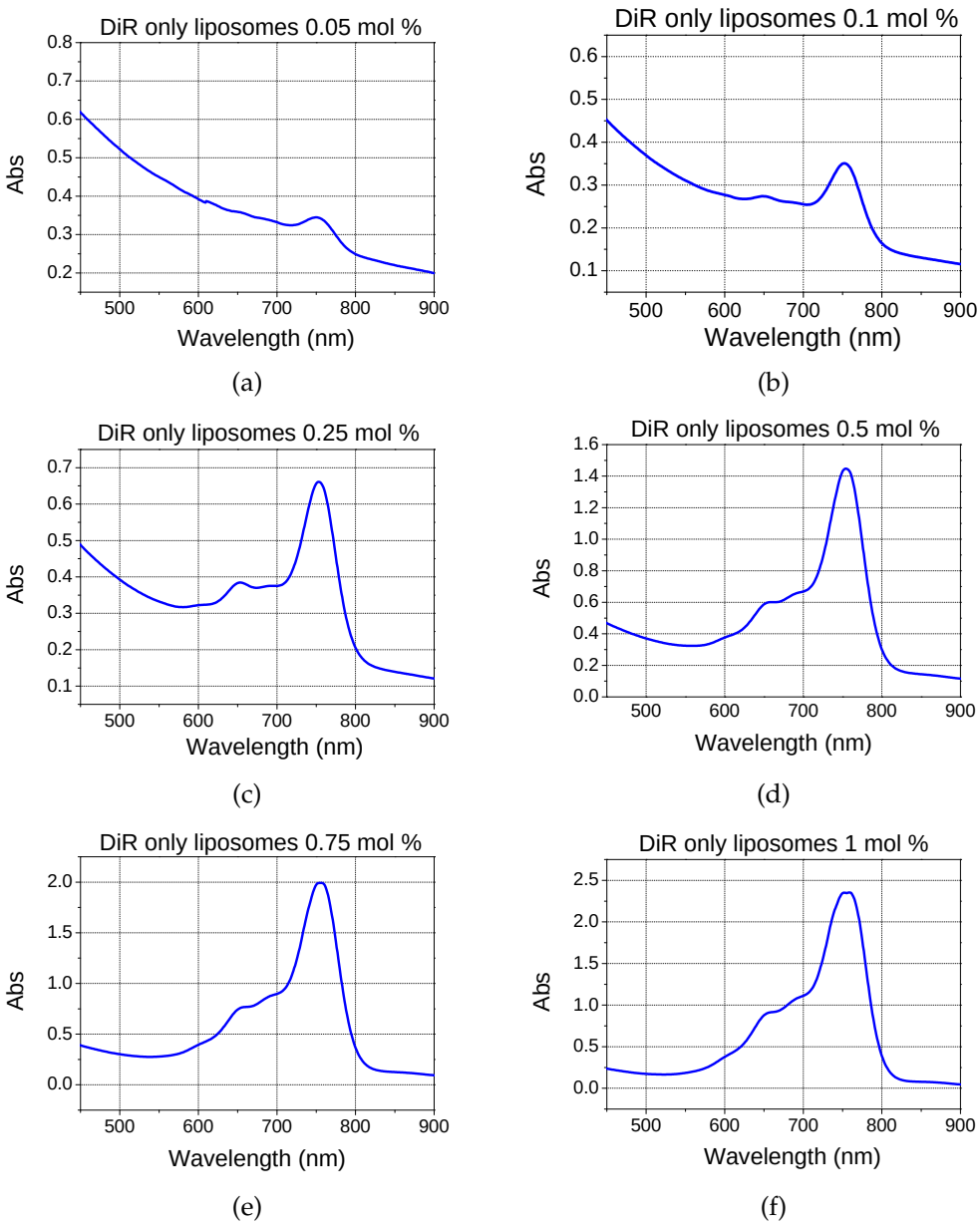


Figure D.2: Absorbance (Abs) spectra of DiR only liposomes at (a) 0.05 mol%; (b) 0.1 mol%; (c) 0.25 mol%; (d) 0.5 mol%; (e) 0.75 mol%; (f) 1 mol%.

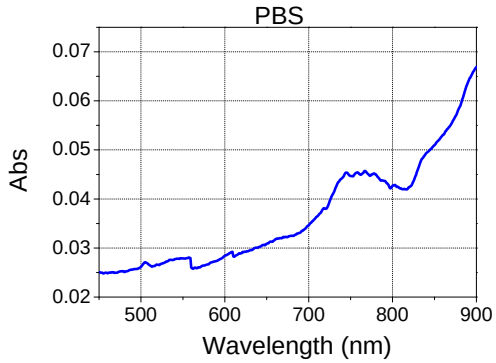
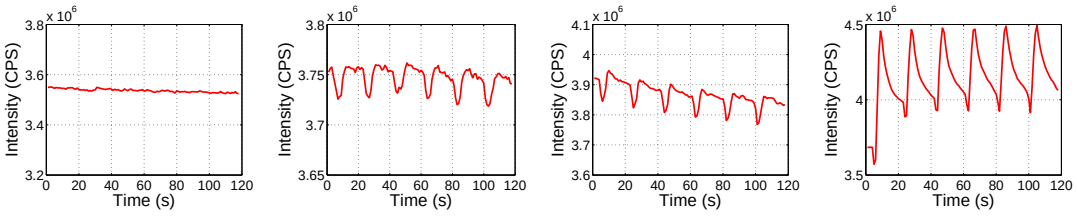


Figure D.3: Absorbance (Abs) spectra of PBS buffer.

APPENDIX E

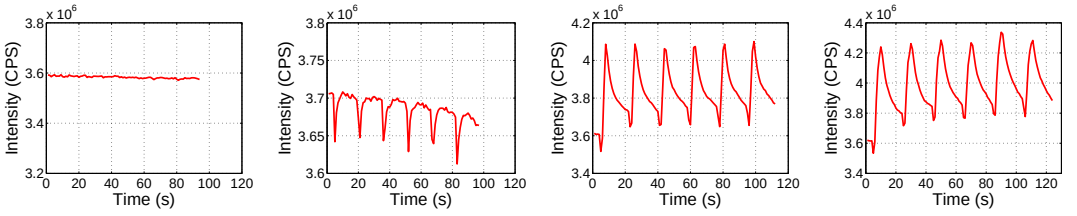
Influence of US pressure and exposure time

The dependance of the intensity difference and On-to-Off ratio on US pressure and exposure time were investigated in Section 5.5.3 of Chapter 5. Here the US mediated variations of the fluorescence emission intensity at individual US pressure and exposure time are provided.



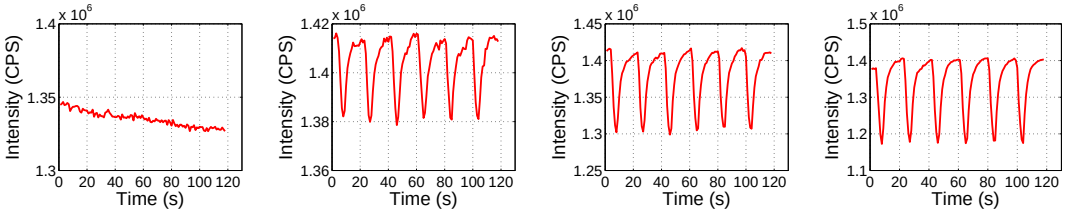
(a) (b) (c) (d)

Figure E.1: US mediated variation of fluorescence emission intensity at US pressures (a) 0.26 MPa; (b) 0.7 MPa; (c) 1.21 MPa; (d) 2 MPa when detecting at DiD emission wavelength from DiD-DiR labelled liposomes with 0.1 mol % concentration.



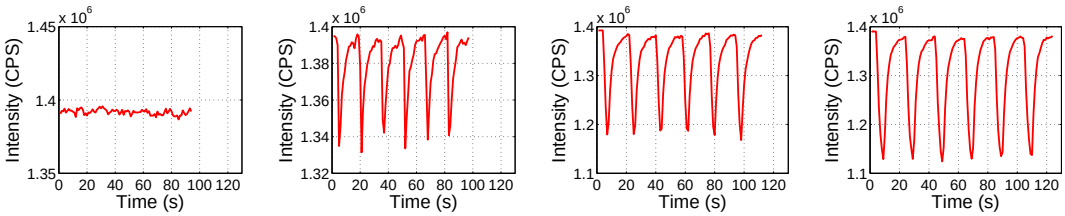
(a) (b) (c) (d)

Figure E.2: US mediated variation of fluorescence emission intensity at US exposure times (a) 0.01 s; (b) 0.5 s; (c) 3 s; (d) 5 s when detecting at DiD emission wavelength from DiD-DiR labelled liposomes with 0.1 mol % concentration.



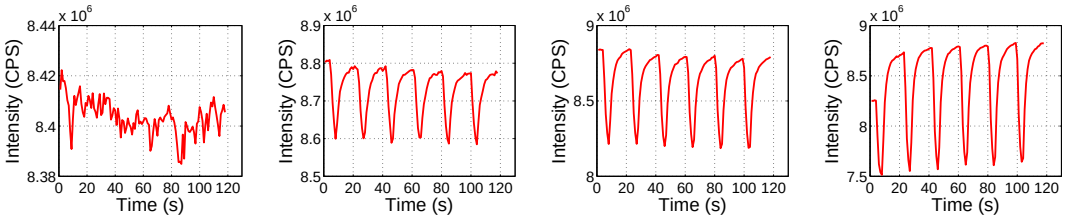
(a) (b) (c) (d)

Figure E.3: US mediated variation of fluorescence emission intensity at US pressures (a) 0.26 MPa; (b) 0.7 MPa; (c) 1.21 MPa; (d) 2 MPa when detecting at DiR emission wavelength from DiD-DiR labelled liposomes with 0.1 mol % concentration.



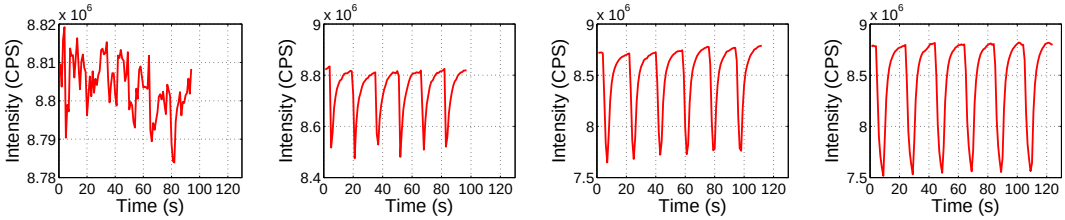
(a) (b) (c) (d)

Figure E.4: US mediated variation of fluorescence emission intensity at US exposure times (a) 0.01 s; (b) 0.5 s; (c) 3 s; (d) 5 s when detecting at DiR emission wavelength from DiD-DiR labelled liposomes with 0.1 mol % concentration.



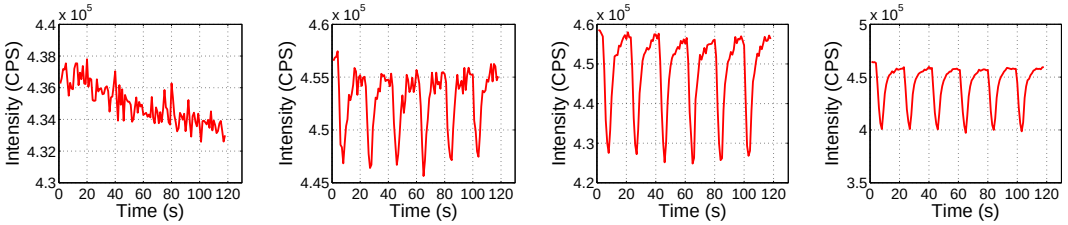
(a) (b) (c) (d)

Figure E.5: US mediated variation of fluorescence emission intensity at US pressures (a) 0.26 MPa; (b) 0.7 MPa; (c) 1.21 MPa; (d) 2 MPa when detecting at DiD emission wavelength from DiD labelled liposomes with 0.1 mol % concentration.



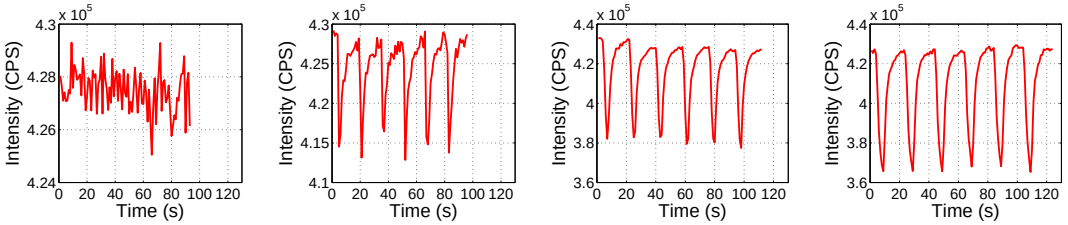
(a) (b) (c) (d)

Figure E.6: US mediated variation of fluorescence emission intensity at US exposure times (a) 0.01 s; (b) 0.5 s; (c) 3 s; (d) 5 s when detecting at DiD emission wavelength from DiD labelled liposomes with 0.1 mol % concentration.



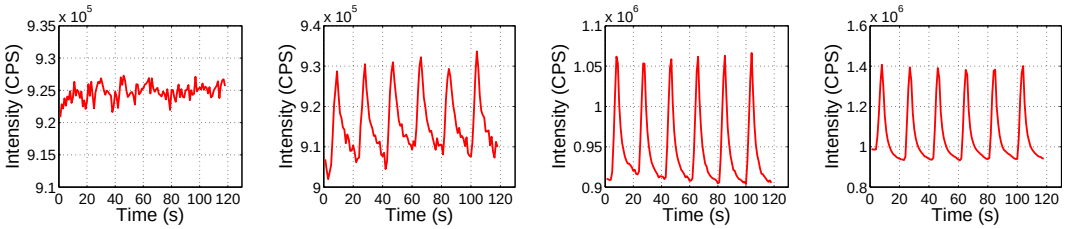
(a) (b) (c) (d)

Figure E.7: US mediated variation of fluorescence emission intensity at US pressures (a) 0.26 MPa; (b) 0.7 MPa; (c) 1.21 MPa; (d) 2 MPa when detecting at DiR emission wavelength from DiD labelled liposomes with 0.1 mol % concentration.



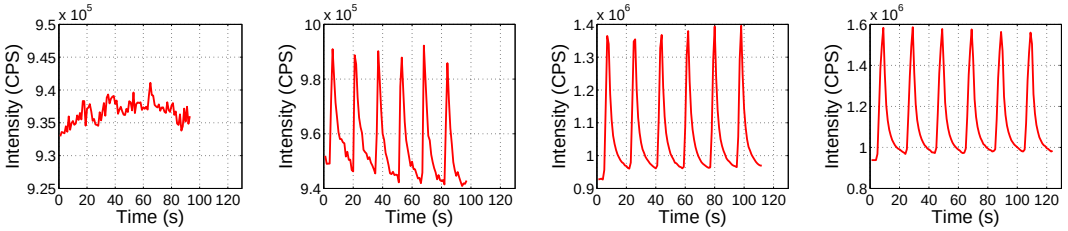
(a) (b) (c) (d)

Figure E.8: US mediated variation of fluorescence emission intensity at US exposure times (a) 0.01 s; (b) 0.5 s; (c) 3 s; (d) 5 s when detecting at DiR emission wavelength from DiD labelled liposomes with 0.1 mol % concentration.



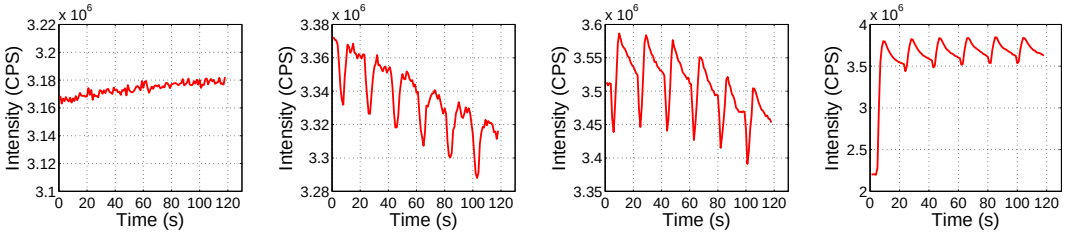
(a) (b) (c) (d)

Figure E.9: US mediated variation of fluorescence emission intensity at US pressures (a) 0.26 MPa; (b) 0.7 MPa; (c) 1.21 MPa; (d) 2 MPa when detecting at DiD emission wavelength from DiD-DiR labelled liposomes with 0.5 mol % concentration.



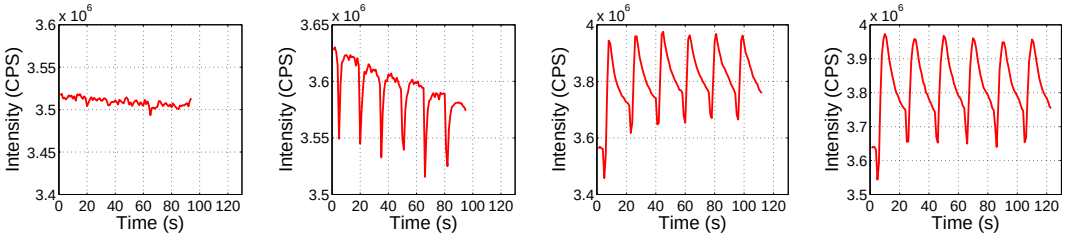
(a) (b) (c) (d)

Figure E.10: US mediated variation of fluorescence emission intensity at US exposure times (a) 0.01 s; (b) 0.5 s; (c) 3 s; (d) 5 s when detecting at DiD emission wavelength from DiD-DiR labelled liposomes with 0.5 mol % concentration.



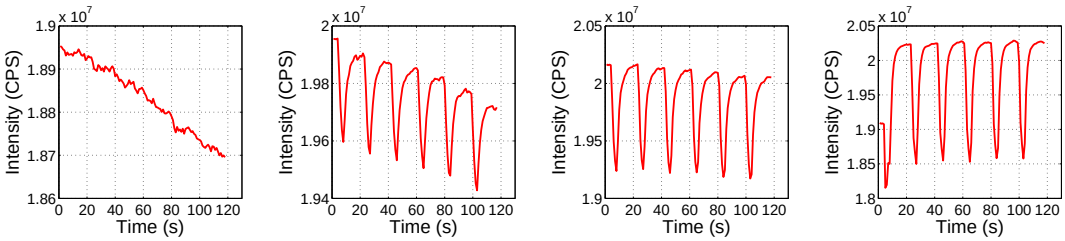
(a) (b) (c) (d)

Figure E.11: US mediated variation of fluorescence emission intensity at US pressures (a) 0.26 MPa; (b) 0.7 MPa; (c) 1.21 MPa; (d) 2 MPa when detecting at DiR emission wavelength from DiD-DiR labelled liposomes with 0.5 mol % concentration.



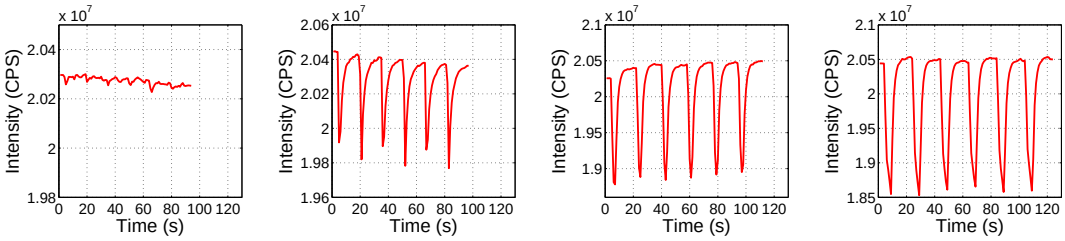
(a) (b) (c) (d)

Figure E.12: US mediated variation of fluorescence emission intensity at US exposure times (a) 0.01 s; (b) 0.5 s; (c) 3 s; (d) 5 s when detecting at DiR emission wavelength from DiD-DiR labelled liposomes with 0.5 mol % concentration.



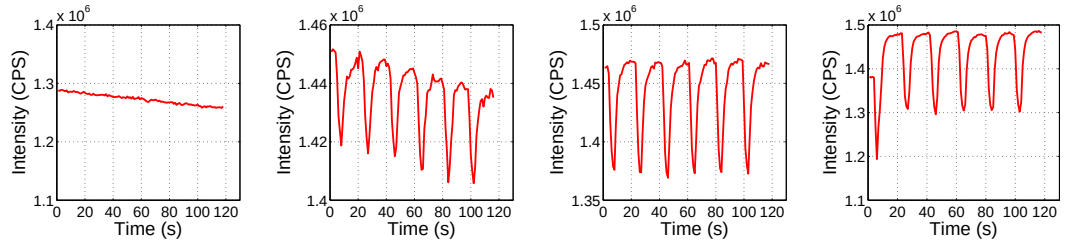
(a) (b) (c) (d)

Figure E.13: US mediated variation of fluorescence emission intensity at US pressures (a) 0.26 MPa; (b) 0.7 MPa; (c) 1.21 MPa; (d) 2 MPa when detecting at DiD emission wavelength from DiD labelled liposomes with 0.5 mol % concentration.



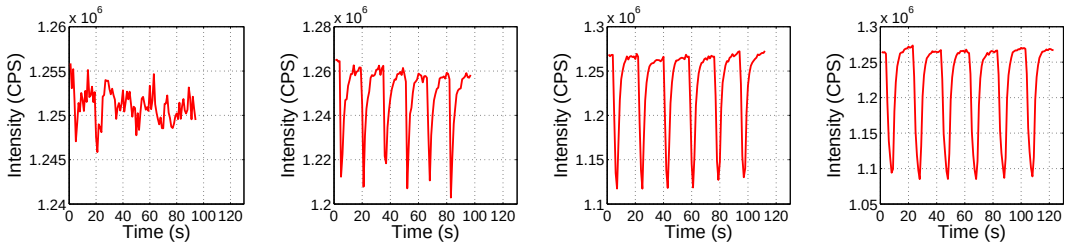
(a) (b) (c) (d)

Figure E.14: US mediated variation of fluorescence emission intensity at US exposure times (a) 0.01 s; (b) 0.5 s; (c) 3 s; (d) 5 s when detecting at DiD emission wavelength from DiD labelled liposomes with 0.5 mol % concentration.



(a) (b) (c) (d)

Figure E.15: US mediated variation of fluorescence emission intensity at US pressures (a) 0.26 MPa; (b) 0.7 MPa; (c) 1.21 MPa; (d) 2 MPa when detecting at DiR emission wavelength from DiD labelled liposomes with 0.5 mol % concentration.



(a) (b) (c) (d)

Figure E.16: US mediated variation of fluorescence emission intensity at US exposure times (a) 0.01 s; (b) 0.5 s; (c) 3 s; (d) 5 s when detecting at DiR emission wavelength from DiD labelled liposomes with 0.5 mol % concentration.